# Effects of the Unsteady Blade Loading on the Aero-Acoustic Performance of a Boundary Layer Ingesting Propeller

Donato Melpignano

TU Delft

# Effects of the Unsteady Blade Loading on the Aero-Acoustic Performance of a Boundary Layer Ingesting Propeller

Thesis report

by

Donato Melpignano

to obtain the degree of Master of Science
at the Delft University of Technology
to be defended publicly on September 5, 2024 at 14:00

*Thesis committee*:

| | |
|---|---|
| Chair: | Prof.dr.ing. G. Eitelberg |
| Supervisors: | Dr.ir. T. Sinnige |
| | Ir. Daamanjyot Barara |
| External examiner: | Dr.R. Merino Martinez |
| Place: | Faculty of Aerospace Engineering, Delft |
| Student number: | 5627613 |

An electronic version of this thesis is available at `http://repository.tudelft.nl/`.

Faculty of Aerospace Engineering · Delft University of Technology

Cover image A400 M propeller, source: https://pixabay.com/it/photos/a400m-elica-scimitarra-elica-4416895/

# Preface

This thesis represents the result of a year of hard work and the final step in my university journey, which began six years ago at a different university in a different country. Writing this thesis has been both challenging and rewarding, fueled by my deep interest in aviation, propulsion, and my passion for unconventional design. Completing this work required me to use all the tools and knowledge I've gained over the years.

I want to express my deepest gratitude to my supervisors, Tomas Sinnige and Daaman Barara. Tomas's guidance and expertise were invaluable, and I've always relied on Daaman's support throughout this process.

I also want to thank the faculty and staff at TU Delft for their support and the resources that made this research possible. I'm very grateful for the insightful discussions with colleagues I've met during my studies at Politecnico di Milano and TU Delft. Their ideas and perspectives have greatly enriched my experience.

I'd like to thank my friends—both those who have been with me since high school and the new ones I met during my university years. The time I spent with the people at Milano Accademia made my three years in Milan truly special.

Lastly, a special thanks to my family, who have always encouraged and supported me. I'm especially grateful to my parents, who, in allowing me to follow my passion, had to endure the challenge of having their only child live far from home. A special thanks also goes to my uncle Franco, who first sparked my passion for aviation and encouraged me to apply to TU Delft.

While this journey had its challenges, it was also full of growth and learning. These experiences have only strengthened my passion for this field. I hope this work contributes to sustainable aviation efforts and inspires future research.

# Summary

In recent years, the civil aviation sector has increasingly focused on optimizing propulsion designs and aircraft configurations to improve efficiency, reduce fuel consumption, and lower $CO_2$ emissions. Propellers have regained attention due to their superior propulsive efficiency and adaptability with various power units, including full electric applications. However, high noise emissions remain a significant challenge for propeller performance.
This thesis investigates the aerodynamic and acoustic performance of Boundary Layer Ingesting (BLI) propellers as part of the Advanced Propulsion and Power Unit (APPU) project, a collaboration involving TU Delft, Airbus, and Safran, aimed at reducing $CO_2$ emissions in high subsonic transport planes like the A320. In this setup, the BLI propeller is installed at the end of the fuselage behind the vertical tail, where it encounters non-uniform inflow, leading to time-varying loads on the blades, affecting both aerodynamic and acoustic performance.
The primary objective of this thesis is to analyze the unsteady blade loading experienced by a propeller in a BLI configuration and assess its impact on aerodynamic and aero-acoustic performance. Additionally, the study explores whether increasing the blade count or modifying the blade sweep distribution can enhance the benefits or mitigate the drawbacks of this installation.

A numerical investigation was performed, starting with the development of aerodynamic and acoustic tools to estimate propeller performance. The aerodynamic tool uses the Unsteady Vortex Lattice Method, which is suitable for modeling propellers with various blade geometries under time-varying inflow conditions. This method, based on potential theory, was enhanced to account for viscosity and flow separation, resulting in an Unsteady Non-Linear Vortex Lattice Method. The acoustic solver employs Hanson's Helicoidal Surface Theory to model noise emissions from propellers in both isolated and installed conditions, accounting for thickness, steady loading, and unsteady loading noise sources. This analytical method was chosen for its computational efficiency and ability to incorporate various features, such as the change in phase of noise contributions along the blade span due to sweep.

Simulations were conducted for a baseline propeller in both isolated and installed BLI configurations. The baseline model adopted was a modified version of the 6-bladed XPROP-S, characterized by a large hub-to-tip ratio to fit the BLI installation. The propeller was simulated at a fixed inflow velocity of $U_\infty = 40m/s$ and a pitch setting of $\beta = 45^\circ$ to maintain operating conditions similar to those used in the validation process. The inflow for the BLI propeller was taken from velocity profiles at the propeller disk obtained from CFD simulations of the fuselage with the vertical tail mounted. The propellers were analyzed at two conditions, one characterized by a larger spinning velocity ($J = 1.2$) representing the climb phase and one at a lower thrust setting ($J = 1.8$) representing the cruise condition.

The complex inflow field resulted in periodic increases in blade loading when the blades passed below the fuselage and more abrupt changes when passing behind the vertical tail. This led to oscillations in the thrust and power produced by the propeller. Despite flow separation during the climb phase—caused by an excessive pitch setting and triggered by the abrupt reduction in axial velocity due to the distorted inflow—propellers not specifically designed for this configuration still demonstrated increased thrust-to-power ratios, ranging from $2\%$ to $5\%$, depending on the geometry and operating conditions. This performance increase was accompanied by in-plane forces in both vertical and horizontal directions, which scaled with the thrust generated and remained within $3\%$ of the thrust.
Noise emissions significantly increased upon installation due to the introduction of unsteady loading noise sources. In isolated conditions, steady loading noise—particularly the torque component—was the dominant factor, with maximum emissions occurring in the rotational plane of the propeller ($SPL_{Max} = 62dB$ during climb, $SPL_{Max} = 32dB$ during cruise). However, once the propeller was installed, the peak emissions shifted to align with the propeller axis ($SPL_{Max} = 77dB$ during climb, $SPL_{Max} = 78dB$ during cruise), where the thrust component's loading contribution was more pronounced. This shift occurred because the unsteady loading noise sources exhibited maximum propagation efficiency in the direction of the thrust component's propagation.

The parametric study revealed that increasing the blade count from two to six resulted in a steadier performance response and reduced in-plane force oscillations due to the reduced relative importance of the blade undergoing the most abrupt change in inflow behind the vertical tail. Regarding noise levels, despite increasing disk loading with more blades, noise levels decreased in isolated conditions due to the reduced propagation efficiency of steady loading noise sources. However, in installed conditions, the addition of unsteady loading noise sources counterbalanced this reduction, leading to overall increased noise levels. For example, in isolated conditions, maximum loading noise emissions were $SPL_{Max} = 71dB$ for the two-bladed propeller and $SPL_{Max} = 32dB$ for the six-bladed propeller, while in installed conditions, they were $SPL_{Max} = 74dB$ for the two-bladed propeller and $SPL_{Max} = 75dB$ for the six-bladed propeller.

The parametric study in which the baseline straight blade was swept backward at the tip and forward near the hub revealed that the angle of attack along the blade sections increased under both isolated and installed conditions. This led to an increase in loading, particularly at the tips, where the relative air velocity is highest due to propeller rotation, and generally, an increase in thrust and power required by up to $20\%$ compared to the baseline straight blades. In installed conditions, the chord-wise displacement of various sections meant that the blade sections did not simultaneously encounter the flow distortion. This resulted in a reduction of the overall change in blade loading when the blades were swept backward and an increase when the blades were swept forward, compared to the baseline straight blade.
Regarding noise emissions, the analysis demonstrated that sweep affects them through three primary mechanisms: changes in loading toward the tip, changes in the phase of noise sources along the blade span in isolated conditions, and changes in the phase of unsteady loading contributions along the blade span in installed conditions. In isolated propellers, sweep application resulted in a noise level increase of up to $\Delta SPL = +0.6dB$, primarily due to the adverse effects of increased loading toward the outboard sections. In installed conditions, where unsteady loading noise was dominant, the phase change of the unsteady loading contribution from the different blade sections played a significant role, leading to noise reduction by up to $\Delta SPL = -4.7dB$ with backward sweep, or an increase of up to $\Delta SPL = +2.2dB$ with forward sweep.

The analysis demonstrated that noise emissions are highly sensitive to the spinning tip Mach number ($M_t$). Since the aerodynamic analysis was restricted to low-speed propellers, the aero-acoustic results discussed earlier were obtained at a low spinning tip Mach number of $M_t = 0.2$. However, when an aero-acoustic analysis was conducted using the scaled loading coefficients from the aerodynamic solver with a higher spinning tip Mach number of $M_t = 0.8$, the results indicated that, even for the 6-bladed baseline propeller, steady loading noise remained dominant, with the highest emissions occurring in the propeller's rotational plane. This dominance is due to the increased efficiency of noise propagation at higher Mach numbers, particularly for steady loading noise sources.
The spinning tip Mach number also significantly influences the effectiveness of sweep in reducing noise emissions. At higher rotational speeds, the wavelength of the noise emissions shortens relative to the blade section's displacement due to sweep, resulting in a more substantial reduction in noise emissions. Therefore, it is recommended that future research continue investigating this topic using methodologies capable of accurately modeling propellers at high Mach numbers, ensuring that relevant conclusions can be drawn for applications like the APPU project.

In summary, the methodology adopted in this research successfully balanced fidelity and computational time, achieving the thesis objectives for scaled propellers operating at low speeds. The inclusion of unsteady blade loading had significant effects on aerodynamic and aero-acoustic performance, justifying the focus on this area of research. The study's findings on the effects of sweep on unsteady loading and aero-acoustic performance are particularly noteworthy. However, the inherent limitations of this approach may restrict the applicability of the conclusions to propellers operating under conditions similar to those studied in this thesis.

# Contents

# Nomenclature

### List of Abbreviations

| | |
|---|---|
| BLI | Boundary Layer Ingestion |
| BPF | Blade Passage Frequency |
| CFD | Computational Fluid Dynamics |
| FA | Face Alignment |
| HST | Helicoidal Surface Theory |
| MCA | Mid-Chord-Alignment |
| RANS | Reynolds Averaged Navier-Stokes |
| RMS | Root Mean Square |
| SPL | Sound Pressure Level |
| TSSP | Thrust Specific Sound Pressure |
| UNVLM | Unsteady Non-Linear Vortex Lattice Method |
| UVLM | Unsteady Vortex Lattice Method |
| VLM | Vortex Lattice Method |

### List of Symbols

| | |
|---|---|
| $\alpha$ | Angle of attack |
| $\beta$ | Twist angle |
| $\beta_{0.7R}$ | Pitch setting |
| $\eta$ | Propulsive Efficiency |
| $\Gamma$ | Circulation |
| $\Lambda$ | MCA at the tip (Sweep Parameter) |
| $\lambda_1$ | Backward sweep at the tip (Sweep Parameter) |
| $\lambda_2$ | Forward sweep at the hub (Sweep Parameter) |
| $\phi$ | Inflow angle - In-rotational plane observer angle |
| $\phi'$ | Azimuth Blade angle |
| $\phi_o$ | Lean Phase Delay |
| $\phi_s$ | Sweep Phase Delay |
| $\Psi$ | Noise source term |
| $\sigma$ | Solidity |
| $\theta$ | Observer angle in the plane along the observer axis |
| $B$, $N_B$ | Number of Blades |
| $C_D$ | Drag Coefficient |
| $C_L$ | Lift Coefficient |
| $C_P$, $P_C$ | Power Coefficient |
| $C_Q$ | Torque Coefficient |
| $C'_Q$ | Sectional Torque Coefficient |
| $C_T$, $T_C$ | Thrust Coefficient |
| $C'_T$ | Sectional Thrust Coefficient |
| $C_Y$ | Horizontal in-plane Force Coefficient |
| $C_Z$ | Vertical in-plane Force Coefficient |
| $D$ | Propeller Diameter |
| $F_N$ | In-plane Force |
| $F_Q$ | Tangential Force |
| $J$ | Advance Ratio |
| $J_n$ | Bessel function of order n |
| $k$ | Loading Harmonic |
| $k_x$ | Thickness Wave Number |
| $k_y$ | Chordwise Wave Number |
| $m$ | Noise Harmonic |
| $M_r$ | Radial Mach Number |
| $M_s$ | Spinning Mode Tip Mach Number |
| $M_t$ | Spinning Tip Mach Number |
| $M_x$ | Free-stream Mach Number |
| $n$ | Angular velocity $[RPS]$ |

| | |
|---|---|
| $N_C$ | Number of sections along the chord |
| $N_S$ | Number of sections along the blade span |
| $N_{W0}$ | Number of rows of the pre-allocated wake |
| $N_{W1}$ | Number of wake rows considered in the computations |
| $p_{ref}$ | Pressure of Reference |
| $p_{rms}$ | Root Mean Square of the Acoustic Pressure |
| $Q$ | Torque |
| $R_{hub}$ | Propeller hub radius |
| $R_{Tip}$ | Propeller tip radius |
| $T$ | Thrust |
| $U_\infty$ | Axial velocity component |
| $V_T$ | Tangential velocity component |

# List of Figures

# List of Tables

# Part I

## Background

# 1

# Introduction

This chapter initiates the thesis report, offering a comprehensive introduction to the forthcoming research. It begins by delving into the motivations behind investigating contemporary BLI propeller technology. The purpose of this thesis project is reaffirmed, and to provide clarity and guidance, an outline of the report is provided.

## 1.1. Historical Background

The study of propellers predates aviation itself, making it a field with a long and storied history. However, interest in this propulsion method waned once alternatives like turbojets and turbofans became available in the second half of the 20th century. Figure 1.1 compares the performance of propellers and turbofans at different speed regimes, emphasizing the wider range of flight speeds of closed propulsors but at the cost of significantly lower propulsive efficiency, resulting in higher fuel consumption. This issue is attributed to the fact that turbojets and turbofans generate thrust by accelerating a relatively small mass flow at higher velocities compared to propellers, which accelerate a larger volume of air to a lower speed due to their larger disk area. Consequently, a greater amount of kinetic energy is wasted in the jet of closed propulsors, leading to reduced propulsive efficiency.

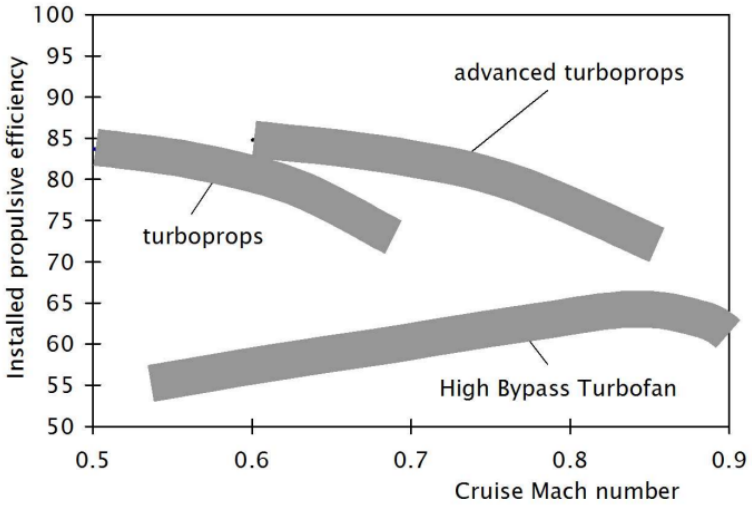


**Figure 1.1:** Comparison of propulsive efficiency of different propulsors at different cruise speeds by [1]. Turboprops use the propeller as a propulsor, while advanced turboprops refer to those which use the propfan.

The interest in open rotors for large transport planes resurged whenever the industry sought to reduce fuel consumption, such as in 1973 when the Yom Kippur War led to the OPEC Embargo and the Oil Crisis, causing a steep increase in fuel costs. At that time, engineers aimed to address two critical issues of open rotors: mitigating noise emissions, inherently louder due to the absence of noise-damping casings, and enhancing performance at high speeds as elucidated in [2]. This historical period is crucial as significant contributions made by researchers during this time, especially in the acoustic field, have been utilized in this thesis.

Another research field that has been active for a long time regards the installation location of the propeller. This is a very active research area at the Delft University of Technology, where researchers have studied a wide range of installations, from the most conventional, like wing-mounted propellers subjected to non-zero angle of attack inflows, to more innovative ones like wingtip-mounted propellers. The purpose of this research is twofold: to evaluate the effect of non-uniform flow on the propeller and to quantify the influence of the propeller on the airframe, proposing installation locations that can overall improve flight efficiency and reduce fuel consumption.
One such innovative installation configuration involves placing the propeller at the end of the fuselage, where it ingests the slower boundary layer flow to generate thrust. This concept, known as a Boundary-Layer-Ingesting (BLI) propeller, has shown promising results, with a net gain in efficiency and energy savings compared to uninstalled propellers with uniform inflow. While this concept has been employed in military and maritime applications for some time, as explained by Smith in [3], it has only recently gained prominence in aviation studies. In recent years, manufacturers and research institutes, including TU Delft, Safran, and Airbus, have shown a keen interest in this innovative concept. Since 2020, they have collaborated on the Advanced Propulsion and Power Unit (APPU) Project [4], aimed at enhancing the efficiency of the widely used Airbus A-320 through extensive modifications. This includes the integration of a BLI propeller positioned at the rear of the fuselage, behind the vertical tail, as shown in Figure 1.2. The same velocity profiles at the disk plane used in this project were applied to characterize the inflow for the propeller in the BLI configuration studied in this thesis.


**Figure 1.2:** Artistic depiction of the APPU project, a modified version of the Airbus A320 studied at TU Delft [4].

## 1.2. Research Motives

In recent years, there has been a resurgence of interest in propellers, driven by diverse applications, including electric-powered devices such as drones and urban air mobility vehicles. The exceptional efficiency of propellers enhances the endurance of these platforms, making them an attractive choice. However, this resurgence is not limited to emerging technologies; it has also extended to more conventional sectors, particularly civil aviation, where turbofan engines have long been the standard choice. The renewed interest in propellers can be attributed to heightened public awareness regarding aviation's environmental impact.

As emphasized by Lee et al. [5], aviation contributes significantly to global warming, accounting for approximately $5\%$ of anthropogenic radiative forcing. The industry's rapid growth [6] underscores the urgent need for advancements in aircraft efficiency to mitigate its environmental footprint. To address these concerns, the Advisory Council for Aviation Research in Europe (ACARE) has set ambitious goals for the aviation industry to achieve by 2050 [7]. These objectives include a $50\%$ reduction in $CO_2$ emissions and a substantial $90\%$ reduction in $NO_x$ emissions compared to early 2000s aircraft. Consequently, manufacturers and research institutes are revisiting propellers as a promising choice for reducing fuel consumption, aligning with the industry's sustainability targets.

The previously mentioned APPU project is of particular interest, as it combines the use of propellers with a BLI configuration, bringing the objectives set by ACARE within closer reach. Nevertheless, enhancing performance solely in terms of aerodynamic efficiency is insufficient. Multiple studies in the medical literature have revealed the adverse effects of aircraft noise emissions on human health, including conditions such as hypertension and heart diseases, as documented in [8]. This latter aspect becomes especially pertinent in the context of BLI propellers. Given the unique placement of the propeller in such a configuration, the resulting non-axisymmetric inflow engenders unsteady blade loading. As observed in various scholarly works, the nature of this non-uniformity in the inflow has significant implications: unsteady blade loading has been identified as a primary contributor to worsened acoustic performance [9, 10] and, in some cases, unexpected phenomena such as side forces [11, 1].

## 1.3. Research Objective and Questions

The comprehensive literature survey has elucidated the critical influence of unsteady effects on both the aerodynamics and noise generation of propellers installed in configurations similar to the APPU project. However, it has also brought to light a conspicuous gap in the existing body of research. Specifically, very few studies on BLI propellers have taken into account the unsteady blade loading resulting from non-axisymmetric inflow, and none have incorporated a comprehensive aero-acoustic analysis.

This glaring gap in the literature serves as the primary motivation for the research pursued in this thesis.

**Research Objective**

**The overarching objective of this study is to capture the unsteady loading experienced by the blades of a propeller in a Boundary Layer Ingestion (BLI) installation and evaluate its impact on aerodynamic and aero-acoustic performance. Additionally, this study assesses whether altering the number of blades or the blade sweep distribution can enhance the benefits or mitigate the drawbacks of this installation.**

Once the numerical tools developed to estimate the propeller performance in both isolated and installed conditions are ready and have been validated, the analysis campaign required to achieve the research objective can begin. The research path is guided by the following research questions, which mark the phases and milestones of this journey.

The following research question addresses the impact of the BLI installation on a generic propeller not optimized for this installation, operating at different thrust settings

**Research Question 1**

**What are the challenges arising from the installation of a propeller in a Boundary Layer Ingestion (BLI) position, particularly when accounting for the unsteady effects during the climb and the cruise phase?**
This question can be answered by addressing the single issues highlighted by the following subquestions:

1. **How does the non-uniform inflow influence the blade loading?**
2. **What are the consequences of the altered loading on the overall aerodynamic properties of the propeller?**
3. **How are the tonal noise emissions affected by the installation?**

The last two research questions aim to evaluate the impact on the BLI propeller performance of two design choices usually referred to in the literature as effective to improve the aero-acoustic performance of propellers in isolated conditions. To address these questions, two parametric studies are conducted.

The first design parameter studied is the number of blades.

**Research Question 2**

**Is increasing the number of blades a valuable strategy to improve the aerodynamic performance while reducing the noise emissions of BLI propellers?**
The study aims to dissect:

1. **What effect does increasing the number of blades have on the overall aerodynamic performance?**
2. **What effects does increasing the number of blades have on the acoustic performance?**
3. **Is the sensitivity of the aerodynamic and aero-acoustic performance to the number of blades the same in installed conditions as in the isolated conditions?**

The last parameters studied are the ones describing the sweep distribution

**Research Question 3**

**Is the adoption of swept blades an effective design choice to improve the aerodynamic and aero-acoustic performance of BLI propellers?**
Expanding the above question leads to the following subquestions:

1. **How do the aerodynamic performance and the blade loading of the propeller with swept blades in installed conditions compare to the propeller with straight blades?**
2. **How does the aero-acoustic performance of the propeller with swept blades in installed conditions compare to the propeller with straight blades?**
3. **How do the propellers with swept blades perform in installed conditions compared to isolated conditions?**

To address these questions, a series of parametric studies are conducted, where the previously mentioned geometric characteristics are progressively varied to analyze the aerodynamic and acoustic performance of the propeller under both installed and isolated conditions. Although several numerical tools are capable of modeling the aerodynamics of installed propellers, the large number of simulations required to explore all relevant variables and conditions necessitates the use of low-fidelity or analytical models due to their lower computational demands. However, this approach sacrifices some accuracy and limits the range of operating conditions that can be simulated, given the limitations of the chosen solvers.

As a result, this study is performed on a model-scale version of the propeller, operating at low velocities to keep the tip Mach number below 0.3, minimizing the effects of compressibility. In the installed configuration, the propeller is treated as detached from the fuselage, similar to an isolated setup, but subjected to a distorted inflow. The velocity distributions at the propeller disk are provided by researchers at TU Delft working on the APPU project, derived from CFD simulations of the isolated fuselage. This approach allows

for modeling only the propeller, without accounting for the fuselage, but it also limits the accuracy of the results since the influence of the propeller installation on the airframe, and consequently on the inflow, is not considered.

## 1.4. Thesis Outline

The purpose of this report is to illustrate how the research guided by the previous questions was conducted and how the results obtained from the analysis help achieve the research objective by answering the research questions formulated.

The structure of the report is divided into four parts as follows. Firstly, Part I illustrates the background information gathered during the literature review and used as a starting point for the thesis research. This part includes Chapter 1, where the research motives and objectives are stated, Chapter 2, where the main known aerodynamic and aero-acoustic features of isolated and installed propellers are discussed, and Chapter 3, where the impact of some design choices on aero-acoustic propellers is introduced based on the results of previous works on the subject.
Then, Part II introduces the methodologies used in this thesis work. The Chapter 4 explains how the propeller geometry is parameterized and then discretized to be used in the subsequent numerical solvers. Chapter 5 illustrates the theoretical model on which the aerodynamic solver is based and then provides a brief description of the steps followed by the solver along with a discussion of its inherent limitations. The same information is provided in Chapter 6 for the aero-acoustic model.
After outlining the methodology, the validation of the numerical tools and the presentation of results are detailed in Part III. Chapter 7 demonstrates how the developed numerical tools can accurately estimate the aero-acoustic performance of propellers within an acceptable computational timeframe. Chapter 8 provides an overview of the analysis setup. Finally, Chapter 9 presents and discusses the results obtained from the analysis conducted to address the research questions. The insights from this chapter are then used to inform the conclusions.
Finally, Part IV embodies the conclusions and the recommendations by the author for future studies on this subject. Chapter 10 contains the closing remarks with a brief summary of the research conducted and then the research questions are reinstated and answered using the results discussed in Chapter 9. In Chapter 11, a final discussion regarding the limitations of the study is carried out, and in light of these, the author presents recommendations for researchers interested in the subject.

# 2

# Propeller Aerodynamics and Aero-Acoustics Performance

The objective of this research requires a multidisciplinary approach, integrating both the aerodynamic and aero-acoustic characteristics of a propeller. This chapter provides a comprehensive exploration of these two disciplines, covering both isolated and installed propeller conditions.

## 2.1. Isolated Propeller Aerodynamics

This section addresses the aerodynamics of isolated propellers, explaining the mechanisms underlying the generation of aerodynamic forces by propeller blades in Section 2.1.1 and detailing the main metrics used to assess propeller aerodynamic performance in Section 2.1.2.

### 2.1.1. Blade Loading

The thrust generated by a propeller originates from the rotation of its blades around a common axis. Each blade functions like a rotating wing, with the relative air velocity achieved through its rotation. Consequently, the aerodynamic principles applicable to wings are also relevant to propeller blades, with adjustments for variations in spanwise velocity and load distribution.

Figure 2.1 visually represents the forces acting on propeller blades, which depend on the velocity at the radial section. This velocity has two main components: a tangential component (aligned with the rotational direction) and an axial component (aligned with the freestream direction). The axial component primarily results from the propeller's forward motion, while the tangential component arises from propeller rotation, with its magnitude proportional to the radial position, denoted as $r$. Both components must also consider induced velocities, resulting from the wake vortex system shed behind the blades. Figure 2.3 illustrates the vortex system behind the propeller blades, explaining how additional velocity components are induced at the propeller disk.

Key angles in this context include $\beta$ (the pitch angle), which represents the angle between the blade section's chord and the propeller blade's tangential direction. The angle $\phi$, also known as the inflow angle (often referred to as $\theta$ in the literature), is the angle between the effective velocity vector and the tangential component. The angle $\alpha$ represents the effective angle of attack, defined as the angle between the effective velocity vector and the blade chord. Similar to an airfoil section of a wing, the blade section experiences sectional lift and drag forces, which are described by Equations 2.1 and 2.2, respectively.

$$L' = c_L(\alpha, Re, M)\frac{1}{2}\rho V_{eff}^2 c \tag{2.1}$$

$$D' = c_D(\alpha, Re, M)\frac{1}{2}\rho V_{eff}^2 c \tag{2.2}$$

While lift and drag are not directly used to characterize propeller performance, they are combined into thrust and torque components. The thrust component, aligned with the propeller axis, is given by Equation 2.3, and the tangential force component, responsible for the torque required to rotate the propeller, is given by Equation 2.4.

$$T' = L' \cos\phi - D' \sin\phi \tag{2.3}$$

$$F'_Q = L' \sin\phi + D' \cos\phi \tag{2.4}$$

The torque $Q'$ is then calculated as:

$$Q' = F'_Q r \tag{2.5}$$

While the analysis so far has focused on the 2D blade section, extending this analysis to the entire 3D propeller configuration involves summing the sectional contributions for each aerodynamic load. Figure 2.2 provides an overview of the principal forces and moments exerted on the propeller. This depiction includes the thrust and torque necessary for propeller rotation, as well as the normal and side forces that operate within the propeller plane and may arise under specific conditions, explored further in section 2.3.3.

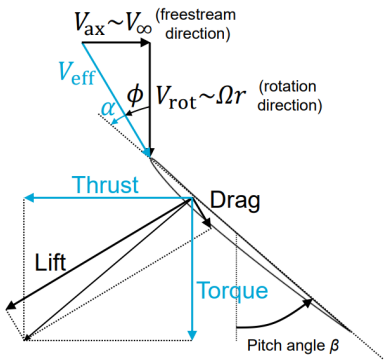


**Figure 2.1:** Velocities and forces acting on a propeller blade section [12]

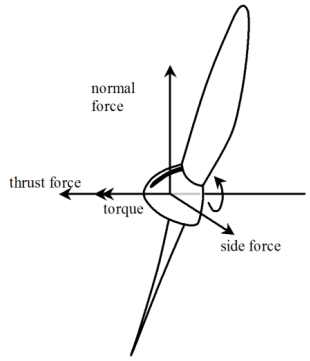


**Figure 2.2:** The Main Forces acting on a propeller from [1]

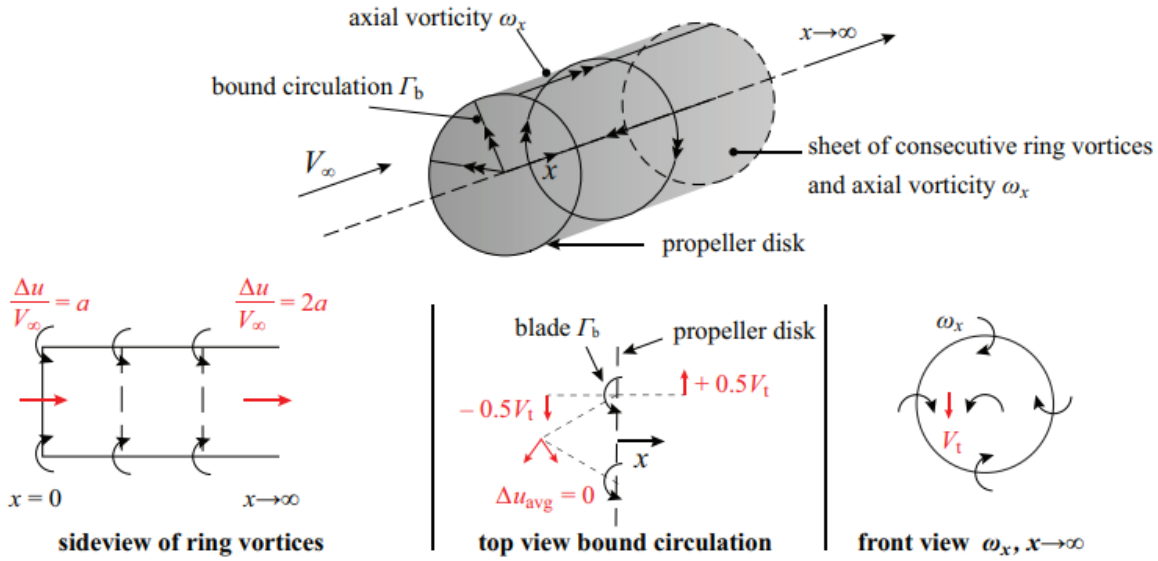


**Figure 2.3:** Vortex system and induced velocities in the slipstream by [13].

### 2.1.2. Propeller Aerodynamics Performance Indicators

The performance of propellers depends on a combination of factors, including the geometric characteristics of the propeller, atmospheric conditions, and specific operational parameters. These critical elements shape the propeller's behavior and efficiency.

- **Geometric Characteristics**: The design of a propeller is defined by its geometric attributes, including the diameter ($D$), the number of blades ($B$), and blade geometry such as chord length ($c$). A detailed examination of these aspects is provided in Chapter 3.
- **Atmospheric Conditions**: Atmospheric conditions, including air density ($\rho_\infty$), speed of sound ($a_\infty$), and dynamic viscosity ($\mu_\infty$), significantly influence propeller performance.
- **Operational Conditions**: Operational parameters such as the propeller's rotational speed ($\Omega$), pitch setting ($\beta$), and advancement velocity ($V_\infty$) also play a crucial role in determining propeller performance.

To facilitate comparisons among propellers with different geometries operating under varied conditions, performance outputs such as thrust and torque are scaled using performance indicators. One such indicator is the advance ratio ($J$), which combines geometric and operational considerations, as shown in Equation 2.6. The advance ratio is the ratio between the distance traveled forward by the propeller in a revolution and the propeller diameter, illustrated in Figure 2.4.

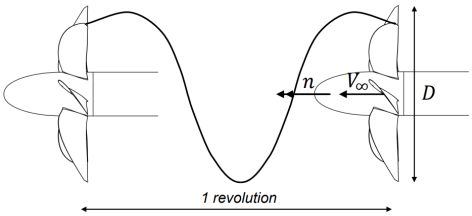


**Figure 2.4:** Visualization of the advance ratio from [12]

$$J = \frac{V_\infty}{nD} \tag{2.6}$$

Atmospheric conditions are combined with operational conditions and propeller geometry in the Mach number (Equation 2.7) and the Reynolds number (Equation 2.8).

$$M_\infty = \frac{V_\infty}{a_\infty} \tag{2.7}$$

$$Re_D = \frac{\rho_\infty V_\infty D}{\mu_\infty} \tag{2.8}$$

The blade pitch setting (usually is used the twist at the radial section at $70\%$ of the propeller radius $\beta_{0.7R}$) influences the local angle of attack ($\alpha$) of each blade section ($\alpha \propto \beta_{0.7R}$), as shown in Figure 2.1.

Thrust and shaft power ($P_{shaft} = 2\pi nQ$) depend on these parameters and are usually expressed as thrust ($T_C$) and power ($P_C$) coefficients.

$$T_C = \frac{T}{\rho_\infty V_\infty^2 D^2} \tag{2.9}$$

$$P_C = \frac{P}{\rho_\infty V_\infty^3 D^2} \tag{2.10}$$

Various performance coefficient definitions exist, depending on the scaling approach. The above definitions are suitable for describing propellers operating at fixed RPM with different inflow velocities ($V_\infty$). However,

for propellers operating at fixed inflow velocities, alternative definitions of thrust, torque, and power coefficients are used (Equations 2.11, 2.12, 2.13).

$$C_T = \frac{T}{\rho_\infty n^2 D^4} \tag{2.11}$$

$$C_Q = \frac{Q}{\rho n^3 D^5} \tag{2.12}$$

$$C_P = 2\pi C_Q \tag{2.13}$$

Propeller efficiency is defined as shown in Equation 2.14, where it is implied that the goal is to maximize thrust while minimizing the shaft power required.

$$\eta = \frac{T_C}{P_C} = J\frac{C_T}{C_P} \tag{2.14}$$

The performance coefficients ($T_C$, $P_C$, $\eta$, etc.) inherently depend on various parameters, including ambient and operational conditions ($J$, $\beta_{0.7R}$, $M_\infty$, $Re_D$). Figure 2.5 briefly summarizes the relationship between these performance coefficients and the advance ratio and pitch setting.

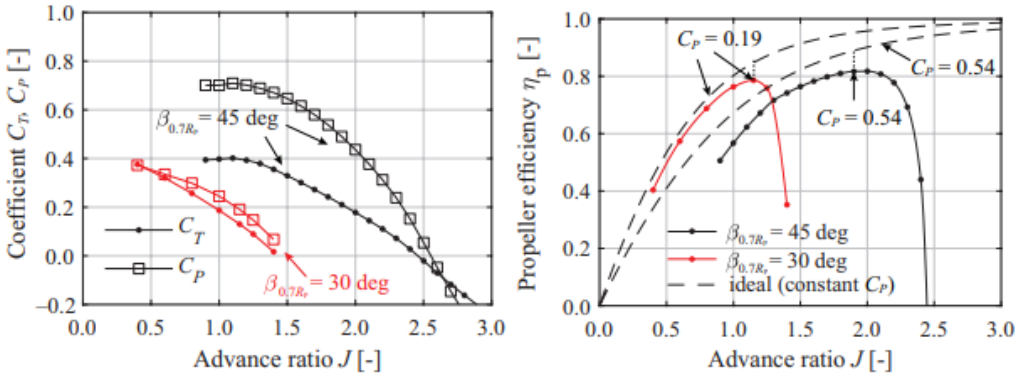


(a) Thrust and power coefficients

(b) Propeller efficiency. Indicated ideal efficiency at constant $C_P$ and constant $n$

**Figure 2.5:** Typical Performance Curves obtained from CFD Analysis for two pitch setting $\beta$ of the XPROP propeller [13]

The relationship between thrust coefficient ($C_T$) and advance ratio ($J$) for a given pitch setting ($\beta_{0.7R}$) reveals two distinct regions. At high advance ratios, the thrust coefficient increases almost linearly as $J$ decreases. However, at lower advance ratios, the slope progressively flattens and eventually declines as $J$ continues to decrease. This behavior is attributed to changes in the inflow angle, which decreases as $J$ increases, leading to a higher angle of attack. In the high $J$ region, the angle of attack remains below the critical value, resulting in linear aerodynamic flow where the loading is proportional to the angle of attack. When $J$ decreases significantly, the angle of attack exceeds the critical value in certain blade sections, causing nonlinear flow phenomena such as flow separation, which reduces the loading. The power coefficient exhibits a similar trend to the thrust coefficient.
Efficiency increases with advance ratio until it peaks at a certain $J$ value within the linear region. Beyond this point, the thrust is significantly lower than the power consumed, eventually becoming null and then negative. At higher advance ratios, the propeller acts more as a brake, with the power coefficient turning negative, making the propeller function like a windmill.
Adjusting the pitch setting ($\beta$) allows the thrust coefficient and efficiency curves to shift along the advance ratio range. This adaptability is advantageous for maintaining high efficiency across various operating conditions, even with constant RPM. However, it introduces additional complexity and weight due to the variable pitch mechanism.

## 2.2. Isolated Propeller Aero-Acoustics

This section summarizes the noise emissions from isolated propellers. It addresses the classification and definition of primary noise sources 2.2.1, the principal mechanisms governing noise propagation in the atmosphere 2.2.2, and the key indicators used to assess noise performance 2.2.3.

### 2.2.1. Noise Sources

Noise sources can be categorized into distinct groups based on their spectral characteristics, as outlined by B. Magliozzi et al. [2]. These categories include harmonic/tonal noise, broadband noise, and narrow-band noise.

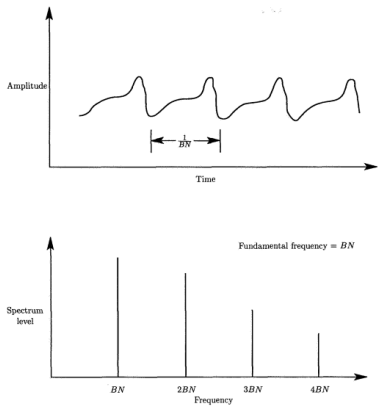


**Figure 2.6:** Tonal noise in the time domain (top) and frequency domain (bottom) [2].

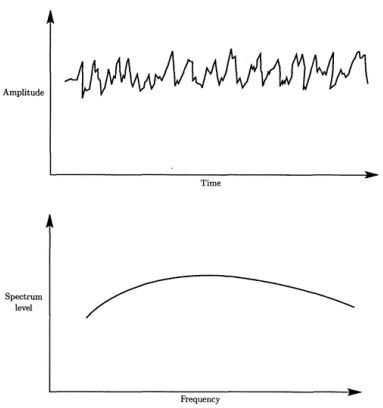


**Figure 2.7:** Broadband noise in the time domain (top) and frequency domain (bottom) [2].

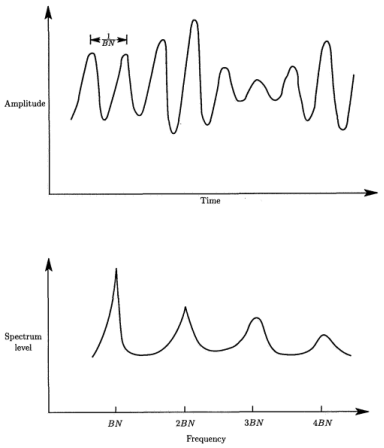


**Figure 2.8:** Narrow-band noise in the time domain (top) and frequency domain (bottom) [2].

**Harmonic Noise**

Harmonic noise exhibits periodic characteristics, with its time signature resembling a repeating pulse at a consistent rate. For an ideal propeller with $B$ blades operating at a constant rotational speed $N$, the resulting noise forms a signal with a fundamental frequency of $BN$, known as the blade passage frequency (BPF). The generated pulse is not a pure sinusoid, resulting in multiple harmonics at integer multiples of the fundamental frequency. Figure 2.6 illustrates harmonic noise in both time and frequency domains. There are four primary mechanisms for generating tonal noise:

- **Thickness Noise**: This noise is produced by the periodic displacement of air by the propeller blade and is proportional to the volume of air displaced.
- **Steady Loading Noise**: This noise arises from pressure disturbances caused by the blade loading and appears steady in the blade's reference frame.
- **Unsteady Loading Noise**: This noise is associated with time-dependent loading in the rotating blade reference frame, caused by circumferential flow variations. It becomes significant when the inflow is non-axisymmetric.
- **Quadrupole Noise**: This noise accounts for transonic effects and is relevant for high-tip-speed propellers with unswept blades.

**Broadband Noise**

Broadband noise, unlike harmonic noise, has a random nature and spans a wide range of frequencies, as shown in Figure 2.7. According to Parry [14], broadband noise is more significant at higher frequencies, while tonal noise dominates at lower frequencies.
Three primary mechanisms contribute to broadband noise [2]:

- **Turbulence-Ingestion Noise**: From the interaction of inflow turbulence with the propeller blade's leading edges.

- **Trailing-Edge Noise**: Resulting from the turbulent boundary layer's scattering at the trailing edge.
- **Blade-Wake and Tip-Vortex Impingement Noise**: Occurs when turbulent wakes and tip vortices interact with downstream blades.

**Narrow-band Noise**
Narrow-band noise results from the combination of broadband and tonal noise, exhibiting an almost periodic nature. Its energy is spread out rather than concentrated at isolated frequencies, as depicted in Figure 2.8.

### 2.2.2. Noise Propagation Effects

Noise propagates through space and can be altered by various mechanisms before reaching an observer. Magliozzi et al. [2] provide a detailed description of these mechanisms. One such mechanism is the Doppler Effect, which is considered by the aero-acoustic solver described in Chapter 6.

**Doppler Frequency Shift**
The Doppler Effect occurs when either the observer or the noise source is moving relative to the surrounding medium, causing a shift in the perceived frequency of the noise. For example, when an aircraft is cruising and an observer is stationary on the ground, the frequency shift can be calculated using Equation 2.15, where $f_0$ is the observed frequency, $f_s$ is the source frequency, $M_x$ is the flight Mach number, and $\theta$ is the angle between the observer's line of sight and the aircraft's flight path, as shown in Figure 2.9. Approaching the observer ($\theta > 0$) increases the frequency, while moving away decreases it.

$$f_0 = \frac{f_s}{1 - M_x \cos\theta} \tag{2.15}$$

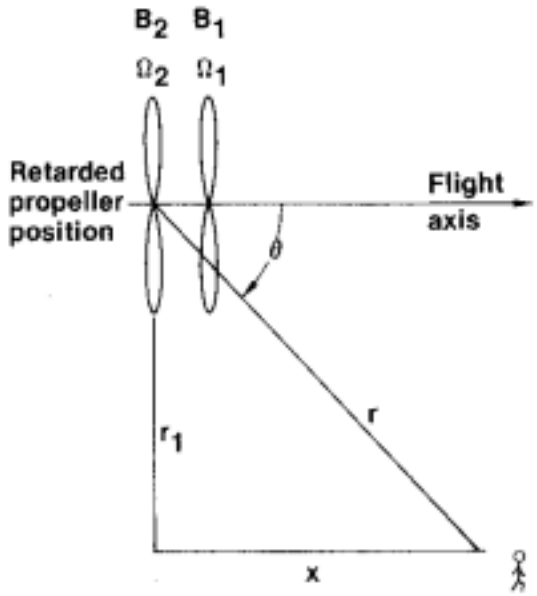


**Figure 2.9:** Observer coordinates [2], illustrating the angle $\theta$.

### 2.2.3. Propeller Noise Performance

Assessing the acoustic performance of a propeller requires specific performance indicators. Acoustic pressures, $p(t)$, at the observer's location are quantified using the root mean square (RMS) form, as shown in Equation 2.16.

$$p_{rms} = \sqrt{\frac{1}{T_2 - T_1} \int_{T_1}^{T_2} p(t)^2 dt} \tag{2.16}$$

The resulting value is often expressed on a logarithmic scale using the sound pressure level (SPL), defined by Equation 2.17, where the RMS pressure is divided by a reference pressure of $20\mu Pa$.

$$SPL = 20\log_{10}\frac{p_{rms}}{p_{ref}} \tag{2.17}$$

SPL does not provide specific information about the propeller itself, as it is scaled to a reference pressure unrelated to propeller design and operating conditions. An alternative measure is the thrust-specific sound pressure (TSSP), which allows for comparing propeller designs with varying dimensions (diameter $D$) and performance levels (thrust $T$), as defined in Equation 2.18.

$$TSSP = 20\log_{10}p_{rms}\frac{D^2}{T} \tag{2.18}$$

In addition to noise amplitude, frequency considerations are crucial. As explained in Section 2.2.1, tonal noise causes SPL peaks at multiples of the Blade Passage Frequency (BPF). Frequency is often normalized by the BPF, resulting in SPL peaks at $n = 1, 2, 3, \ldots$, as shown in Figure 2.6.

## 2.3. Aerodynamics and Aero-Acoustic of Installed Propellers

Most of the considerations made in the previous sections pertain to propellers in isolated conditions, meaning that the propellers are analyzed without accounting for their installation and the interference effects between them and the airframe. Consequently, such propellers experience a uniform inflow with constant velocity across the entire propeller disk. However, this uniform inflow assumption does not hold true when the propeller is installed, as the velocity field around it is influenced by the volume displaced by the fuselage or wing. Figure 2.10 provides examples of possible installation locations for the propeller, including the Boundary Layer Ingesting (BLI) propeller of the APPU project.

In such installations, the propeller is located at the end of the fuselage, behind the vertical tail, in a pusher configuration where it is subjected to a highly distorted inflow. The primary distortion arises from the developing boundary layer, which, at the end of the fuselage, reaches a thickness comparable to the extension of the blade and is characterized by a velocity gradient in the direction perpendicular to the fuselage's surface.

This section explores the effects of the distorted inflow ingested by the propeller on both aerodynamics and aero-acoustics. First, the desirability of such an installation location is discussed in Section 2.3.1. This is followed by an analysis of the main interaction effects between the propeller and airframe, typical of this installation, in Section 2.3.2. After establishing the presence of unsteady loading, its impact on aerodynamics and aero-acoustics is hypothesized in Sections 2.3.3 and 2.3.4, respectively.

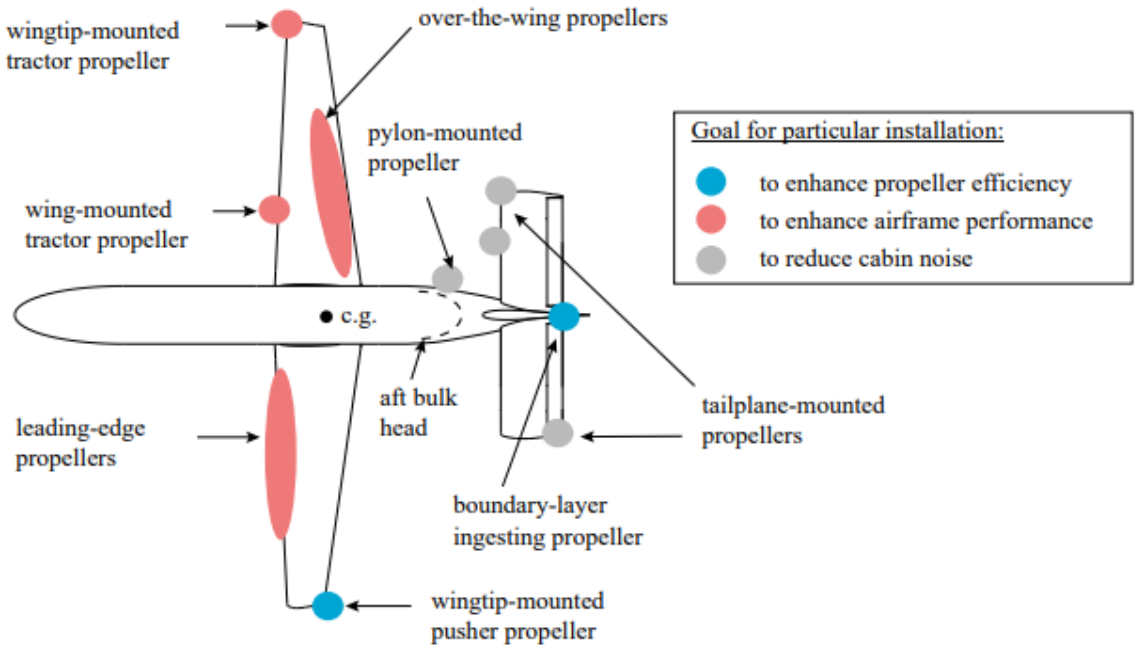


**Figure 2.10:** Examples of propeller airframe integration configurations [13].

### 2.3.1. Boundary Layer Ingesting Propulsor Concept

D.K. Hall in [15] employs the energetic approach described by Drela [16] to validate the concept of the BLI propulsor. Figure 2.11 illustrates the control volume around an aircraft equipped with a BLI configuration. To sustain flight at a velocity of $U_\infty$, the aircraft must exchange power with the surrounding fluid, as depicted in Equation 2.19, which includes various dissipation mechanisms denoted as $\Phi$.

In Equation 2.19, the left-hand side represents the power added to the fluid by the propulsor, $P_K$, which is directly proportional to fuel consumption. The BLI (Boundary Layer Ingestion) configuration facilitates a close integration between the propulsor and the airframe, allowing for a reduction in both the jet dissipation term, $\Phi_{Jet}$, and the wake dissipation term, $\Phi_{Wake}$. As a result, the power requirement for the propulsor is reduced enabling energy and fuel savings.

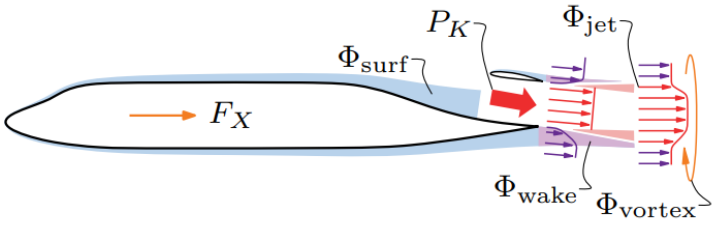


**Figure 2.11:** The Control Volume around a plane with a BLI propusor by D.K. Hall [15]. The wake structure and the main dissipation mechanisms are visualized.

$$P_K - \phi_{Jet} = \Phi_{Surf} + \Phi_{Wake} + \Phi_{Vortex} - F_X U_\infty \tag{2.19}$$

In a BLI configuration, the propulsor ingests airflow that has been decelerated by the upstream body. This implies that to generate the same thrust, the airflow needs to be accelerated to a lower velocity. Consequently, the kinetic energy of the outflow is reduced, leading to a decrease in jet dissipation.
Moreover, the outflow behind the aircraft becomes more uniform, resulting in reduced kinetic energy losses due to mixing and, consequently, lower wake dissipation. The reduction in these two terms is maximized when the airflow accelerated by the propulsor precisely offsets the velocity deficit in the airframe wake. Although this ideal condition, described by Drela in [16], is challenging to achieve in practical scenarios, it serves as a benchmark for understanding the advantages of a BLI configuration.

### 2.3.2. BLI propeller Interaction Effects

Most studies on Boundary Layer Ingestion (BLI) propellers consulted [17] [18], which will be further discussed in Chapter 3, have utilized an axisymmetric fuselage shape to isolate the BLI effect. As a result, the inflow at the propeller disk in these studies is uniform in the circumferential direction. However, in practical applications, such as the APPU airplane [4], the fuselage must accommodate a vertical tail and rudder for stability and control. Additionally, to avoid tail strikes and maintain ground clearance during takeoff and landing, the tail cone is typically inclined upwards.
Consequently, boundary layer ingestion is not the only effect of interest when studying a BLI propeller. Van Arnhem's categorization of interaction effects between propeller and airframe in [13] helps identify the main interaction effects relevant to a pusher BLI propeller:

- **Suction Effects**: In a pusher configuration, the propeller generates significant suction forces, influencing the pressure distribution and boundary layer characteristics of the upstream fuselage. This suction can alter airflow patterns and pressure distributions, all of which affect the conditions experienced by the propeller at its plane.
- **Boundary Layer Ingestion (BLI)**: This effect is associated with the velocity gradient within the boundary layer, which characterizes the axial velocity distribution. At the fuselage surface, the velocity is zero due to the no-slip condition and increases further from the surface.
- **Wake Interaction**: This effect arises from the interaction between the propeller and the wake generated by the airframe ahead of it. Two notable effects are the wake impingement from the vertical tail and the non-axisymmetric nature of the fuselage. The former results in a thin vertical region of slower-moving air above the fuselage, while the latter leads to a non-uniform reduction in axial velocity. Both effects introduce circumferential variations in the flow, leading to unsteady blade loading.

Wake interaction creates circumferentially variable flow conditions, leading to unsteady loading on the propeller blades. This unsteadiness significantly impacts both aerodynamic performance and noise generation.
Understanding and quantifying these interaction effects are crucial for designing BLI propellers and evaluating their overall aerodynamic and aero-acoustic performance. Addressing unsteady loading due to these interactions is essential for mitigating noise emissions, a topic that will be further explored in the final sections of this chapter.

### 2.3.3. Unsteady Loading Effects on Aerodynamics

When considering BLI propellers operating in non-axisymmetric inflow environments, it becomes essential to examine research focused on this subject.
The study by Fernandez and Smith [11] is particularly notable as it is one of the few that includes non-axisymmetric inflow in analyzing a BLI propulsor. They focus on a subsonic transport aircraft, similar in class to the Boeing 737 or Airbus A320, and introduce a third fan installed in a position analogous to the APPU project's propeller. Using computational fluid dynamics (CFD) techniques and a realistic fuselage model, their study aims to uncover the potential aerodynamic benefits of such a setup.
A key aspect of their research is the non-axisymmetric shape of the fuselage, which significantly influences the surrounding airflow, leading to non-symmetric variations in boundary layer thickness. Consequently, the inflow at the propulsor plane exhibits a pronounced non-axisymmetric character, profoundly affecting the BLI propulsor's aerodynamic behavior.
Their analysis extends beyond performance improvements due to the third fan's installation, revealing that the BLI propulsor generates in-plane forces due to the non-axisymmetric inflow. While these findings are specific to a BLI ducted fan configuration, they closely relate to similar phenomena observed in propellers operating under extreme inflow conditions, which also generate in-plane forces from non-axisymmetric inflow patterns.

A well-documented scenario in the literature involves a propeller mounted on a wing experiencing distorted inflow due to an angle of attack. Here, the propeller's axis is not aligned with the oncoming airflow, causing the propeller disk to appear inclined relative to the inflow direction. This misalignment generates an in-plane velocity component, as shown in Figure 2.12.
Under such conditions, the propeller blades experience unsteady flow, leading to fluctuations in their loading. As depicted in Figure 2.12, the down-going blade encounters a higher effective velocity and angle of attack, increasing thrust and torque forces. Conversely, the up-going blade experiences reduced values for these parameters. The increase in torque force on the down-going blade exceeds the reduction on the up-going blade, resulting in an in-plane force denoted as $F_N$. The coefficients for these in-plane forces are expressed as follows: for the vertical component in Equation 2.20 and for the lateral component in Equation 2.21.

$$C_Z = \frac{F_Z}{\rho_\infty n^2 D^4} \tag{2.20}$$

$$C_Y = \frac{F_Y}{\rho_\infty n^2 D^4} \tag{2.21}$$

A similar phenomenon may occur when the propeller is installed at the rear of the fuselage, as in the APPU project. In this configuration, the axial velocity $U_\infty$ is expected to vary circumferentially, leading to changes in the local advance ratio and resulting in cyclic variations in blade loading. These variations could generate in-plane forces, similar to those described in [11], which would not only affect the propeller's performance but also impact the aircraft's stability, making them crucial considerations during the design process.

Another extensively studied aspect in propeller literature is the effect of wake impingement at the propeller plane. Typically, these studies focus on propellers installed on nacelles, examining the effects of upstream pylons. However, similar considerations apply to the impingement of the vertical tail on a BLI propeller. The wake flow is characterized by a lower axial velocity, leading to local changes in the advance ratio and resulting in cyclic variations in propeller blade loading.
The wake's characteristics depend on the relative position between the propeller and the upstream surface and the propeller's thrust setting, as demonstrated by Sinnige et al. [9] (see Figure 2.13). At lower advance ratios, the propeller generates more thrust and exerts a larger suction effect. As aforementioned, the larger suction exerted on the oncoming flow modifies the streamline and, in this particular case, leads to a reduction of the effective velocity deficit behind the vertical tail, reducing the wake thickness while increasing its axial velocity. Hence, at larger thrust settings, the flow appears more uniform to the propeller. Studies by Gentry et al. [10] and Sinnige et al. [9] found that wake impingement does not significantly impact propeller performance because the wake-affected flow portion is relatively small compared to the entire propeller disk, leaving overall forces and efficiency largely unaffected. However, the impact on noise

emissions is more pronounced, as observed by Sinnige et al. [9]. This aspect is discussed in detail in the final section of this chapter.

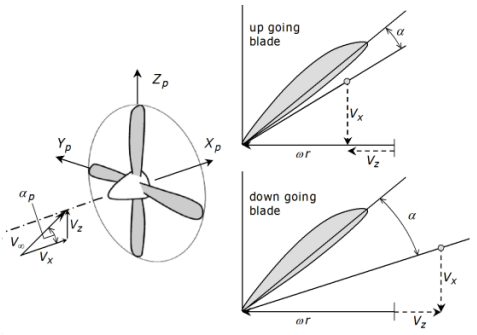


**Figure 2.12:** Representation of the distorted inflow experienced by a propeller at an angle of attack $\alpha_p$ by Veldhuis[1]. The in-plane velocity component $V_z$ generates unsteady loading. On the right, the effect on the blade section: the down-going blade experiences larger loading, while the up-going blade experiences the opposite.

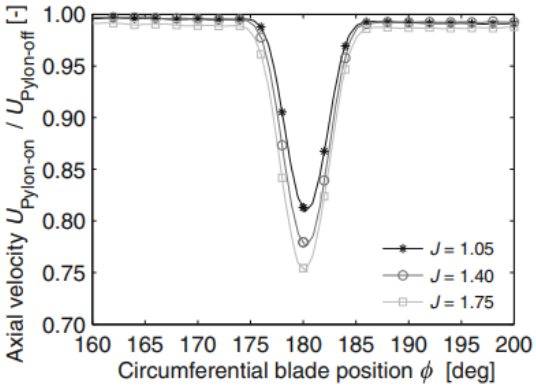


**Figure 2.13:** Axial velocity as a function of circumferential position for different thrust settings [9]. The velocity deficit due to wake impingement is visible at $\phi = 180°$, where the pylon is located upstream. This configuration resembles the BLI case discussed in this thesis.

### 2.3.4. Unsteady Loading Effects on Aero-Acoustics

The aeroacoustic performance of a propeller operating in non-uniform inflow, such as when encountering an angle of attack, experiences only minor impacts [19]. This is because the distributed nature of the non-uniformity results in a gradual rather than abrupt change in blade loading around the azimuth. Consequently, the blade undergoes a sinusoidal variation in loading, leading to a noise penalty that is not significantly greater than the dominant noise sources associated with isolated propeller thickness and steady loading. Conversely, the effects of wake impingement on noise emissions are more pronounced, as illustrated by Sinnige et al. [9]. The periodic unsteady loading caused by wake interaction generates tonal noise, stemming from the interaction between the wake and the propeller. The magnitude of the noise penalty attributed to wake impingement largely depends on the propeller's operational parameters. At higher thrust settings, there is a reduction in peak blade loading. Wind tunnel experiments have indicated that installation noise penalties due to wake impingement are diminished for high thrust levels and low advance ratios. Figure 2.14 illustrates the associated noise spectra for three different thrust levels.

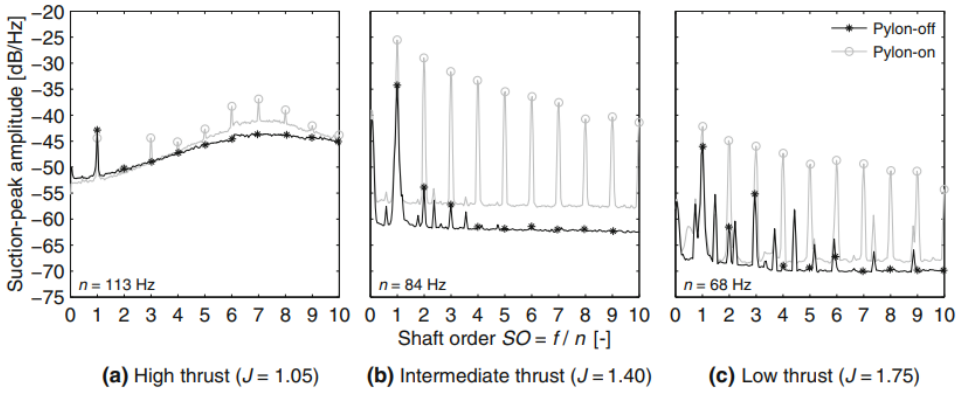


**Figure 2.14:** Propeller noise spectra for three different thrust levels and advance ratios with and without considering the pylon by [9].

# 3

# Design Considerations

This chapter is dedicated to exploring the relationship between propeller design and its impact on aero-acoustic performance. Section 3.1 provides an in-depth examination of the primary design variables, elucidating how they influence propeller performance. Subsequently, Section 3.2 delves into previous research articles focused on the design study of BLI propellers and aero-acoustic analyses of propellers.

## 3.1. Propeller Design Variables

Propeller design variables can be divided into two primary categories, as detailed in [12]. These categories include top-level parameters, which offer insights into the overall architecture of the propeller, and geometric variables, which specifically describe the characteristics of the propeller blades.

### 3.1.1. Propeller Architecture

This section offers a detailed list of these variables along with explanations of their impact on propeller performance.

- **Number of blades**: $B$
- **Diameter at the tip**: $D$
- **Hub to tip diameter ratio**: $\frac{D_{hub}}{D}$
- **Solidity**: $\sigma$

Solidity is defined as the ratio of the blade area to the total disk area. The total disk area is determined by the top-level parameters mentioned earlier, while the blade area depends on both the number of blades and their geometric characteristics, such as chord distribution. Equation 3.1 provides a possible mathematical expression for calculating solidity.

$$\sigma = \frac{2N_B c}{\pi D} \tag{3.1}$$

The interaction between these variables has an impact on the following performance indicator:

- **Disk Loading**
- **Blade Loading**

The disk loading, defined as the ratio of thrust produced to the disk area, and the blade loading, defined as the ratio of thrust to the area occupied by the blades, are linked through the concept of solidity, as shown in Equation 3.2. Thus, changes in one parameter influence the other. Decreasing solidity while maintaining constant disk loading leads to higher blade loading. Conversely, increasing solidity while keeping blade loading fixed results in higher disk loading.

$$\textbf{Blade Loading} = \frac{\textbf{Disk Loading}}{\sigma} \tag{3.2}$$

These two performance indicators are interconnected, affecting aerodynamic efficiency, noise emissions, and structural integrity. A propeller with high disk loading, when maintaining constant thrust, produces thrust by generating significant axial and tangential velocities, leading to greater kinetic energy loss and reduced propulsive efficiency. Moreover, blade loading is a crucial factor in noise emissions, as the loading component significantly contributes to dominant tonal noise, with its intensity being directly proportional to the blade loading.

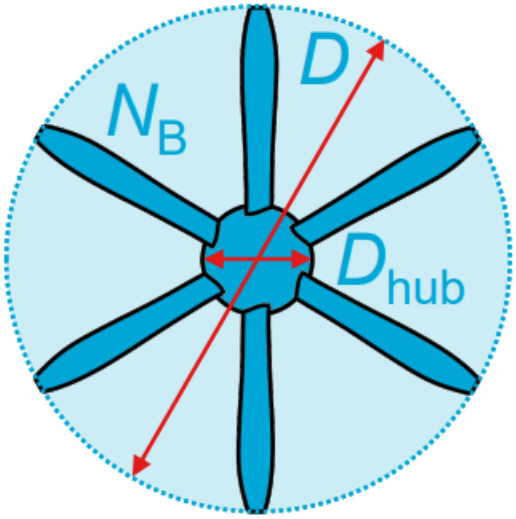


**Figure 3.1:** Top view of a propeller with the top level parameters shown [12]. Here $N_B$ represents the number of blades $B$.

Increasing the blade count can positively impact aerodynamics and noise emissions, as highlighted by C. A. Negulescu [20]. With constant blade area, a higher blade count increases solidity, thereby reducing blade loading while maintaining constant disk loading. Alternatively, maintaining solidity constant results in a decrease in chord distribution with more blades, leading to slender blades with higher aspect ratios. This reduction in chord minimizes tip losses, enhancing propeller efficiency. When the propeller is installed and subjected to a non-axisymmetric inflow, such as at a non-zero angle of attack ($\alpha \neq 0$), unsteady blade loading occurs, leading to oscillations in the thrust and power produced by the propeller over time. Increasing the blade count can reduce the amplitude of these oscillations [12]. A greater number of blades shifts tonal noise to higher frequencies, reducing perceived noise by the human ear. However, factors such as the complexity of the variable pitch mechanism, maintenance, manufacturing costs, structural stresses, and flutter issues can impose limitations on the number of blades.

A larger diameter allows for an increase in disk area, which in turn reduces disk loading and enhances efficiency. This can also positively impact noise emissions by lowering the loading noise component. However, several factors can constrain propeller diameter. These include considerations for ground clearance during takeoff and landing, the risk of reaching unacceptable tip speeds at higher diameters, and the potential necessity for a gearbox to reduce rotational speed. The addition of a gearbox introduces complexity, costs, and weight. Moreover, if tip speeds reach transonic regimes, shockwaves are formed, leading to wave drag penalties and an increase in the quadrupole noise source, as highlighted by Hanson [21].

The hub size is influenced by various factors and tends to correlate with the complexity of the propulsor system. A greater number of blades usually demands a more complex variable pitch mechanism, leading to an enlargement of the hub diameter. Moreover, if a gearbox is needed and these components are integrated into the hub, it further increases its size. A high hub-to-tip ratio, which indicates a lower disk area when the propeller diameter remains constant, can result in heightened disk loading, ultimately affecting propeller efficiency.

### 3.1.2. Blade Geometry

Having explored the top-level variables that influence propeller performance, it is crucial to shift focus towards the parameters describing propeller blade geometry. These parameters encompass: the radial distribution of chord, twist, airfoil profile, and sweep and lean angles.

**Chord**

The arrangement of chord along the radial span of a propeller blade plays a significant role in blade loading. In contemporary propellers, a common practice is to maintain substantial chord values up to approximately $80\%$ of the radial span, gradually decreasing towards the tip [20]. This strategy, termed "loading shifting," aims to minimize loading at the tip, thereby reducing acoustic loading noise. However, it results in a loading distribution diverging from the one optimal for aerodynamic efficiency, leading to a decrease in effective diameter and efficiency, as illustrated in Figure 3.6.

For Boundary Layer Ingestion (BLI) propellers, chord values are notably higher near the hub, as shown in Figure 3.3. This design is advantageous for redistributing the loading toward the inboard section of the propeller, as elucidated by Lv and Rao in [22] and illustrated in Figure 3.2. A greater concentration of loading in the inboard region supplies more energy to the low-velocity areas, particularly near the hub, resulting in a more uniform total pressure distribution in the outflow. This design strategy is expected to enhance overall efficiency by reducing dissipation mechanisms associated with non-uniform total pressure distributions.

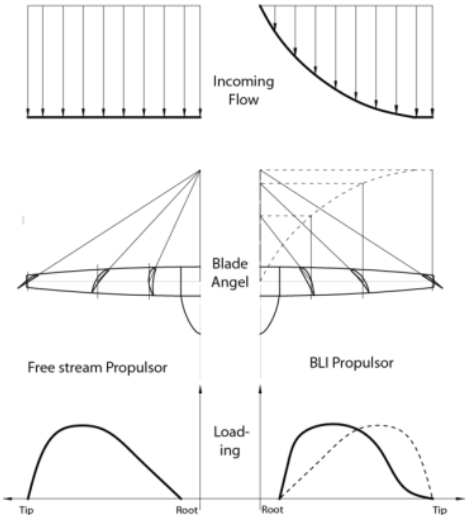


**Figure 3.2:** BLI Propulsor Concept as discussed by [22]. The left side illustrates a conventional propulsor designed for uniform inflow, while the right side depicts a BLI propeller, which is characterized by a loading distribution shifted toward the inboard section.

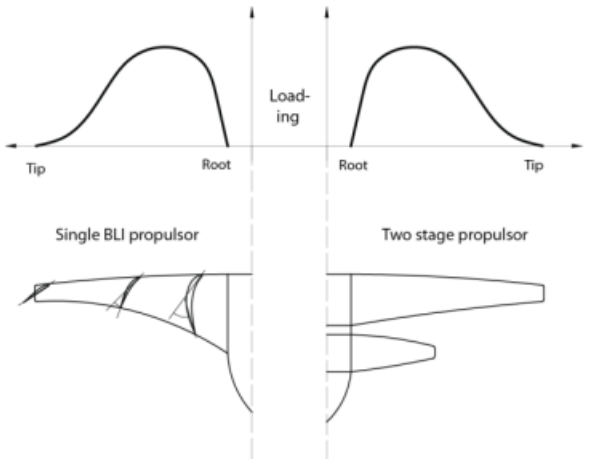


**Figure 3.3:** Innovative propulsor architectures as presented by [22]. The figure shows two potential configurations: on the left, a single-blade design with a larger chord near the inboard section; on the right, a tandem architecture featuring two propulsors.

**Twist**

The twist distribution refers to the variation in local pitch angle $\beta$ along the blade span, optimized to achieve the desired loading while minimizing drag.

**Airfoil Profiles**

The distribution of the airfoil profile influences two crucial aspects: thickness and camber distribution. Thickness distribution is a result of both aeroacoustic and structural considerations. Aero-acoustic concerns advocate for thin blade sections to mitigate thickness noise and compressibility losses, while structural requirements necessitate sections with sufficient thickness to withstand stresses. Balancing these factors often leads to larger thickness at the root where centrifugal stresses are the highest, and minimum thickness at the tip where the velocity is at the highest.

On the other hand, camber distribution is determined in a similar fashion to twist distribution, aiming to achieve the most efficient loading distribution along the blade span, while keeping the distribution along the chord as much uniform as possible to reduce the noise intensity [23].

**Sweep**

Sweep is a prominent feature in modern propeller blades, providing benefits in both aerodynamics and acoustics. Much like its role in reducing wave drag on wings at high speeds, sweep ($\Lambda$) in propeller blades is designed to lower the local perpendicular Mach number below the drag divergence Mach number ($M_{DD}$) at cruise conditions. However, unlike the uniform sweep typically seen in wings, propeller blades usually have a more varied sweep distribution. Near the hub, blades often exhibit negative sweep angles that move sections forward, while further along the span, positive sweep angles (backward displacement) are common. This distribution minimizes the overall displacement along the blade's chord, optimizing structural integrity.

Figure 3.4 compares two propellers with different sweep distributions and their respective cantilevers ($I_C$). The red blade, featuring non-negative sweep near the hub, has a longer moment arm, leading to higher stresses and deformations. Conversely, the black swept blades have zero sweep near the mid-span, which reduces stress but increases drag.

Additionally, sweep impacts noise emissions beyond just reducing quadrupole noise through nonlinear loading mitigation. Sweep alters the relative positions of noise sources along the blade span, introducing a phase lag. This mechanism, extensively discussed by Hanson [23] and depicted in Figure 3.5, ensures that the combined noise contributions from various blade sections are lower than when these sources are in phase.

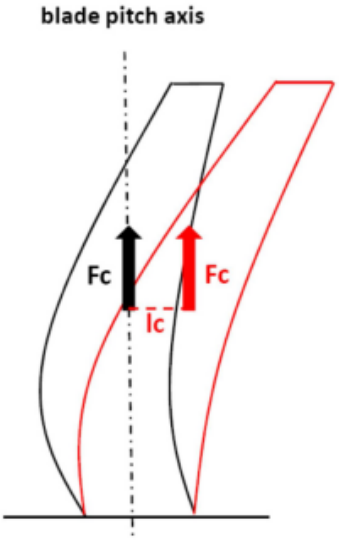


**Figure 3.4:** Comparison of blades with different sweep distribution by [20]

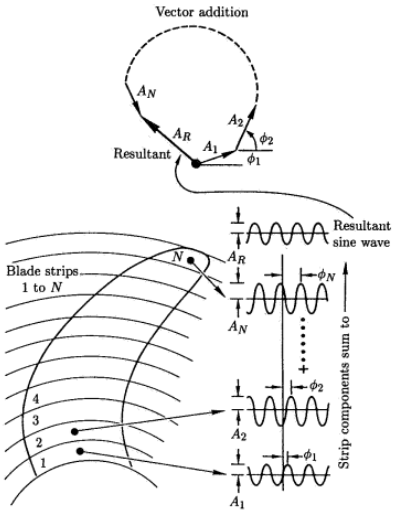


**Figure 3.5:** Sweep phase change effect on propeller noise emissions [23]

**Lean**

In modern propellers, a lean distribution is often integrated, akin to the dihedral angle in wing design primarily for structural reasons. The blade leans forward toward the suction side to generate a centrifugal moment that counteracts the aerodynamic bending moment. Like sweep, introducing lean induces a phase change at noise sources along the blade span, leading to diminished noise emissions. However, due to the limited lean angle achievable, the noise reduction attained is typically less significant.

Due to time constraints, it is not feasible to explore the effects of all geometric variations on the aerodynamics and acoustics of installed propellers. Therefore, this study will focus on the number of blades and the application of sweep, as these characteristics significantly impact both aerodynamic and acoustic performance.

## 3.2. Previous Studies

This section offers a concise review of the past research efforts dedicated to propeller design and aero-acoustic analysis that were encountered during the literature study in preparation of the thesis.

### 3.2.1. BLI Propellers Analysis

All the studies reviewed on BLI propellers focus on optimizing aerodynamic performance without addressing aero-acoustic considerations. Despite the variety of numerical tools and conditions applied, optimized BLI propellers consistently share certain geometric features, such as broader chords near the hub, as initially conceptualized in the single-row BLI propeller design by Lv and Rao [22].

An early example of BLI propeller optimization is presented in the work by van Arnhem [17]. This study, using an aerodynamic solver based on XROTOR, successfully modeled a BLI propeller subjected to axisymmetric inflow. Similarly, F.P. Costa et al. [18] employed a high-fidelity Computational Fluid Dynamics (CFD) model to conduct an in-depth aerodynamic performance analysis of a BLI propeller under axisymmetric inflow conditions. The study by Sinnige et al. [24] is the only one that considers non-axisymmetric inflow. However, due to the limited focus on the effects of unsteady loading in this configuration, this aspect was not extensively explored.

### 3.2.2. Aero-acoustic analysis

Several key studies in the field of aero-acoustic analysis and optimization provide insights into the complex trade-offs between aerodynamic efficiency and noise emissions in isolated propellers.

The investigation by Miller et al. [25] stands out as an early exploration into the intricate trade-offs inherent in designing propellers optimized for both aerodynamic efficiency and noise emissions. Figure 3.6 illustrates various strategies discussed in their work. While increasing the number of blades improves both aerodynamic efficiency and noise performance, other approaches primarily focus on noise reduction, sometimes compromising efficiency.

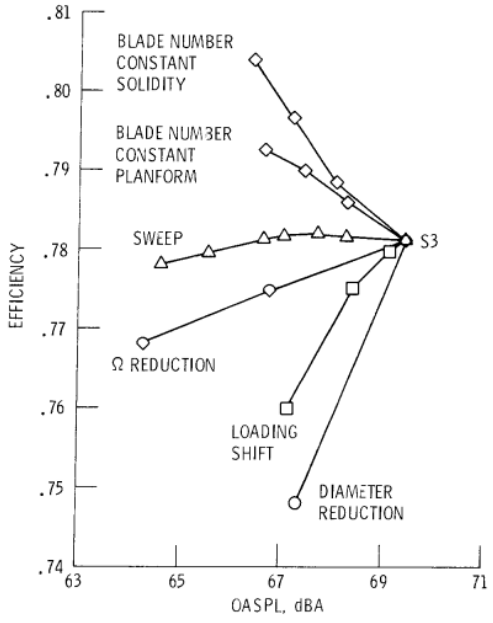


**Figure 3.6:** Optimized noise/propulsive efficiency trade-offs for a three bladed straight blade baseline configuration at a design point of J =0.8 and a Cp = 0.154 [25].

In a recent study by Ingraham [26], an unsteady vortex lattice method (UVLM) is combined with a streamlined version of Farassat's Formulation 1A to optimize the aero-acoustic performance of both an isolated propeller and a wing-mounted tractor propeller. The study simplifies the problem from a multi-objective to a single-objective optimization, prioritizing aerodynamic efficiency while imposing constraints on noise emissions at varying levels of stringency. Design variables include spanwise chord distribution and operational

parameters such as collective pitch and rotational speed.
Another significant aero-acoustic optimization study by Marinus et al. [27] employs a higher-fidelity approach using Fluent software for periodic steady RANS simulations in the aerodynamic domain, while acoustic analysis is performed using Farassat's Formulation 1A. This multi-objective problem addresses three key functions: propeller power requirement, sound pressure level (SPL) at a receiver located on the vertical plane of the propeller, and the aggregate SPL value across all receivers. The mission profile includes both climb and cruise phases, with performance during these phases weighted according to their respective durations. Figure 3.7 illustrates the blade designs obtained at the end of the optimization process, which demonstrated the most promising results.

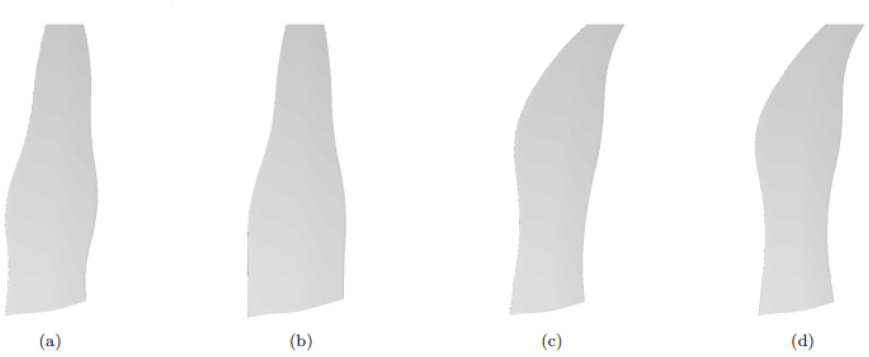


**Figure 3.7:** Blade geometries of optimized propellers obtained by Marinus et al. [27].

# Part II

## Methodology

# 4

# Blade Geometry Parametrization and Propeller Discretization

This chapter outlines the process of defining blade geometry and discretizing the propeller for numerical analysis. Section 4.1 details the methodology for defining the blade geometry, while Section 4.2 explains how the propeller is discretized for numerical solvers.

The numerical tools used for generating the blade and propeller geometry are derived from the Smart Rotors Project [28], developed at TU Delft under the supervision of G. Margalida. This project integrates various numerical tools for comprehensive propeller analysis and design optimization, spanning aerodynamics, aero-acoustics, and structural analysis. Figure 4.1 provides an overview of the project's architecture.

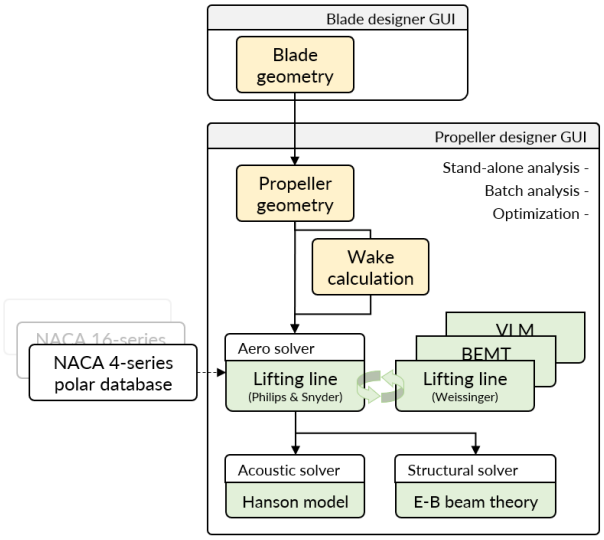


**Figure 4.1:** The Smart Rotors Project framework [28]. The tools in the Blade designer GUI and the propeller geometry generator in the Propeller designer GUI are used in this thesis.

## 4.1. Blade Geometry Parameters

The parametrization of the propeller top-level geometrical variables is straightforward, with each parameter described by a single number:

1. B: the number of blades
2. $R_{tip}$: the propeller tip radius
3. $R_{hub}$: the propeller hub radius

As seen in Chapter 3, the propeller blade geometry is described by a series of characteristics listed in Section 3.1.2, here represented in a parametrized form:

- **Chord**: ratio between the local chord and the propeller tip radius.
- **Twist**: local pitch angle of the blade section.
- **Maximum Thickness**: ratio between the maximum thickness and the local chord length.
- **Maximum Camber**: ratio between the maximum camber and the local chord length.
- **Maximum Camber position**: ratio between the maximum camber position and the local chord length.
- **Sweep**: in form of the Mid Chord Alignment (MCA), the axial displacement of the local profile quarter of chord ($x/c = 1/4$) from the Pitch Change Axis (PCA) as in Figure 4.2.
- **Lean**: in form of the Face Alignment (FA), the vertical displacement of the local profile quarter of chord ($x/c = 1/4$) from the Pitch Change Axis (PCA) as in Figure 4.3.

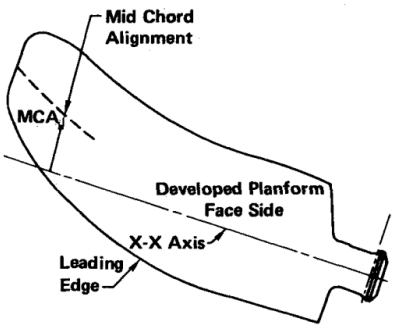


**Figure 4.2:** Definition of $MCA$ by Hanson [29]

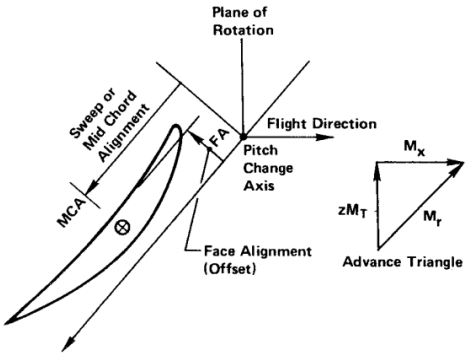


**Figure 4.3:** Definitions of $MCA$, $FA$ by Hanson [30]

The blade parameters are represented not by simple values but as radial distributions, as they need to vary along the blade span, as discussed in Chapter 3. These distributions can be specified either as vectors or through cubic Bézier curves.
Figure 4.4 illustrates the radial distribution for the XPROP blade geometry, which is used in Chapter 7 to validate the developed solvers. Since this is a straight blade with no lean, the parameters related to lean are not applicable here. For a detailed explanation of the sweep parametrization, please refer to Chapter 8.

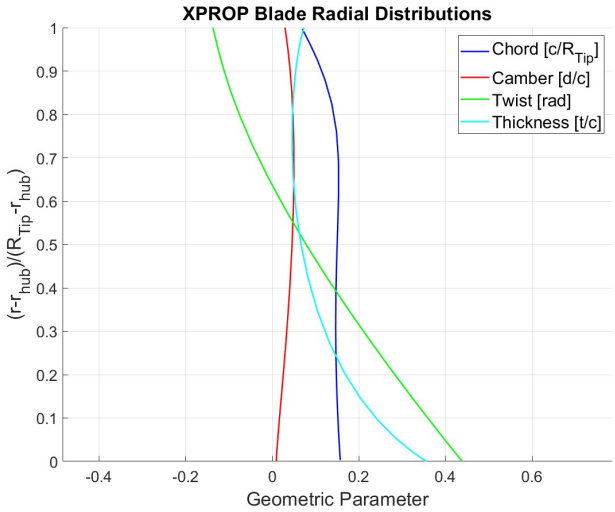


**Figure 4.4:** The chord, camber, twist, and thickness radial distributions of the XPROP geometry.

## 4.2. Propeller Discretization

Once the propeller geometry is provided through the described parameters, the discretized propeller can be modeled. The first step involves detailing the desired resolution of the modeled propeller blades, requiring two parameters: the number of spanwise sections (radial stations) $N_S$and the number of chordwise sections $N_C$. The Propeller Geometry designer can use various distributions ranging from uniform to non-uniform spacing. In this research, cosine spacing was adopted to increase resolution at the hub, tip, and leading edge (L.E.), where loading changes more abruptly.

After determining the resolution, the propeller blade can be discretized. The airfoil profile at each spanwise section is constructed based on the local maximum thickness, camber, and camber positions, scaled according to the chord distribution, and stacked based on the twist, sweep, and lean. Figure 4.5 provides a visualization of the XProp blade, while Figure 4.6 shows the whole 6-bladed XProp propeller obtained using the Smart Rotor functions.

It is important to note that the airfoil sections are assumed to be NACA-4 series profiles. When analyzing the XPROP geometry, this assumption leads to discrepancies since the XPROP does not use NACA 4 series profiles. However, since the camber distribution required by the aerodynamic solver (discussed in Chapter 5) has the same maximum camber and camber position as the original distribution, this discrepancy does not significantly affect the results.

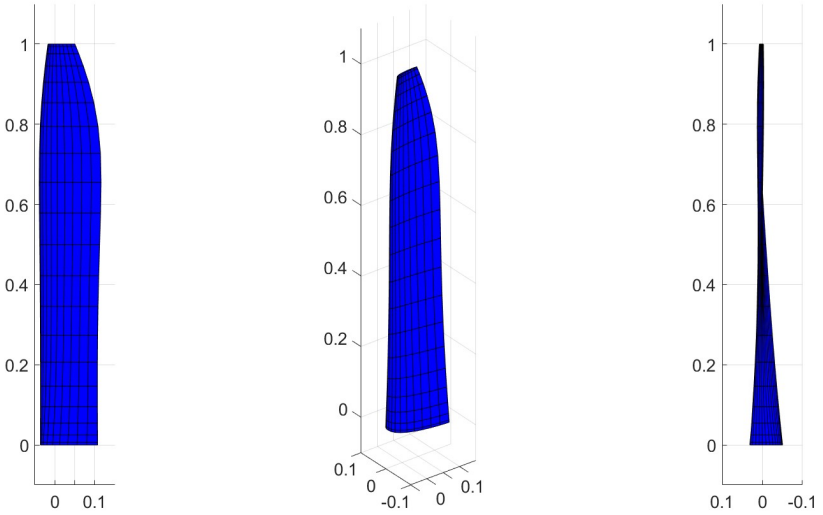


**Figure 4.5:** Visualization of the XProp blade with $N_S = 20$ sections along the span and $N_C = 10$ along the chord. Non-uniform spacing with higher resolution at the L.E., tip, and hub is recognizable.

Once the propeller blade geometry is discretized, the tool can proceed with modeling the entire propeller. The blades are scaled based on the propeller tip radius and rotated according to the desired blade pitch, which is the twist at the radial station $r = 0.7R_{Tip}$. Finally, the geometry is reproduced and rotated to match the number of blades.

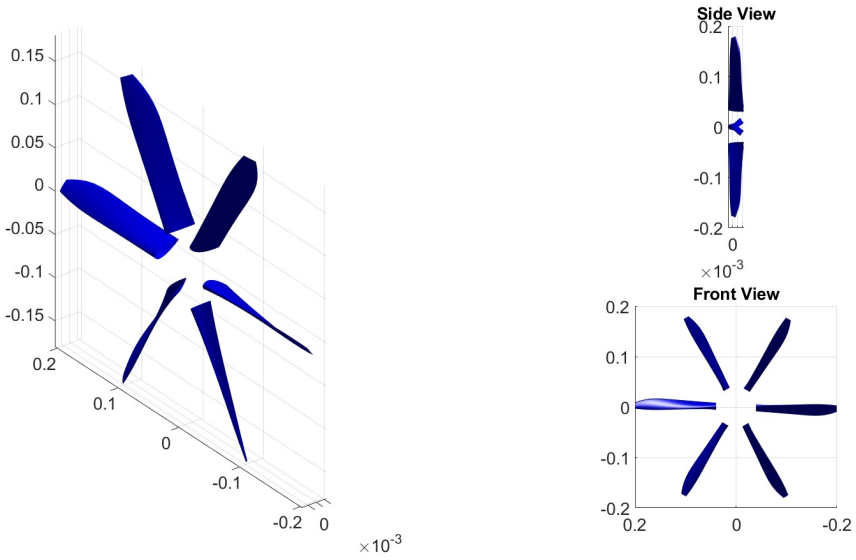


**Figure 4.6:** Visualization of the XProp 6-bladed propeller with a collective pitch of $\beta_{Pitch} = 45°$. The tip radius is $R_{Tip} = 0.2032m$, and the hub-to-tip radius ratio is $0.195$.

# 5

# Aerodynamic Solvers

This chapter introduces the aerodynamic tools developed by the author for the necessary analyses in this study. Numerical methods for modeling propeller aerodynamics are classified by their fidelity, which reflects their ability to accurately simulate real-world phenomena [31]. Low-fidelity methods, such as Blade Element Theory (BET) and Vortex Lattice Methods (VLM), are computationally efficient and well-suited for optimization studies and rapid parametric analysis. In contrast, high-fidelity methods like Computational Fluid Dynamics (CFD) provide greater accuracy but demand significantly more computational resources. Given the extensive number of simulations required and the constraints on computational resources, the research for a suitable aerodynamic solver focuses on low-fidelity models for aerodynamic performance estimation, specifically BET [32] [33] and VLM, some of which are integrated within the Smart Rotor Project [28]. While various BET models are available, none adequately handle the sweep and unsteady effects typical of installed propellers simultaneously. Therefore, the study has shifted towards VLM, which effectively models low-aspect-ratio and swept blade geometries and offers an unsteady implementation particularly similar to the steady solution.

Section 5.1 presents an overview of the theory of the steady Vortex Lattice Method (VLM). Section 5.2 details the functioning of the developed solver based on unsteady variant of the Vortex Lattice Method (UVLM). Section 5.3 focuses on the Unsteady Non-Linear Vortex Lattice Method (UNVLM), a modified version of the traditional UVLM that accounts for non-linearities due to viscosity. Finally, Section 5.4 discusses the influence of the wake models on estimated propeller performance and the computational cost of simulations. All these solvers have been programmed in MATLAB for compatibility with the blade design and propeller discretization tools from the Smart Rotor Project [28] presented in the previous chapter.

## 5.1. Steady Vortex Lattice Method

The Vortex Lattice Method (VLM) used in the Smart Rotor Project [28] was developed by a colleague, J. Thielen, during his master thesis [34], adapting the general method for fixed wings found in Chapter 12 of Katz and Plotkin's "Low-Speed Aerodynamics" [35] to the propeller case. Here, a general overview of the VLM is provided.

This method relies on potential theory and makes the following assumptions about the flow:

- Inviscid
- Incompressible
- Irrotational

The VLM discretizes the lifting surface in both the spanwise direction, with $N_S$ sections, and the chordwise direction, with $N_C$ sections. This results in a grid or lattice of $N_S \times N_C$ panels representing the surface. This approach can reproduce complex surface geometries characterized by large tapering ratios, sweep, lean, and camber without needing the profile polars of each section, as required by the Blade Element Momentum (BEM) method. In VLM, only the mean surface between the upper and lower surfaces is considered, meaning the wing or propeller blade thickness is ignored.
On each panel, vortex rings with strength $\Gamma_i$ are placed. For propellers, it is advantageous to use a vortex ring consisting of four straight vortex line segments with constant vorticity. This preference arises because the wake shed by the blades can also be described using the same vortex ring structure. Given

its helicoidal shape, it is more accurately represented by these structures. A vortex ring is associated with each blade panel, with the front and rear bound vortex lines positioned on the quarter chord of the local panel and the panel immediately behind it, respectively. The trailing vortex lines connect these two bound vortex lines. Collocation points are situated at the three-quarter chord position of the panels in the spanwise center, with the normal vector orthogonal to the camber line at the collocation point.
To satisfy the Kutta condition, which requires zero vorticity at the three-dimensional trailing edge (T.E.), a wake extends infinitely into the far field. The position of the wake panels can be prescribed arbitrarily, and when fixed, the model is referred to as a fixed-wake model. For propellers, it is convenient to place the wake panels on helicoidal sheets defined by the operating conditions (inflow velocity and rotational velocity). In reality, the wakes are force-free and follow the local velocity, causing them to roll up near the blade tip. The wake circulation strength is set equal to that of the trailing edge vortex line. Each collocation point is then subjected to the Biot-Savart law to determine the induced velocity, from which the velocity potential and boundary conditions are obtained. This process results in a linear system of $N_S \times N_C$ equations for the circulation distribution, which can be solved for the $N_S \times N_C$ unknowns. A final step is needed to evaluate the velocities induced by the shed vorticity at the propeller rotation plane and add these components to the freestream velocity to determine the angle of attack and blade loading.

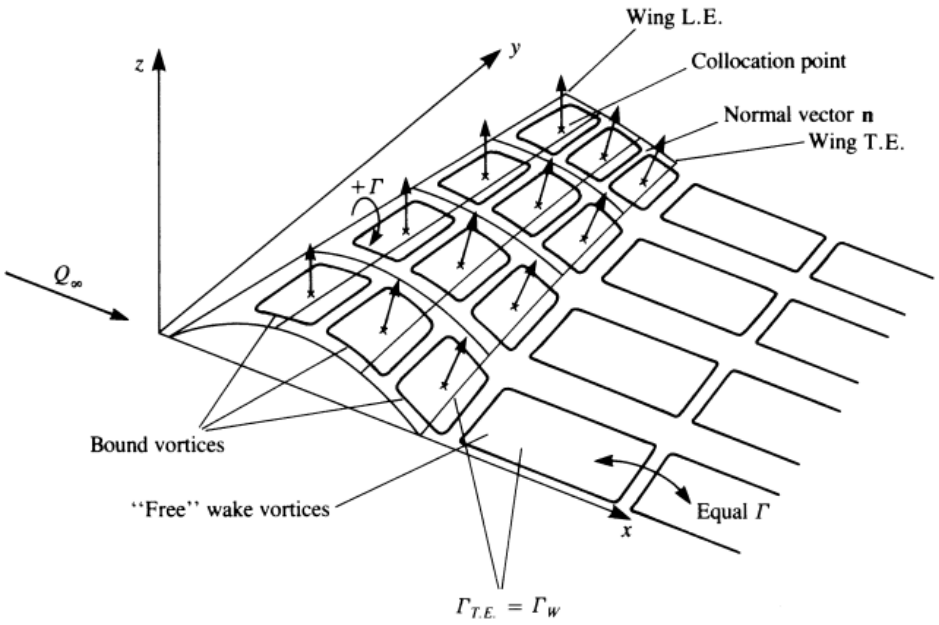


**Figure 5.1:** VLM with Vortex Ring Model on a cambered Lifting Surface by [35]. It is clearly visible that also the wake is described using vortex rings.

In panel methods, a Neumann boundary condition is imposed at each collocation point to ensure that the velocity perpendicular to the camber line is zero. This makes the lifting surface impermeable to the flow. The normal velocity at a collocation point results from a combination of components: the freestream velocity and the induced velocities from vortex rings. The first component is attributed to the kinematics of the propeller and consists of an axial component due to the flight velocity $\vec{U}_\infty$ and a tangential component due to the spinning of the propeller $\vec{V}_t = \Omega \times \vec{r}$. The latter is the sum of all components induced by the vortex rings composing the lattice. Equation 5.1 is the mathematical representation of this condition on a generic collocation point, where $V_{ind}$ is the induced velocity component from the $kth$ vortex ring and $n$ denotes the normal vector of the camber line at the collocation point.

$$\left( \sum_{k=0}^{N} (\vec{V} ind_k) + \vec{U}\infty + \vec{V}_T \right) \cdot \vec{n} = 0 \tag{5.1}$$

Equation 5.2 and Figure 5.2 show that the induced velocity component $\vec{V}_{ind_k}$ results from the sum of the

components induced by each of the four vortex segments that constitute the ring. To compute the induced velocity of a straight vortex line segment with constant circulation $\Gamma$, the Biot-Savart law in Equation 5.3 is utilized. In this equation, $\vec{r}_{1P}$ and $\vec{r}_{2P}$ represent the vectors from the start and end points of the line segment of length $r_0$ towards an arbitrary point in space, respectively. These position vectors are schematically depicted in Figure 5.3.

$$\vec{V}_{ind_k} = \vec{q}_{1,2} + \vec{q}_{2,3} + \vec{q}_{3,4} + \vec{q}_{4,1} \tag{5.2}$$

$$\vec{q}_{1,2} = \frac{\Gamma}{4\pi} \frac{\vec{r}_{1P} \times \vec{r}_{2P}}{|\vec{r}_{1P} \times \vec{r}_{2P}|^2} \vec{r}_0 \cdot \left( \frac{\vec{r}_{1P}}{r_{1P}} - \frac{\vec{r}_{2P}}{r_{2P}} \right) \tag{5.3}$$

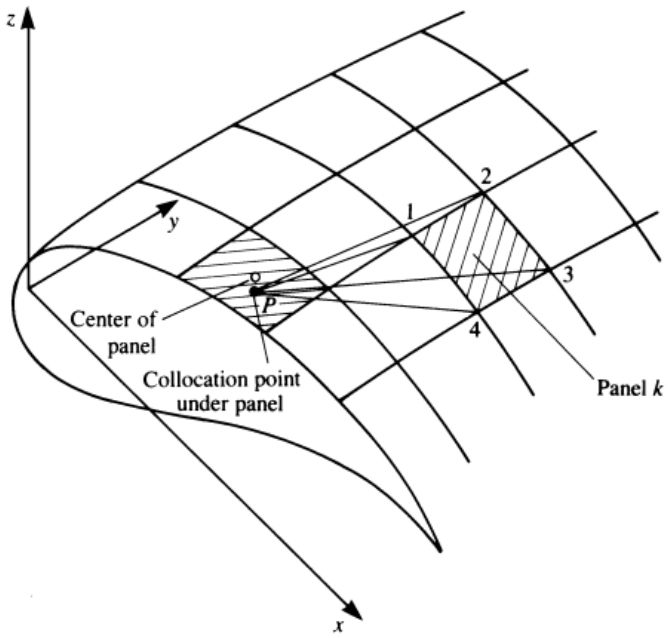


**Figure 5.2:** Influence of Panel $k$ on point $P$ by [35].

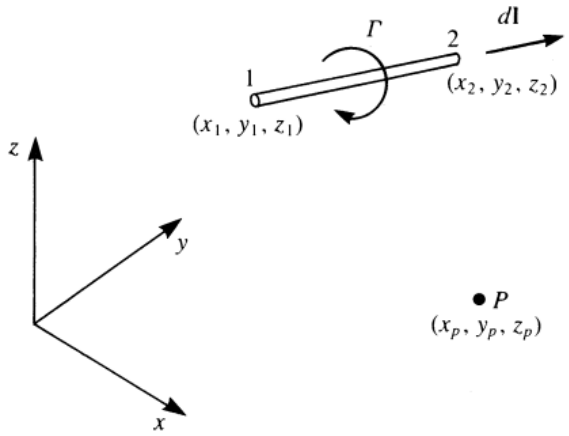


**Figure 5.3:** Influence of segment $12$ on point $P$ by [35].

A solvable linear system of equations is obtained when the boundary condition is enforced at each panel's collocation point. Solving the linear problem yields the previously unknown circulation distribution, which

can be used to compute the surface loading. The calculation of inviscid lift and drag relies on the solved panel circulations. The lift is determined by evaluating the forces acting on the body using the Kutta-Joukowski theorem.
The solver developed by J. Thielen [34] is a steady VLM intended for the analysis of isolated propellers. For this reason, the author of this study could adopt some interesting simplifications:

- A fixed wake model is used, in which the wake vortex panels are positioned in a helical structure and do not resent the induced velocity.
- Since the loading is the same for all the propeller blades, the Neumann condition is applied only to a single blade surface. The velocity induced by the other blades and their respective wakes is accounted for, but since the loading is the same, the circulation values are also the same. This reduces the overall dimension of the system, considering only $N_S \times N_C$ control points instead of $N_S \times N_C \times N_B$, where $N_B$ is the number of propeller blades.

While the second simplification significantly reduces computational time without compromising result quality, it limits the method's applicability to studies of installed propellers, particularly when evaluating the effects of unsteady loading, where each blade experiences a different loading distribution. Therefore, the work by J. Thielen [34] was chosen as a foundation for developing an Unsteady Vortex Lattice Method (UVLM) tailored to studying the aerodynamics of installed propellers under significant unsteady loading conditions.

## 5.2. Unsteady Vortex Lattice Method

The Unsteady Vortex Lattice Method (UVLM) follows a procedure similar to its steady counterpart, with a key difference: instead of completing the simulation in a single time step with a pre-allocated wake, the unsteady method adopts a time-marching approach. In UVLM, the loading distribution is recalculated at each time step while the wake grows by adding a row of panels shed behind the trailing edge of the lifting surfaces. The Kutta condition is applied at every time step, ensuring that each new row of wake panels has the same circulation distribution as the trailing edge of the blade when it was shed. Once assigned, the strength of each wake vortex panel remains unchanged in subsequent iterations. This process is illustrated in Figure 5.4 for a general fixed-wing case and in Figure 5.5 for a propeller modeled by the developed solver.

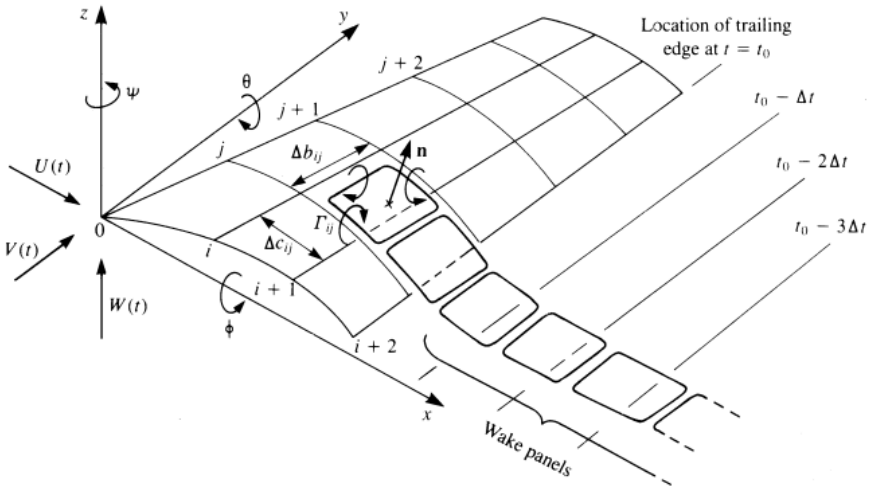


**Figure 5.4:** Unsteady VLM representation for a wing case, showing the wake panels added at each time iteration [35].

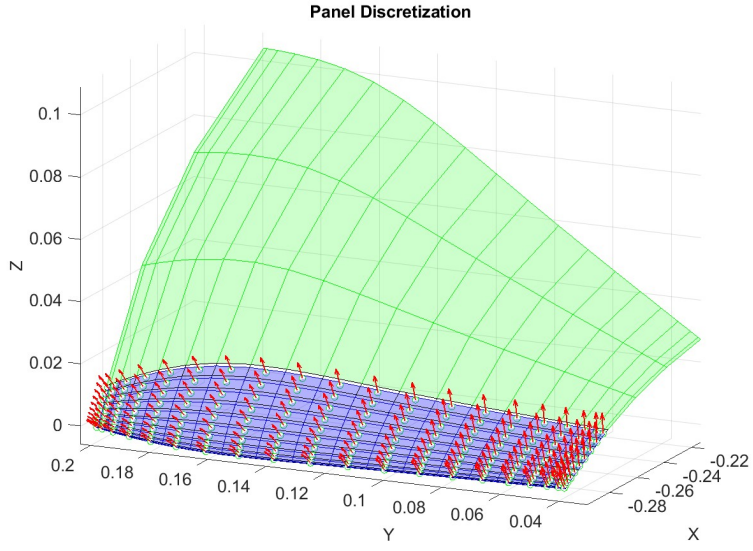


**Figure 5.5:** Detailed view of one of the propeller blades modeled in the UVLM solver developed for this thesis. The features include the blade panels (blue surface), the bound vortex lattice (black grid), the control points and normal vectors (red arrows), and the wake panels (green surface).

### 5.2.1. Solver Flow-chart

The solver procedure is based on chapter 13 of Katz and Plotkin's "Low-Speed Aerodynamics" [35]. Figure 5.6 presents a flowchart to clarify the steps and sequence followed. Initially, the propeller geometry and operating conditions are defined. For installed conditions, the non-uniform inflow velocity distributions at the propeller disk can be provided as input. The propeller is then discretized into panels using the Smart Rotor functions [28], along with the desired simulation parameters, wake model, overall simulation time, and its discretization as wake parameters.

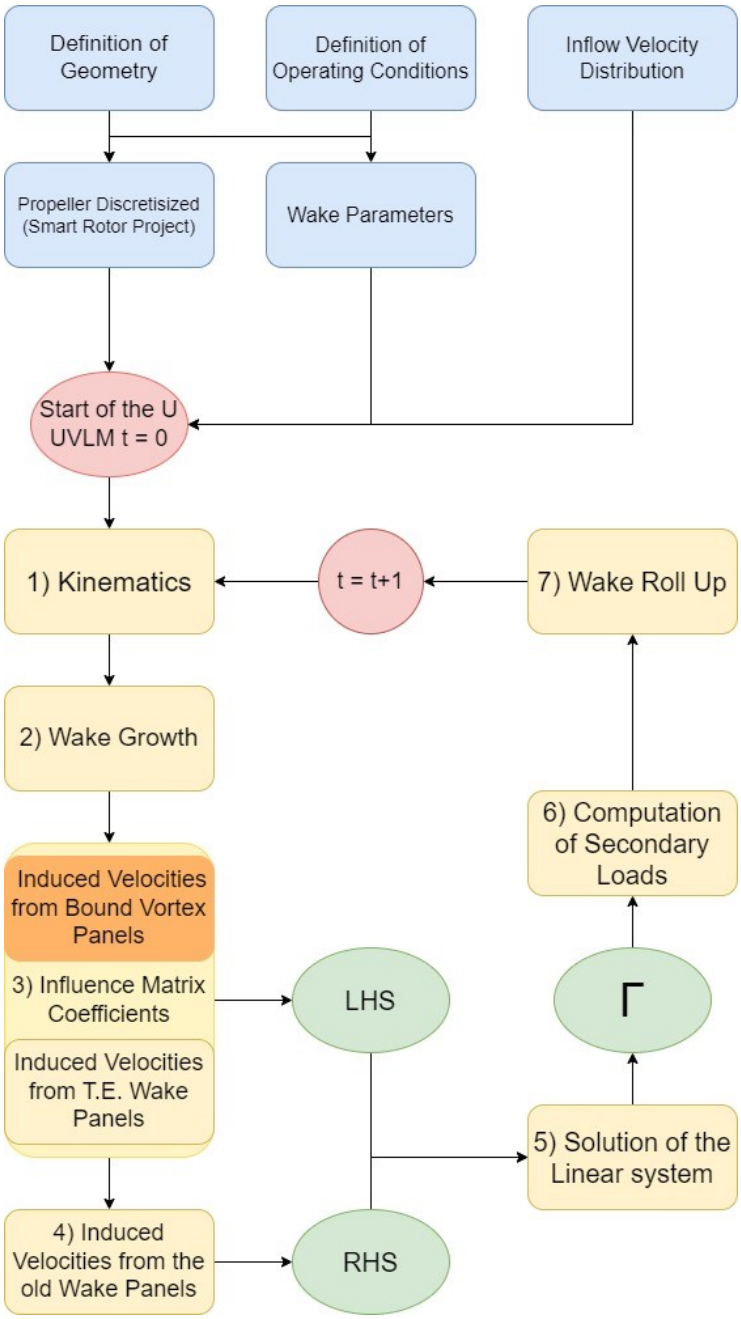


**Figure 5.6:** This flowchart illustrates the unsteady Vortex Lattice Method (VLM) developed for this thesis. Blue boxes indicate steps performed only once during the initialization phase, outside the time iteration cycle. Yellow boxes represent processes that are repeated at each time iteration. The orange box within the time iteration cycle denotes a step executed only at the first time step ($t = 0$).

Below is a brief illustration of the main steps.

**Kinematics**
Two reference systems are used: a general inertial system and a local system fixed to the propeller, which rotates and translates with the propeller motion. The geometric description of the propeller in the Smart Rotor application uses this local coordinate system.
At each time step, the orientation of the propeller blades in the inertial reference frame is computed, and the relative velocities between the propeller sections and the air are obtained. For installed conditions, the velocity changes due to distortion with respect to the uniform case ($\Delta\vec{V}_{inflow}$) are included. Equation 5.4 shows how the relative velocity at each blade section $V_K$ is found.

$$\vec{V}_K = \vec{V\infty} + \Omega \times \vec{r} + \Delta\vec{V}_{inflow} \tag{5.4}$$

Figure 5.7 shows the coordinates of the inertial reference system and the propeller kinematics. The propeller is considered to be flying in the negative x-direction while rotating counterclockwise.

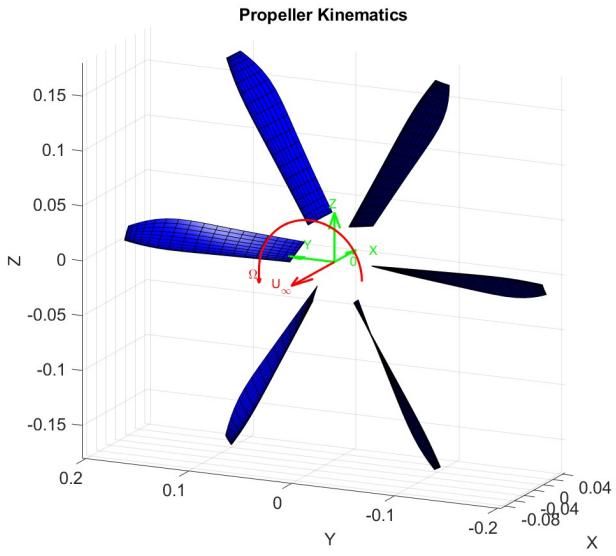


**Figure 5.7:** Visualization of the propeller's panel surfaces (blue), inertial system coordinates (green), and the propeller's flight velocity $U_\infty$ and angular velocity $\Omega$.

**Wake Growth**
In UVLM, at every time step, a new row of vortex panels is shed behind the trailing edge of each blade. The position of the new wake panels is determined by the last row of bound vortex rings' extremes (right after the trailing edge) and the position of these extremes in the previous time step.
Figure 5.5 shows the discretized propeller and the new row of wake vortex panels just shed at the first time step. The bound vortex rings (black lines) and wake vortex rings (green lines) form a continuous sheet, with the last bound vortex line coinciding with the first wake vortex line.

**Influence Matrix Coefficients**
The UVLM relies on the circulation distribution obtained by applying the non-permeability condition on each panel and the Kutta condition at the trailing edge panels. This corresponds to solving Equation 5.5 at each panel.

$$\left(\sum_{j=0}^{N}(\vec{V}_{ind_j}) + \vec{V}_K\right) \cdot \vec{n} = 0 \tag{5.5}$$

Here, $\vec{V}_K$ are the velocity components associated with the kinematics and inflow distribution, while $\vec{V}_{ind_j}$ are the induced velocities by the system of vortex rings, and $\vec{n}$ is the panel's normal vector. Equation 5.5

can be rewritten as Equation 5.6 for each $ith$ panel, where $a_{ij}$ represents the normal component of the induced velocity at the control point of panel $i$ by the $jth$ vortex ring, assuming unit circulation strength as shown in Equation 5.7. This results in the linear system of equations (Equation 5.8).

$$\sum_{j=0}^{N} a_{ij}\Gamma_j = -\left(\vec{V}_K + \sum_{j=1}^{N} \vec{V}_{wake_j}\right) \cdot \vec{n}_i \tag{5.6}$$

$$a_{ij} = (\vec{V}_{ind})_{ij} \cdot \vec{n}_i \tag{5.7}$$

$$\begin{bmatrix} a_{11} & a_{12} & \cdots & a_{1m} \\ a_{21} & a_{22} & \cdots & a_{2m} \\ \vdots & \vdots & \ddots & \vdots \\ a_{m1} & a_{m2} & \cdots & a_{mm} \end{bmatrix} \begin{bmatrix} \Gamma_1 \\ \Gamma_2 \\ \vdots \\ \Gamma_m \end{bmatrix} = \begin{bmatrix} RHS_1 \\ RHS_2 \\ \vdots \\ RHS_m \end{bmatrix} \tag{5.8}$$

The setup of the induction matrix requires computing the influence coefficients for every control point $i$ from each bound vortex ring $j$. The matrix size $m \times m$ depends on the resolution of the discretized blade surface and the number of blades, $m = N_S \times N_C \times B$. Since the propeller geometry remains unchanged during the simulation, the reciprocal position of the bound vortex panels and, thus, the values inside the influence matrix are constant. Therefore, the influence coefficients representing the bound vortex rings are computed only once.

**Induced Velocities from the Old Wake Panels**
The induced velocities computed earlier come from the bound vortex panels and the newly added wake panels. The influence of older wake vortex panels must also be included, as their circulation distribution and relative positions to the blade surface are known. Using the Biot-Savart law, the influence matrix of the wake is set up, representing the velocity induced by the wake vortex ring $j$ on the control point of blade panel $i$ as shown in Equation 5.3. This process is repeated for all $n$ wake vortex panels at each time step. The induced velocities by the wake are then summed to the velocity components at the right-hand side of the linear system of equations (Equation 5.9).

$$\begin{bmatrix} RHS_1 \\ RHS_2 \\ \vdots \\ RHS_m \end{bmatrix} = -\left(\begin{bmatrix} \vec{V}_{k1} \\ \vec{V}_{k2} \\ \vdots \\ \vec{V}_{k3} \end{bmatrix} + \begin{bmatrix} c_{11} & c_{12} & \cdots & c_{1n} \\ c_{21} & c_{22} & \cdots & c_{2n} \\ \vdots & \vdots & \ddots & \vdots \\ c_{m1} & c_{m2} & \cdots & c_{mn} \end{bmatrix} \begin{bmatrix} \Gamma_{wake_1} \\ \Gamma_{wake_2} \\ \vdots \\ \Gamma_{wake_n} \end{bmatrix}\right) \cdot \vec{n}_i \tag{5.9}$$

$$c_{ij} = \left(\vec{V}_{ind_{wake}}\right)_{ij} \tag{5.10}$$

The matrix setup ensures that the influence coefficients are computed only once for the bound vortex panels, while for wake vortex panels, the calculation repeats at each time step due to their continuously changing positions.

**Solution of the Linear System**
Once the right-hand side (RHS) and the induction matrix are established, the linear system can be solved to determine the circulation distribution. With the circulation distribution known, the correct circulation value is assigned to the newly shed wake vortex rings, allowing the procedure to continue.

**Computation of Loads**
After obtaining the circulation distribution, the next step is to compute the velocity and loading distribution on the blade surfaces. A crucial aspect of this computation is determining the effective inflow angle ($\phi$) and the angle of attack ($\alpha$) at each blade span. The inflow angle ($\phi$) depends not only on the kinematic

velocity but also on the induced velocities from the vortex system responsible for the downwash for each $ith$ panel, as described by Equation 5.12.

$$\phi_i = \arctan \frac{\left(\vec{V}_{ki} + \vec{u}_{ind_i}\right) \cdot \vec{i}_{ax_i}}{\left(\vec{V}_{ki} + \vec{u}_{ind_i}\right) \cdot \vec{i}_{tan_i}} \tag{5.11}$$

The induced velocities $\vec{u}_{ind}$ at each control point are calculated using the known circulation of the bound vortex system, as shown in Equation 5.12. These velocities include contributions from both the wake ($\vec{u}_{wake}$) and the trailing bound vortex lines as shown in Equation 5.13. Here $\vec{V}_{ind_{Tbound}}$ represents the induced velocity by only the trailing vortex lines of the panel, assuming a unitary circulation strength, as depicted in Figure 5.2.

$$\begin{bmatrix} \vec{u}_{ind_1} \\ \vec{u}_{ind_2} \\ \vdots \\ \vec{u}_{ind_m} \end{bmatrix} = \begin{bmatrix} b_{11} & b_{12} & \cdots & b_{1m} \\ b_{21} & b_{22} & \cdots & b_{2m} \\ \vdots & \vdots & \ddots & \vdots \\ b_{m1} & b_{m2} & \cdots & b_{mm} \end{bmatrix} \begin{bmatrix} \Gamma_1 \\ \Gamma_2 \\ \vdots \\ \Gamma_m \end{bmatrix} + \begin{bmatrix} \vec{u}_{wake_1} \\ \vec{u}_{wake_2} \\ \vdots \\ \vec{u}_{wake_m} \end{bmatrix} \tag{5.12}$$

$$b_{ij} = (\vec{V}_{ind_{Tbound}})_{ij} = (\vec{q}_{23} + \vec{q}_{41})_{ij} \tag{5.13}$$

Accounting for wake influence in the unsteady method is crucial because the circulation distribution changes with each iteration due to varying inflow conditions, directly affecting the blade surfaces. This interaction introduces a delay between changes in loading and subsequent changes in inflow, a phenomenon that is explored further in Chapter 7.

The second part involves calculating the loading distribution. Katz and Plotkin (Chapter 13) suggest using the Bernoulli equation for the unsteady case instead of the Kutta-Joukowsky theorem. However, this thesis adopts a similar procedure to the steady VLM version, using the Kutta-Joukowsky theorem. Although this approach does not account for the circulation change between time steps, it simplifies the process and aligns with the reference approach used in [36], which includes viscosity correction (Section 5.3).
The lift generated by each blade panel is computed using Equation 5.14. For panels at the leading edge ($i = 1$), the vortex line's intensity is solely affected by the local vortex ring's circulation. For panels positioned after the leading edge ($i > 1$), the vortex line's intensity results from the difference in circulation between the current ($i$) and preceding ($i - 1$) panels.

$$\vec{L}_{ijb} = \begin{cases} \rho \vec{V}_{K_{ijb}} \times \Delta \vec{y}_{ijb} \Gamma_{ijb} & \text{if the panel is at the leading edge } i = 1 \\ \rho \vec{V}_{K_{ijb}} \times \Delta \vec{y}_{ijb} \left(\Gamma_{ijb} - \Gamma_{i-1jb}\right) & \text{if the panel is after the leading edge } i > 1 \end{cases} \tag{5.14}$$

Compressibility effects on the loading are considered using the Prandtl-Glauert correction, as shown in Equation 5.15. This approach, suggested by Katz and Plotkin [35], was successfully implemented by Ingraham [26] in a similar study for aeroacoustic analysis of low-speed propellers.

$$\vec{L}_{ijb} = \frac{\vec{L}_{ijb}}{\sqrt{1 - M^2}} \tag{5.15}$$

Drag is computed using the induced velocity from the downwash, following a similar process to the lift calculation 5.16.

$$\vec{D}_{ijb} = \begin{cases} \rho \vec{u}_{ind_{ijb}} \times \Delta \vec{y}_{ijb} \Gamma_{ijb} & \text{if the panel is at the leading edge } i = 1 \\ \rho \vec{u}_{ind_{ijb}} \times \Delta \vec{y}_{ijb} \left(\Gamma_{ijb} - \Gamma_{i-1jb}\right) & \text{if the panel is after the leading edge } i > 1 \end{cases} \tag{5.16}$$

The overall aerodynamic force generated by all panels is then calculated using Equation 5.17.

$$\vec{F}_{ijb} = \vec{L}_{ijb} + \vec{D}_{ijb} \tag{5.17}$$

With the surface loading distribution known, the final steps involve computing the thrust and torque components (as defined in Section 2.1.1), integrating them to obtain the distribution along each blade span, and then determining the overall propeller performance. This method enables the solver to model features such as in-plane forces caused by unsteady blade loading, as each propeller blade is simulated individually and subjected to distinct inflow conditions.

**Wake Roll Up**
The final step is updating the positions of the wake panels, which move according to the local fluid velocity since they are free from aerodynamic loads. This is done using Equation 5.18, where the position $\vec{X}_l$ of a generic $lth$ extreme of one of the wake vortex panels in the previous time step is updated by the displacement obtained from the product of the local velocity and the time interval width.

$$(\vec{X}_l)_t = (\vec{X}_l)_{t-1} + \vec{u}_{wake_l} \Delta t \tag{5.18}$$

The local velocity ($\vec{u}_{wake}$) comprises contributions from the bound vortex system ($d_{ij}$), the wake vortex system itself ($e_{ij}$), and the inflow distorted velocity field ($\Delta\vec{V}_{inflow}$), as shown in Equation 5.19.

$$\begin{bmatrix} \vec{u}_{wake_1} \\ \vec{u}_{wake_2} \\ \vdots \\ \vec{u}_{wake_k} \end{bmatrix} = \begin{bmatrix} d_{11} & d_{12} & \cdots & d_{1m} \\ d_{21} & d_{22} & \cdots & d_{2m} \\ \vdots & \vdots & \ddots & \vdots \\ d_{k1} & d_{k2} & \cdots & d_{km} \end{bmatrix} \begin{bmatrix} \Gamma_1 \\ \Gamma_2 \\ \vdots \\ \Gamma_m \end{bmatrix} + \begin{bmatrix} e_{11} & e_{12} & \cdots & e_{1n} \\ e_{21} & e_{22} & \cdots & e_{2n} \\ \vdots & \vdots & \ddots & \vdots \\ e_{k1} & e_{k2} & \cdots & e_{kn} \end{bmatrix} \begin{bmatrix} \Gamma_{wake_1} \\ \Gamma_{wake_2} \\ \vdots \\ \Gamma_{wake_n} \end{bmatrix} + \begin{bmatrix} \Delta\vec{V}_{inflow_1} \\ \Delta\vec{V}_{inflow_2} \\ \vdots \\ \Delta\vec{V}_{inflow_k} \end{bmatrix} \tag{5.19}$$

This comprehensive approach ensures accurate modeling of the wake dynamics and its interaction with the propeller blades, contributing to a detailed understanding of the propeller's aerodynamic performance.

## 5.2.2. Limitations

The aerodynamic solver based on the Unsteady Vortex Lattice Method is built on several assumptions, limiting its application:

- Potential flow assumption: No viscous correction is present, limiting the solver's reliability for scenarios involving complex flow phenomena such as flow separation, leading-edge vortices, and crossflow, particularly when analyzing propellers with highly swept blades or operating under highly loaded conditions.
- Compressibility: Addressed using the Prandtl-Glauert correction, suitable only when the sectional Mach number is below $M = 0.6$. This limits the propeller's simulation conditions regarding tip Mach number ($M_t$).
- Blade thickness: Neglected in the model, which uses mean surfaces defined by sectional camber lines, affecting the reliability of loading distribution along the chord.

Despite its limitations, the solver can provide satisfactory results for estimating the aerodynamic performance of low-speed propellers operating in linear flow regimes. However, in the case of a Boundary Layer Ingestion (BLI) configuration, the significant changes in axial velocity may induce flow separation, even when an isolated propeller under similar conditions remains within the linear flow regime. To address this, a second aerodynamic solver has been developed, capable of accounting for viscosity and modeling the stall of blade sections when the local angle of attack exceeds the critical value. This viscous solver, known as the Unsteady Non-Linear Vortex Lattice Method (UNVLM), models the propeller blades as vortex lattices and corrects the circulation distribution using the tabulated lift polar curves of the blade sections' airfoils. The procedure is detailed in Section 5.3.

## 5.3. Unsteady Non-Linear Vortex Lattice Method

In the literature study, several approaches to modifying the Vortex Lattice Method (VLM) to account for viscosity and include features like flow separation have been explored. Most of these methods employ an iterative process, where the circulation distribution obtained from the linear problem is gradually corrected using the tabulated lift polars of the blade sections' airfoils.

Some methods are based on the decambering approach, where, as explained by Gopalarathnam et al. [37][38], the camber of the local section is progressively corrected until the lift generated by the vortex lattice matches the lift according to the tabulated data. A solver based on a modified version of this approach has been applied to the study of a fixed wing in steady simulations by E. Ebbens [39].

H. Lee et al. [40] provide a comprehensive overview of VLM applications in rotor studies, encompassing propellers, helicopter rotors, and wind turbines. In their article [36] focused on wind turbines, they propose a viscosity correction for the unsteady VLM based on the iterative correction of the circulation using tabulated lift and drag coefficients and the distribution of the angle of attack. Unlike the decambering approach, the camber line of the blades' sections is not modified, and the condition of non-permeability of the lifting surface is abandoned after the first iteration, which uses the solution from the linear problem as the initial guess for the circulation distribution. The solution is considered converged once the lift obtained from the updated circulation distribution matches the lift according to the tabulated lift polars data and the distribution of the angle of attack.

Both the decambering and iterative circulation correction approaches are valid options for the viscosity correction of the aerodynamic solver in this thesis project. Since the circulation correction approach has already been applied to rotor aerodynamics in unsteady simulations, it is chosen for this project. With the inclusion of tabulated lift polars, the resulting viscous aerodynamic solver can account for non-linear flow phenomena, such as the stall of blade sections when the local angle of attack exceeds the critical value. Therefore, it is called the Unsteady Non-Linear Vortex Lattice Method (UNVLM).

### 5.3.1. Solver Flow-chart

The procedure followed by the viscous solver is described in this section. Figure 5.8 provides the method's flowchart, similar to the scheme for the potential UVLM method described in Figure 5.6.

A new input is provided: the tabulated data containing the polars of the XPROP blade's airfoils. This data was collected by D. Barara, a researcher at TU Delft, who conducted simulations using the software XFoil [41] for each of the 25 baseline airfoils of the XPROP propeller. The viscous analysis was carried out at a zero Mach number ($M = 0$) and for a range of Reynolds numbers from $50000$ to $300000$ with a step-size of $25000$. The polar data was originally generated for angles of attack ranging from $-25°$ to $25°$ with a step-size of $0.1°$. To expand the range of angles of attack from $-90°$ to $90°$, the data was modified using the Viterna extrapolation [42]. The polars were generated by assigning a forced transition at $x/c = 0.05$ of the airfoils.

The solver interpolates this data to provide the lift and drag coefficients for each section based on the radial coordinate, local Reynolds number, and angle of attack. The radial coordinate of the section identifies the profile, the Reynolds number selects the closest polar curve to the local flow conditions, and the angle of attack is used to obtain the specific lift and drag coefficients generated by the section. When the local Reynolds number exceeds the interval, the closest value is applied.

Similar to the potential UVLM, the UNVLM is an unsteady method that repeats the procedure at every time step. The first step involves updating the propeller blades' positions in the inertial reference system and computing the local velocities at each blade section. New wake panels are then added immediately behind the trailing edge, and the setup of the linear problem begins. The influence matrix coefficients and the right-hand side of the linear problem are set as explained for the potential UVLM in Section 5.2.1. Once the linear system is ready, the iterative circulation strength correction procedure begins. This new step, shown in the red box in Figure 5.8, is the primary difference between the potential and viscous solvers. It allows for the viscosity correction but demands greater computational resources. Once the corrected circulation distribution is known, the loading distribution is computed, and the wake panels' positions are updated similarly to the potential UVLM solver. As with the potential UVLM, the simplifications to the wake model discussed in Section 5.2.1 are available for the viscous UNVLM as well.

A detailed explanation of the circulation strength correction process is provided below.

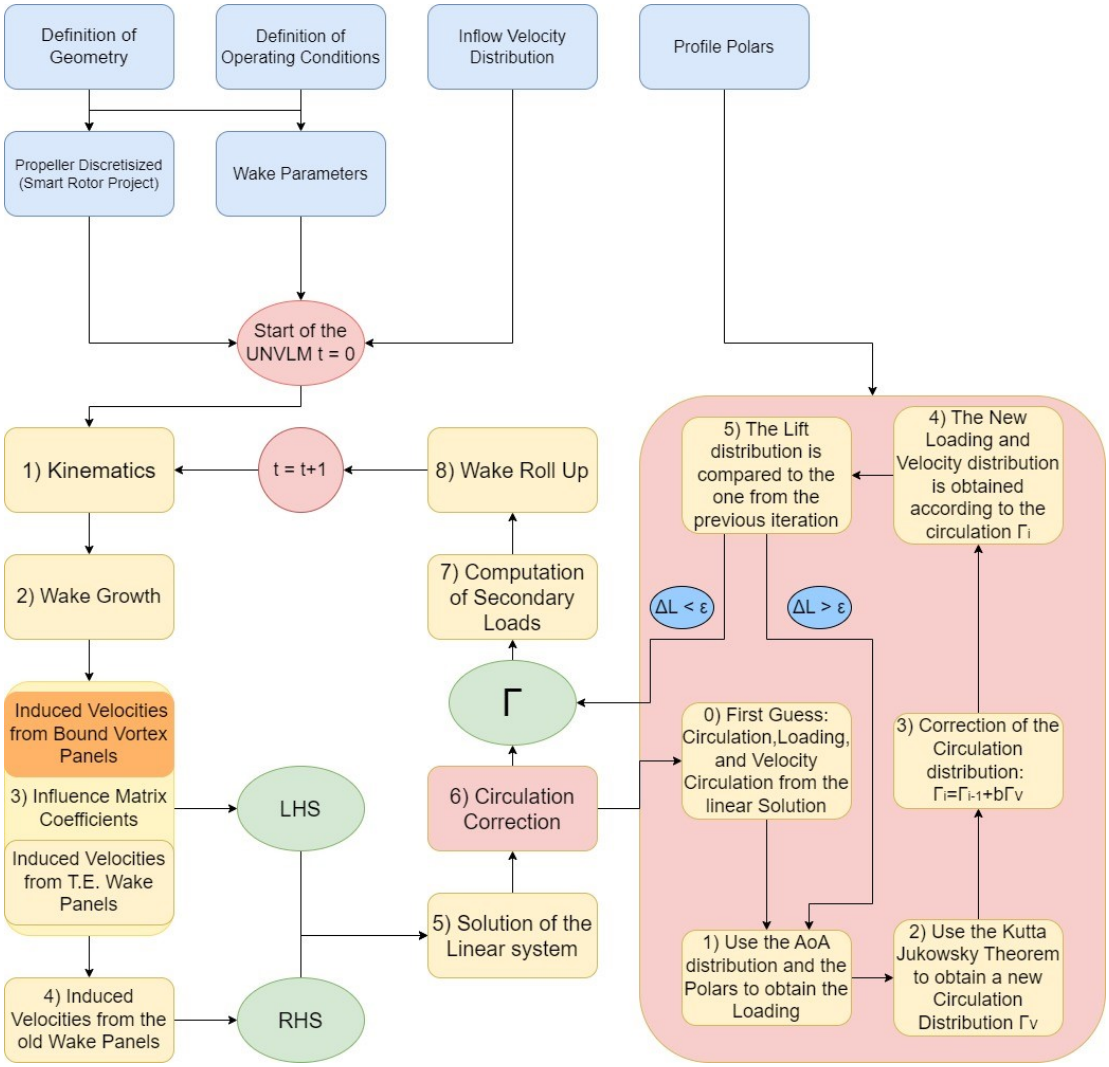


**Figure 5.8:** Schematic flowchart of the UNVLM. The diagram highlights a new passage in the red box: the circulation strength correction, an iterative process that includes the effects of viscosity and profile thickness by utilizing the tabulated lift polars of the sections' profiles.

**Circulation Strength Correction**

The first step involves computing the effective velocity distribution at all panels, defined as the sum of the components due to kinematics and downwash. As shown in Equation 5.12, the circulation distribution of the bound and free vortex systems, together with the influence matrices, is used to compute the downwash velocities. Once the effective velocities at each panel are known, the local inflow angle, angle of attack, and Reynolds number are computed. These distributions are then used to obtain the local lift and drag coefficients for each blade section using the tabulated polar data.

An ambiguity arises: any VLM model discretizes the lifting surfaces in both the spanwise and chordwise directions, while using airfoil polar curves requires considering the lifting surface only discretized along the blade span. A control point in the chordwise direction must be chosen to estimate the angle of attack and effective velocity for each section along the blade. The article [36] suggests using the mid-chord point for airfoils with parabolic camber distributions. During the development of the UNVLM solver, it was verified that the results obtained using the mid-chord control point almost match those obtained using the average value of the distribution of angle of attack and effective velocity along the chord of each section. It was found that the maximum difference in performance estimated was lower than $0.5\%$. Thus, this approach was adopted for the polars obtained by the airfoil of the XProp blade sections used in this study.

Finally, the lift according to the polar of each section can be computed using Equation 5.20, and the circulation according to the tabulated value can be obtained by applying the Kutta-Joukowsky theorem as

in Equation 5.21.

$$\delta L_{table,j} = \frac{1}{2}\rho_\infty \left|\vec{V}_{K,j} + \vec{u}_{ind,j}\right|^2 C_{l_{table},j} c \tag{5.20}$$

$$\Gamma_{table,j} = \frac{\delta L_{table,j}}{\rho_\infty \left|\vec{V}_{K,j}\right|} \tag{5.21}$$

Once the circulation according to the tabulated lift polar of the blade sections is obtained, the circulation distribution from the previous step can be effectively corrected. To do so, a single circulation value must be chosen for every spanwise section. However, due to the chordwise discretization of the propeller blade surfaces in the VLM, the ambiguity discussed earlier reoccurs. The article by Lee et al. [36] suggests using the average value of the circulation distribution along the chord. However, this thesis opts to use the circulation strength of the vortex ring at the trailing edge of each section, as it better represents the overall lift generated by the entire section, as shown in Equation 5.22.

$$\delta L_j = \sum_{i=1}^{N_C} L_{i,j} = \rho V_{K,j}\Gamma_{1,j} + \sum_{i=2}^{N_C} \rho V_{K,j}\left(\Gamma_{i,j} - \Gamma_{i-1,j}\right) = \rho V_{K,j}\Gamma_{N_C,j} = \rho V_{K,j}\Gamma_{T.E.,j} \tag{5.22}$$

Therefore, the circulation can be corrected as shown in Equation 5.23. A damping factor $b$ is applied to reduce the change in the circulation distribution at each iteration. This is done to ensure gradual changes in velocities and angles of attack ($\alpha$), avoiding abrupt increments or reductions that could introduce numerical instabilities and prevent convergence. Induced velocities can change significantly at the blade extremes (tip and hub) when relatively small variations in the circulation distribution are introduced. This region is more prone to instability because the change in circulation along the blade span is larger at the blade extremes, making the trailing vortex lines stronger and consequently amplifying the induced velocity changes.
Choosing a damping factor involves a trade-off: a low value ensures method stability but requires a high number of iterations, increasing computational time. Conversely, a high value can destabilize the numerical code, negating the utility of the viscous correction. The value suggested by [36] appeared too high, and it was found that the need for the damping factor was higher at the blade extremes. Therefore, a parabolic distribution of the damping factor along the blade span was adopted, as shown in Equation 5.27. This distribution has a maximum value of $b_{Max} = 0.01$ at the mid-span ($r = 0.5$), where a smaller damping is less needed, and $b_{min} = 0.005$ at the blade extremes (hub $r = 0$ and tip $r = 1$).

$$\Gamma_{T.E.new} = \Gamma_{T.E.old} + b(\Gamma_{table} - \Gamma_{T.E.old}) \tag{5.23}$$

$$b(r) = a_1 r^2 + a_2 r + a_3 \tag{5.24}$$
$$a_1 = 4(b_{Min} - b_{Max}) \tag{5.25}$$
$$a_2 = 0 \tag{5.26}$$
$$a_3 = b_{Max} \tag{5.27}$$

The next iteration requires a surface distribution of the circulation for the computation of the induced velocities by the vortex lattice and the angle of attack. However, the corrected circulation obtained in Equation 5.23 is the strength of the vortex panel at the trailing edge, as explained before. The article [36] suggests defining a circulation strength factor $\lambda_{i,j}$ for all the panels along the chord of each blade section, which relates the local circulation value with the reference of the whole section $\Gamma_{T.E.,j}$. The strength factor for each spanwise section, defined in Equation 5.28, is determined at the first iteration using the circulation distribution from the linear problem. At the end of each iteration, the surface circulation distribution is obtained from the corrected circulation distribution described in Equation 5.23 by inverting the strength factor definition, as shown in Equation 5.29.
The circulation factor definition presented here differs from that in [36] because it includes a term $\delta\Gamma$

defined in Equation 5.30. This term ensures that the entire surface circulation distribution is positive before calculating the strength factor, particularly when the minimum circulation value found in the distribution is negative ($\Gamma_{min} < 0$). This modification is necessary because, when the circulation distribution is not entirely positive across the lifting surface (e.g., at high advance ratios where some blade regions generate negative thrust), the numerical procedure can converge to unrealistic, discontinuous distributions. Specifically, the angle of attack and lift distributions exhibit a peak in correspondence of the section where the circulation from the linear solution is the closest to zero, which do not reflect the expected near-null local loading.
This issue arises because, when the circulation at the trailing edge of a section $\Gamma_{T.E.,j}$ approaches zero, the circulation at the leading edge $\Gamma_{L.E.,j}$ has a much larger value. Hence, when the circulation value at the trailing edge is varied as shown in Equation 5.23 while adopting the definition of the circulation factor in [36], the change in circulation at the trailing edge is small, while the change at the leading edge is much larger. This results in a circulation distribution with an anomalous profile at the section discussed at the end of the correction process. The outcome is an anomalously high local angle of attack and lift coefficient, which does not meet the expectation of a nearly null local loading. To resolve this issue, it is sufficient to derive the strength factor using a circulation distribution that is positive across the entire surface.

$$\lambda_{i,j} = \frac{\Gamma_{i,j} + \delta\Gamma}{\Gamma_{T.E.,j} + \delta\Gamma} \tag{5.28}$$

$$\Gamma_{i,j} = \lambda_{i,j} \times (\Gamma_{T.E.,j} + \delta\Gamma) - \delta\Gamma \tag{5.29}$$

$$\begin{cases} \delta\Gamma = 0, & \text{if } \Gamma_{min} \geq 0 \\ \delta\Gamma = -2\Gamma_{min}, & \text{if } \Gamma_{min} < 0 \end{cases} \tag{5.30}$$

The procedure is repeated until the chosen convergence criterion is met and the iteration residual $\Delta$ is lower than the imposed tolerance $\epsilon = 5 \times 10^{-3}$. As shown in Figure 5.8. The code is considered converged once the lift produced by each propeller blade at the end of the circulation correction process is sufficiently close to the lift computed using the angle of attack distribution and the tabulated lift polar. Lift, rather than circulation, is used as the convergence metric because the solver estimates the loading, which is proportional to the lift. The lift is a product of both the circulation and the local velocity, which increases towards the blade tip. Therefore, discrepancies in circulation estimates have a larger impact near the tip, whereas the difference in lift provides a consistent measure of loading irrespective of the radial position. In a typical simulation, using this convergence criterion, the viscous circulation correction converges within approximately 150-200 iterations at each time step.

$$\Delta = max\left(\left|\frac{(L_{table,b} - L_{bound,b})}{L_{bound,b}}\right|\right) < \epsilon \tag{5.31}$$

The updated circulation of the panels at the trailing edge is associated with the newly shed wake panels to enforce the Kutta condition. This way, the influence of the wake on the blade surface is also corrected.

**Computations of Loads**

The procedure for computing the loads is similar to the method in the potential solver discussed in Section 5.2. Since the velocities and angle of attack distributions have already been determined during the circulation strength correction, the process begins directly with calculating the aerodynamic loading. The lift is computed using the Kutta-Joukowski theorem, followed by the application of the compressibility correction. To avoid exacerbating changes in circulation that could introduce numerical instabilities, the compressibility correction is not included in the circulation strength correction.
A significant difference between the potential and viscous solvers is that the UNVLM can incorporate the profile drag component using the tabulated drag polars, as shown in Equation 5.33. After calculating the induced drag component as in Equation 5.32, the total drag for each vortex panel is the sum of these components.

$$D_{i,j,b} = D_{induced,i,j,b} + D_{profile,i,j,b} \tag{5.32}$$

$$D_{profile,i,j,b} = \frac{1}{2}\rho_\infty \left|\vec{V}_{K,i,j,b} + \vec{u}_{ind,i,j,b}\right|^2 C_d S \tag{5.33}$$

### 5.3.2. Limitations

The viscous solver, like the potential solver, is subject to inherent limitations:

- The viscous correction is present, but complex flow phenomena such as leading-edge vortices and crossflow are not accounted for, potentially affecting the accuracy of aerodynamic loading, especially for blades with large sweep.
- The tabulated lift and drag coefficients are obtained from XFoil, a low-fidelity software based on a viscous panel method. The transition to turbulent flow is fixed at the leading edge, excluding some aerodynamic features typical of low Reynolds numbers, such as flow separation bubbles, which could result in delayed stall prediction.
- The tabulated data includes the viscous lift and drag polars only for the profiles of the sections composing the XProp blade, limiting the range of profile sections available for study.
- The post stall data is predicted using Viterna extrapolation, which might not depict the reality for high angles of attack.
- Compressibility is accounted for using the Prandtl-Glauert correction, a simple method suitable only when the sectional Mach number stays below $M = 0.6$.
- Despite accounting for thickness in the tabulated data, the loading distribution along the chord is still derived from the mean surface distribution used in the VLM, which may compromise the quality of these results.

In conclusion, compared to the potential solver, the UNVLM can account for profile thickness and some flow phenomena associated with viscosity at the cost of greater computational resource demands. However, as a low-fidelity model, it still excludes some complex features caused by viscosity, and the adopted compressibility correction limits the maximum tip Mach number simulated.

## 5.4. Wake Model

Before employing these solvers, it is essential to discuss the wake structure's definition, as its discretization is closely tied to the time discretization of the simulation. The wake structure significantly influences not only the aerodynamic performance but also the computational resources required to complete the simulations. These demands can become substantial when using the free-wake model described in previous sections. Therefore, this section defines the wake parameters that determine wake resolution, discusses their impact on the estimated aerodynamic performance and computational time, and compares the results obtained using the free-wake model with those derived from adopting a simplified wake model.

### 5.4.1. Wake Parameters

The discretization of the wake shed by each blade into vortex panels is determined by several key parameters: the number of panels along the blade span $N_S$, the number of revolutions $n$ completed by the propeller by the end of the simulation, and the angle swept by the propeller blade at each time step $\Delta\phi$, which directly affects the length of each wake panel. These parameters are closely tied to those typically used for time discretization in unsteady simulations, such as the total simulation time $T$ and the time interval for a single time step $\Delta t$, as described by Equations 5.34 and 5.35.

$$T = n \times \frac{2\pi}{\Omega} \tag{5.34}$$

$$\Delta\phi = n \times 2\pi \frac{\Delta t}{T} \tag{5.35}$$

The smaller the angle swept by the propeller at each time step, the shorter the corresponding time interval, leading to a higher resolution of the wake. This increased resolution results in a greater number of wake panel rows by the end of the simulation, denoted as $N_W$ and defined in Equation 5.36. This value $N_W$ also coincides with the total number of time steps required for the simulation.

$$N_w = \frac{\Delta\phi}{n2\pi} = \frac{\Delta t}{\Delta T} \tag{5.36}$$

In the developed solver, instead of prescribing the total simulation time and the time interval for each time-step, the number of revolutions and the desired angle swept by the propeller in a time step are specified. This approach allows direct control over the wake resolution, independent of operating conditions.

### 5.4.2. Wake Resolution

The time-marching approach described prescribes that the wake grows at every time step, with the number of panels increasing by $B \times N_S$. Consequently, the number of calculations as well the computational time required to solve the system grows with each time step, becoming computationally unsustainable when the number of blades $B$ or the propeller's discretization resolution is high. Therefore, the number of revolutions simulated and the resolution of the wake must be chosen to provide satisfactory aerodynamic analysis without excessive computational time.

A series of simulations with different resolutions were performed on the 6-bladed XPROP propeller operating in isolated conditions with a pitch setting of $\beta_{0.7R} = 45°$ and a fixed flight velocity of $U_\infty = 40$m/s. Two conditions are studied: one at a high advance ratio and low thrust setting ($J = 1.8$), and another at a lower advance ratio and moderate thrust setting ($J = 1.4$). The solver used in this analysis is the potential UVLM described in Section 5.2, without viscosity correction, but the considerations made also apply to the UNVLM solver with the viscous correction.

The time interval was set to allow the propeller to complete half a revolution ($n = 0.5$). This limitation was necessary to ensure that the computer used for the simulations could complete them within an acceptable timeframe, specifically under one hour.

Figure 5.9 illustrates a comparison of the wake structures generated from simulations with varying resolutions. The wake with a higher number of rows ($N_W = 36$) exhibits a smoother and more detailed shape, indicating a higher resolution compared to the wake with fewer rows ($N_W = 9$). The simulation employed the free-wake model, which is characterized by the folding of the wake sheet at its extremes.

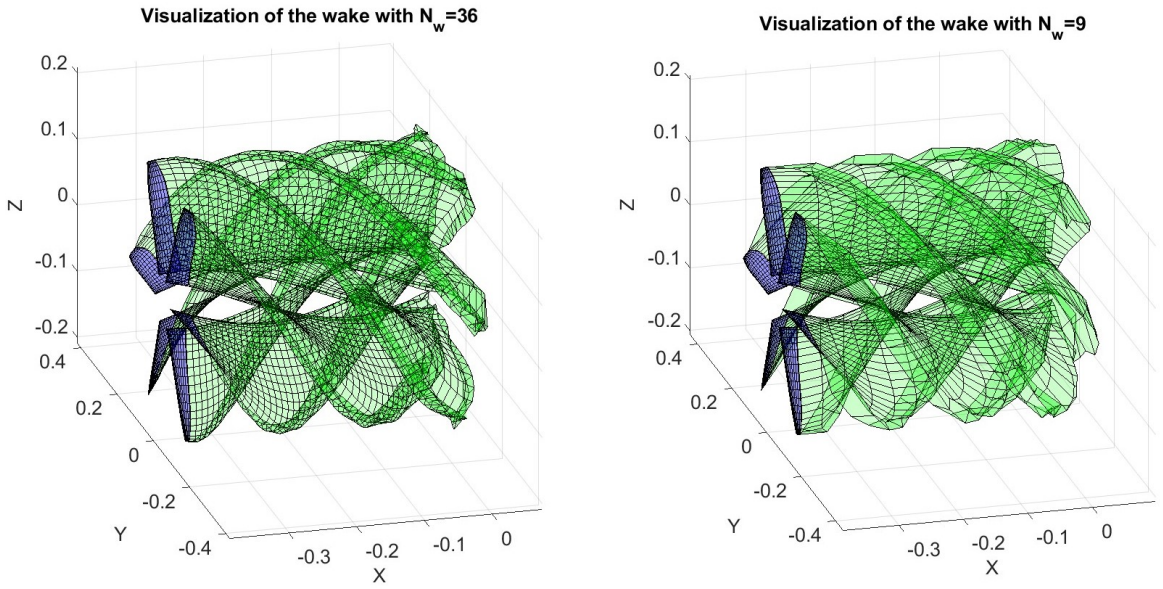


**Figure 5.9:** Visualization of the wake obtained by simulation with different numbers of wake panel rows. The operating condition is fixed at $J = 1.8$.

Figure 5.10 presents the performance estimates derived from simulations with varying resolutions, indicated by the increasing number of time steps ($N_W$). The first two graphs within each figure depict the thrust and power coefficients, demonstrating how these performance metrics evolve with increasing resolution. The third graph highlights the computational cost, specifically the time required by the solver to complete the simulation. This comparison underscores the trade-off between the accuracy of the performance predictions and the computational resources necessary as the resolution increases.

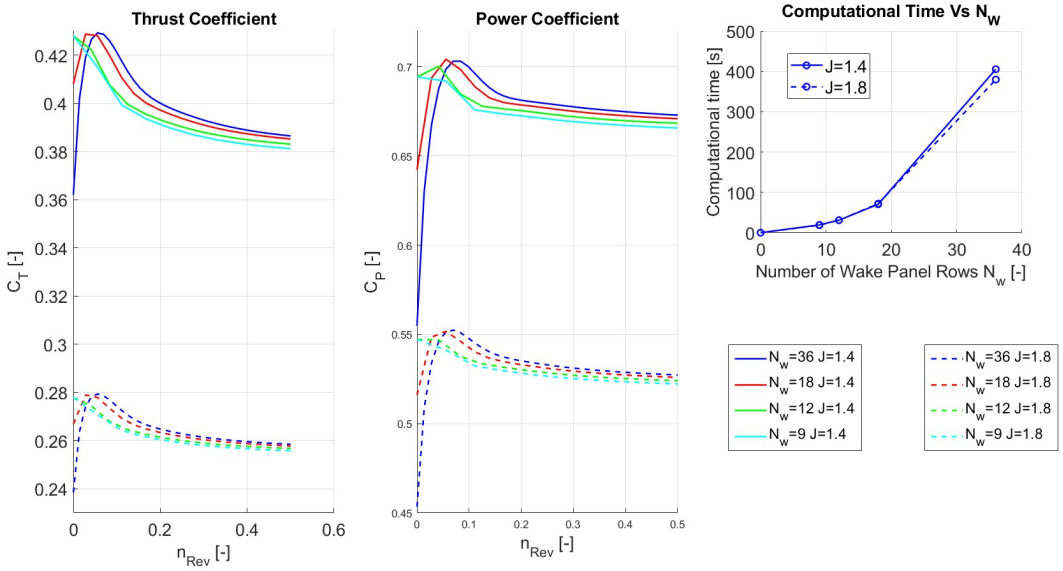


**Figure 5.10:** Left and Center: Propeller performance during the simulation. Right: Computational time required by the solver to complete the simulation.

As wake panel rows are added with each iteration, the geometry of the wake evolves, impacting its influence on the flow and, consequently, altering the circulation distribution and loading generated by the propeller blades. Initially, during the first quarter of the propeller's rotation ($n < 0.25$), the rate of change in these

parameters is more pronounced. This is because the wake is shorter, and newly added wake panels play a significant role in shaping the overall wake structure. As the wake extends, corresponding to roughly half of a propeller rotation ($n \approx 0.5$), the rate of change diminishes, eventually becoming negligible. This reduction occurs because the influence of panels shed earlier in the simulation decreases due to their increased distance from the propeller blades.
The right graph of Figures 5.10 demonstrates that the simulation time does not grow linearly with the number of time steps $N_W$, as at each time step, the wake grows, increasing the computational load. This holds true regardless of the operating conditions within this range.
The results indicate that for isolated propeller conditions, the higher computational cost associated with high-resolution wake analysis ($N_W = 36$, $\Delta\phi = 5°$) does not translate into a significant improvement in performance estimates. For instance, at an advance ratio $J = 1.4$, the difference in thrust coefficient between the highest and lowest resolutions is less than $1.4$%. This limited improvement does not justify the increased computational burden. Conversely, in installed conditions, wider angles ($\Delta\phi$) may not adequately capture local inflow variations, making high-resolution wakes essential.
A practical compromise is a wake discretized with an angle of $\Delta\phi = 10°$, as demonstrated in the simulation with $N_W = 18$ wake panel rows. Chapter 9 shows that this level of resolution is sufficient for the BLI inflow scenarios of interest, providing satisfactory results.
However, a significant challenge arises regarding the time required for the propeller to reach convergence. In isolated propeller simulations, this issue is less critical since the output is steady and performance indicators from the final time interval are typically sufficient. In contrast, for installed propellers where capturing unsteady blade loading is crucial, the convergence time can become prohibitive. The steep increase in computational time, as illustrated in the right graph of Figure 5.10, underscores the need for efficiency improvements. Consequently, a series of simplifications has been implemented to accelerate simulations without compromising accuracy.

### 5.4.3. Simplifications

The first simplification implemented is the suspension of the wake roll-up process, which is the final step in the solver's time-iteration procedure. By eliminating the calculations required for this step, the wake model transitions from being fully free to semi-fixed. In this semi-fixed model, the wake continues to grow, but once the wake panels are shed, their positions remain fixed. Figures 5.12 and 5.11 illustrate the impact of adopting the semi-fixed wake model on the wake panel positions. As shown, the wake sheets in the semi-fixed model do not fold at the extremes, in contrast to the fully free wake model. This adjustment simplifies the wake modeling process while aiming to reduce the computational load.

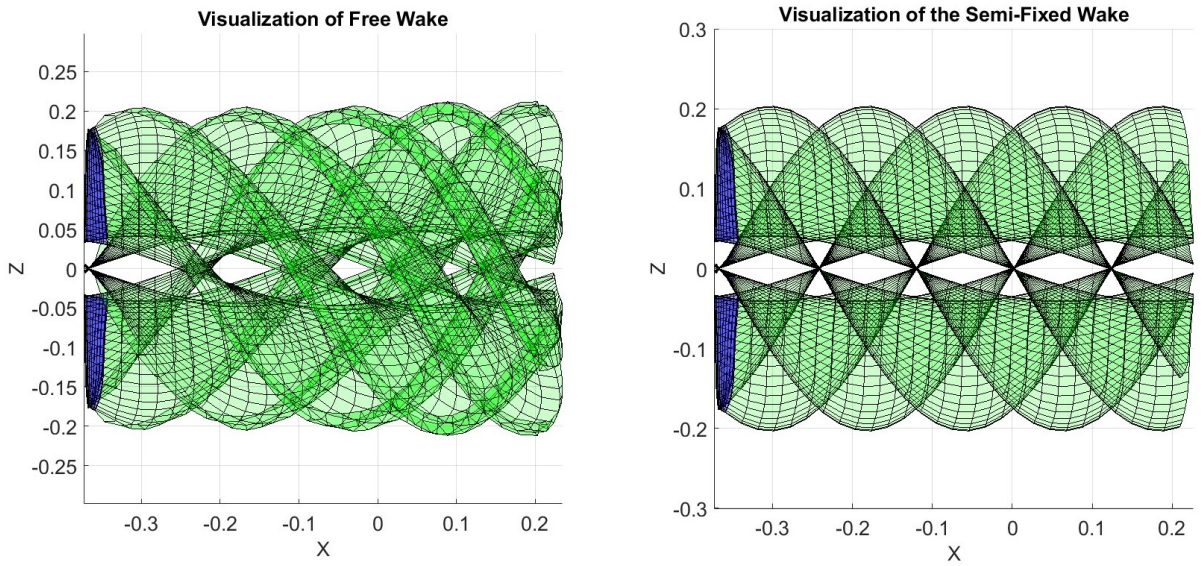


**Figure 5.11:** Visualization of the wakes in a simulation with a free-wake model and a simulation with a semi-fixed wake model. The advance ratio is $J = 1.8$.

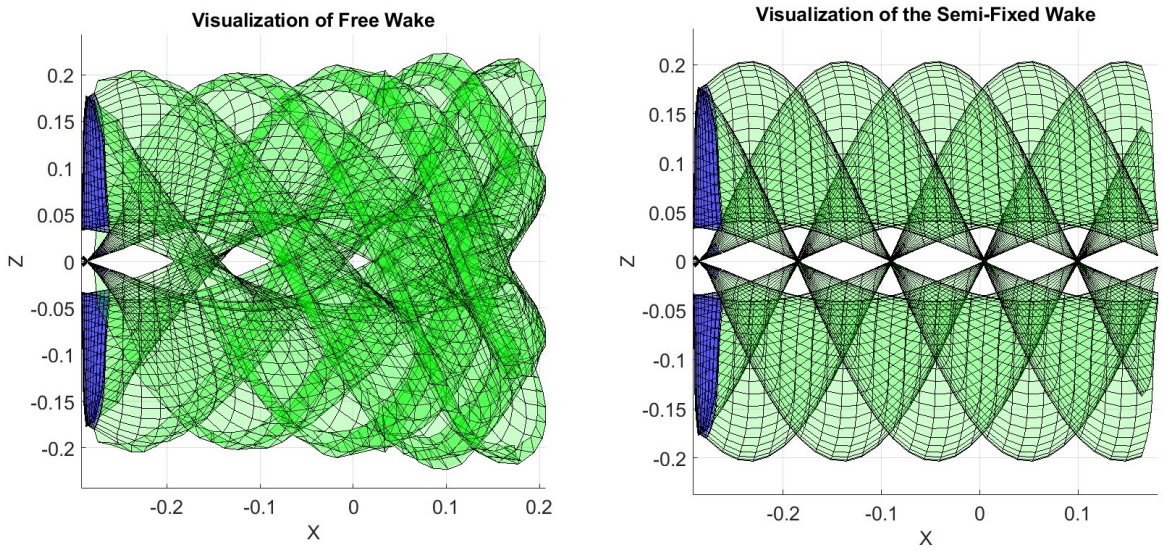


**Figure 5.12:** Visualization of the wakes in a simulation with a free-wake model and a simulation with a semi-fixed wake model. The advance ratio is $J = 1.4$. The lower advance ratio is evident as the propeller has moved a shorter distance forward in half a revolution compared to the case shown in Figure 5.11.

The second simplification involves pre-allocating the wake. In this approach, an initial wake structure composed of $N_{W0}$ rows is created in the first time step. These vortex panels are assigned the same circulation strength as the last bound vortex panels at the trailing edge. This method mimics the steady Vortex Lattice Method (VLM) and reduces the relative importance of newly shed vortex panels, thereby significantly decreasing the rate of change in circulation and loading.

The final simplification pertains to the influence of vortex lines, which, according to the Biot-Savart law (Equation 5.3), is inversely proportional to the distance between the vortex line and the point of measurement. Therefore, after a certain number of time iterations ($N_{W1}$), the influence of wake panels on the propeller diminishes as the propeller advances and moves farther away. Consequently, the code can stop considering the panels if they were shed earlier than $N_{W1}$ time steps.

Figure 5.13 compares the performance outcomes of simulations with no simplifications ($N_{W0} = 1$,$N_{W1} = 20$) against simulations using the free wake model and the semi-fixed wake model with pre-allocated wake ($N_{W0} = 18, N_{W1} = 20$). In the first case, with fewer iterations, the $N_{W1}$ limit does not come into play. In contrast, for the second and third cases, where the pre-allocated wake comprises 18 rows, the simplification allows ignoring older and farther panels from the propeller.
The primary benefit of pre-allocating the wake is the reduction of the transient region at early time steps, where performance changes are more significant. This approach shortens the overall simulation time and allows for earlier data collection. This is particularly advantageous for simulating propellers in installed conditions, where a sufficient angle of rotation must be completed to cover the entire propeller disk with the available blades. Reducing the early transient phase can decrease the number of revolutions needed for simulation, thus lowering the total computational time.
Setting a maximum limit on wake panel rows behind the propeller prevents excessive growth of variables at each time step, reducing computational time. For instance, a simulation with $N_W + N_{W0} = 18 + 18 = 36$ panels takes approximately 125 seconds, about one-fourth of the time required for a simulation with $N_W = 36$ panels, as shown in the right graphs of Figure 5.10. With the semi-fixed model, the simulation time is further reduced to around 40 seconds, highlighting the computational expense of modeling the wake roll-up. This efficiency is even more crucial when using the viscous Unsteady Non-Linear Vortex Lattice Method (UNVLM), which includes an iterative viscous circulation correction step at each time step, increasing computational costs. For instance, the UNVLM with similar wake parameters ($n = 0.5$, $\Delta\phi = 10°$, $N_{W0} = 18$, $N_{W1} = 20$) took approximately 400 seconds to complete.
The results indicate that the performance estimates from the potential solver with varying wake parameters show minimal variation, with the maximum difference in thrust coefficient at $J = 1.4$ being within $1.1\%$.

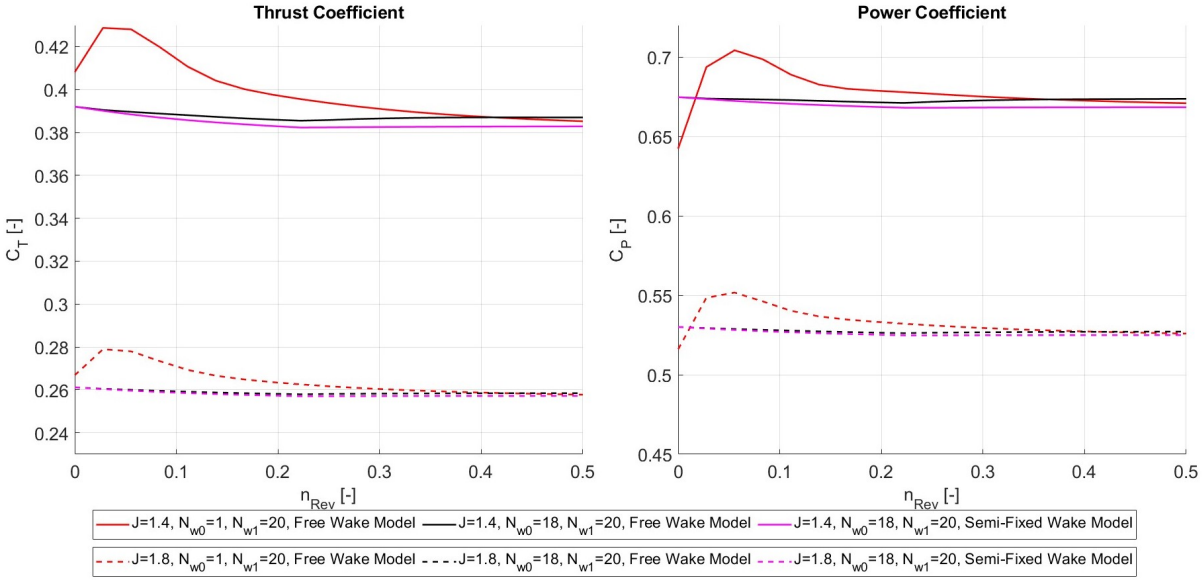


**Figure 5.13:** Estimated propeller performance during the simulation with an advance ratio $J = 1.4$ and $J = 1.8$. Results from the simulation with $N_W = 18$ and no simplifications (red line) are shown alongside those with pre-allocated wake and $N_{W1}$ limit (black line) and a fixed wake model with the same simplifications (magenta line).

For the purposes of this thesis, the pre-allocated wake and $N_{W1}$ panel limit offer a satisfactory balance between computational efficiency and model fidelity. For studies requiring further reductions in computational time, such as optimization studies, the semi-fixed wake model along with these simplifications could provide valuable benefits.

# 6

# Aero-Acoustic Solver

This chapter discusses the acoustic solver used to estimate the aero-acoustic performance of the propellers. Most contemporary noise prediction methods are based on the Ffowcs-Williams and Hawkings (FW-H) equations [43], which model the three primary sources contributing to tonal noise: thickness, loading, and quadrupole sources. Methods for solving these equations fall into two main categories: the time domain, exemplified by Farassat's implementation [44], and the frequency domain, such as Hanson's Helicoidal Surface Theory (HST) [29]. The solver developed by J. Goyal [45], based on the steady version of the HST, has been used as a starting point and has been modified to incorporate the unsteady loading noise source as described in [30]. This additional noise source is expected to play a significant role due to the non-axisymmetric nature of the non-uniform inflow studied in this thesis, as discussed in Section 2.3.4.

Section 6.1 provides a brief overview of Hanson's Surface Theory for steady cases, while Section 6.2 presents its modified version to account for unsteady loading sources. Section 6.3 illustrates how the aerodynamic and acoustic solvers are coupled. Finally, Section 6.4 discusses the limitations of the solvers due to the models used and their implementation. Similar to the propeller geometry parametrization, discretization, and aerodynamic solvers, the acoustic solvers are also programmed in MATLAB.

## 6.1. Hanson's Helicoidal Theory

In the Helicoidal Surface Theory, the pressure wavefront experienced by the observer is calculated using a Fourier series, as shown in equation 6.1. In this equation, $P_{mB}$ represents the Fourier coefficient of the pressure at the $m$-th harmonic of the blade passage frequency (BPF). The term $\Omega_D$ is defined as $2\pi$ times the shaft rotation rate, adjusted to include the Doppler shift, as expressed in equation 6.2. Here, $\theta$ represents the radiation angle, as previously defined in Figure 2.9 in Section 2.2.2, and $M_x = V/c_0$ corresponds to the flight Mach number.

$$p(t) = \sum_{m=-\infty}^{\infty} P_{mB} e^{-imB\Omega_D t} \tag{6.1}$$

$$\Omega_D = \frac{\Omega}{(1 - M_x \cos\theta)} \tag{6.2}$$

The noise harmonic $P_{mB}$ comprises various components associated with different sources, as outlined in equation 6.3. Here, $P_{Vm}$ corresponds to the thickness source (monopole), $P_{Dm}$ represents the drag component of the loading source (dipole oriented in the local convection direction), and $P_{Lm}$ signifies the lift component of the loading source (dipole oriented normal to the local convection direction). Additionally, the loading noise component, the sum of drag and lift contributions, can be represented as the torque $P_{Qm}$ and thrust $P_{Tm}$ components. Quadrupole noise components are not considered because the aerodynamic solvers employed in this study provide data only at the surface, while these sources are volumetric in nature.

$$P_{mB} = P_{Vm} + P_{Dm} + P_{Lm} = P_{Vm} + P_{Qm} + P_{Tm} \tag{6.3}$$

Hanson's work in [29] offers a comprehensive derivation of the harmonic terms defined in Equation 6.4.

$$\begin{bmatrix} P_{Vm} \\ P_{Dm} \\ PL_{Lm} \end{bmatrix} = -\frac{\rho_0 c_0^2 B \sin\theta \exp\left[imB\left(\frac{\Omega_D r}{2} - \frac{\pi}{2}\right)\right]}{8\pi(y/D)(1 - M_x \cos\theta)} \int_{hub}^{tip} M_r^2 \exp(i(\phi_s + \phi_o)) \\ J_{mB}\left(\frac{mBzM_t \sin\theta}{1 - M_x \cos\theta}\right) \begin{bmatrix} k_x^2 t_b \, \Psi_V(k_x) \\ ik_x\left(\frac{c_D}{2}\right)\Psi_D(k_x) \\ ik_y\left(\frac{c_L}{2}\right)\Psi_L(k_x) \end{bmatrix} dz \tag{6.4}$$

The terms in this equation are defined below.

- $z$: Radial coordinates of each blade section.
- $y$: Observer's distance from the propeller axis.
- $r$: Distance between the observer and the propeller in the retarded system as defined in Figure 2.9.
- $M$: Mach numbers, with $M_x$ being the free-stream Mach number, $M_r$ the relative Mach number at the radial section, and $M_t$ the tip Mach number.
- $\phi$: Phase delays, where $\phi_s$ is due to sweep, and $\phi_o$ is associated with lean.
- $J_{mB}$: Bessel function of the first kind with an order of $mB$.
- $k_x$: Chordwise wave number.
- $k_y$: Thickness wave number.
- $C_L$ and $C_D$: Sectional lift and drag coefficients.
- $t_b$: Maximum thickness-to-chord ratio of the radial section.
- $\Psi$: Noise source terms.

The phase delay factors are defined as follows:

- The sweep phase shift, denoted as $\phi_s$, is defined in equation 6.5.
- The lean phase shift, represented as $\phi_o$, is defined in equation 6.6.
- "MCA" stands for Mid-Chord Alignment, and "FA" stands for Face Alignment. These terms are alternative definitions for sweep and lean, as illustrated in Figures 4.2 and 4.3 when discussing the parametrization of the propeller blade geometrical radial distribution in Section 4.1.

These phase delay factors play a crucial role in characterizing the effects of sweep and lean on the acoustic field. As explained in Section 3.1.2 and depicted in Figure 3.5, the phase lag introduced by sweep between the blade sections is responsible for the destructive interference phenomena, leading to an overall reduction of the noise level when the contributions from all the sections are summed.

$$\phi_s = \frac{2mBM_t}{M_r(1 - M_x \cos(\theta))} \frac{MCA}{D} \tag{6.5}$$

$$\phi_o = \frac{2mB}{zM_r}\left(\frac{M_r^2 \cos(\theta) - M_x}{1 - M_x \cos(\theta)}\right) \frac{FA}{D} \tag{6.6}$$

The frequency noise source transforms $\Psi_V$, $\Psi_D$, and $\Psi_L$ are defined in equation 6.7. These transforms depend on the sectional thickness $H(X)$, lift $f_L(X)$, and drag $f_D(X)$ normalized distributions along the chord and are crucial in modeling the noise sources.

$$\begin{bmatrix} \psi_V(k_x) \\ \psi_D(k_x) \\ \psi_L(k_x) \end{bmatrix} = \int_{-\frac{1}{2}}^{+\frac{1}{2}} \begin{bmatrix} H(X) \\ f_D(X) \\ f_L(X) \end{bmatrix} e^{ik_x X} dX \tag{6.7}$$

The dimensionless chordwise wave number $k_x$, defined in equation 6.8, determines the intensity of the noise source terms together with the chordwise distributions, as shown in Figures 6.1 and 6.2. It appears that the thickness noise source is not particularly affected by the thickness distribution along the chord, while the loading noise sources are considerably more affected by the normalized distribution along the chord, generally showing larger emission when the distribution is characterized by a strong peak.

$$k_x = \frac{2mBB_D M_t}{M_r(1 - M_x \cos(\theta))} \tag{6.8}$$

In this implementation, the actual thickness distribution of the XProp blade sections is adopted, while the loading distribution along the chord is approximated using normalized parabolic profiles shown in Equation 6.9. This decision was made due to the low reliability of the estimated loading distributions along the chord by the aerodynamic solver. Despite the loading source being particularly affected by the loading distribution, as observed in Figure 6.2 shows that the overall difference between the values obtained from the approximated and the real distributions is sensibly reduced, given that the chordwise wave number $k_x$ does not exceed 3, given the geometry of the propeller and the operating conditions at which it is studied.

$$f_L(x) = f_D(x) = 1.5 - 6x^2 \tag{6.9}$$

A second wave number is defined in Equation 6.10, which is used in the computation of the lift noise component.

$$k_y = \frac{2mBB_D}{zM_r}\left(\frac{M^2\cos(\theta) - M_x}{1 - M_x\cos(\theta)}\right) \tag{6.10}$$

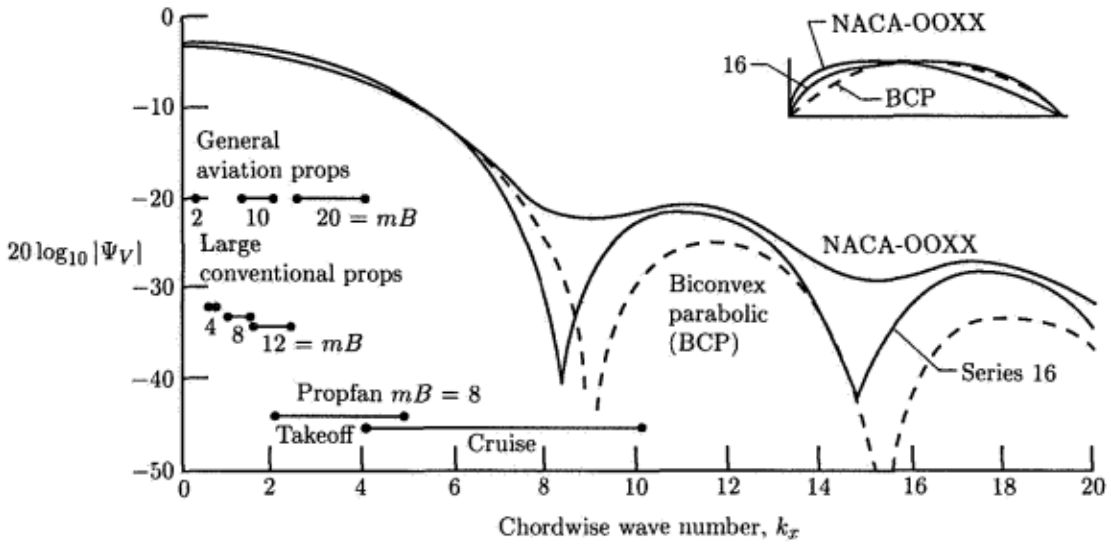


**Figure 6.1:** The thickness noise source as a function of the chordwise wave number $k_x$ and the thickness distribution $H(X)$ [2].

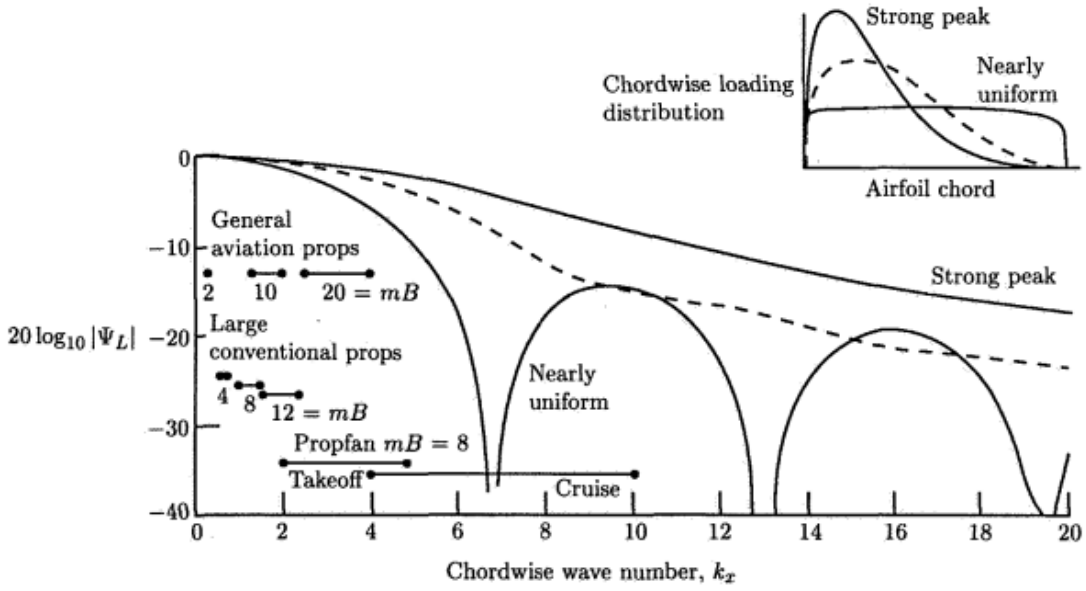


**Figure 6.2:** The loading noise source as a function of the chordwise wave number $k_x$ and the loading distribution $f_L(X)$ or $f_D(X)$ [2].

The noise levels depend not only on the noise source intensity but also on the propagation efficiency, which in the HST is modeled using the Bessel function $J$. Figure 6.3 displays the general behavior of this function when the order is non-null. They peak for arguments about equal to the order, diminish toward zero for smaller arguments, and oscillate for large arguments. As a result, noise propagation is affected by both the tip Mach number $M_t$ and the observer angle $\theta$, as well as the noise harmonic $mB$. The efficiency of propagation drops to zero when the observer is aligned with the propeller axis ($\theta = 0°$, $\theta = 180°$). Hence, the characteristic shape of the noise directivity plots in the plane along the propeller axis obtained in Part III is explained.

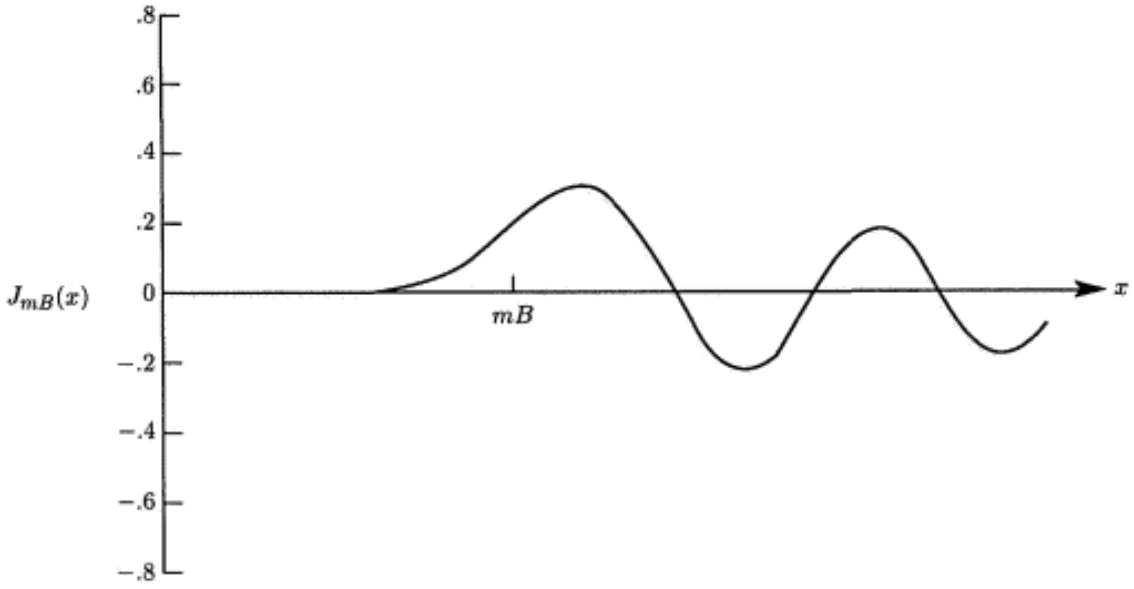


**Figure 6.3:** The general behavior of the Bessel function when the order is non-null [2].

## 6.2. Hanson's Helicoidal Theory for Non-Uniform Flow

Hanson's theory, initially developed for analyzing the noise emissions of isolated propellers, has been extended to account for the effects of non-uniform inflow in [30]. Various situations are analyzed, ranging from the complex case of counter-rotating propellers to the simpler fixed distortion case, which is the focus of this thesis. Equation 6.11 allows for the computation of loading noise originating from both steady and unsteady loading sources. This model has been successfully employed by Wouter de Gruijl in his master's thesis [46] to study the noise emissions of propellers subjected to non-zero angle of attack inflows.
Before proceeding with the description of the equation, two important points must be noted. Firstly, compared to Equation 6.4, the loading noise in Equation 6.11 is already transformed into the time domain with the lift and drag sources combined. Secondly, Equation 6.11 differs from the transcription for the fixed distortion case found in the original article [30]. By applying the appropriate simplifications for the fixed distortion case ($\Omega_{12} = 0, B_1 = 1$) to the general counter-rotating propeller case, it is possible to verify that the transcription for the fixed distortion case in the article contains an error in the argument of the first exponential. Another reference [2] suggests that the substitutions, when correctly applied, lead to Equation 6.11.

$$
\begin{aligned}
p(t) = &-\frac{\rho_0 c_0^2 B \sin\theta}{8\pi(y/D)(1 - M_x \cos\theta)} \\
&\times \sum_{m=-\infty}^{\infty} \sum_{k=-\infty}^{\infty} \exp\left\{ i \left[ \left( (mB - k) \cdot (\phi - \phi^{(2)}) - \frac{\pi}{2} \right) + mB\Omega \left( \frac{r}{c_0} - t \right) \right] \right\} \\
&\times \int_{\text{tip}}^{\text{root}} M_r^2 e^{i(\phi_s + \phi_o)} J_{mB-k} \left( \frac{mBzM_t}{1 - M_x \cos\theta} \right) \times \left[ k_x \frac{C_{Dk}}{2} \Psi_{Dk}(k_x) + k_y \frac{C_{Lk}}{2} \Psi_{Lk}(k_x) \right] dz
\end{aligned} \tag{6.11}
$$

Notable changes in this version include the introduction of the loading harmonic term, denoted as $k$, in addition to the sound harmonics $m$. As the loading is unsteady, the lift and drag coefficients of the blade sections are expressed in Fourier series, as shown in Equations 6.12 and 6.13. These Fourier series represent the loading history experienced by a propeller blade during a revolution in terms of lift and drag. In Equation 6.11, they are expressed in the frequency domain using the Fourier coefficients of the sectional lift and drag coefficients, $C_{Lk}$ and $C_{Dk}$.

$$
C_L = \sum_{k=-\infty}^{\infty} C_{Lk} \exp\{(-i\omega_k t)\} \tag{6.12}
$$

$$
C_D = \sum_{k=-\infty}^{\infty} C_{Dk} \exp\{(-i\omega_k t)\} \tag{6.13}
$$

The observed frequencies of noise emissions are still multiples of the blade passage frequency (BPF), but the additional loading harmonic changes the definition of the terms in Equation 6.11 compared to the steady version of the HST.
Firstly, the order of the Bessel function becomes $n = mB - k$, which means that, depending on the noise harmonic, the number of blades, and the loading harmonic considered, the order of the Bessel function can become null. Consequently, the propagation efficiency changes with the harmonic loading considered, resulting in the fact that the steady loading noise component and the unsteady loading components do not add up uniformly in all directions. Hence, the shape of the directivity plots when the unsteady loading component is considered greatly differs from the one with only steady sources.
The wave numbers also change, as indicated in Equations 6.14 and 6.15. Additionally, the new phase delays due to sweep and lean are altered, and their updated versions can be derived from Equations 6.16 and 6.17. This means that the non-compactness and sweep effects are not homogeneously applied to all loading harmonics.

Equation 6.11 with the modified terms illustrated above can still be reduced to the steady case formulation shown in Equation 6.4 when only the steady loading harmonic ($k = 0$) is considered. It has been verified that, when this is done, the directivity plots obtained from the unsteady solver match the ones provided by the steady solver.

$$k_x = \frac{2M_t}{M_r}\left(\frac{mB}{1 - M_x \cos\theta} - k\right) B_D \tag{6.14}$$

$$k_y = -\frac{2}{z_0 M_r}\left(\frac{mB(M_r^2 \cos\theta - M_x)}{1 - M_x \cos\theta} + kM_x\right) B_D \tag{6.15}$$

$$\phi_s = \frac{2M_t}{M_r}\left[\frac{mB}{1 - M_x \cos\theta} - k\right] \frac{MCA}{D} \tag{6.16}$$

$$\phi_o = \frac{2}{z_0 M_r}\left[\frac{mB\left(M_r^2 \cos\theta - M_x\right)}{1 - M_x \cos\theta} + kM_x\right] \frac{FA}{D} \tag{6.17}$$

When considering the effects of distorted inflow and unsteady loading, it's important to account for variations in noise emissions not only in the plane along the propeller axis, as visualized in Figure 2.9, but also inside the rotational plane. To address this additional complexity, two new angles, denoted as $\phi$ and $\phi^{(2)}$, are introduced in Equation 6.11. In this notation, $\phi^{(2)}$ represents the azimuthal position of the blade at $t = 0$, while $\phi$ represents the observer's angle, the angle between the reference axis chosen and the distance between the propeller axis and the observer. Figure 6.4 visualizes the definitions of these angles.

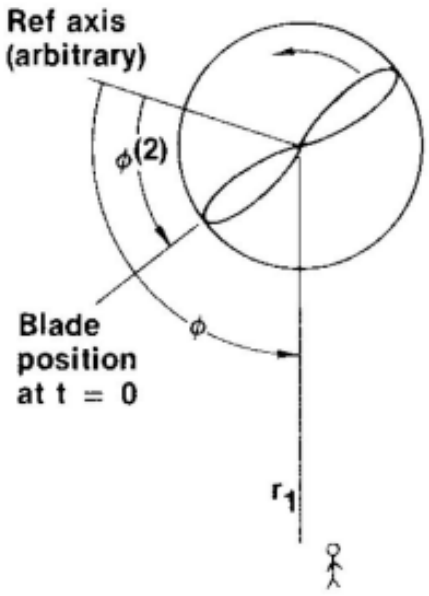


**Figure 6.4:** Geometric definition of $\phi$ and $\phi^{(2)}$ [30].

The chosen position of the reference axis is such that when the propeller blade is aligned with this axis, the azimuthal angle $\phi$ is $180°$.

## 6.3. Coupling of the numerical tools

The aero-acoustic analysis involves using both aerodynamic and aero-acoustic solvers to estimate the performance of interest for the study. Figure 6.5 provides a schematic view of the integration of these solvers.

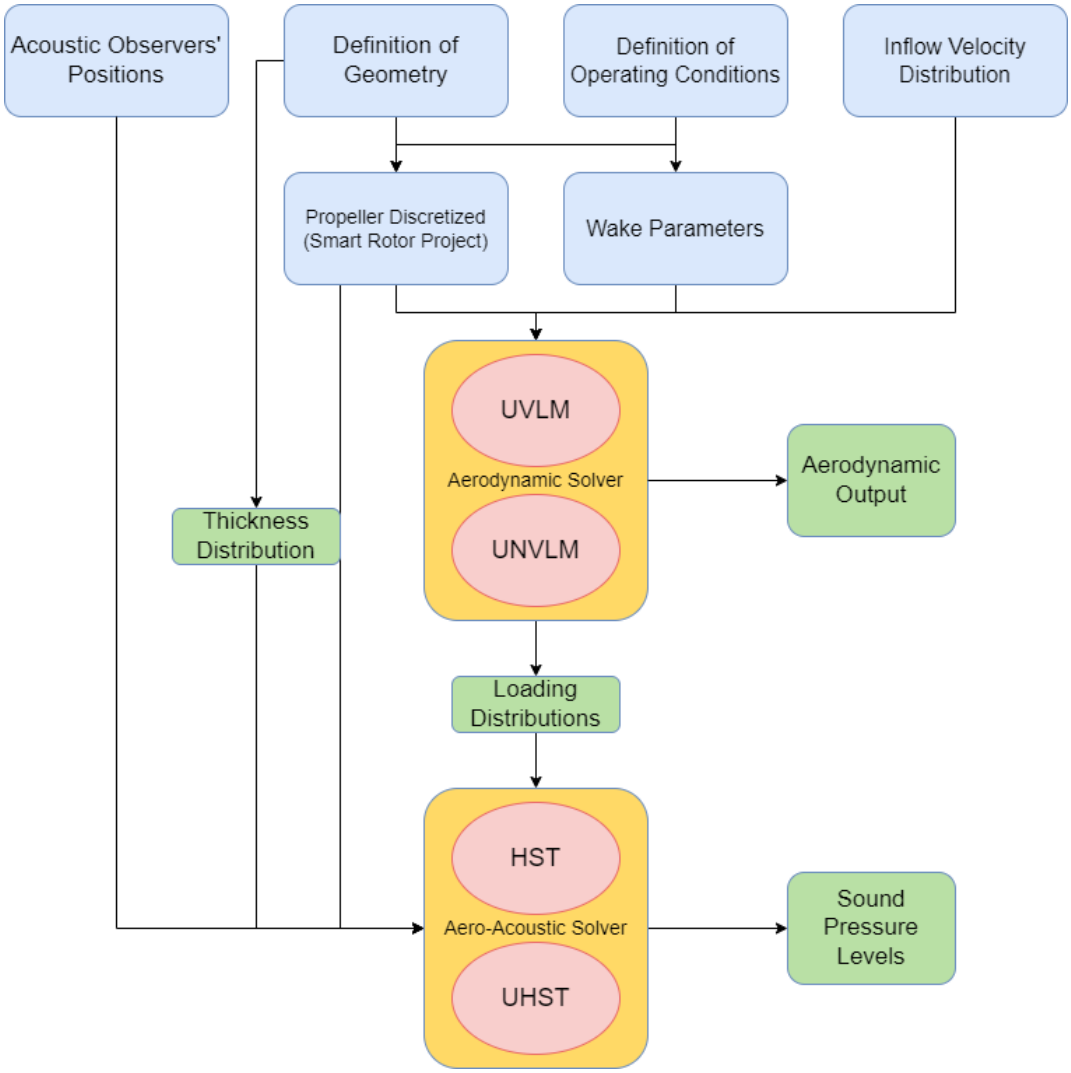


**Figure 6.5:** Flowchart of the aerodynamic and aero-acoustic system coupling.

The aerodynamic solvers require only the propeller geometry and operating conditions to complete the simulation and obtain the aerodynamic data, while the aero-acoustic solver also requires the loading distribution to compute noise emissions from the loading sources. Therefore, the aerodynamic solver is run first, followed by the aero-acoustic solver.

Two aerodynamic solvers are available, as described in Chapter 5: the potential UVLM and the viscous UNVLM, both capable of simulating the propeller in isolated and installed conditions. The viscous solver, capable of accounting for viscosity and non-linear flow phenomena, is used in the analysis in Chapter 9, while the potential solver is used only within the validation analysis in Chapter 7.

Two types of analysis can be performed: the propeller in isolated and installed conditions, where the non-uniform inflow velocity distribution at the propeller disk is provided.

Once the aerodynamic performance is computed, the thickness distribution and aerodynamic loading distribution are provided to the aero-acoustic solver. When the simulation of the performance is in isolated conditions and the loading distribution is steady, the steady implementation of HST is used. When unsteady loading must be included, the solver based on UHST is used.

The noise emissions estimated depend on the relative position between the propeller and the observer. In this analysis, the acoustic solvers are used in a directivity analysis where observers are positioned around the propeller at regular angular intervals at a constant distance $y = 10R_{Tip}$. Figure 6.6 provides the visualization of the observers' positions in the directivity analysis when the observers are inside the plane along the propeller axis ($\theta$ varying) and when they are inside the plane of rotation ($\phi$ varying). The same graphs shows also the blade azimuth coordinate $\phi'$ which differ from the observer angle $\phi$ as it is null when the blade is ascending on the left, while the observer angle is null when the observer is aligned with the vertical axis above the propeller.

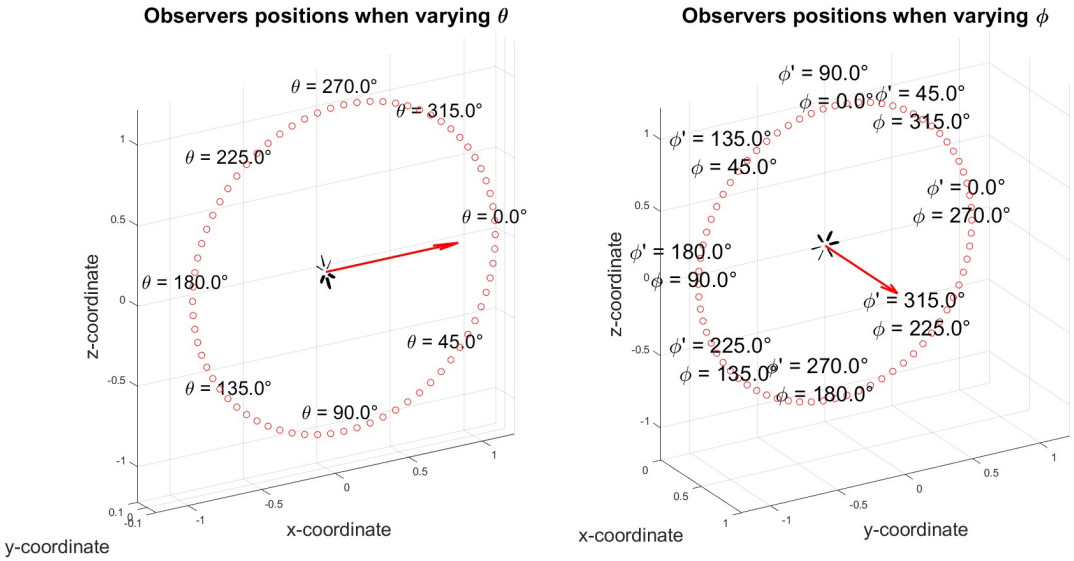


**Figure 6.6:** Position of the observers for the directivity analysis. The propeller is shown with the flight velocity. Left: observers are positioned in the plane along the rotational axis, with the variable $\theta$ varying while $\phi = 0°$. Right: observers are positioned in the rotational plane, with the variable $\phi$ varying while $\theta = 0°$. On the right graph it is also provided the blade azimuth coordinate $\phi'$.

## 6.4. Limitations

Like the aerodynamic solver, also the aero-acoustic tool is subject to inherent limitations from the models on which it is based and from their practical implementation.

- The noise sources accounted for are only of the tonal category, encompassing the thickness, steady, and unsteady loading sources. Noise originating from broadband and quadrupole sources is neglected.
- The thin blade assumption posits that the noise sources act on the mean surface of the blade rather than its upper and lower surfaces, thereby neglecting the phase lag resulting from the face alignment of these sources. This assumption holds true for far-field analysis, as the negligible distance between the upper and lower surfaces compared to the distance between the blade and the observer validates this simplification.
- The normalized loading distributions are approximated by parabolic profiles. As discussed earlier, this simplification does not excessively alter the estimations for chordwise wave numbers that do not exceed 4.

# Part III

## Model Validation and Analysis

# 7

# Verification and Validation

This chapter delves into the verification and validation process employed in this thesis to ensure the reliability of the results generated by the aerodynamic and aero-acoustic tools. These steps are essential for deriving meaningful conclusions from the analyses conducted using these tools. First, the aerodynamic tools undergo evaluation in Section 7.1, followed by testing of the aero-acoustic solvers in Section 7.2.

## 7.1. Aerodynamic Solvers

The validation process of the aerodynamic solvers begins with the simulation of propellers operating in isolated conditions in Section 7.1.2. Then the solvers are tested in simulations of installed propellers in Section 7.1.2.

### 7.1.1. Validation of Isolated Propeller Performance

The aerodynamic results provided by the tools developed in this thesis for analyzing isolated propellers are validated against both experimental data and results obtained from higher-fidelity models. Given that this study does not focus on propellers operating under windmill conditions, the simulations are conducted at low to moderate advance ratios. The reference geometry used is the XPROP propeller, a design extensively studied at Delft University of Technology, which offers abundant high-fidelity and experimental data for validation.

#### Validation against CFD

CFD simulations of the XPROP-S model, a half-scale version of the XPROP propeller, were performed by Van Arnhem [13]. The XPROP-S model, used to assess propeller performance in both isolated and installed conditions, differs slightly from the original TU Delft model, particularly in the airfoil profiles, where the trailing edge of the outboard blade section is thicker due to structural constraints. In the simulations conducted for this thesis, the geometry of the original XPROP was scaled to half its radius without modifications to the airfoil profiles.

Figure 7.1 presents a comparison between the results from Van Arnhem's CFD simulations and those obtained using the potential UVLM and the viscous UNVLM solvers developed in this thesis.
Both the UVLM and UNVLM solvers show good alignment with the CFD simulations, particularly within the advance ratio range $1.4 < J < 2.2$, which corresponds to the linear flow regime where viscous effects are minimal, as discussed in Section 2.1.2. In this range, the thrust estimated by the UVLM and UNVLM is nearly identical, though the viscous UNVLM slightly overestimates the power consumed by the propeller. This discrepancy arises because the UNVLM accounts for the profile drag generated by the blade sections in addition to the induced drag computed by the UVLM. Despite this, the UNVLM provides an efficiency curve closer to that obtained from CFD simulations, capturing the characteristic peak at higher advance ratios, where viscosity increases power consumption and reduces efficiency.
However, the potential UVLM solvers are less suitable for studying propellers at high thrust settings and low advance ratios ($J < 1.4$). This limitation is evident in the thrust coefficient graph in Figure 7.1, where the UVLM maintains a linear trend, while the CFD results display a curved profile due to non-linear viscous effects such as flow separation. As a result, the UVLM tends to overestimate both power consumption and efficiency in this regime. Conversely, the viscous UNVLM shows a closer match to the CFD results, with its thrust curve similarly bending at low advance ratios, reflecting the impact of viscous phenomena.

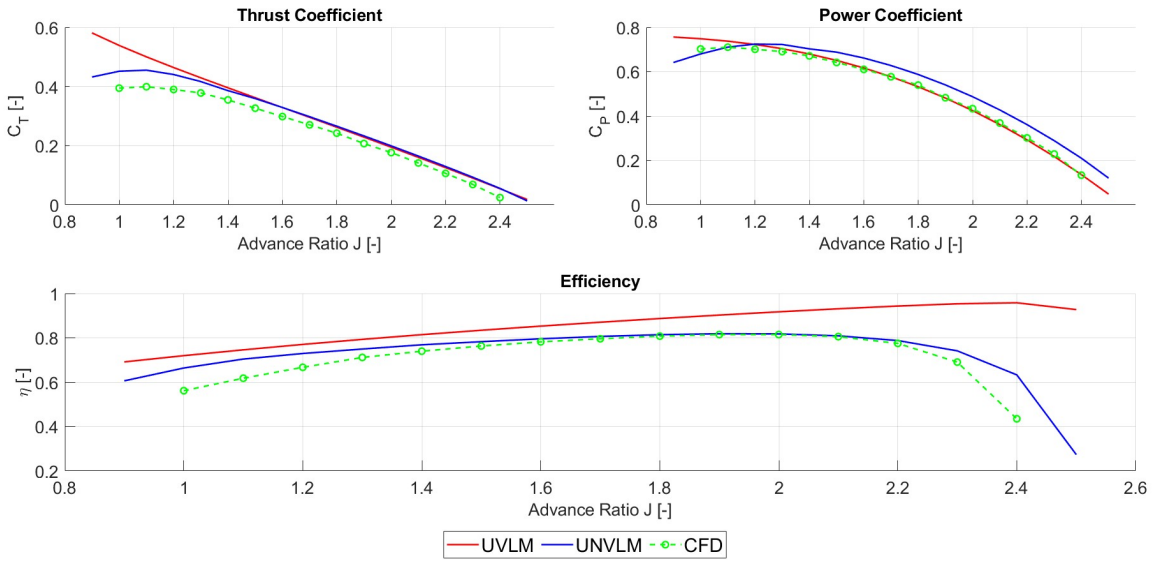


**Figure 7.1:** Performance coefficient of the XProp-S propeller obtained by Van Arnhem [13] compared to the UVLM and UNVLM results. The axial velocity is uniform $U_\infty = 40$ m/s and the pitch setting $\beta_{0.7R} = 45°$.

Figure 7.2 illustrates the distributions along the blade span of the angle of attack, the lift coefficients and the thrust coefficients estimated by the two solvers at a low advance ratio ($J = 1.1$) and a higher advance ratio ($J = 1.8$).

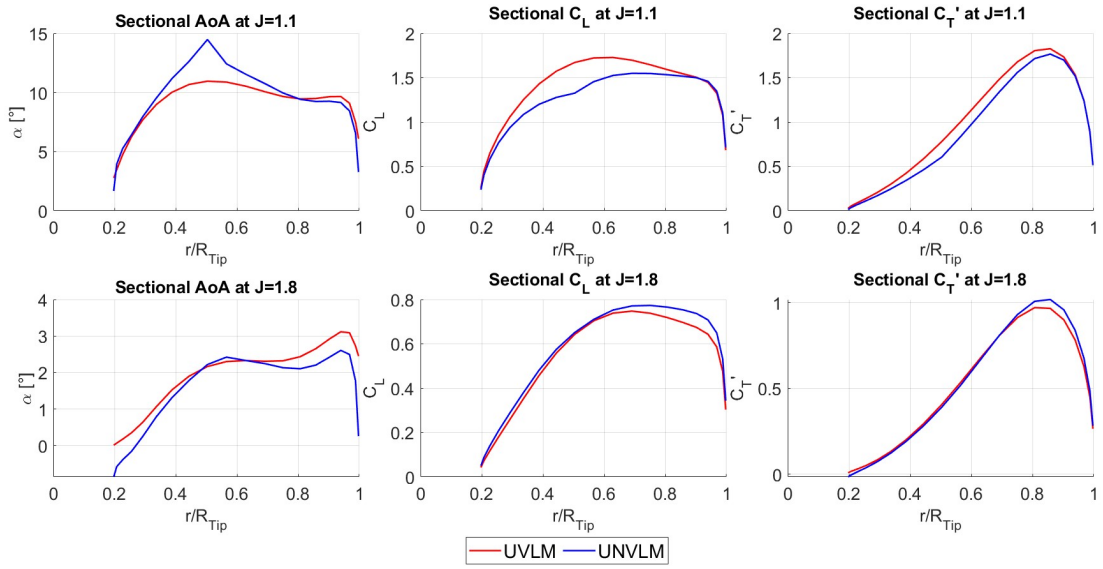


**Figure 7.2:** Distribution along the blade span of the angle of attack, the sectional lift coefficient, and the thrust coefficient obtained by the potential and viscous solvers at $J = 1.1$ and $J = 1.8$.

At a higher advance ratio ($J = 1.8$), the spanwise distributions of aerodynamic quantities predicted by both the potential and viscous solvers are quite similar. The UNVLM solver provides slightly larger estimates for the lift and thrust coefficients at the outboard sections of the blade, while the potential solver tends to predict higher angles of attack. The primary distinction between the two solvers lies in the UNVLM's incorporation of profile thickness effects and the additional boundary layer thickness, which are accounted for through the viscous polar lift curves. These factors slightly alter the lift distribution predicted by the

UNVLM, leading to the observed differences in the outboard sections of the blade.
However, at a lower advance ratio ($J = 1.1$), the differences between the predictions from the two solvers become more pronounced. The viscous solver estimates a notably lower lift coefficient in the central part of the blade ($0.4 < r/R_{Tip} < 0.8$) compared to the potential solver. This discrepancy leads to the potential solver predicting a larger thrust coefficient, as observed in Figure 7.1. The central regions of the blade experience flow separation, causing some sections to stall. The viscous solver models this phenomenon using the circulation correction method described in Section 5.3, which reduces the circulation values of vortex panels where the angle of attack exceeds the stall limit. This correction is evident in the angle of attack distribution, which exhibits a significant peak in the flow separation region ($r/R_{Tip} = 0.5$), resulting from the altered induced velocity distribution, with larger upwash where circulation is reduced.
These results confirm that the UNVLM viscous solver effectively accounts for viscosity by not only adding profile drag to induced drag but also by simulating non-linear phenomena such as flow separation and local blade section stall. This capability is particularly valuable when studying propellers in installed conditions, where characteristic inflow variations may induce such phenomena.

**Validation against Experiments**
The XPROP propeller has been extensively studied at TU Delft through various experimental campaigns. In this section, the results from the UVLM and UNVLM solvers are compared with experimental data obtained by Sinnige et al. [47] and Van Arnhem et al. [13]. The first series of tests were conducted with a full-scale XPROP model at an inflow velocity $U_\infty = 30$ m/s and a pitch setting $\beta_{0.7R} = 30°$, while the second series was conducted with the half-scale model, XPROP-S, at an inflow velocity $U_\infty = 20$ m/s and a pitch setting $\beta_{0.7R} = 45°$.

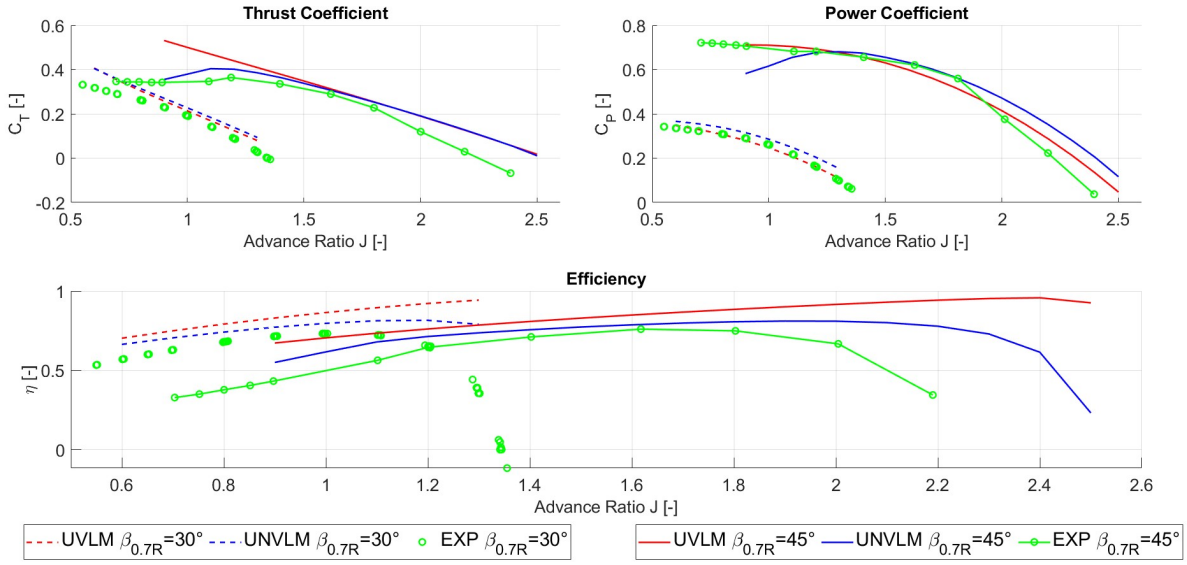


**Figure 7.3:** Results obtained from the UVLM and UNVLM compared to experimental data. The green lines represent data obtained by Sinnige et al. [47], while the red lines represent data obtained by Van Arnhem et al. [13].

In comparing the results from the UVLM and UNVLM solvers with experimental data, similar trends and observations to those seen in the comparison with CFD results are evident. The UNVLM, which includes viscous effects, generally produces results that are closer to the experimental data, particularly at lower advance ratios where non-linear aerodynamic phenomena, such as flow separation, play a significant role. Both solvers tend to overestimate the thrust, power, and efficiency metrics compared to experimental data, as illustrated in Figure 7.3. This overestimation is more pronounced at higher advance ratios.
The shift in the efficiency curve's peak to higher $J$ values and the less steep drop in efficiency may indicate that the solvers overestimate the aerodynamic loading generated by the propeller sections at these advance ratios. This discrepancy could be due to the solvers not fully capturing low Reynolds number phenomena

such as laminar separation bubbles, which can significantly impact performance.
At lower advance ratios, especially when $\beta_{0.7R} = 45°$, the UNVLM shows its ability to detect flow separation, but it predicts this onset at a lower advance ratio $J$ than observed experimentally. This may stem from the use of polar data in the viscous solver, which includes fixed turbulent transition at the leading edge, potentially altering the onset of stall. Moreover real flow separation is a complex three-dimensional phenomenon, and its modeling using two-dimensional polar curves may delay the onset of separation in the simulations, leading to an overestimation of thrust and efficiency at lower advance ratios.
The operating conditions where the solvers align most closely with experimental and CFD results are within the advance ratio range of $1.2 < J < 1.8$ at a pitch setting of $\beta_{0.7R} = 45°$. Given this alignment, the aero-acoustic study of the XPROP-based propeller has been conducted at this pitch setting to ensure that the analysis is based on conditions where the aerodynamic predictions are most reliable.

### 7.1.2. Validation of Installed Propeller Performance

To verify the accuracy of the aerodynamic solvers developed, this section compares their results with those obtained from CFD simulations in a well-documented installed propeller case [13], [48] . This reference case involves an XPROP-S propeller subjected to an inflow velocity $U_\infty = 40m/s$ and an angle of attack $\alpha = 5°$, with an advance ratio $J = 1.8$ and a pitch setting $\beta_{0.7R} = 45°$. The results from CFD simulations by Van Arnhem will be compared against those from the potential UVLM and the viscous UNVLM solvers developed in this thesis.
The installation location of the propeller introduces an in-plane velocity component oriented upwards. This has specific effects on the effective tangential velocity component experienced by the propeller blades. When the propeller is ascending, the in-plane velocity component reduces the effective tangential velocity. This reduction occurs because the upward motion of the propeller adds to the inflow velocity component, effectively decreasing the relative velocity of the blade's motion through the air. Conversely, when the propeller is descending, the in-plane velocity component increases the effective tangential velocity. Here, the downward motion of the propeller subtracts from the inflow velocity component, thereby increasing the relative velocity of the blade's motion through the air.
As a result of these effects, the effective local advance ratio $J$ varies along the circumferential direction as shown in Figure 7.4.

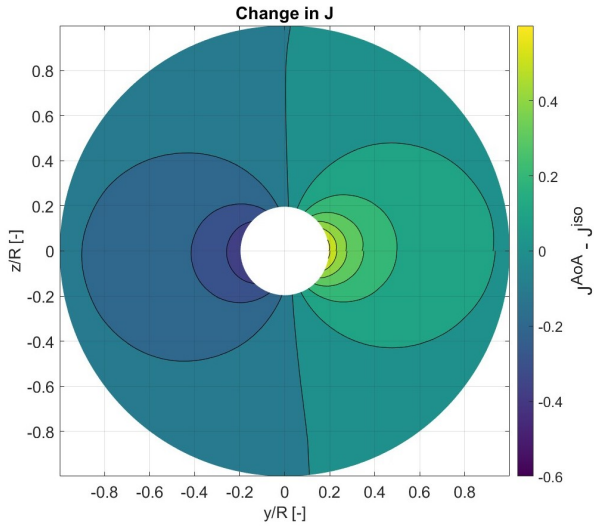


**Figure 7.4:** Change in advance ratio due to operation at $\alpha = 5°$. The propeller rotates counterclockwise; when ascending, it is on the right ($\phi' = 0°$), and when descending, it is on the left ($\phi' = 180°$).

The variations in the inflow leads to unsteady loading on the blades. When the propeller blade is ascending ($\phi' = 0°$), the effective advance ratio increases. This is accompanied by a rise in the local inflow angle and a reduction in the angle of attack. As a result, the blade experiences a decrease in loading because the lower angle of attack reduces the aerodynamic forces acting on it. Conversely, during descent ($\phi' = 180°$), the advance ratio decreases. This change leads to a decrease in the local inflow angle and an increase in

the angle of attack. Consequently, the blade loading increases as the higher angle of attack enhances aerodynamic forces.
These variations are illustrated in Figure 7.5. The figure compares the distribution of several aerodynamic parameters along the blade span for both isolated and installed conditions. It shows how the blade's angle of attack, inflow angle, lift and drag coefficients, as well as thrust and torque coefficients, vary with the blade's azimuthal position $\phi'$.

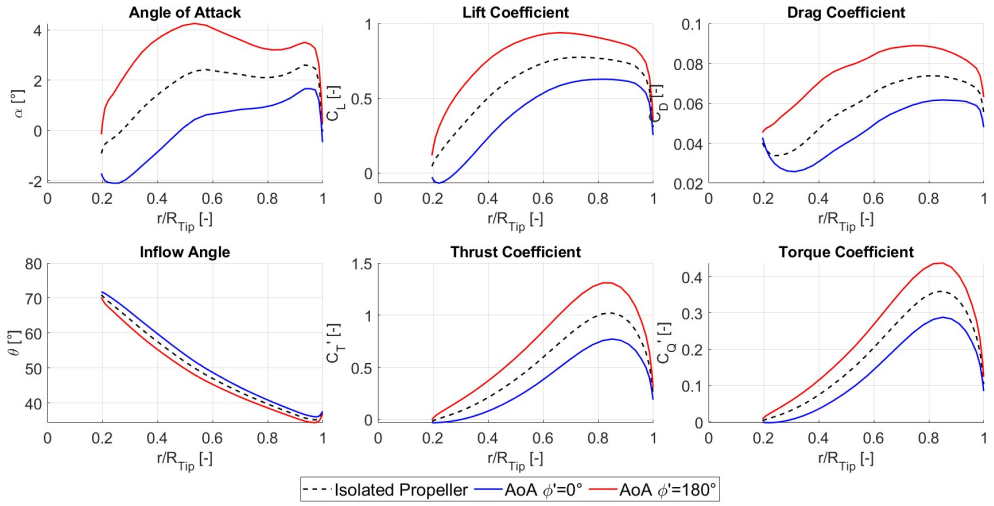


**Figure 7.5:** Comparison of the distributions along the blade span obtained by the propeller simulated in isolated conditions (dashed black) and in installed conditions with the blade ascending (blue) and the blade descending (red).

Figure 7.6 illustrates the change in blade thrust coefficient $\Delta C_{TB}$ experienced by a blade over a complete revolution when the propeller is subjected to an inflow at an angle of attack $\alpha = 5°$ compared to a symmetric inflow condition.

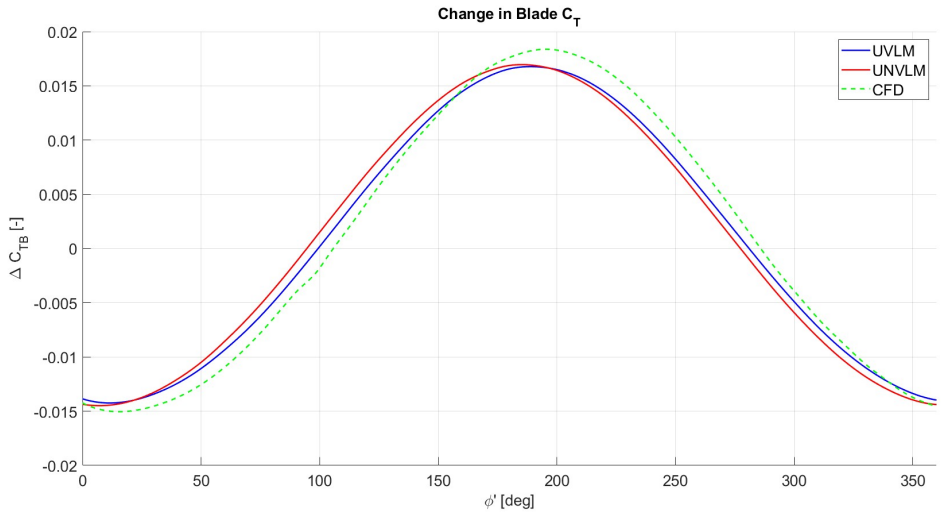


**Figure 7.6:** Change in blade loading during a revolution expressed as the difference in blade thrust coefficient between the simulation of the isolated propeller and the installed propeller subjected to an inflow with an angle of attack. The change in thrust coefficient generated by a single blade is plotted as a function of the azimuthal blade coefficient, assuming the beginning ($\phi' = 0$) when the propeller is ascending on the left of the graph.

The graph presents results from the potential and viscous solvers developed in this thesis, alongside those from CFD simulations by van Arnhem on the same study case [48]. The comparison reveals a good overall agreement, as all the profiles exhibit a sinusoidal shape. However, the amplitude of the blade thrust coefficient change $\Delta C_{TB}$ is slightly underestimated by the VLM-based solvers. Specifically, the maximum $\Delta C_{TB}$ predicted by the UNVLM solver is about $8$% lower than the value derived from CFD simulations.
Another noteworthy difference among the curves is the phase shift. The maximum $\Delta C_{TB}$ does not occur at the same azimuthal position $\phi' = 180°$, which corresponds to the peak change in inflow as seen in Figure 7.4. Instead, there is a delay in the phase. The smallest phase delay between the maximum change in blade loading and the advance ratio $\Delta\phi'$ is estimated by the viscous solver UNVLM at approximately $7°$. In contrast, the potential solver UVLM estimates a phase delay of around $13°$, which is closer to the CFD result of $15°$.
This phase lag is a characteristic feature of unsteady loading on propeller blades. As van Arnhem explains [13], the magnitude of this lag is influenced by factors such as the propeller's geometry (e.g., solidity), the operating conditions, and the nature of the distorted inflow that leads to unsteady loading.
The misalignment between the maximum change in inflow and blade loading is more clearly illustrated in Figure 7.7. This figure depicts the change in sectional thrust coefficient across the entire propeller disk, comparing the conditions where the propeller is installed with an inflow at $\alpha = 5°$ to those where it is isolated with $\alpha = 0°$. The results from both the solvers and the CFD simulations by van Arnhem [48] are displayed, providing a detailed visualization of how the inflow distortion affects the thrust generated by different sections of the blade as it rotates.

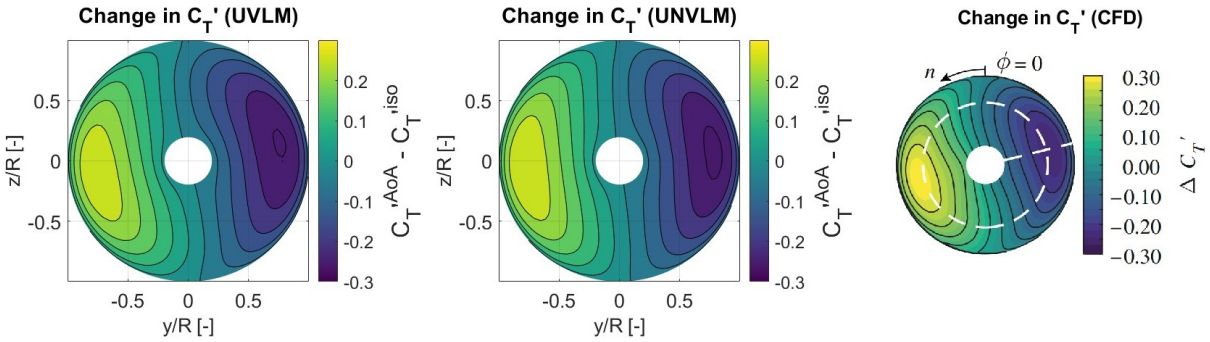


**Figure 7.7:** Change in sectional thrust coefficient along the propeller disk obtained by the solvers developed in the thesis (on the left: UVLM, at the center:UNVLM) and by the CFD simulation by van Arnhem et al. [48] (on the right).

The UVLM and UNVLM solvers account for the phase lag in blade loading due to unsteady aerodynamic effects through their respective wake models. In these unsteady simulations, the wake model is characterized by a progressive change in circulation distribution along the wake length. As the circulation gradually changes, the induced velocities from the wake panels also vary over time, causing a delay in the maximum change in effective inflow and, consequently, in the blade loading.
However, the two solvers incorporate the wake influence on the propeller blades through distinct mechanisms. In the UVLM solver, the circulation distribution on the blades is directly determined by solving a linear system of equations that satisfies the non-permeability boundary condition on the blade surface. The velocities induced by the wake vortex system directly impact the circulation distribution, which in turn affects the blade loading.
In contrast, the UNVLM solver employs the linear solution from the UVLM as an initial guess for an iterative process that corrects the circulation using polar data to account for viscous effects. During this iteration, the sectional angle of attack distribution is used as input to derive the viscous lift ($C_L$) and drag ($C_D$) coefficients from airfoil polar curves. Consequently, the phase of the variation in propeller loading aligns more closely with the phase of the variation in the angle of attack.
Figure 7.8 illustrates the change in sectional angle of attack across the propeller disk when comparing the angle of attack case ($\alpha = 5°$) with the symmetric inflow case. The figure shows that a phase lag

of approximately $8°$ exists between the change in effective angle of attack and the change in inflow, demonstrating that the wake's influence also affects the effective inflow angle through induced velocities, delaying its change. However, this phase delay is lower than the delay between the change in thrust and inflow estimated by the potential solver UVLM and the CFD simulation. Due to this different mechanism of accounting for the wake's influence, the viscous solver provides the lowest estimate of the phase delay.

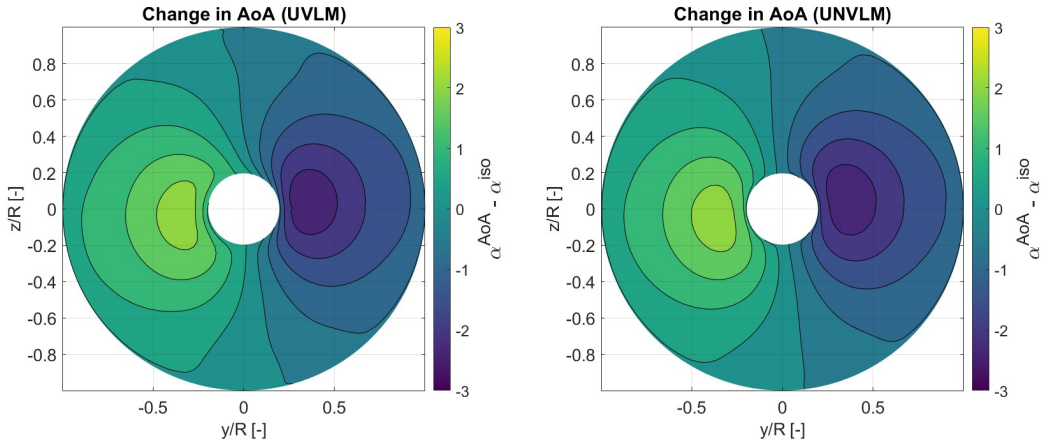


**Figure 7.8:** Change in sectional angle of attack along the propeller disk.

Figure 7.9 illustrates the overall propeller performance coefficients over time, obtained from a simulation that models a full revolution of the propeller under both installed conditions ($\alpha = 5°$) and isolated conditions ($\alpha = 0°$).

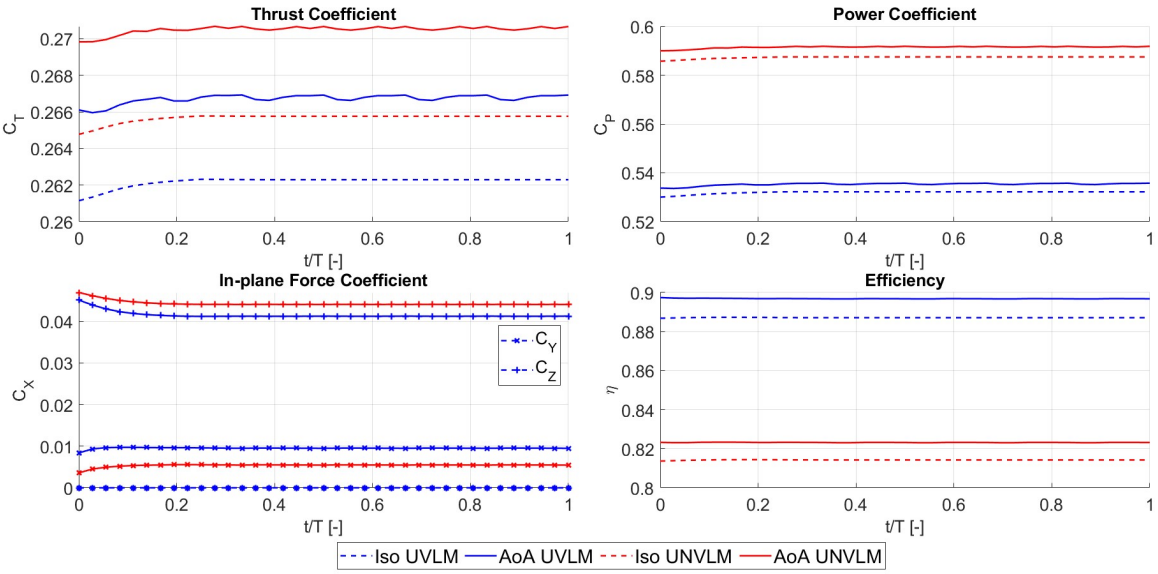


**Figure 7.9:** Propeller performance in isolated and installed conditions over a revolution. Top Left: Thrust Coefficient, Top Right: Power Coefficient, Bottom Left: In-Plane Force Coefficient, Bottom Right: Efficiency

It can be observed that the simulation outputs for the propeller in isolated conditions become steady after

approximately a quarter of a revolution ($t/T \approx 0.25$). In contrast, the output for the installed propeller shows subtle oscillations throughout its operation. When comparing the performance of the installed propeller to the isolated one, the installed propeller generates higher overall thrust. This increased thrust, however, comes at the cost of higher power consumption, yet it results in an overall performance improvement. This occurs because the increase in blade loading when it passes through regions of lower advance ratio is greater than the reduction in loading when the blade moves through regions of higher advance ratio, as demonstrated in the blade loading changes shown in Figure 7.6.
This uneven distribution of loading also influences the generation of in-plane forces. The reduction in tangential force when the blade is ascending is overcompensated by an increase in tangential force when the blade is descending. As a result, the propeller generates a net vertical force, which is evident in the in-plane force graph. Additionally, since the maximum change in blade loading does not align perfectly with the change in inflow, as seen in Figure 7.7, horizontal side forces are also generated, which are proportional to the phase lag between the loading and the inflow changes.
These dynamics are depicted in the graph showing the in-plane force coefficients in Figure 7.9. Both the UVLM and UNVLM methods predict the presence of vertical and horizontal in-plane force components, with the vertical force being the more dominant of the two. Due to its prediction of a larger phase lag, the potential UVLM method also predicts a larger horizontal force component compared to the viscous UNVLM method.

In conclusion, the unsteady vortex lattice methods developed in this project have proven effective, delivering results that align closely with higher fidelity models and experimental data across various operating conditions, including installed scenarios. The potential UVLM is recommended for its simplicity and fast computational times, making it ideal for analyses where speed is critical. However, its inability to model viscosity limits its use to linear flow conditions. The viscous UNVLM solver, though more complex and time-consuming, is better suited for high-thrust or installed propeller analyses, especially where non-linear effects like flow separation are significant. A key limitation of the UNVLM is its underestimation of phase lag, due to differences in how wake influence is modeled.
Figure 7.10 compares the change in thrust coefficient due to Boundary Layer Ingestion (BLI). While both solvers produce similar distributions, the linear solver generally underestimates the thrust change, especially at $\phi' = 90°$, where the vertical tail's wake impinges. Despite this discrepancy, it was deemed sufficient to recognize this difference and proceed with the viscous solver for the remaining phases of the research.

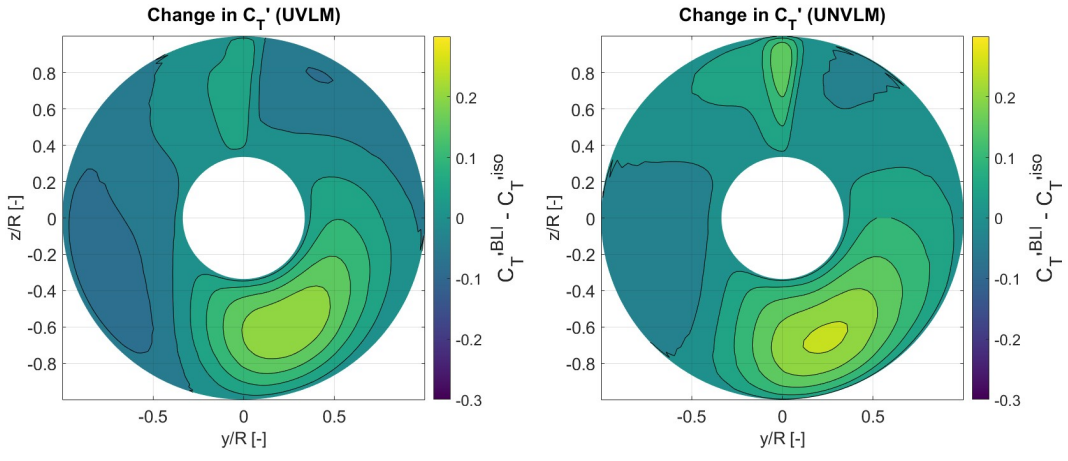


**Figure 7.10:** Change in sectional thrust coefficient due to the BLI installation along the propeller disk obtained by the solvers developed in the propeller installed in a BLI configuration at $J = 1.8$.

## 7.2. Acoustic Solvers

The verification process of the aeroacoustic solver begins with analyzing the propeller in isolated conditions using the steady implementation of Hanson's Helicoidal Surface Theory (HST) [29], as discussed in Section 7.2.1. This is followed by verifying the unsteady HST model [30] in Section 7.2.2, where the propeller is studied in installed conditions.
While there was no direct validation against experimental data, previous research by other TU Delft students and researchers provided a basis for qualitative comparison, helping to confirm the correct implementation of the models.

### 7.2.1. Steady Helicoidal Surface Theory

Hanson's Helicoidal Surface Theory (HST) is a prominent analytical model used to estimate noise emissions from open rotors. It is typically employed under axis-symmetric inflow conditions, such as for isolated propellers, where there is no circumferential inflow variation and unsteady noise sources can be neglected. Despite its average prediction error, HST is effective at capturing trends related to changes in propeller geometry or operating conditions, as demonstrated by M. Kowitz-Hernitzek [49] and other TU Delft studies [50], [46], [34]. This model's accuracy in predicting noise trends justifies its use for preliminary design sensitivity studies in this research.
To verify the correct implementation of the HST solver, a series of aero-acoustic analyses is performed on the 3-bladed XProp variant, chosen for its extensive study by previous researchers in both isolated and installed conditions. Figure 7.11 shows the directivity plots of the primary noise sources for the propeller in isolated conditions at $U_\infty = 40$ m/s, $J = 1.8$, and $\beta_{0.7R} = 45°$. This operating condition is chosen because the aerodynamic solver was extensively validated in both isolated and installed conditions. Observers positioned around the propeller in the plane along its axis as shown in Figure 6.6 were used to capture variations in the observer angle $\theta$.

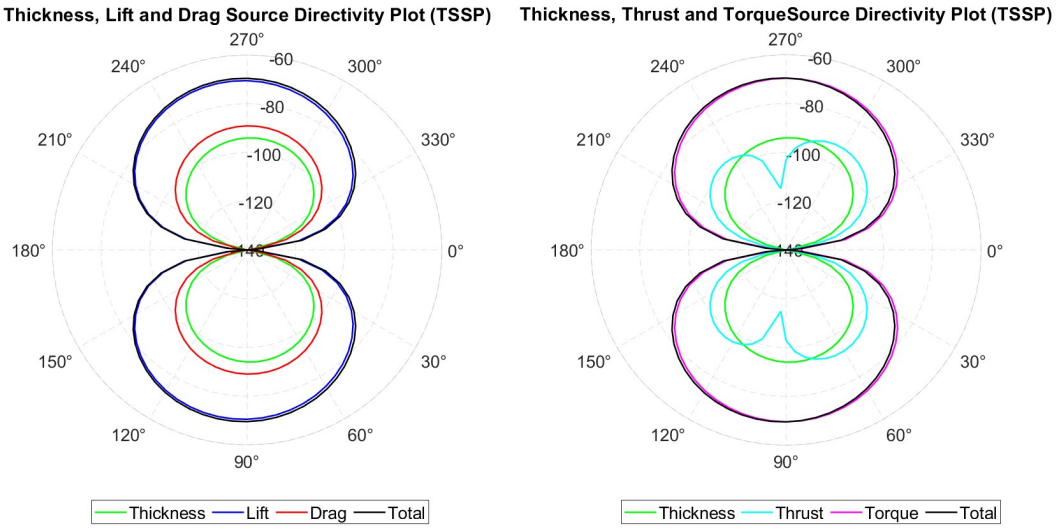


**Figure 7.11:** Directivity plots of the noise sources obtained from the XPROP propeller in isolated conditions at $U_\infty = 40m/s$ $J = 1.8$ $\beta_{0.7R} = 45°$. The sound pressure levels are expressed in terms of TSSP (Thrust Specific Sound Pressure).

The noise emissions from thickness and torque sources exhibit similar patterns, characterized by their propagation efficiency modeled by the Bessel function $J$. These emissions are minimal when the observer aligns with the propeller axis ($\theta = 0°$ or $180°$) and peak when aligned with the propeller disk ($\theta = 90°$ or $270°$). Conversely, thrust noise shows a sharp reduction when the observer aligns with the propeller disk, resulting in four distinct lobes.
The analysis reveals that loading noise, which combines lift and drag, and the sum of thrust and torque noise, are the dominant sources. The predominance of torque noise over thrust is due to the high advance

ratio and low thrust setting, yielding a low thrust-to-torque ratio. The HST model's correct implementation is further confirmed by the agreement between estimated loading noise from lift and drag components and from thrust and torque components.

The noise emission profiles displayed in Figure 7.12 align well with theoretical expectations, confirming the accurate implementation of the HST model.

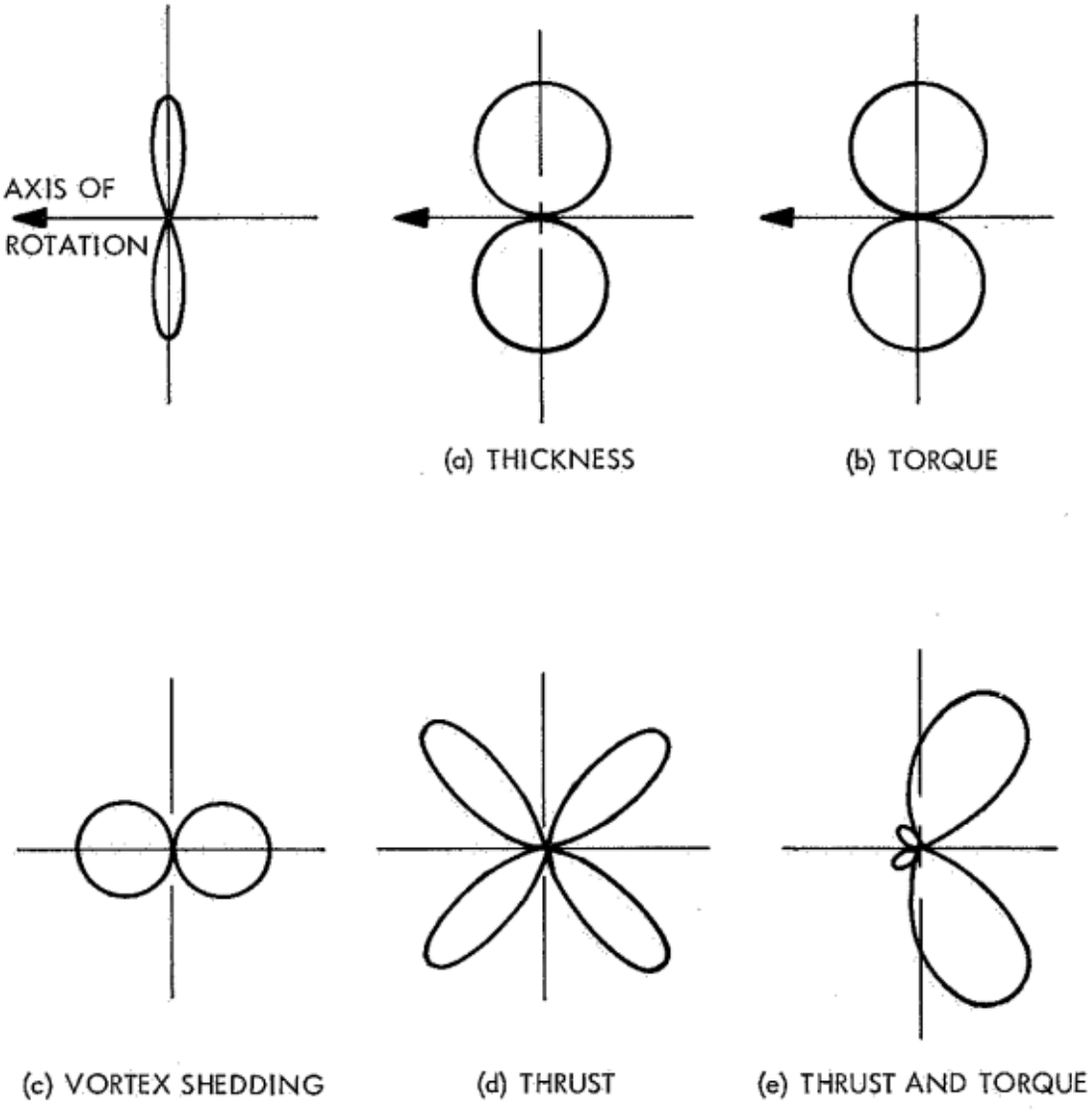


**Figure 7.12:** Theoretical noise patterns of the various noise sources according to [51].

Subsequently, a sensitivity study is performed to determine the number of noise harmonics $m$ needed to accurately estimate the aero-acoustic performance. Figure 7.13 illustrates the directivity plots of total noise emissions from simulations with increasing numbers of harmonics. The minimal differences in profile shapes indicate that including only the first noise harmonic $m$ provides sufficiently accurate results. This conclusion is supported by Table 7.1, which shows the maximum change in Thrust Specific Sound Pressure Level (TSSP) between simulations with different numbers of harmonics. The findings align with similar analyses by W. de Gruijl and W. de Haan [46], [50], validating the accuracy of the HST implementation. However, it is important to note that this result may not apply to propellers in installed conditions, where unsteady loading effects should also be considered alongside thickness and steady loading sources.

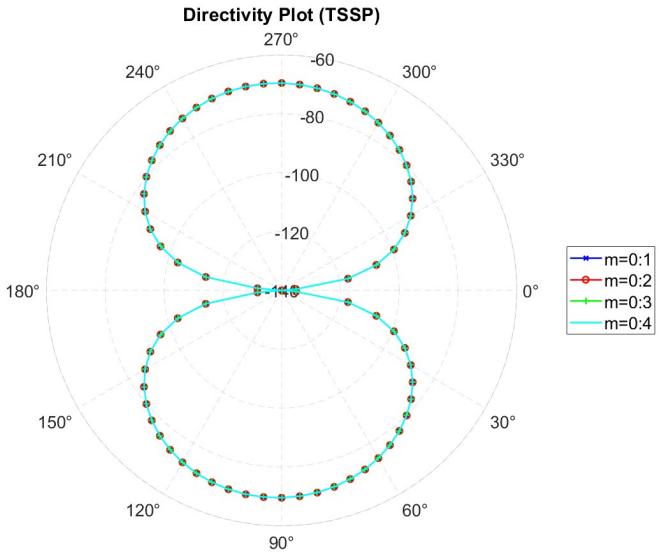


**Figure 7.13:** Total noise estimated for varying numbers of noise harmonics.

| Noise Harmonics | $TSSP_{Max}$ | $\Delta TSSP_{Max}$ |
|---|---|---|
| m = 1 | $-57.4859$ | $0$ |
| m = 1:2 | $-57.4697$ | $0.016$ |
| m = 1:3 | $-57.4696$ | $6.22 \times 10^{-5}$ |
| m = 1:4 | $-57.4696$ | $2.56 \times 10^{-7}$ |
| m = 1:5 | $-57.4696$ | $1.11 \times 10^{-9}$ |
| m = 1:6 | $-57.4696$ | $5.03 \times 10^{-12}$ |

**Table 7.1:** Change in maximum TSSP estimated by the HST when gradually increasing the number of noise harmonics $m$.

### 7.2.2. Unsteady Hanson Surface Theory

To verify the implementation of the unsteady HST model, a series of analyses are conducted on the 3-bladed XProp propeller under installed conditions. The propeller is subjected to an inclined inflow with an angle of attack $\alpha = 5°$ and a flight velocity $U_\infty = 40m/s$. This configuration is chosen due to the prior validation of aerodynamic solvers with this test case and the availability of related aero-acoustic analysis data from other researchers. Notably, de Gruijl [46] performed similar analyses using a BEM solver for aerodynamic loading and the unsteady HST for noise estimation. Additionally, J. Goyal et al. [52] employed higher-fidelity models, including the Lattice Boltzmann Method (LBM) for aerodynamic analysis and Farassat's Formulation 1A for the aero-acoustic analysis, to study the performance of the same propeller at a non-zero angle of attack.

Figure 7.14 presents the directivity plot of the noise sources of the propeller along the propeller axis. When comparing the results for isolated and installed propellers, it is observed that the thickness noise remains unchanged, while the loading noise shows significant variation. This difference arises because, in installed conditions, the loading noise is influenced by both steady and unsteady loading due to inflow variations. As the propeller rotates, the Mach number changes along the azimuth, affecting both thickness and loading noise components. However, the unsteady HST model does not account for variations in Mach number, resulting in identical thickness noise modeling for both isolated and installed cases, while unsteady loading noise is represented by variations in lift and drag (or thrust and torque) coefficients in the frequency domain via Fourier transform.
The directivity plots reveal that the installed propeller's loading noise is asymmetric, unlike the isolated

case, and emissions are not zero when the observer is aligned with the propeller axis. This occurs because noise emissions from different loading harmonics $k$ do not propagate uniformly due to changes in the Bessel function's order and argument. Specifically, when the harmonic $k$ increases and the order becomes zero, the Bessel function output remains non-zero at $\theta = 0°$ or $\theta = 180°$, allowing noise from the loading harmonic $k = mB$ to propagate along the propeller axis.

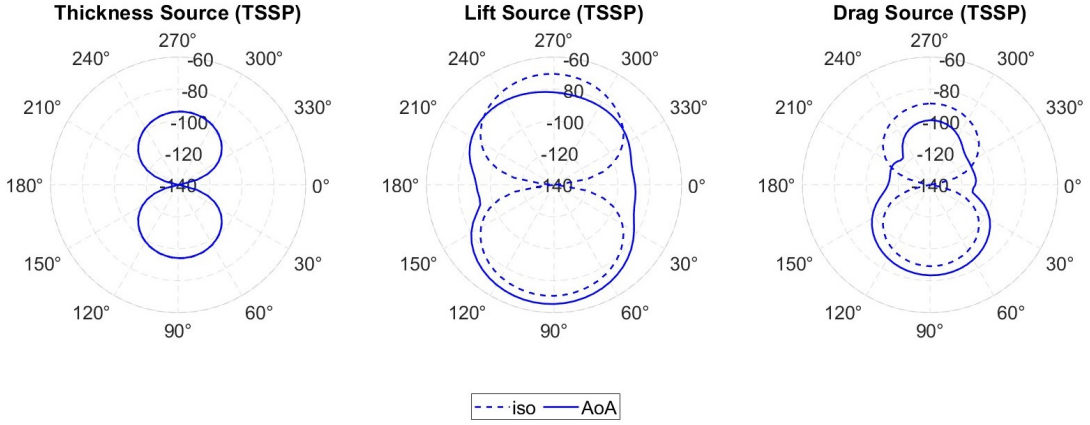


**Figure 7.14:** The directivity source noise patterns as a function of the observer angle $\theta$ for the isolated and installed ($\alpha = 5°$) XPROP-S propeller at $J = 1.8$, $\beta_{0.7R} = 45°$.

Comparing these results with de Gruijl's analysis [46], who studied a similar setup, the directivity plots differ in shape. De Gruijl's results show zero noise along the propeller axis, attributed to observers being on the ground in a flyover case, leading to an infinite distance at $\theta = 0°$ or $\theta = 180°$, which effectively nullifies the emissions. In contrast, this analysis uses observers placed around the propeller, as illustrated in Figure 6.6.

As outlined in Chapter 6, the noise levels also vary with circumferential position when the propeller is installed. Figure 7.15 illustrates the noise source patterns with observers positioned in the propeller's rotational plane, comparing isolated and installed conditions. These graphs show variations in noise emissions with the observers' angle $\phi$ in the azimouthal direction.

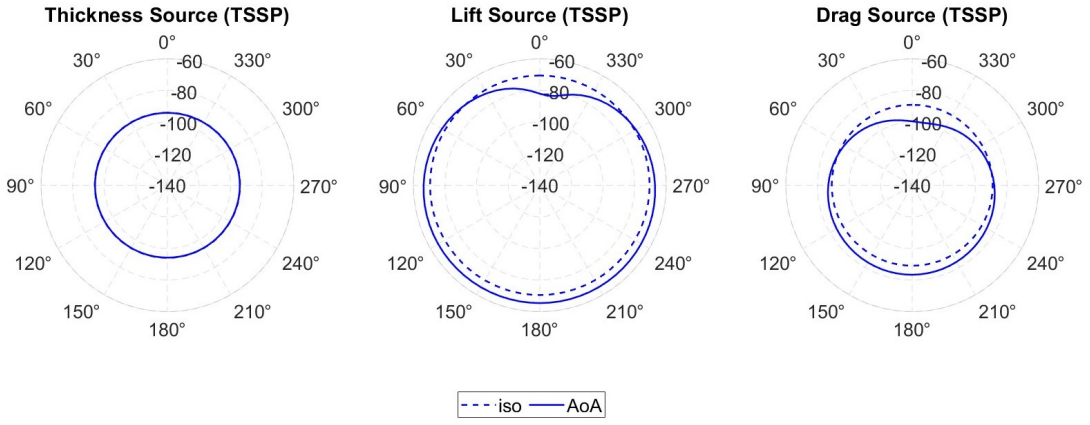


**Figure 7.15:** The directivity source noise patterns as a function of the observer angle $\theta$ for the isolated and installed ($\alpha = 5°$) XPROP-S propeller at $J = 1.8$, $\beta_{0.7R} = 45°$.

It is evident that while the thickness noise pattern remains unchanged in installed conditions, the loading noise pattern differs from that of the isolated propeller. In isolated conditions, the axis-symmetric inflow leads to steady loading and consistent loading noise levels across the azimuth, similar to the thickness noise. However, in installed conditions, the loading noise varies: it decreases as the blade ascends and

increases as the blade descends. Consequently, noise emissions are lower above the propeller ($\phi \approx 0°$) and higher below it ($\phi \approx 180°$).

To accurately estimate sound levels, a sensitivity study was performed to determine the minimum number of noise harmonics $m$ required. This study also accounted for loading harmonics $k$. When $k = 0$, only the time-averaged loading is considered, producing results similar to those of the isolated propeller, as expected since this case matches the steady HST model. Increasing $k$ affects the noise levels and directivity plots. The necessary number of loading harmonics depends on the number of blades $B$ and the noise harmonic $m$. The efficiency of noise propagation is influenced by both the argument and order $n = mB - k$ of the Bessel function $J_n$. As shown in Figure 6.3, the propagation efficiency diminishes when the ratio between the argument and order is small, which allows for neglecting higher loading harmonics. According to [2], a suitable indicator for this ratio is the spinning mode tip Mach number $M_S$, defined in Equation 7.1.

$$M_s = \left(\frac{mB}{n}\right) M_t = \left(\frac{mB}{mB-k}\right) M_t \tag{7.1}$$

When the spinning mode tip Mach number $M_S$ is much less than 1 ($M_s \ll 1$), the corresponding noise emissions can be considered negligible. This condition depends on several factors: the loading harmonic $k$, the noise harmonic $m$, the number of blades $B$, and the spinning tip Mach number $M_t$. Keeping the other parameters constant, as the number of loading harmonics $k$ increases, the order of the Bessel function decreases and reaches zero when $k = m \times B$. This reduction in order increases $M_s$ and improves the overall noise propagation efficiency. When the Bessel function's order becomes sufficiently negative, the contribution of the loading harmonics to the noise emissions becomes minimal. For the analyses performed, it was determined that including $k = (m+1) \times B$ harmonics was adequate. Higher values of $k$ did not significantly affect the noise pattern.

Figure 7.16 illustrates the directivity patterns for the installed propeller at $J = 1.8$ with a pitch setting of $\beta_{0.7R} = 45°$, showing how the directivity patterns evolve as the number of harmonics $m$ increases.

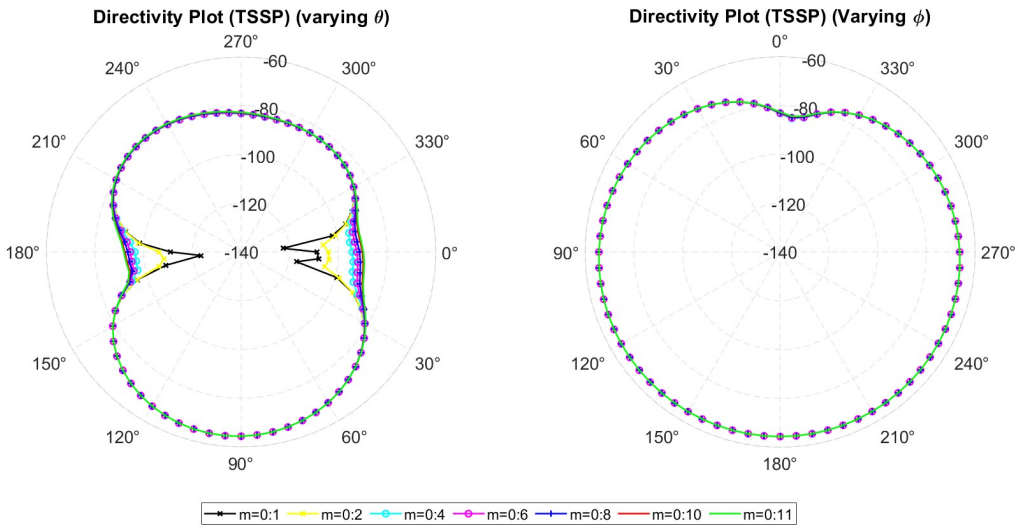


**Figure 7.16:** The directivity plots of the total noise source from the installed propeller in the propeller plane along the propeller axis (Left) and in the plane of rotation (Right).

Table 7.2 provides the change in maximum noise emissions estimated.

| Noise Harmonics | $TSSP_{Max}$ ($\theta$) | $\Delta TSSP_{Max}$ ($\theta$) | $TSSP_{Max}$ ($\phi$) | $\Delta TSSP_{Max}$ ($\phi$) |
|---|---|---|---|---|
| m = 1 | $-64.33$ | $0$ | $-64,39$ | $0$ |
| m = 1:2 | $-64.33$ | $3.2 \times 10^{-4}$ | $-64,39$ | $2.7 \times 10^{-4}$ |
| m = 1:3 | $-64.33$ | $3.1 \times 10^{-4}$ | $-64,39$ | $4.0 \times 10^{-4}$ |
| m = 1:4 | $-64.33$ | $8.3 \times 10^{-4}$ | $-64,39$ | $7.7 \times 10^{-4}$ |
| m = 1:5 | $-64.33$ | $5.9 \times 10^{-4}$ | $-64,38$ | $9.8 \times 10^{-4}$ |
| m = 1:6 | $-64.33$ | $1.2 \times 10^{-3}$ | $-64,38$ | $7.7 \times 10^{-4}$ |
| m = 1:7 | $-64.33$ | $1.2 \times 10^{-3}$ | $-64,38$ | $1.4 \times 10^{-3}$ |
| m = 1:8 | $-64.33$ | $1.1 \times 10^{-3}$ | $-64,38$ | $1.3 \times 10^{-3}$ |
| m = 1:9 | $-64.33$ | $7.9 \times 10^{-3}$ | $-64,38$ | $9.7 \times 10^{-4}$ |
| m = 1:10 | $-64.33$ | $1.0 \times 10^{-3}$ | $-64,38$ | $1.2 \times 10^{-3}$ |
| m = 1:11 | $-64.33$ | $1.3 \times 10^{-4}$ | $-64,38$ | $1.4 \times 10^{-4}$ |

**Table 7.2:** Change in maximum TSSP estimated by the UHST when gradually increasing the number of noise harmonics $m$.

When the observers are aligned with the plane of rotation of the propeller ($\theta = 90°$ and $\theta = 270°$), the results indicate that, similar to the isolated propeller analysis, the predominant noise contribution is from the first harmonic. However, when observers are positioned along the propeller axis ($\theta = 0°$ and $\theta = 180°$), the noise contribution from the unsteady loading noise becomes significant. Therefore, it is crucial to consider a number of noise harmonics greater than $m = K_L/B$, where $k_L$ is the loading harmonic threshold above which the unsteady loading contributions become negligible.

These findings are particularly relevant for propellers installed in a BLI (Boundary Layer Ingestion) setup, where the highest noise levels are emitted along the propeller axis. Figure 7.17 illustrates the noise patterns for the 3-bladed BLI propeller under the same operating conditions as discussed for the angle of attack case. Additionally, Table 7.3 shows the estimated change in maximum noise levels.

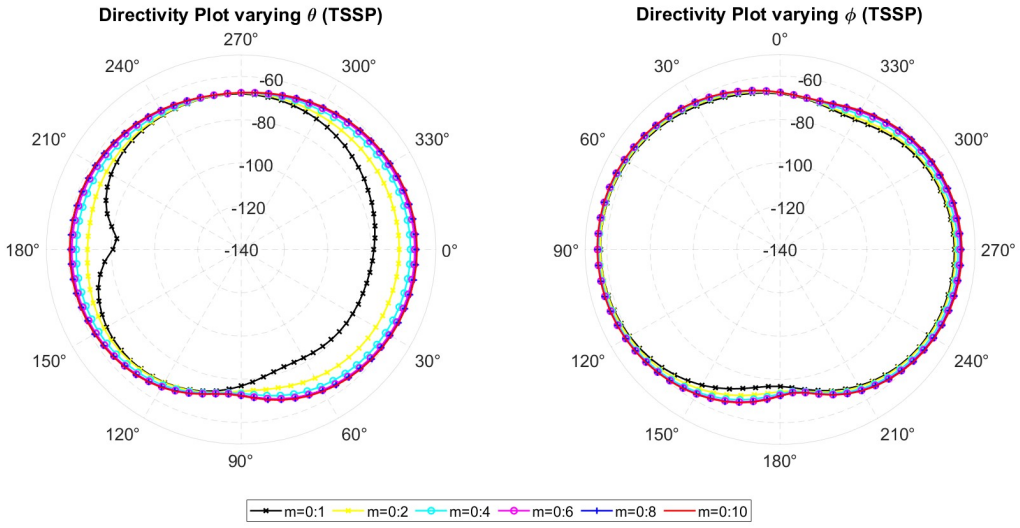


**Figure 7.17:** The directivity plots of the total noise source from the installed BLI propeller in the propeller plane along the propeller axis (Left) and in the plane of rotation (Right).

| Noise Harmonics | $TSSP_{Max}$ ($\theta$) | $\Delta TSSP_{Max}$ ($\theta$) | $TSSP_{Max}$ ($\phi$) | $\Delta TSSP_{Max}$ ($\phi$) |
|---|---|---|---|---|
| m = 1 | $-67.61$ | $0$ | $-57.03$ | $0$ |
| m = 1:2 | $-66.79$ | $0.82$ | $-56.92$ | $0.11$ |
| m = 1:3 | $-63.86$ | $2.9$ | $-56.47$ | $0.45$ |
| m = 1:4 | $-61.68$ | $2.2$ | $-56.17$ | $0.30$ |
| m = 1:5 | $-60.48$ | $1.2$ | $-55.90$ | $0.27$ |
| m = 1:6 | $-59.68$ | $0.80$ | $-55.76$ | $0.15$ |
| m = 1:7 | $-59.20$ | $0.48$ | $-55.65$ | $0.11$ |
| m = 1:8 | $-58.90$ | $0.30$ | $-55.60$ | $0.046$ |
| m = 1:9 | $-58.75$ | $0.15$ | $-55.58$ | $0.022$ |
| m = 1:10 | $-58.69$ | $0.065$ | $-55.58$ | $3.1 \times 10^{-3}$ |
| m = 1:11 | $-58.67$ | $0.012$ | $-55.58$ | $6.1 \times 10^{-4}$ |

**Table 7.3:** Change in maximum TSSP estimated by the UHST when gradually increasing the number of noise harmonics $m$ for the propeller installed in the BLI configuration.

For the BLI configuration study, it was determined that considering the first 5 noise harmonics was adequate for the 6-bladed baseline propeller. In contrast, for the 2-bladed propeller analyzed in Section 9.2, it was necessary to include up to 15 harmonics. Beyond $K_L \approx 36$, the impact of additional loading harmonics on noise levels becomes minimal. This is supported by the spectral analysis of the loading signal shown in Figure 9.12 in Chapter 8, which confirms that the amplitude of the unsteady loading becomes negligible above $K \approx 30 - 35$.

The aero-acoustic analysis conducted in this thesis demonstrated that both the steady and unsteady implementations of Hanson's Surface Theory were correctly applied. Sensitivity studies involving the number of harmonics $m$ and $k$ revealed that, for both Angle of Attack (AoA) and Boundary Layer Ingesting (BLI) inflow scenarios, the inclusion of unsteady loading noise sources resulted in more intense noise propagation at higher harmonics $m$ compared to the isolated case, particularly along the propeller axis. Although the unsteady Hanson's Surface Theory has not yet been experimentally validated, the analysis results are deemed accurate and suitable for the objectives of this thesis, with reliability comparable to the steady version.

# 8

# Analysis Set Up

This chapter outlines the analysis setup used to study the propeller installed in a Boundary Layer Ingesting (BLI) configuration. Section 8.1 details the BLI inflow conditions applied to the installed propeller. Section 8.2 describes the baseline propeller geometry used in the study. Section 8.3 explains the parametrization approach for the Sweep radial distributions. Finally, Section 8.4 highlights the variables modified in the parametric study.

## 8.1. APPU BLI inflow

Figure 8.1 shows the velocity distributions at the intended tail section for the BLI propeller installation used in the APPU Project [4]. These velocity profiles were derived from time-averaged unsteady RANS CFD simulations of a fuselage similar to an Airbus A320 and have been previously utilized in a BLI propeller optimization study [24], as discussed in Chapter 3.

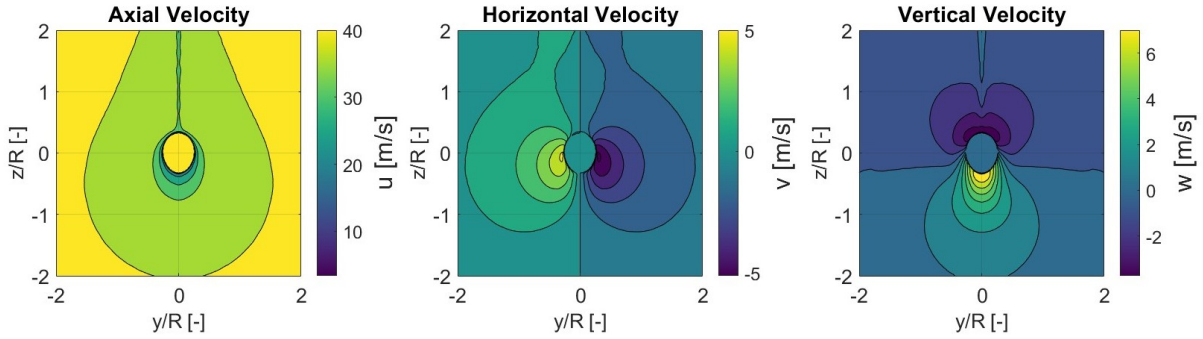


**Figure 8.1:** Inflow field used in the study to consider the BLI installation, as in the study by Sinnige et al. [24]. The missing data inside the hub region has been replaced by the freestream velocity for the axial direction and zero velocity for the in-plane components.

Two of the interaction effects discussed in Section 2.3.2—boundary layer ingestion and wake interaction—are evident in the velocity distribution. The boundary layer is identified by the strong velocity gradient near the fuselage in the axial velocity graph. Additionally, the inflow is not axis-symmetric, as shown by the vertical tail's wake impingement, visible in the thin vertical region above the fuselage with reduced axial velocity, and by the non-axis-symmetric shape of the fuselage, which results in a larger low-velocity area underneath the fuselage. This non-uniformity affects not only the axial velocity across the propeller disk but also the horizontal and vertical velocity components. Due to the fuselage's tapering at the tail, in-plane velocities in the propeller plane are directed towards the center of the fuselage, introducing an additional radial velocity component.

The same velocity distribution is used in this study, incorporating the following simplifications:

- The velocity profiles were derived from simulations where no propulsor was installed at the tail, meaning the propeller's suction effect is not accounted for.
- The velocity distribution suggests that the local fuselage section has an oval shape. However, in the simulation, it was assumed to be circular due to the installation of the propeller hub, which has a diameter equal to the maximum diameter of the local fuselage section.
- The inflow is assumed to be steady, so any unsteady blade loading arises solely from the propeller blades' motion through the non-uniform inflow.

The first simplification implies that the favorable pressure gradient created by the propeller at the tail's end will alter the inflow and consequently affect the propeller's performance. Specifically, the velocity deficit in the area influenced by the vertical tail's wake impingement is expected to diminish, as observed in Figure 2.13 from [9].

## 8.2. Baseline propeller

The baseline propeller used in this study is closely related to the XPROP geometry discussed in Chapter 4, with the primary difference being the hub-to-tip ratio. As outlined in Chapter 3, the fuselage radius at the propeller location determines the hub radius, while the need for ground clearance to prevent tail-strikes constrains the tip radius. Consequently, the original XPROP propeller was unsuitable due to its excessively low hub-to-tip ratio. D. Barara, a researcher at TU Delft involved in the APPU project [4], identified that the optimal hub-to-tip ratio for the propeller in the BLI configuration should be 0.335.
Thus, the baseline propeller for this study, designated as X1, retains the same characteristics as the XPROP-S propeller but features a hub-to-tip ratio of 0.335 instead of 0.195. The scaled XPROP-S propeller model was selected because of its extensive use in the validation process, which confirmed the aerodynamic solver's accuracy in predicting the propeller's aerodynamic performance. Figure 8.2 illustrates the radial distribution of the propeller blade geometry, while Figure 8.3 provides a visualization of the propeller.

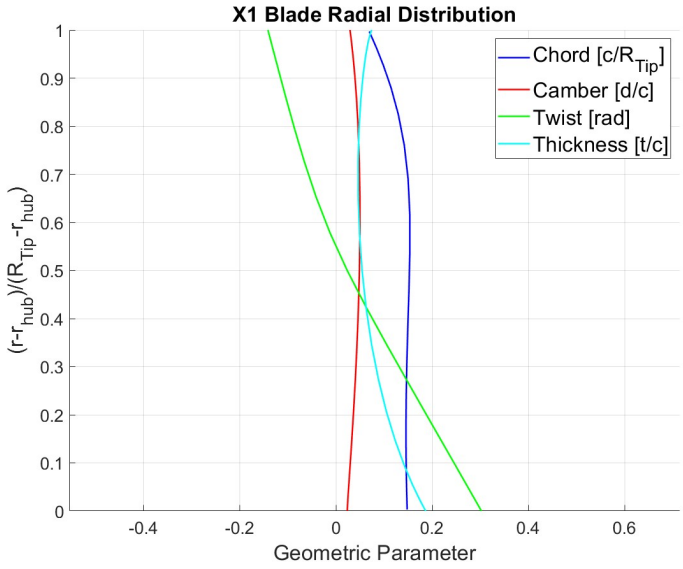


**Figure 8.2:** Chord, camber, twist, and thickness radial distributions of the X1 geometry.

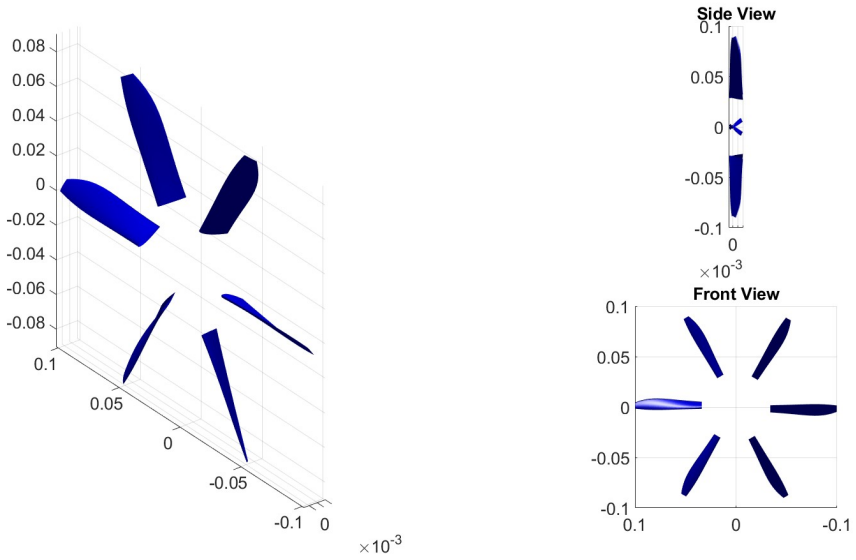


**Figure 8.3:** Visualization of the X1 6-blade propeller with a collective pitch $\beta_{0.7R} = 45°$. The radius of the tip is $R_{Tip} = 0.1016m$, and the hub-to-tip radius ratio is $0.335$.

## 8.3. Sweep Parametrization

As discussed in Chapter 4, the blade designer function allows for the description of the blade geometry's radial distributions using either a vector that specifies the geometric parameters at each radial station or the Bezier coefficients. The latter approach is preferred when the number of parameters needs to be kept minimal, such as in optimization or parametric studies. Therefore, in the sweep parametric study, the sweep distribution, represented as the mid-chord alignment (MCA), is parameterized using cubic Bezier curves.

A cubic Bezier curve is defined by four control points $P_0$, $P_1$, $P_2$, and $P_3$. Here, $P_0$ and $P_3$ are the endpoints of the curve, while $P_1$ and $P_2$ shape the curve's trajectory. The mathematical expression for a cubic Bezier curve is provided in Equation 8.1.

$$B(t) = (1-t)^3 P_0 + 3(1-t)^2 t P_1 + 3(1-t) t^2 P_2 + t^3 P_3 \quad \text{for } t \in [0,1]. \tag{8.1}$$

This equation ensures that as the parameter $t$ varies from 0 to 1, the curve smoothly interpolates between the endpoints, shaped by the intermediate control points. In the blade designer function, the control point coordinates are determined by first defining the positions of the endpoints $P_0$ and $P_3$. The intermediate control points $P_1$ and $P_2$ are then defined using vectors $\vec{P_0 P_1}$ and $\vec{P_3 P_2}$, which are specified by their distances and directions. Given that $P_0$ is fixed at $t = 0$ and $P_3$ at $t = 1$, the total number of parameters needed to describe a radial distribution is reduced to 6. Additionally, since the sweep is expressed as mid-chord alignment (MCA) and the displacement at the hub must be zero, the number of parameters can be further reduced to 5, with $P_0$ fixed at the origin.

Figure 8.4 illustrates the MCA radial distribution with the 5 primary parameters: $\Lambda$, the coordinate of control point $P_3$; the angles $\lambda_1$ and $\lambda_2$, representing the orientation of the vectors; and the lengths of the vectors $r_h$ and $r_t$. Some of these parameters have clear geometric meaning: $\Lambda$ represents the MCA at the blade tip, $\lambda_1$ is the backward sweep angle at the tip, and $\lambda_2$ is the forward sweep angle at the hub.

To further streamline the parameter set, the distances between the control points were fixed at $r_k = 0.5$ and $r_t = 0.4$. This approach allows the sweep distribution to be expressed as a function of just two parameters: the MCA at the tip $\Lambda$ and the sweep at the hub $\lambda_2$. The tip sweep angle $\lambda_1$ is then derived from these two parameters using Equation 8.2.

$$\lambda_1 = (30/0.2)\Lambda + (2/3)\lambda_2 \tag{8.2}$$

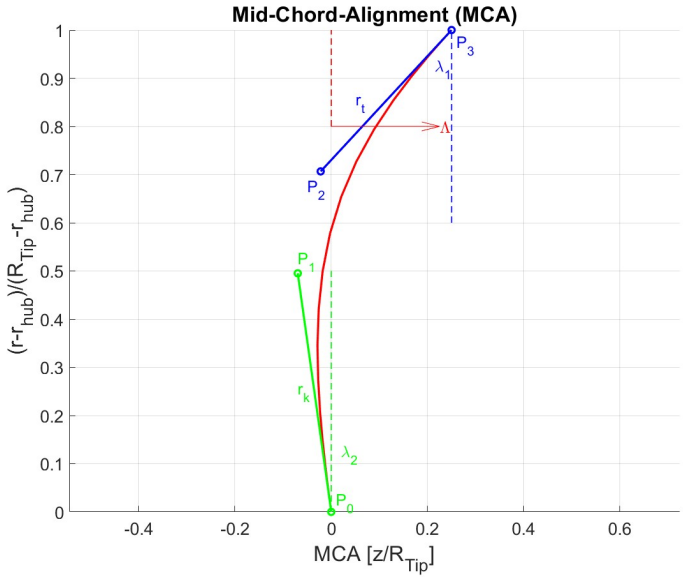


**Figure 8.4:** Sweep distribution parametrization in terms of Mid-Chord-Alignment (MCA).

The relationship in Equation 8.2 is designed so that when forward sweep is applied, the same tip sweep angle can be achieved with a lower MCA at the tip, as previously explained. Conversely, when only $\Lambda$ is increased, only backward sweep is applied, as illustrated in Figure 8.5.

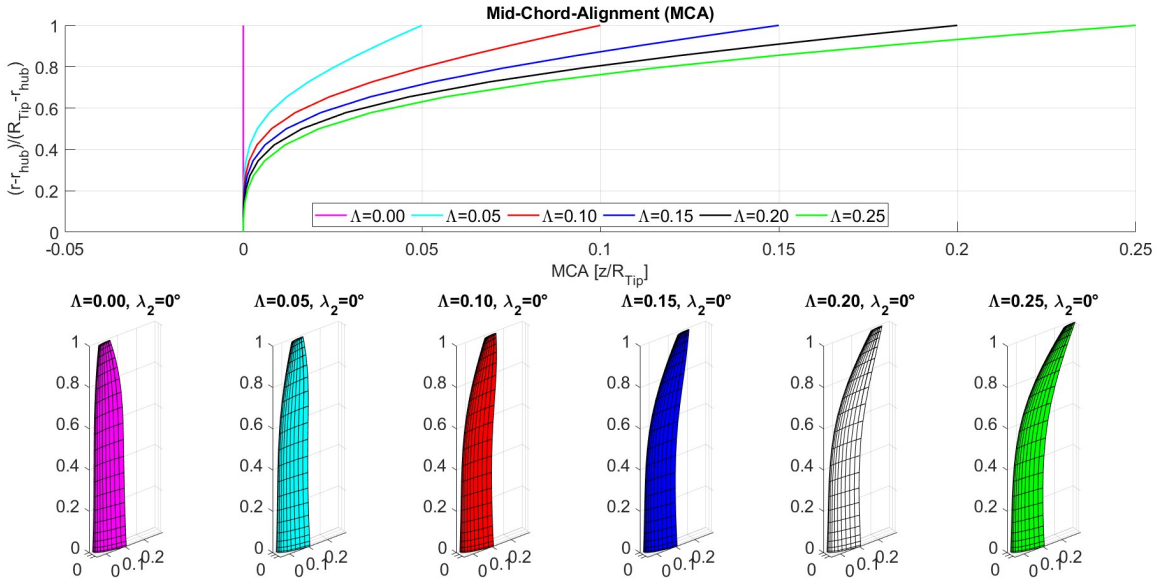


**Figure 8.5:** Top: MCA distribution of blades designed with no forward sweep and different MCA at the tip ($\Lambda$). Bottom: the backward swept blades.

The parameter $\lambda_2$ introduces forward sweep, as illustrated in Figure 8.6.

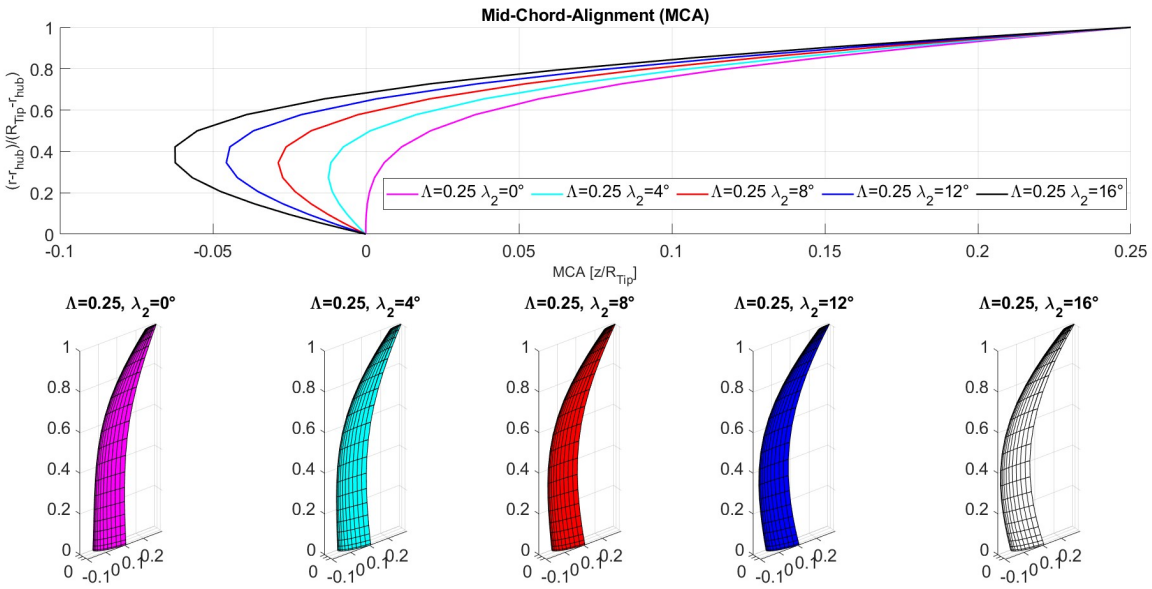


**Figure 8.6:** Top: MCA distribution of blades designed with both forward and backward sweep. The sweep at the hub ($\lambda_2$) is varied while the MCA at the tip is fixed ($\Lambda = 0.25$). Bottom: the forward-backward swept blades.

## 8.4. Design Variables

The objective of this analysis is to evaluate the impact of installing the propeller in a Boundary Layer Ingesting (BLI) configuration on both aerodynamic and aero-acoustic performance. To achieve this, a series of simulations are performed, initially assessing the propeller in isolated conditions and subsequently under installed conditions. This study also investigates the effects of varying certain design variables. The X1 propeller is examined under different operating conditions to simulate installation effects similar to those encountered by an aircraft. As detailed in Chapter 3, both the blade count and blade sweep influence the aero-acoustic performance of propellers. A parametric study is conducted to analyze how variations in these parameters affect propeller performance.

### 8.4.1. Operating Conditions

The propellers analyzed in this study are assumed to operate at ground level. The ambient conditions are summarized in Table 8.1.

| Temperature $[°C]$ | Pressure $[Pa]$ | Density $[Kg/m^3]$ | Viscosity $\mu$ $[Ns/m^2]$ |
|---|---|---|---|
| 15 | 101325 | 1.225 | $1.8015 \times 10^{-5}$ |

**Table 8.1:** Ambient conditions at $h = 0m$.

The operating conditions for propeller analysis are determined by the advance ratio $J$, the pitch setting $\beta_{0.7R}$, and the inflow velocity, which is the sum of the flight velocity $U_\infty$ and the velocity components due to inflow distortion in installed conditions. As discussed in Chapter 7, the aerodynamic solver provides results that align closely with experimental data and CFD results when the collective pitch is set to $\beta_{0.7R} = 45°$ and the advance ratio falls within the range $1.0 < J < 2.0$ at moderate inflow velocities $U_\infty < 40$ m/s. To focus this research and ensure alignment with validated numerical tools, the pitch setting is fixed at $\beta_{0.7R} = 45°$. The advance ratio is varied with the flight velocity maintained at $U_\infty = 40$ m/s. Two conditions are simulated: one representing a cruise phase with a moderate thrust setting and a high advance ratio ($J = 1.8$), and another simulating a climb phase with a high thrust setting and a lower advance ratio ($J = 1.2$).

$$J = [1.2, 1.8] \tag{8.3}$$

### 8.4.2. Number of Blades

As discussed in Chapter 3, the number of blades on a propeller significantly impacts both its aerodynamic performance and acoustic characteristics. Generally, increasing the blade count enhances efficiency and reduces noise levels.

To explore the effects of blade count in an installed configuration, a parametric study is conducted where the number of blades is varied from two to six, as the original XPROP propeller. This range encompasses the typical number of blades found in conventional propellers while also remaining within computational limits for modeling. As detailed in Chapter 5, increasing the number of blades raises computational demands due to the additional lifting surfaces that must be modeled.

$$B = [2, 3, 4, 5, 6] \tag{8.4}$$

This study is performed under a fixed operating condition of $U_\infty = 40$ m/s and $J = 1.8$. This particular operating point is chosen to confine the scope of the study and to emphasize the effects of unsteady blade loading, which tends to exhibit significant amplitude variations during the cruise phase, making this condition particularly relevant.

Since the propeller blade geometry is held constant, the solidity $\sigma$ increases with the number of blades. Consequently, with the pitch setting fixed at $\beta_{0.7R} = 45°$ and the RPM maintained constant across tests, an increase in blade count leads to greater thrust or torque and, thus, higher disk loading. Therefore, it is crucial to interpret the results with these factors in mind.

### 8.4.3. Propeller Sweep

As discussed in Chapter 3, applying sweep to the blade geometry alters the aerodynamic characteristics and introduces a phase lag between noise sources along the blade span. This phase lag can lead to destructive interference and a reduction in noise. Modern propeller designs often incorporate not only backward sweep but also forward sweep in the inboard section of the blade. This forward sweep reduces the mid-chord alignment at the tip while maintaining a similar maximum sweep angle, which can help mitigate structural stresses and deformations caused by inertial forces.

In this study, the 6-blade X1 propeller is modified to explore both backward sweep and a combination of forward-backward sweep. The modifications are controlled using the following parameters:

$$\Lambda = [0.00, 0.05, 0.10, 0.15, 0.20, 0.25] \tag{8.5}$$

$$\lambda_2 = [0°, 4°, 8°, 12°, 16°] \tag{8.6}$$

Here, $\Lambda$ represents the mid-chord alignment (MCA) at the tip, while $\lambda_2$ denotes the forward sweep angle at the hub. As with the blade count study, the modified propellers are simulated under cruise conditions with $J = 1.8$ and $U_\infty = 40$ m/s, and a pitch setting of $\beta_{0.7R} = 45°$.

# 9

# Analysis Results

This chapter explores the performance of a propeller installed in a Boundary Layer Ingestion (BLI) configuration, using inflow conditions similar to those employed in the APPU project. Section 9.1 presents a comparison of the propeller's performance in both isolated and installed configurations under varying operating conditions. Section 9.2 discusses the findings from a sensitivity study on the effects of varying the number of blades. Lastly, Section 9.3 examines the results of a parametric study focused on the impact of different blade sweep distributions.

## 9.1. The BLI Propeller at Different Operating Conditions

The baseline X1 propeller, as described in Section 8.2, is analyzed under two operating conditions: $J = 1.2$ for climb and $J = 1.8$ for cruise, both with a constant flight velocity of $U_\infty = 40$ m/s.

Figure 9.1 illustrates how the advance ratio of the installed propeller varies compared to the isolated condition at these operating points. This variation results from changes in both the axial and in-plane velocity components induced by the BLI configuration. The advance ratio is generally lower in the installed condition, with more significant reductions occurring where axial velocity decreases markedly. These reductions are particularly notable near the hub due to boundary layer ingestion and around the fuselage due to wake interactions, as discussed in Section 8.1.

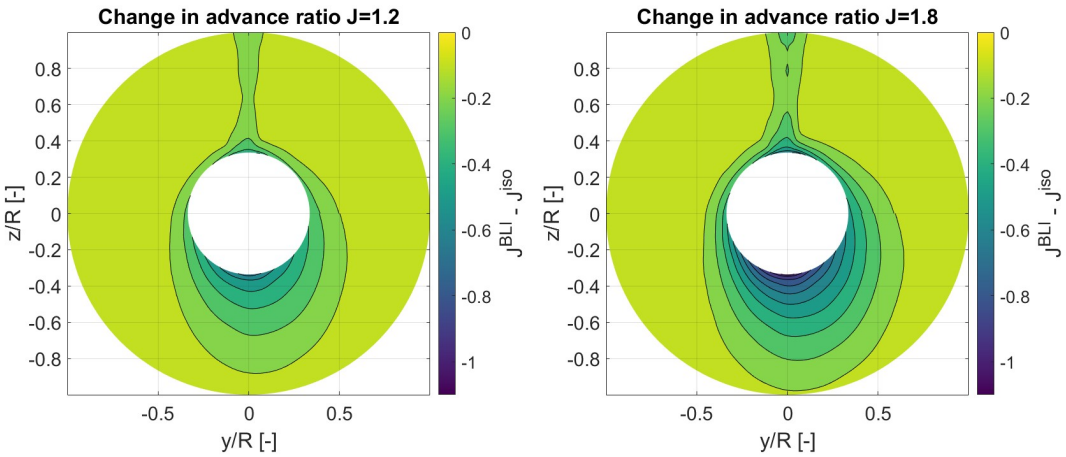


**Figure 9.1:** Change in advance ratio between the installed and isolated conditions. The propeller rotates in the counterclockwise direction, so when it is ascending it is on the right, while when it is descending it is on the left.

The magnitude of the change in advance ratio differs between the operating conditions. At the lower advance ratio ($J = 1.2$), where the propeller spins faster, the tangential velocity component is significantly larger than the axial component. Consequently, the impact of changes in axial velocity on the advance ratio is less pronounced compared to the cruise condition ($J = 1.8$), where the propeller's rotational speed is lower and the axial velocity component has a more substantial effect. Thus, during cruise conditions, variations in inflow have a more significant impact on loading.
As discussed in Chapter 8, the methodology used in this study does not account for the propeller's suction effects on the incoming inflow. Therefore, the inflow variations are considered identical across different thrust settings. It is important to note, as mentioned in Section 2.3, that the velocity deficit due to the vertical tail's wake is expected to diminish with increased thrust. This suggests that the observed changes in inflow and advance ratio, particularly during the climb phase, may be overestimated.

### 9.1.1. Determination of the resolution

Before analyzing the propeller installed in a BLI configuration, it is essential to determine the ideal time resolution for the simulation. As discussed in Section 5.4, the time resolution is related to the wake resolution and the angle $\Delta\phi$ swept by the propeller in one time-step. To accurately estimate the unsteady blade loading, the propeller must sweep the disk with sufficient resolution to capture all inflow distortions. Compared to inflow with a non-zero angle of attack, the BLI installation features both gradual and abrupt inflow changes, as illustrated in Figure 9.1. Particularly significant is the inflow variation due to the vertical tail's wake impingement, which is thin and thus challenging to detect.
Three simulations with different wake parameters, shown in Table 9.1, were conducted to simulate the propeller installed in the BLI configuration during the cruise phase. The resolution was increased by decreasing the angle $\Delta\phi$. Parameters $N_{W0}$ and $N_{W1}$ were varied to maintain constant the length of the pre-allocated wake and the distance for considering wake panels' influence on the propeller across all simulations.

| Simulations | $\Delta\phi$ [deg] | $n_{rev}$ | $N_{W0}$ | $N_{W1}$ | Computational time [s] |
|---|---|---|---|---|---|
| Low resolution | 20 | 1 | 5 | 5 | 103 |
| mid-resolution | 10 | 1 | 10 | 10 | 255 |
| high-resolution | 5 | 1 | 20 | 20 | 849 |

**Table 9.1:** The wake parameters adopted in the simulations of this study. The definitions of these parameters can be found in Section 5.4.

Figure 9.2 shows the thrust coefficient produced by one propeller blade during a revolution as a function of blade azimuth position $\phi'$. The distributions exhibit a peak around $\phi' = 90°$ and a more gradual rise peaking around $\phi' = 270°$. These variations stem from the vertical tail's wake impingement and lower axial velocity beneath the fuselage due to its non-axisymmetric shape. All simulations capture the gradual rise in thrust, but the low-resolution simulation significantly underestimates the peak at $\phi' = 90°$. In contrast, the mid-resolution and high-resolution simulations provide similar peak values, though their profile shapes differ slightly. This indicates that the low-resolution simulation is insufficient to capture the thin inflow variation due to wake impingement.
To visualize a smoother loading trend, the data were interpolated using the Piecewise Cubic Hermite Interpolating Polynomial (PCHIP) method, chosen for its ability to preserve data shape and features, such as monotonicity and local extrema, without introducing new extrema. The unsteady thrust coefficient from the mid-resolution simulation, interpolated using PCHIP, confirms the characteristics mentioned above.

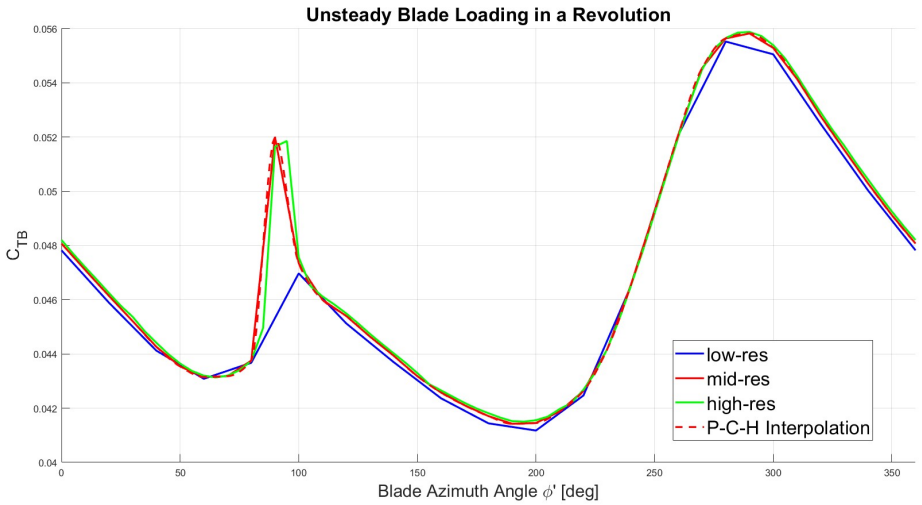


**Figure 9.2:** Blade Thrust coefficient $C_{TB}$ Vs Blade Azimuth Angle $\phi'$ estimated by the simulations with different time-resolutions. $\phi' = 0$ when the blade is oriented orizontally on the left side of the propeller disk while ascending.

Figure 9.3 shows the thrust coefficient during a revolution as a function of the ratio between simulation time and rotation period. Again, the distribution is characterized by peaks resulting from wake impingement. The low-resolution simulation underestimates these peaks, while the mid-resolution and high-resolution simulations provide similar peak values.

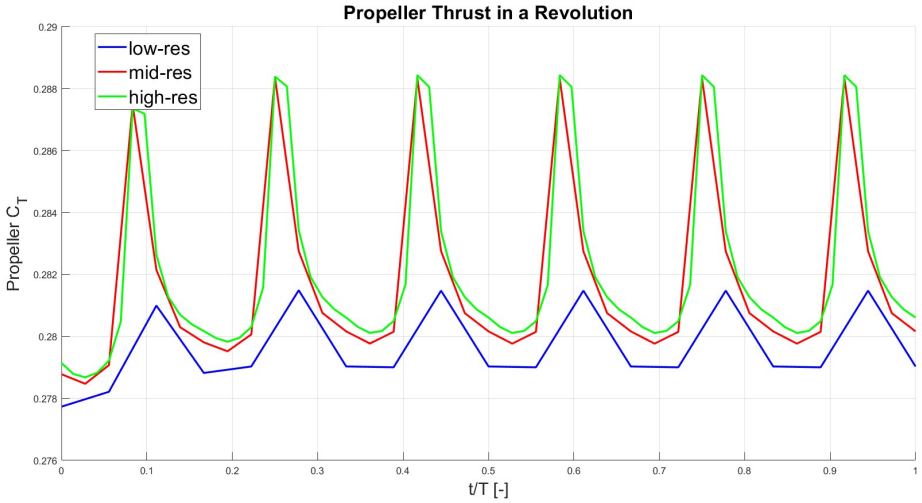


**Figure 9.3:** Thrust coefficient generated by the propeller during a revolution estimated by the simulations with different time-resolutions.

It is anticipated that a simulation with even higher resolution could better capture the peak from wake impingement, providing a slightly higher peak estimate. However, Table 9.1 shows that the high-resolution model already requires considerable computational time, and its results are very close to the mid-resolution simulation. Therefore, the author considered the additional computational burden for a marginal accuracy increase unnecessary. Thus, the mid-resolution parameters are adopted for the subsequent simulations in this study.

### 9.1.2. Aerodynamic Performance

As with the angle of attack case discussed in Chapter 7, circumferential inflow variations induce variable blade loading. Figure 9.4 shows blade loading as a function of blade azimuthal position for the two operating conditions analyzed.

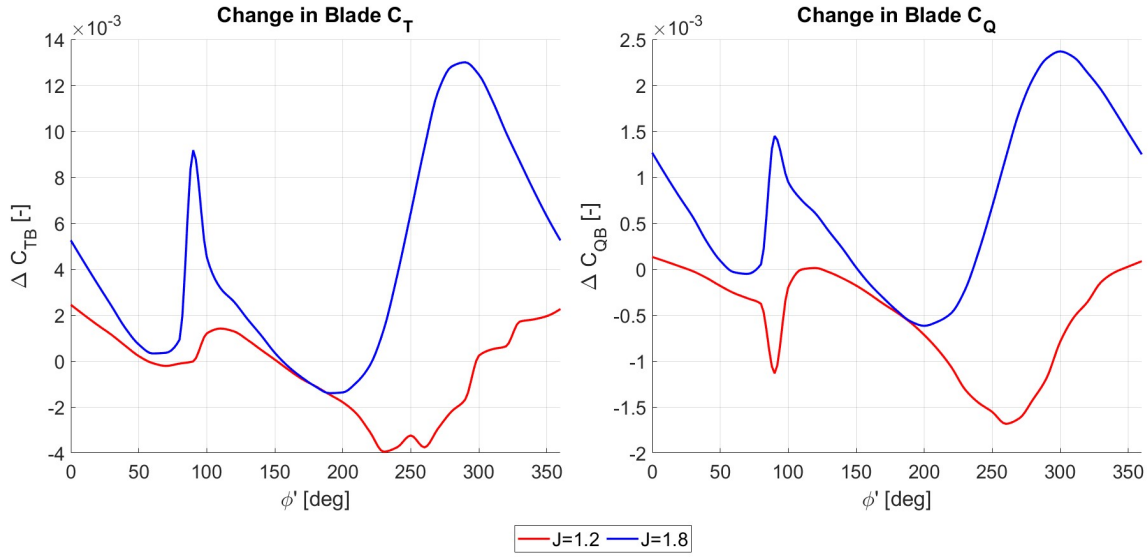


**Figure 9.4:** Change in blade loading during a revolution, expressed as the difference in blade thrust coefficient (left) and blade torque coefficient (right) between the installed and isolated cases.

The trend of the blade thrust coefficient at cruise conditions ($J = 1.8$) has been previously discussed. As expected, the blade experiences two notable thrust increases around $\phi' = 90°$ and $\phi' = 270°$, corresponding to the positions where it is directly above and below the fuselage. These thrust variations are caused by the vertical tail's wake impingement and the non-axisymmetric shape of the fuselage. Specifically, the vertical tail's wake creates a thin, vertical region of reduced axial velocity, while the distortion beneath the fuselage results in a more extensive area of lower velocity. As a result, the thrust increase at $\phi' = 90°$ is more pronounced compared to $\phi' = 270°$. Similarly, the blade torque coefficient exhibits a corresponding pattern, with torque rising in areas where thrust increases.
In the climb phase ($J = 1.2$), the blade loading deviates from expectations. Although the amplitude of loading variations decreases as anticipated due to the reduced change in advance ratio, the loading pattern does not follow the same trend as in the cruise phase. Specifically, while blade loading increases above and below the fuselage during cruise, it unexpectedly decreases in these regions during climb. This is evident from the blade torque coefficient, which shows a notable reduction as the blade passes above and below the fuselage during climb. Similarly, the blade thrust coefficient in the climb phase does not increase as expected when encountering the tail's wake, and it decreases when the blade passes below the fuselage.
This unexpected behavior is attributed to flow separation affecting specific sections of the blade at certain angles. This effect becomes more apparent in Figures 9.5 and 9.6.

Figure 9.5 illustrates the change in sectional angle of attack along the propeller disk for both the installed and isolated conditions at the two operating points considered.
In both flight phases, the angle of attack increases in regions where the advance ratio decreases, as shown in Figure 9.1. Since a larger amplitude of advance ratio variation is observed during cruise, one would expect the angle of attack to increase more at cruise than at climb. However, the results show the opposite. At the cruise condition ($J = 1.8$), the angle of attack increase aligns with the advance ratio variation, reaching a maximum increase of around $6°$. In contrast, during the climb phase, the angle of attack shows a much steeper gradient. When the propeller passes through the tail's wake at $\phi' = 90°$ (green line), the inboard section of the blade experiences a peak increase in angle of attack of about $8°$. Similarly, beneath the fuselage, the angle of attack near the hub increases significantly, with a peak jump

of approximately $12°$.
This discrepancy arises from flow separation affecting certain blade sections during climb. Given the fixed pitch setting ($\beta = 45°$) in both flight phases, the climb condition places the propeller blades closer to the stall regime due to the higher angle of attack. In the installed configuration, the inboard blade sections are subjected to combined effects of boundary layer ingestion and wake interactions at $\phi' = 90°$ and $\phi' = 270°$. Even a modest increase in angle of attack can exceed the critical threshold and induce flow separation. As detailed in Section 7.1, when flow separation occurs, the viscous circulation correction method induces a local peak in the angle of attack, as illustrated in Figure 7.2 for the isolated propeller at $J = 1.1$.

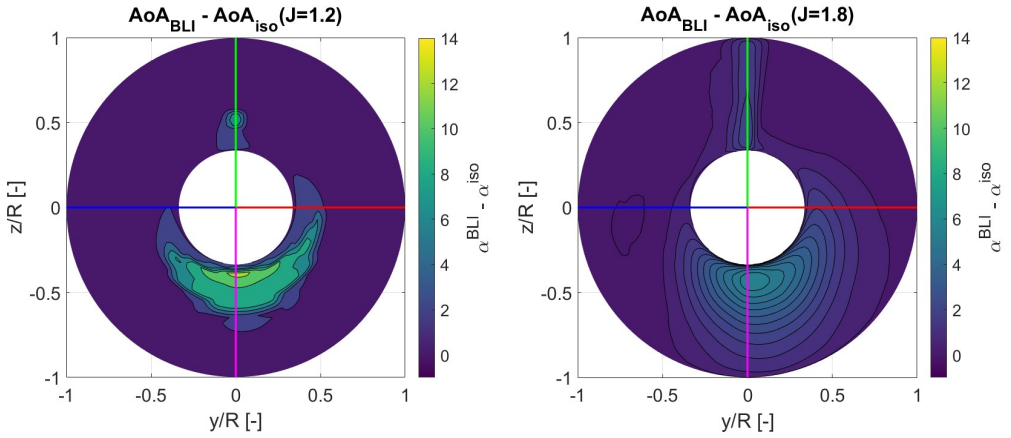


**Figure 9.5:** Difference in sectional angle of attack between the installed and isolated cases. Left: climb phase ($J = 1.2$). Right: cruise phase ($J = 1.8$).

Figure 9.6 shows the change in sectional thrust along the propeller disk between the installed and isolated propeller.

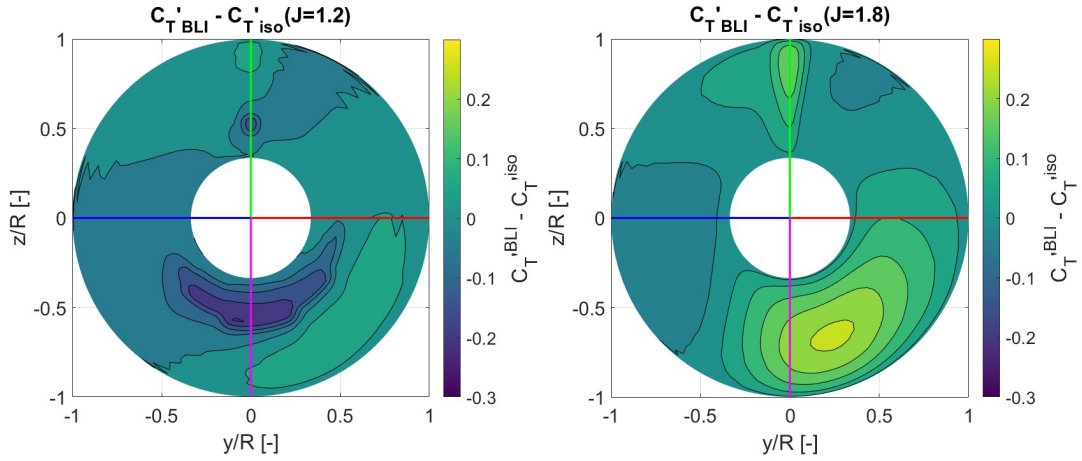


**Figure 9.6:** Difference in sectional thrust coefficient between the installed and isolated cases. Left: climb phase ($J = 1.2$). Right: cruise phase ($J = 1.8$).

The results from the propeller analysis at cruise condition ($J = 1.8$) reveal a clear correlation between areas of increased thrust and regions with a higher angle of attack. However, during the climb phase, regions experiencing the largest increase in angle of attack instead show a reduction in thrust, confirming that these blade sections encounter flow separation, leading to decreased loading.
Figure 9.7 presents the aerodynamic distributions along the blade span during the climb phase. The effective angle of attack distribution indicates that the average angle of attack is already high in isolated conditions, peaking at around $10°$. This high angle is due to the fixed pitch setting, which brings the blade close to stall conditions. Adjusting the pitch setting in conjunction with the advance ratio during climb analysis could potentially prevent flow separation, even under installed conditions. This strategy could also enhance efficiency, as the performance of the isolated propeller demonstrated that efficiency improves when the pitch setting and advance ratio are reduced together.
Focusing on the lift coefficient distributions when the blade passes behind the vertical tail (green line) and beneath the fuselage (magenta line), an uneven profile is observed in the inboard section, with a notable reduction in lift near the hub and an increase near the tips. The thrust coefficient distributions for the installed propeller at these positions mirror this uneven profile, exhibiting less uniformity compared to the isolated conditions.

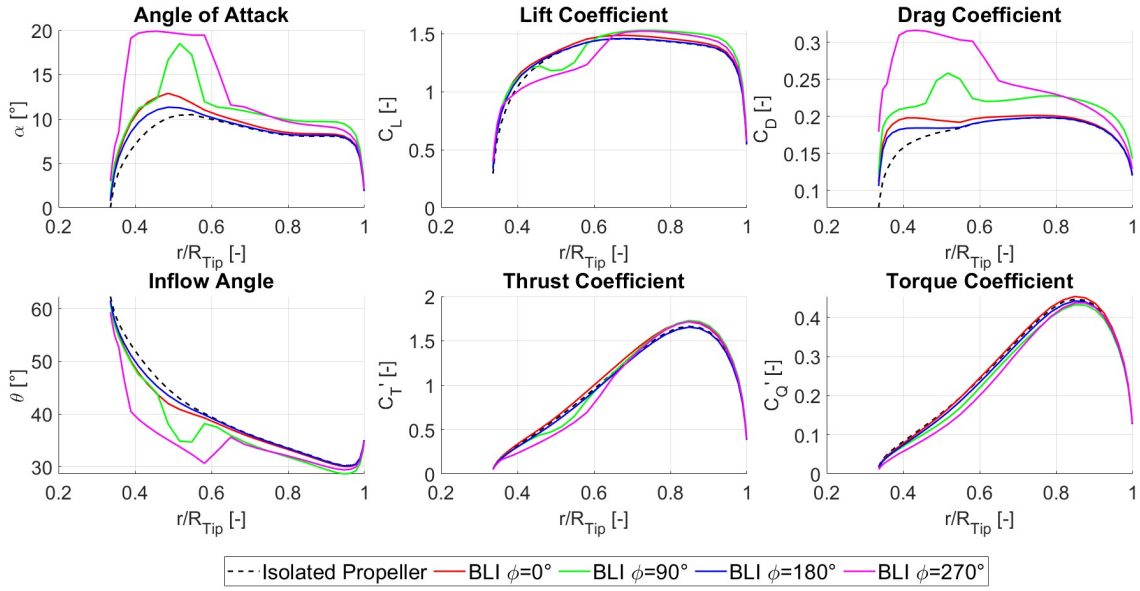


**Figure 9.7:** Comparison of distributions along the blade span for the propeller in isolated conditions (dashed black) and installed conditions (continuous line) at $J = 1.2$. Colors indicate the azimuthal position of the blade as shown in Figures 9.5 and 9.6.

Figure 9.8 shows the aerodynamic distributions along the blade span during the cruise phase. Even when the propeller is installed, and the blade is positioned where boundary layer ingestion combines with wake interaction effects, flow separation does not occur. This is because the angle of attack remains below the stall limit, which, for the inboard sections of the blade, is defined by a critical angle of approximately $\alpha_{crit} = 13°$.
Compared to the isolated propeller, the lift coefficient distributions indicate generally higher values, regardless of the blade's azimuthal position. However, due to the circumferential variations in inflow, the profile shapes differ along the azimuthal direction. When the blade passes behind the vertical tail (green line), the axial velocity reduction is spread across the entire blade span, resulting in a distributed increase in lift coefficient. In contrast, when the blade passes beneath the fuselage (magenta line), the axial velocity reduction is more pronounced near the hub, leading to a lift coefficient peak in the inboard section.
Consequently, the thrust distribution for the blade when it passes beneath the fuselage shifts towards the inboard section. Meanwhile, the increase in blade thrust due to the installation effects when the blade is behind the vertical tail is more evenly distributed along the span.

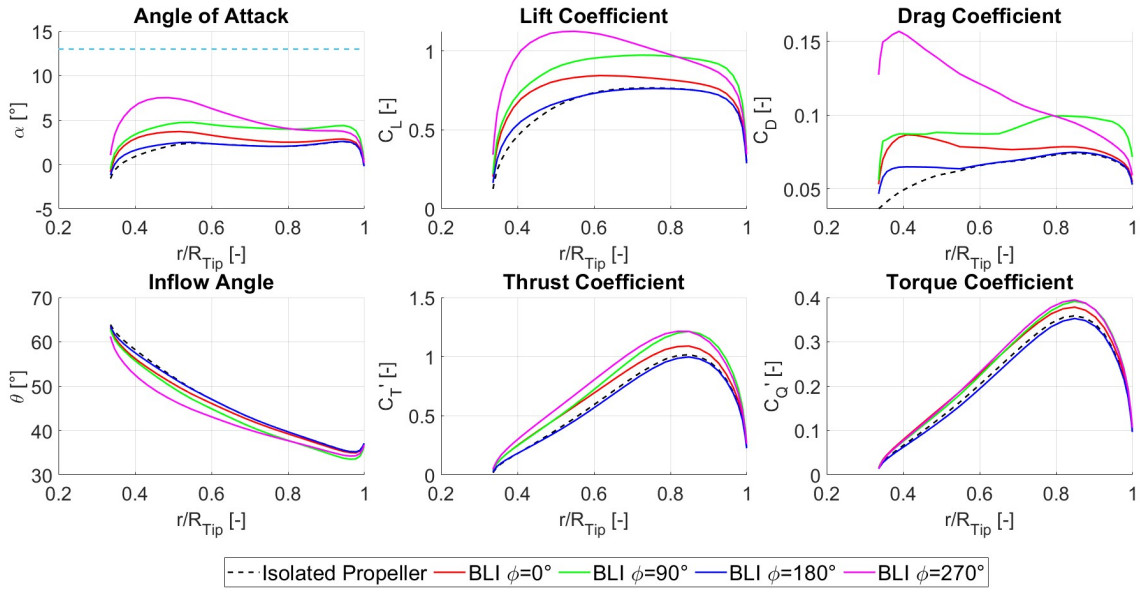


**Figure 9.8:** Comparison of distributions along the blade span for the propeller in isolated conditions (dashed black) and installed conditions (continuous line) at $J = 1.8$. Colors indicate the azimuthal position of the blade as shown in Figures 9.5 and 9.6.

The loading generated by each blade at every time-step combines in the overall propeller performance, as illustrated in Figure 9.9. The graphs depict the thrust coefficient, power coefficient, thrust-to-power ratio, and in-plane forces coefficient during a full revolution.
An interesting observation from the installed propeller's performance is the presence of characteristic peaks, which indicate unsteady performance. These sudden variations occur as a blade passes through the thin region influenced by wake impingement. The number of peaks per revolution corresponds to the number of blades (six in this case). During the cruise phase, these peaks reflect increases in performance (thrust and power coefficients) associated with heightened loading. Conversely, in the climb phase, the peaks denote negative variations, with reductions in the power coefficient due to flow separation, leading to a corresponding decrease in torque coefficient as the blade passes behind the vertical tail.
Circumferential inflow variations also generate in-plane forces, both horizontal and vertical. Similar to the propeller subjected to non-zero angle of attack inflow, as discussed in Section 2.3.3, changes in blade loading result in variations in tangential forces, which in turn create in-plane forces. The vertical force remains relatively constant, while the horizontal force profile shows cusps due to changes in tangential force contributions from blades vertically positioned above and below the fuselage. In the cruise condition, the vertical force coefficient is higher than in the climb phase, owing to larger inflow changes. Additionally, the direction of the horizontal force changes with the operating condition, being positive in cruise and negative in climb. This shift is attributed to flow separation during the climb phase when the blades are vertically aligned. As a blade transits through the thin region affected by the vertical tail, the immediate reduction in advance ratio, caused by decreased axial velocity, results in a sudden loading increase during cruise, while triggering flow separation and loading reduction during climb.
Regarding the thrust-to-power ratio, this metric increases in both the climb and cruise conditions when the propeller is installed. During the cruise phase, the rise in loading leads to an increase in both thrust and power demand, with the thrust increase outpacing the power increase. In the climb phase, cyclic decreases in loading reduce overall thrust and power, but the reduction in power is greater than the reduction in thrust. While this ratio indicates the relationship between generated thrust and power demand, it does not fully define the propeller's efficiency in a boundary layer ingesting configuration due to the non-uniform axial inflow velocity distribution. Nevertheless, it remains a valuable indicator of the balance between thrust generated and power required.
In the cruise condition, the thrust-to-power ratio increases by about $4\%$, whereas in the climb phase, the increase is around $2\%$. These results demonstrate that even a propeller not specifically designed for BLI installation can exhibit improved aerodynamic performance, consistent with the findings discussed in

Chapter 3.

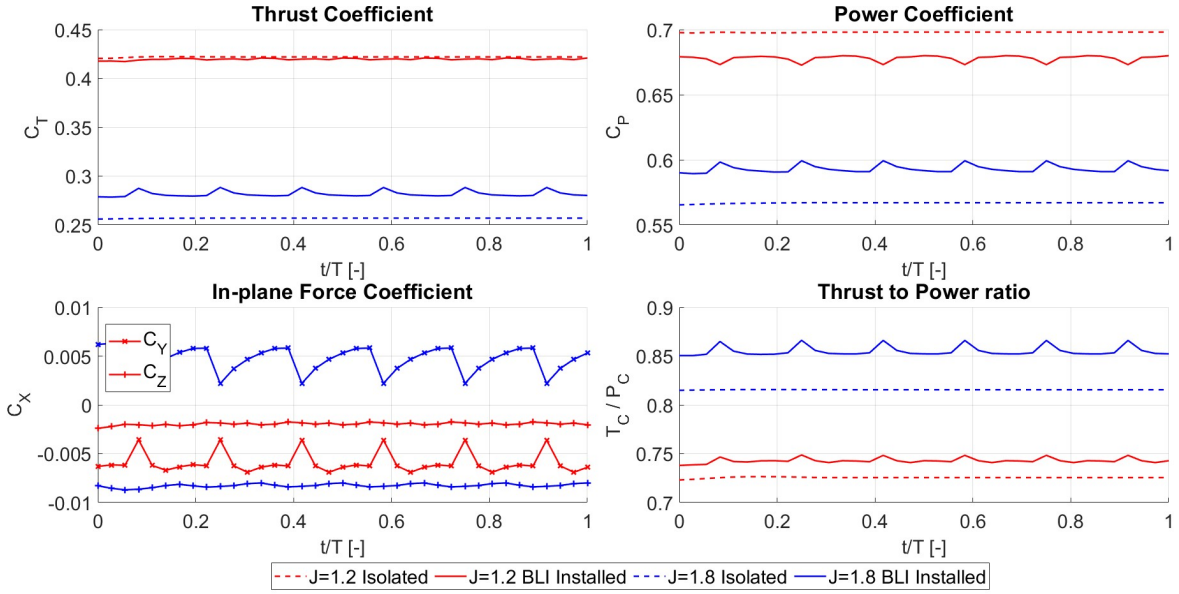


**Figure 9.9:** The propeller performance during a revolution in isolated and installed cases for both climb and cruise conditions.

### 9.1.3. Aero-Acoustic Performance

Once the aerodynamics of the propeller in both isolated and installed conditions are understood, the analysis of noise emissions can proceed.

Figure 9.10 illustrates the sound pressure levels (SPL) emitted by the isolated and installed propeller during the climb and cruise phases, with observers positioned along the propeller's axis. The graph presents both the total noise patterns and the differentiated contributions from individual noise sources.

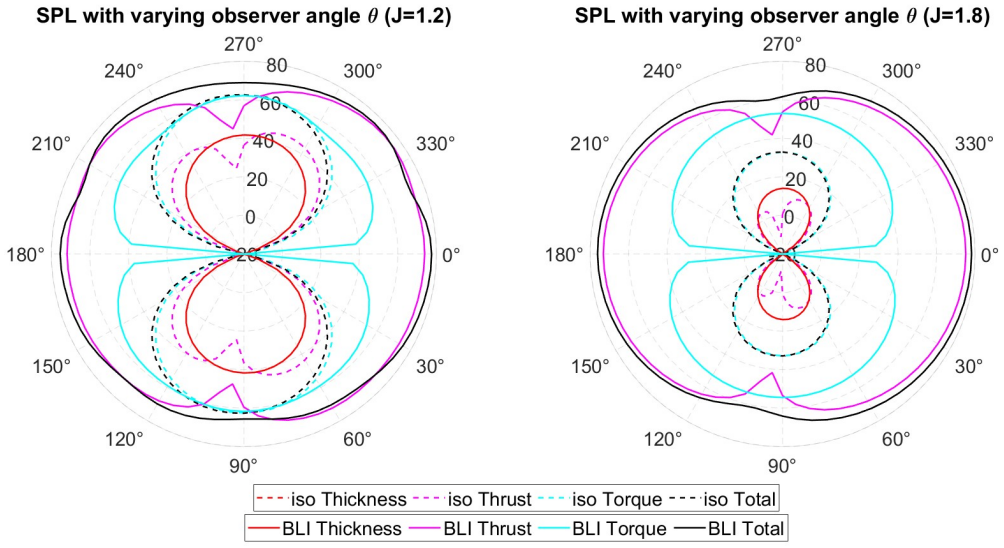


**Figure 9.10:** Directivity plots of the noise emissions in the plane along the propeller axis. Both the results of the isolated (dotted lines) and installed case (continuous lines) are shown. Left: noise emissions during the climb phase. Right: noise emissions during the cruise phase.

Regarding total noise emissions, the maximum SPL increases significantly when the propeller is installed,

by approximately 15 dB during the climb and about 46 dB during the cruise. Additionally, the noise pattern changes shape when the propeller is installed, with the direction of maximum noise emissions shifting from within the plane of rotation ($\theta = 90°$, $\theta = 270°$) to being aligned with the propeller's axis of rotation ($\theta = 0°$, $\theta = 180°$). This shift suggests that unsteady blade loading, associated with the loading harmonics $k > 0$, becomes dominant when the propeller is installed in the BLI configuration.
As discussed in Section 7.2, the thickness noise component remains steady regardless of the propeller's condition. In contrast, the loading noise components vary significantly between the isolated and installed configurations, with the lift noise source being more dominant than the drag source in both cases.
When differentiating the loading noise sources between thrust and torque components, a significant distinction emerges: in the isolated case, the torque component dominates across all operating conditions. However, in the installed configuration, the thrust component becomes predominantly influential along the propeller's axis. The torque component retains its dominance only when observers are aligned with the propeller's plane of rotation.
Figure 9.11 presents the SPL emitted by the isolated and installed propeller during the climb and cruise phases, with observers positioned in the plane of rotation of the propeller. As observed during the acoustic solver verification in Section 7.2, when the propeller operates in isolated conditions with axisymmetric inflow, the absence of circumferential variations ensures that noise emissions remain uniform in all directions. However, when the propeller is installed, only the sound pattern from the thickness noise source remains unchanged. In contrast, the noise from the loading sources varies due to the addition of unsteady loading contributions ($k \neq 0$) to the steady loading ($k = 0$). In both conditions, the torque noise source is stronger than the thrust source, confirming that when observers are aligned with the propeller's rotational plane, the torque noise source remains dominant, even when the propeller is installed.

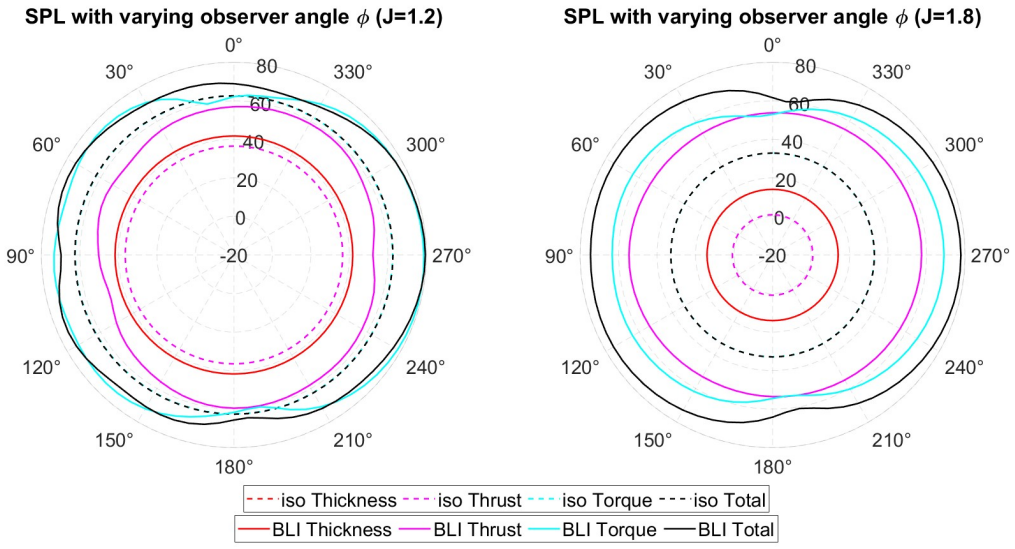


**Figure 9.11:** Directivity plots of the noise emissions in the plane of rotation. Both the results of the isolated (dotted lines) and installed case (continuous lines) are shown. Left: noise emissions during the climb phase. Right: noise emissions during the cruise phase.

Regarding the frequency content, the verification in Section 7.2 demonstrated that noise emissions from the isolated propeller are primarily concentrated in the first noise harmonic ($m = 1$). However, when the propeller is installed, the introduction of unsteady loading sources causes contributions from higher noise harmonics ($m > 1$) to become significant. Specifically, for a given noise harmonic $m$, the noise emissions from a propeller with $B$ blades include contributions from the first $k \approx m \times B$ unsteady loading source harmonics. Contributions from larger loading harmonics are effectively filtered out due to the reduced efficiency of propagation.
Figure 9.12 presents the spectrum of unsteady loading oscillations from the installed propeller during climb and cruise phases, examined at three radial stations. The spectrum reveals that the amplitude of unsteady

loading decreases progressively beyond the loading harmonic $k = 6$, becoming nearly negligible after $k \approx 35$. Consequently, for the 6-bladed baseline propeller, considering the first $m \approx 5 - 6$ noise harmonics is sufficient to adequately capture the overall noise levels. While including higher noise harmonics might increase the propagation efficiency of unsteady loading contributions from loading harmonics beyond $k = 35$, the noise emissions remain minimal. This is because the amplitude of loading oscillations at these higher harmonics is so small that the additional noise emissions are also negligible.

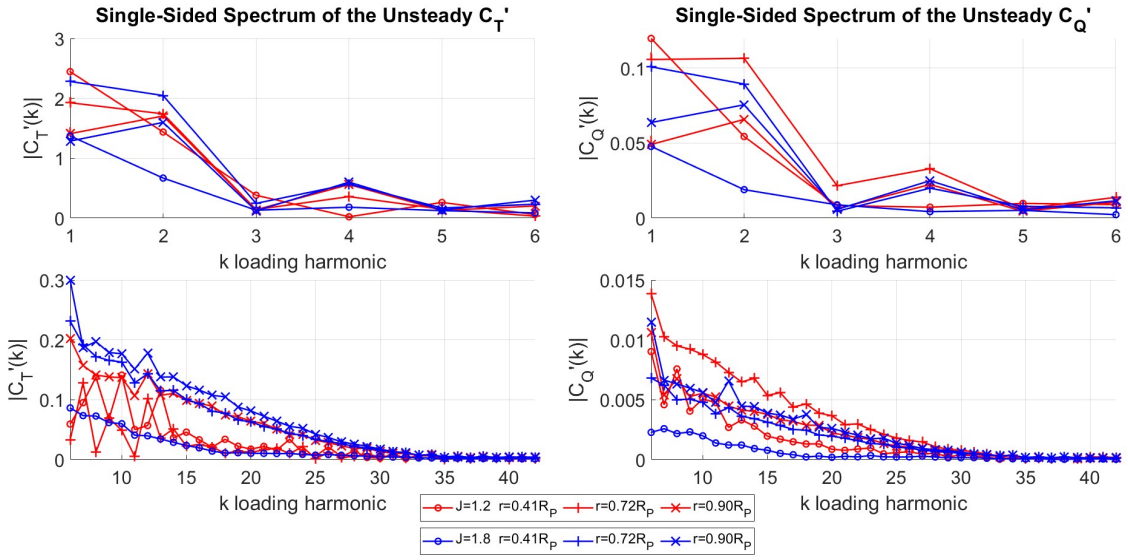


**Figure 9.12:** Single-sided spectrum of the unsteady sectional thrust and torque coefficient for the installed propeller at climb ($J = 1.2$) and cruise ($J = 1.8$) for three radial stations.

Figure 9.13 provide the directivity plots of the noise emissions from the thrust and torque sources respectively at cruise conditions. The graphs provide the single harmonic noise contribution as well as the sum of all the harmonic contributions at both isolated and installed conditions.

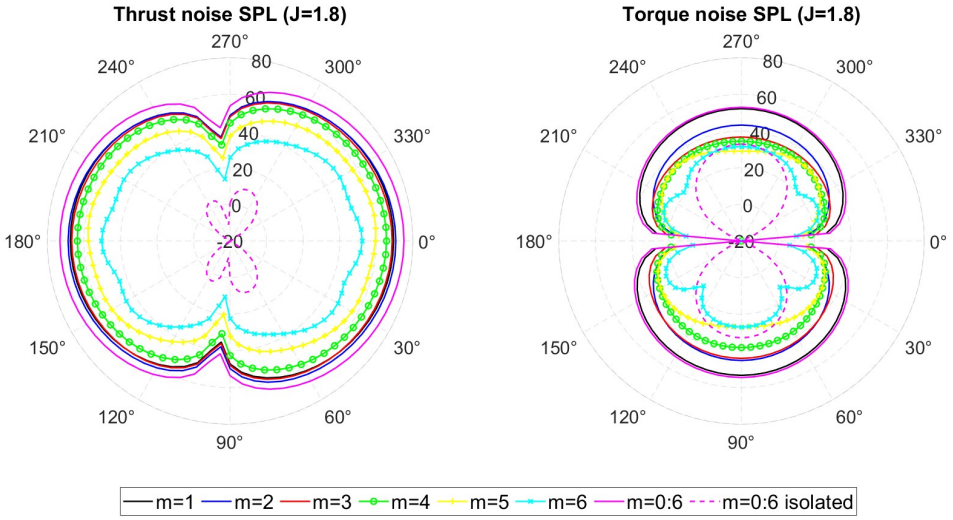


**Figure 9.13:** Directivity plots in the plane along the propeller axis of the noise emissions from the thrust and torque noise sources. The single noise harmonic $m$ contributions are plotted together with the overall sum for the isolated and installed propeller at cruise conditions. The solid lines refer to the propellers in installed conditions.

The results align with expectations, as the contribution from higher noise harmonics progressively decreases due to the reduction in the amplitude of loading oscillations at higher harmonics, as observed in Figure 9.12 for loading harmonics $k > 6$. The minimum difference between the thrust noise contribution from the first noise harmonic ($m = 1$) and the sixth ($m = 6$) is approximately 18 dB, indicating that these higher noise harmonics contribute minimally and could be ignored if the focus is on estimating maximum noise levels. Figure 9.13 further illustrates how the thrust and torque noise sources propagate differently along the plane aligned with the propeller axis. It appears that the direction of maximum thrust noise propagation is orthogonal to the direction of maximum torque noise propagation. As previously noted, the torque noise component is dominant when observers are aligned with the plane of rotation but becomes null when observers are aligned with the propeller axis, regardless of the noise harmonics. Conversely, the thrust component is maximized when observers are aligned with the propeller axis when the propeller is installed. Both thrust and torque noise components increase when unsteady loading contributions are added; however, the greatest increase is seen in the thrust component. This substantial rise in thrust noise is why the torque noise ceases to be the dominant source when the propeller is installed.

Part of this shift in dominance is due to the direction of maximum thrust propagation aligning with the direction of highest unsteady loading noise propagation efficiency. As discussed in Chapter 6, the noise propagation efficiency of all sources is modeled in the HST by the Bessel function, whose output depends on the order $n = m \times B - k$ and the argument, which is proportional to $\cos\theta$. When observers are aligned with the propeller axis ($\theta = 0°$, $\theta = 180°$), the argument is zero, and when the order of the Bessel function is $n \neq 0$, the function's output is also zero. This explains why the thrust noise emissions from the isolated propeller are null when observers are aligned with the propeller axis. However, when the propeller is installed and the unsteady loading component is considered, the efficiency of propagation in the propeller axis direction not only exceeds zero when the loading harmonic $k = m \times B$ but also reaches its maximum. Since the torque noise component is null in this direction, only the thrust noise contribution from the loading harmonic $k = m \times B$ benefits from this enhanced efficiency, explaining the significant increase in thrust noise emissions.

Regarding differences in total noise emissions between climb and cruise operating conditions, the isolated propeller generates significantly more noise during the climb phase ($SPL_{Max} \approx 62$dB) than during the cruise phase ($SPL_{Max} \approx 32$dB). This is due to the higher rotational velocity of the propeller, which generates larger loads and achieves a higher spinning tip Mach number ($M_t$). The increased $M_t$ enhances the propagation efficiency of noise sources, resulting in higher noise levels.

When considering the installed propeller, the addition of unsteady loading emissions reverses the situation, as the noise level increase is larger at cruise ($\approx$ 46dB) than at climb ($\approx$ 15dB). Consequently, the maximum noise level at climb ($SPL_{Max} \approx 77.5$dB) is slightly lower than at cruise ($SPL_{Max} \approx 78$dB). This reduction in the difference between maximum noise levels occurs because the amplitude of unsteady thrust contributions at higher loading harmonics ($k > 6$) is generally greater during cruise, as shown in Figure 9.12.

Table 9.2 compares the maximum TSSP values during climb and cruise for both isolated and installed propellers. The TSSP normalizes the amplitude of the sound waves by the propeller thrust. Since in isolated conditions the noise levels at climb, as SPL, are much larger than at cruise (by around 30 dB), the TSSP at climb is also larger than at cruise. However, in installed conditions, the difference between SPL at climb and cruise is less than 1 dB, resulting in the TSSP at cruise being larger than at climb in installed conditions.

| $TSSP_{Max}$ | Climb $J = 1.2$ | Cruise $J = 1.8$ |
|---|---|---|
| isolated (Varying $\theta$) | $-86.54$ | $-104.9$ |
| isolated (Varying $\phi$) | $-86.54$ | $-104.9$ |
| BLI Installed (Varying $\theta$) | $-71.65$ | $-60.42$ |
| BLI Installed (Varying $\phi$) | $-69.72$ | $-60.76$ |

**Table 9.2:** Maximum TSSP estimated in both the isolated and BLI installed case.

Figure 9.14 provides directivity plots of the thrust specific sound pressure level (TSSP), offering a visual comparison of noise distribution patterns across different operating conditions.

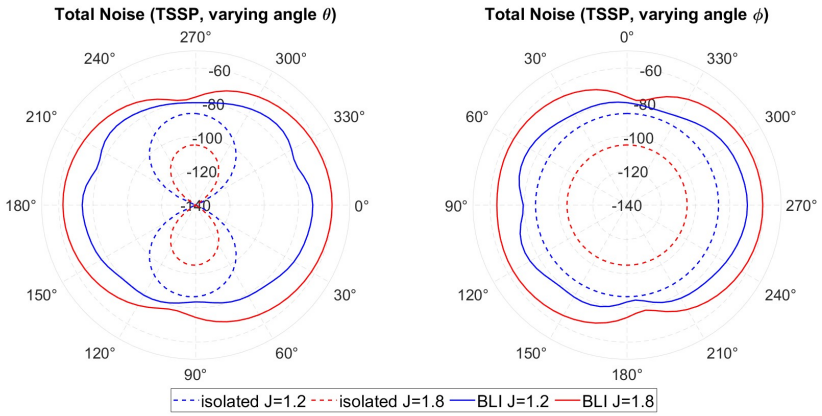


**Figure 9.14:** Directivity plots of the total noise emissions in the isolated (dotted lines) and installed case (continuous lines) at climb conditions $J = 1.2$ and cruise condition $J = 1.8$. Left: the observers are positioned in the plane along the propeller axis. Right: the observers are positioned in the rotational plane.

The results presented above are derived from an aero-acoustic analysis where the acoustic solver received loading distribution, ambient, and operating conditions from the aerodynamic solver, with a flight velocity set at $U_\infty = 40$ m/s. As discussed in Chapter 8, this velocity is selected due to the aerodynamic solver's limited capability to account for compressibility effects. Consequently, the flight Mach number $M_\infty$, along with the spinning tip Mach number $M_t$ and helical tip Mach number $M_{hel}$, are significantly lower than the typical conditions experienced by a transport aircraft like the APPU. The values for these Mach numbers during the climb and cruise phases are shown in the first two rows of Table 9.3. As previously noted, the tip Mach number influences the noise level's propagation efficiency, which is reflected in the spinning mode tip Mach number $M_s$, defined in Equation 7.1. This indicator serves as a useful approximation for estimating propagation efficiency, as demonstrated during the verification of the unsteady acoustic solvers in Section 7.2.
To assess the impact of tip Mach number on noise levels and to determine how applicable the previous results are to higher-speed applications like the APPU project, an additional analysis is conducted. The new operating conditions, detailed in the last two rows of Table 9.3, are selected to ensure that the helical Mach number remains below the threshold at which non-linear flow phenomena characteristic of the transonic regime begin to emerge. The scaled loading distribution, in terms of lift and drag coefficients, is taken from the lower-speed simulations to isolate the effect of the Mach number on noise propagation efficiency.

| Operating Condition | $U_\infty$ $[m/s]$ | $M_{hel}$ [-] | $M_t$ [-] |
|---|---|---|---|
| Climb $J = 1.2$ $M_\infty = 0.11$ | 40 | 0.330 | 0.308 |
| Cruise $J = 1.8$ $M_\infty = 0.11$ | 40 | 0.238 | 0.205 |
| Climb $J = 1.2$ $M_\infty = 0.3$ | 102 | 0.841 | 0.785 |
| Cruise $J = 1.8$ $M_\infty = 0.4$ | 136 | 0.805 | 0.698 |

**Table 9.3:** Comparison of flight velocities and Mach numbers at different operating conditions.

Figure 9.15 illustrates the trend of the spinning mode across different loading harmonics for both climb and cruise conditions, evaluated at various $M_\infty$ values. As discussed in Section 7.2, this indicator represents the ratio of the argument to the order of the Bessel function in Hanson's model, which is used to estimate noise propagation efficiency. When $M_s \ll 1$, propagation efficiency is negligible. For $M_s \approx 1$, propagation efficiency reaches its peak, and for $M_s >> 1$, efficiency progressively declines.

The trends shown in Figure 9.15 reveal that $M_s$ is closer to one for the steady loading harmonic ($k = 0$) and increases more rapidly with the loading harmonic $k$ as the tip Mach number rises. Consequently, the propagation efficiency of steady loading noise sources improves significantly more than that of unsteady

loading noise sources as the tip Mach number increases. This results in increased noise emissions within the propeller's rotational plane, where the maximum noise emissions are observed.

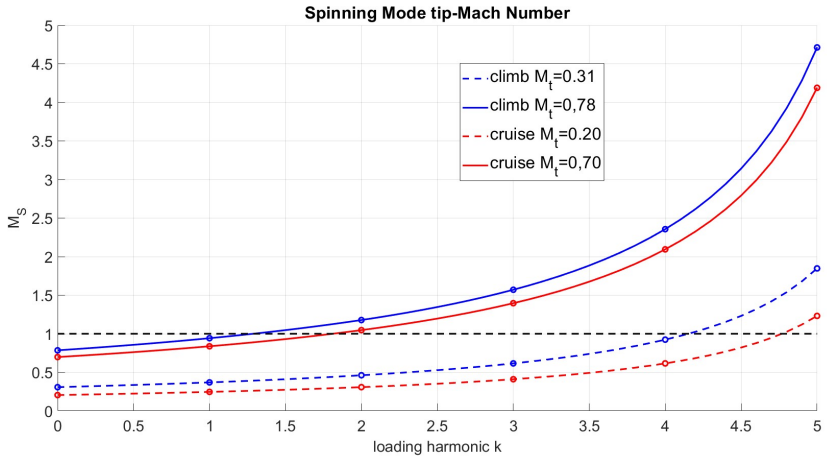


**Figure 9.15:** Spinning mode tip Mach number $M_s$ for the first noise harmonic $m = 1$ as a function of the loading harmonic $k$ for the different operating conditions of the propeller.

The observations discussed above are corroborated by the directivity plots presented in Figures 9.16 and 9.17. Regardless of whether the propeller is in climb or cruise conditions, an increase in flight and spinning tip Mach numbers results in higher noise emissions for the isolated propeller due to the improved propagation efficiency of the steady noise sources.
For installed propellers, an increase in the tip Mach number highlights the dominance of the steady noise component. As shown in Figure 9.16, the peak noise emissions are observed at angles $\theta = 90°$ and $\theta = 180°$, corresponding to the plane of rotation. This pattern is consistent for both isolated and installed propellers.
The dominance of steady noise becomes even more pronounced when examining the directivity plots in the rotational plane, as illustrated in Figure 9.17. At higher tip Mach numbers, the directivity patterns for installed propellers resemble the circular shape typical of isolated propellers, indicating that steady noise sources are the predominant contributors to the overall noise emissions.

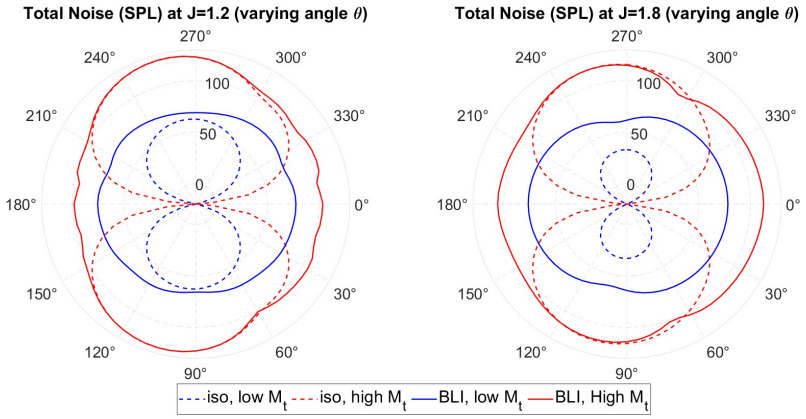


**Figure 9.16:** Directivity plots of the noise emissions in the isolated (dotted lines) and installed case (continuous line) when the observers are positioned in the plane along the propeller axis. Left: climb phase $J = 1.2$. Right: cruise phase $J = 1.8$.

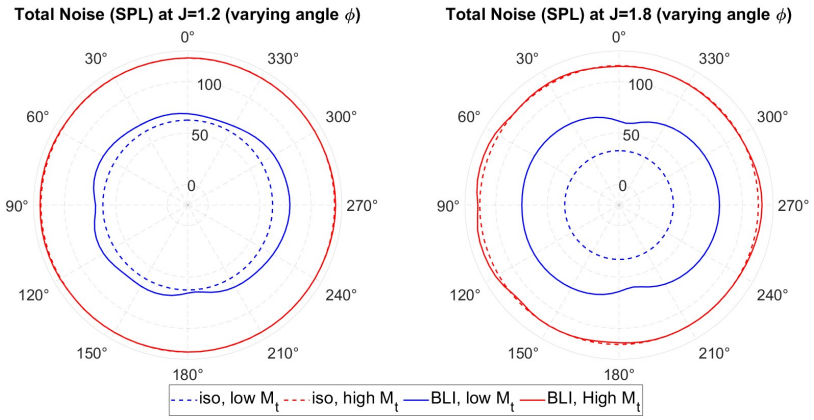


**Figure 9.17:** Directivity plots of the noise emissions in the isolated (dotted lines) and installed case (continuous line) when the observers are positioned in the plane of rotation. Left: climb phase $J = 1.2$. Right: cruise phase $J = 1.8$.

In summary, installing a propeller in a Boundary Layer Ingestion (BLI) configuration induces significant variations in blade loading during a revolution due to circumferential inflow changes. The most substantial loading fluctuations occur in regions affected by the vertical tail's wake, above the fuselage, and beneath the fuselage where axial velocity decreases due to its non-axisymmetric shape. These variations contribute to in-plane forces and influence unsteady performance.

The aerodynamic analysis shows that even a generic propeller, not specifically designed for BLI, can benefit from installation in both cruise and climb conditions. The thrust-to-torque ratio improves in both flight modes, although flow separation during the climb phase can occur due to the reduced axial velocity and advance ratio caused by the BLI installation. This highlights the need for propellers intended for BLI to operate at larger advance ratios or with reduced pitch settings to prevent blade stall.

Noise emissions are notably altered by the installation, with unsteady loading noise sources becoming significant. The noise patterns differ with operating conditions: at cruise with a low tip Mach number, unsteady blade loading is predominant, leading to distinct noise directivity compared to the isolated propeller. However, as the tip Mach number increases, such as in climb conditions, the influence of steady loading noise sources increases.

The study further reveals that at higher tip Mach numbers, typical of real transport planes like those in the APPU project, steady noise sources dominate, as the maximum emissions are observed near the propeller plane. Conversely, unsteady noise sources remain more prominent towards the propeller axis. This finding suggests that results from analyses conducted at lower Mach numbers may not be directly applicable to faster transport planes due to the increased influence of steady loading noise sources at higher Mach numbers.

Given the emphasis on evaluating the propeller's performance in installed conditions and understanding the effects of unsteady loading on both aerodynamics and aero-acoustics, the next phase of the study will focus on analyzing the propeller's performance under conditions where unsteady loading has the most pronounced effects. Specifically, this will involve examining the propeller during cruise conditions ($J = 1.8$) at a lower tip Mach number ($M_t = 0.208$), where the influence of unsteady loading is expected to be more significant.

## 9.2. Impact of the Blade Count

As highlighted in Chapter 3, blade count plays a crucial role in both aerodynamics and aero-acoustics. This section examines how variations in blade count influence propeller performance, specifically when installed in a Boundary Layer Ingestion (BLI) configuration, with a focus on unsteady blade loading effects.

### 9.2.1. Aerodynamic Performance

The aerodynamic analysis starts with evaluating the blade thrust coefficient throughout a revolution for both isolated and installed propellers, as shown in Figure 9.18. In the isolated configuration, the blade loading remains relatively uniform across the revolution. As the blade count increases, however, a slight reduction in loading is observed for both isolated and installed propellers. This decrease is due to the increased interference between blades, which results in each blade carrying a reduced load. Despite these variations, the relative difference in loading between isolated and installed propellers remains approximately constant, as illustrated in Figure 9.4 for the 6-bladed configuration.

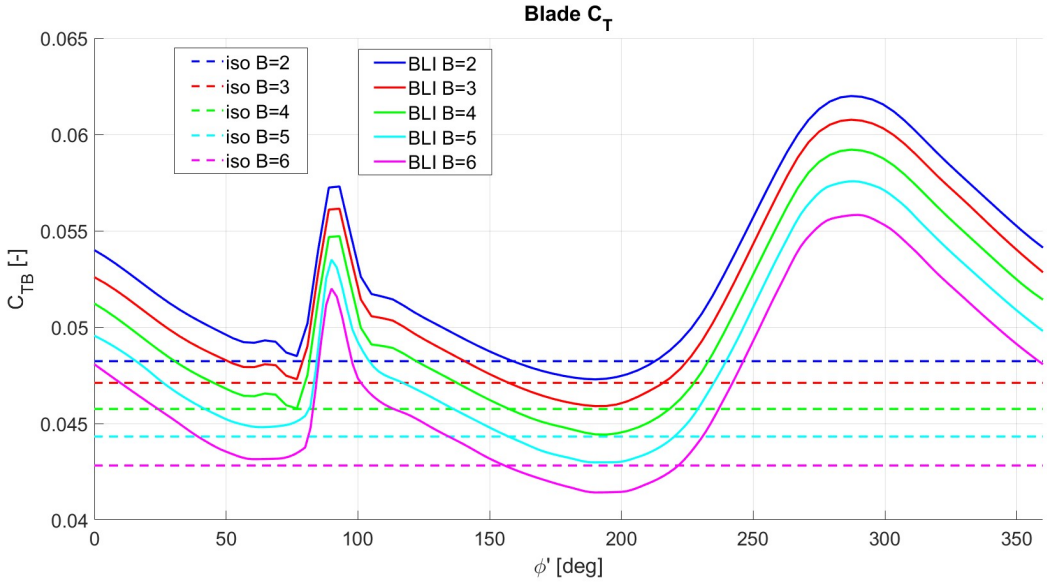


**Figure 9.18:** Blade thrust coefficient during a revolution for the isolated propeller (dotted line) and the installed propeller (solid line).

Figure 9.19 illustrates key propeller performance indicators as a function of the number of blades. As highlighted in the previous analysis (Figure 9.9), these performance metrics vary throughout a revolution based on blade position, which necessitates the use of time-averaged values for a clearer comparison.
With an increasing number of blades, the total blade surface area grows. As shown in Figure 9.18, while the blade loading itself is relatively stable regardless of the blade count, the overall disk loading rises. This increase in disk loading leads to greater forces generated and higher power demands from the propeller. Consequently, the thrust-to-power ratio, which reflects propulsive efficiency for the isolated propeller, decreases. This result does not necessarily conflict with the findings in Chapter 3, which suggest that a higher blade count can improve efficiency. Those considerations apply to propellers designed to meet specific thrust requirements. In this analysis, however, the propellers retain the same blade geometry and operating conditions, leading to increased disk loading and associated energy losses, which ultimately reduce efficiency.
Figure 9.19 demonstrates that the thrust and power curves for both isolated and installed propellers exhibit similar trends, with the installed propellers consistently showing higher performance levels. This performance offset between isolated and installed propellers, while present, tends to increase slightly with the blade count.

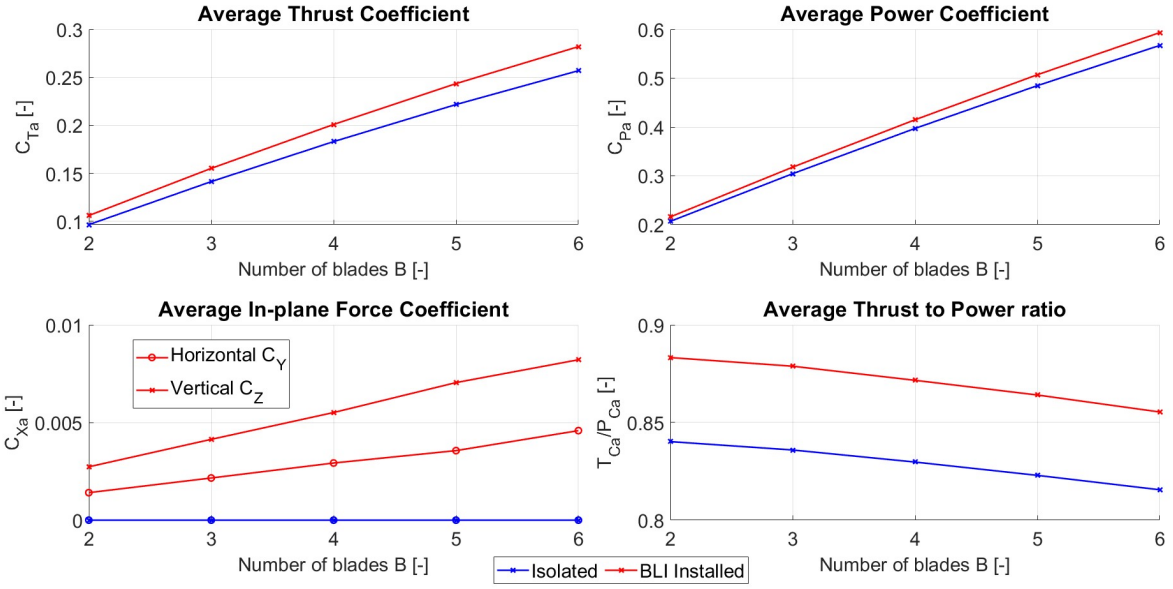


**Figure 9.19:** Time-averaged propeller performance in isolated and installed cases at cruise conditions.

Given the significant variation in thrust with the number of blades, it is important to normalize features such as in-plane forces relative to the average thrust output. Figure 9.20 illustrates the average in-plane forces normalized by the average thrust as a function of the number of blades. As the blade count increases, the in-plane forces relative to thrust show a marginal increase. Despite this trend, the overall increase in in-plane forces is relatively small compared to the increase in thrust.

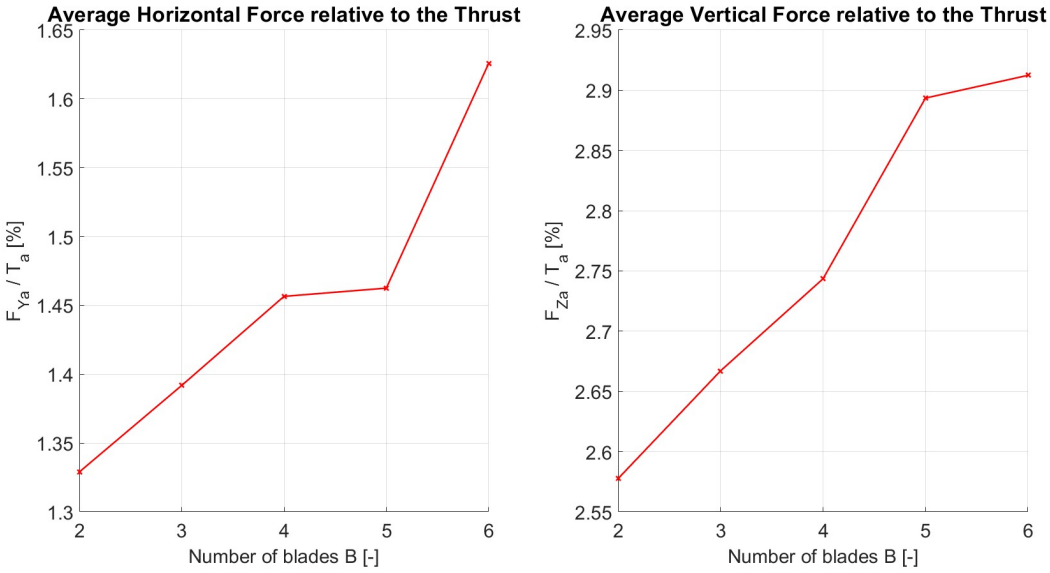


**Figure 9.20:** Ratio between time-averaged in-plane forces and thrust in the installed case at flight condition.

Following the time-averaged performance analysis, the study transitions to examining time-domain performance and its dependence on the number of blades. Figure 9.21 illustrates the variation in thrust produced by propellers with different blade counts, relative to the average thrust over a revolution. The graphs reveal characteristic peaks corresponding to the vertical tail wake impingement. The upper graph in Figure 9.21 shows that the number of peaks corresponds to the blade count, with the frequency of these oscillations

increasing as the blade count rises. The lower graph of Figure 9.21 demonstrates that the amplitude of these oscillations generally decreases with an increasing number of blades, though not in a strictly monotonous fashion—e.g., the amplitude at $B = 4$ is higher than at $B = 3$. This non-monotonic variation might initially suggest that the resolution of the analysis is insufficient to accurately capture the unsteady blade loading. However, as shown in Section 9.1.1, the resolution is adequate to capture even the most abrupt changes in loading, and Figure 9.18 indicates that blade loading variations are nearly identical across different blade counts. Therefore, the non-monotonic behavior of the thrust oscillation amplitudes likely results from how the contributions of individual blades combine as the blade count changes.

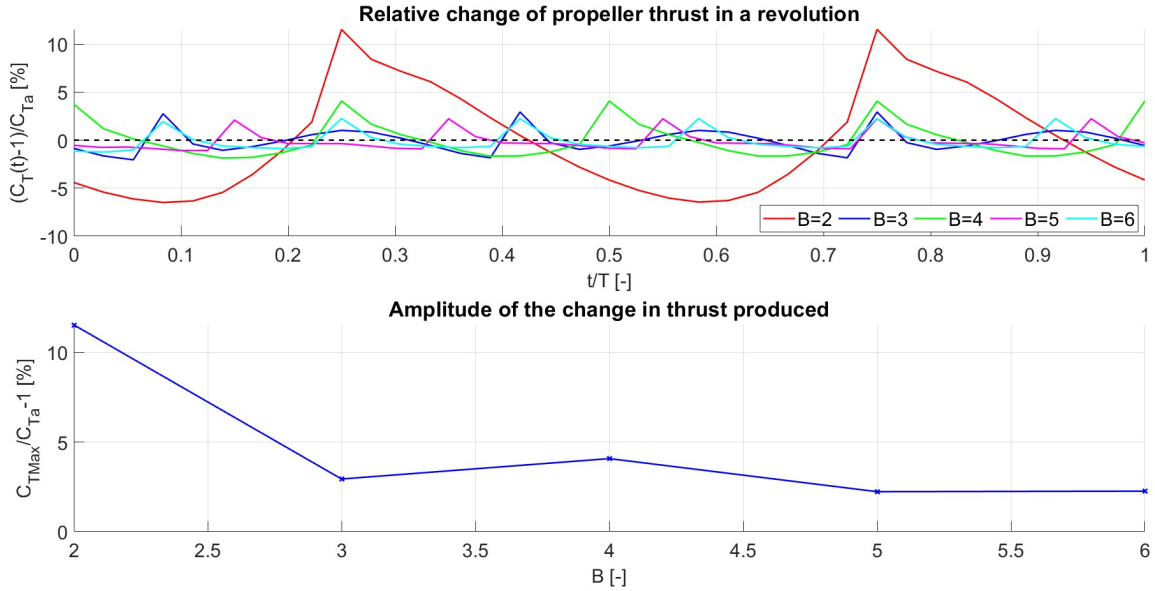


**Figure 9.21:** Change in thrust during a revolution in the installed case at flight condition.

The observed reduction in oscillation amplitude with an increasing number of blades is a recognized phenomenon for various types of non-uniform inflows, such as those experienced by a propeller operating at a non-zero angle of attack [12]. Previous studies, have shown that a higher blade count results in increased interference among oscillations in blade loading, leading to a monotonic reduction in amplitude and a steadier thrust and power output. This effect is particularly noticeable when transitioning from two to three blades. In the context of the more complex flow distortion associated with the BLI configuration, the mechanism for reducing thrust variation amplitude differs slightly.

The inflow variations are more concentrated above the fuselage in a narrow vertical strip and beneath it over a larger area. The narrow region above the fuselage causes abrupt loading increases as a blade passes through it, while the broader area beneath leads to more gradual loading changes, akin to the sinusoidal variations experienced by blades in a propeller operating at a non-zero angle of attack (see Figure 7.6). In cases of more distributed flow distortion, multiple blades are simultaneously affected. However, in the thin, low-speed axial velocity region above the fuselage, only one blade is impacted at a time. As the number of blades increases, the relative impact of the blade passing through the tail wake-affected area diminishes. With the tail wake impingement being a significant factor, this mechanism dominates as the blade count increases, reducing the impact of flow distortion underneath the fuselage. This explains why the oscillation amplitude does not reach zero even with $B = 6$ blades in the BLI configuration.

The unexpectedly larger oscillation amplitude at $B = 4$ in the BLI configuration results from the complex flow distortion characteristics of this installation. When $B = 4$, the thrust increase occurring for a blade above the fuselage is amplified by the thrust increase experienced by the blade passing underneath the fuselage. In contrast, propellers with odd blade numbers do not have blades positioned in a way that simultaneously experiences thrust increases from both wake impingement and the fuselage's non-axisymmetry. This observation is further supported by the fact that the oscillation amplitude at $B = 5$ is slightly lower—about $2\%$ less—compared to $B = 6$.

Figures 9.22 and 9.23 display the variations in in-plane forces for different blade counts during a revolution. Similar to thrust oscillations, the amplitude of in-plane force oscillations decreases with an increasing number of blades, stabilizing at a constant value beyond $B = 4$.
While the vertical component of the in-plane force oscillation stabilizes to nearly zero, the horizontal component does not fall below $0.5\%$ of the thrust. This is because the horizontal force, like the thrust, is significantly influenced by the tail's wake impingement, which induces spikes in the time domain.

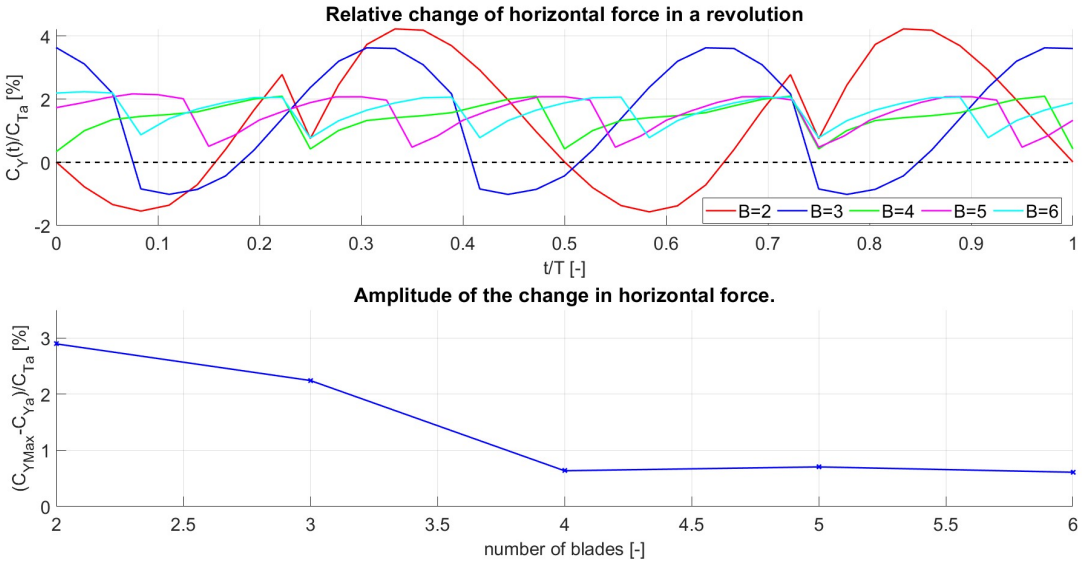


**Figure 9.22:** Change in horizontal force during a revolution in the installed case at flight condition.

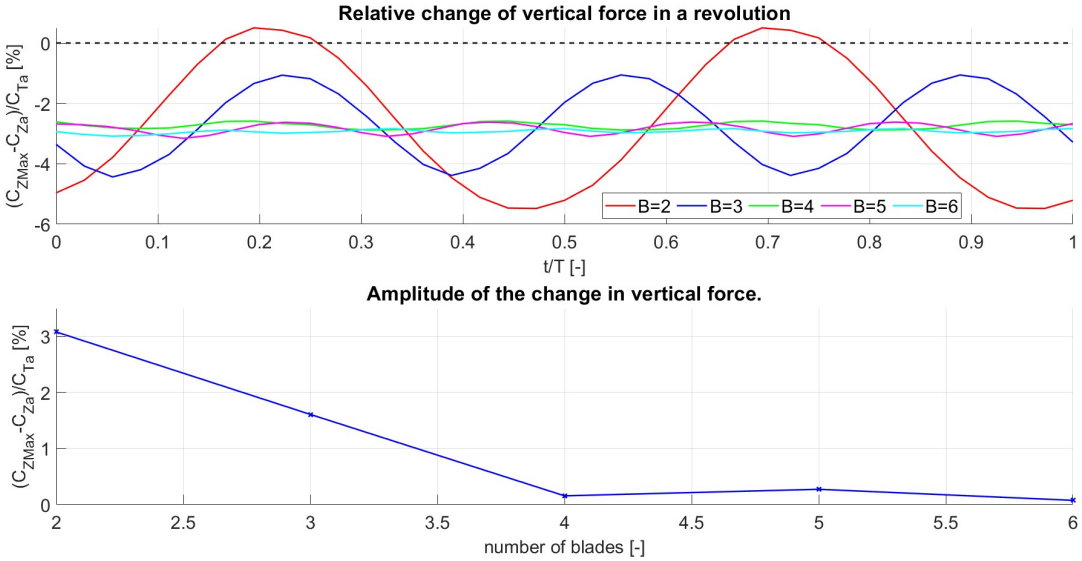


**Figure 9.23:** Change in vertical force during a revolution in the installed case at flight condition.

It is important to address a key aspect concerning the influence of wake impingement. As discussed in Section 2.3.3, the suction effect of the propeller is anticipated to mitigate the velocity deficit in the tail's wake. However, the inflow velocity distribution used in this study was derived from simulations that did not account for this suction effect. Consequently, the impact of the wake on the propeller's performance might be overstated. As a result, the observed peaks and amplitudes of oscillations in thrust and lateral forces could be overestimated.

### 9.2.2. Aero-Acoustic Performance

The analysis of the impact of blade count on noise levels begins with evaluating how different noise sources propagate. Figures 9.24 and 9.25 illustrate the noise levels emitted by isolated and installed propellers with two and six blades.

For isolated propellers, the results reveal that the loading noise source is dominant, primarily consisting of the torque component regardless of blade count. As the blade count increases, the loading noise level decreases significantly, dropping from $SPL_{Max} = 71$ dB to $SPL_{Max} = 32$ dB at the rotational plane when the blade count increases from $B = 2$ to $B = 6$. This trend aligns with the general design principle outlined in Chapter 3, which suggests that noise emissions decrease with a higher number of blades. The six-blade propeller, despite having the highest loading, is the quietest. This reduction in noise is attributed to the decreased efficiency of steady loading noise propagation as the blade count increases. This effect is captured by the Bessel function in the Hanson model, where the efficiency of noise propagation is a function of the Bessel function's order ($n = mB$) and argument. As the number of blades increases, the order of the Bessel function increases, leading to a decrease in the peak output and consequently lower noise propagation efficiency.

When considering the installed propeller, the differences between the noise patterns for two-blade and six-blade configurations become more pronounced. For the six-blade installed propeller, the loading noise is predominantly influenced by the thrust component. This results in characteristic noise patterns with the highest emissions of $SPL_{Max} = 75$ dB directed along the propeller axis ($\theta = 0°$ and $\theta = 180°$). In contrast, for the two-blade installed propeller, the loading noise is dominated by the torque component, with the highest emission of $SPL_{Max} = 74$ dB observed when the observers are aligned with the rotational plane ($\theta = 90°$ and $\theta = 270°$). Although the thrust noise component remains dominant along the propeller axis with a noise emission just $3$ dB lower than for the six-blade configuration, the maximum noise levels are still higher in the plane of rotation for the two-blade propeller.

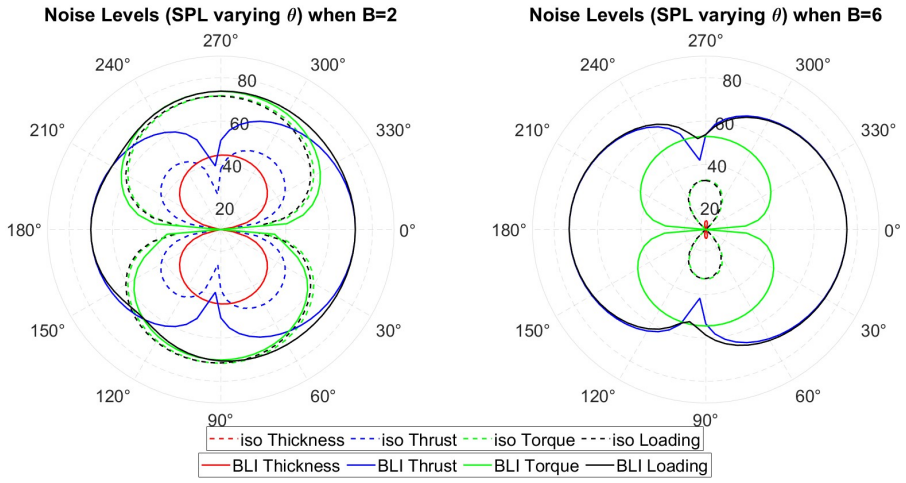


**Figure 9.24:** Directivity plots of the noise sources in the plane along the propeller axis. Left: results from the 2-blade propeller ($B = 2$). Right: results from the 6-blade propeller ($B = 6$).

Examining the difference in noise emissions between installed and isolated propellers with varying blade counts reveals notable trends. For a two-blade configuration ($B = 2$), the maximum noise emissions increase by approximately $\Delta SPL_{Max} = 3$ dB in the same direction. In contrast, for a six-blade configuration ($B = 6$), the increase in maximum noise level is significantly larger, $\Delta SPL_{Max} = 43$ dB, and the direction of maximum emission shifts to being orthogonal between the isolated and installed cases.

This disparity is attributed to the differing efficiencies of noise propagation for steady and unsteady loading components. For $B = 2$, the efficiency of propagation for steady loading noise components is notably high, leading to dominant torque noise components that propagate in the same direction as the steady loading noise. Conversely, the efficiency of propagation for unsteady loading noise decreases with fewer blades, resulting in lower noise emissions in the direction of the propeller axis for $B = 2$ compared to

$B = 6$. This indicates that for $B = 2$, the increase in steady loading noise is more pronounced, producing a noise pattern that resembles the directivity of isolated propellers.
Figure 9.25 illustrates the noise patterns within the rotational plane, where the efficiency of propagation for steady loading noise sources is maximized. The comparison between isolated and installed noise patterns highlights a larger contribution from steady loading noise sources with $B = 2$ compared to $B = 6$. Specifically, for $B = 2$, the noise patterns in installed conditions exhibit minimal circumferential variations, closely resembling the circular shape typical of isolated conditions where noise levels are more uniform.

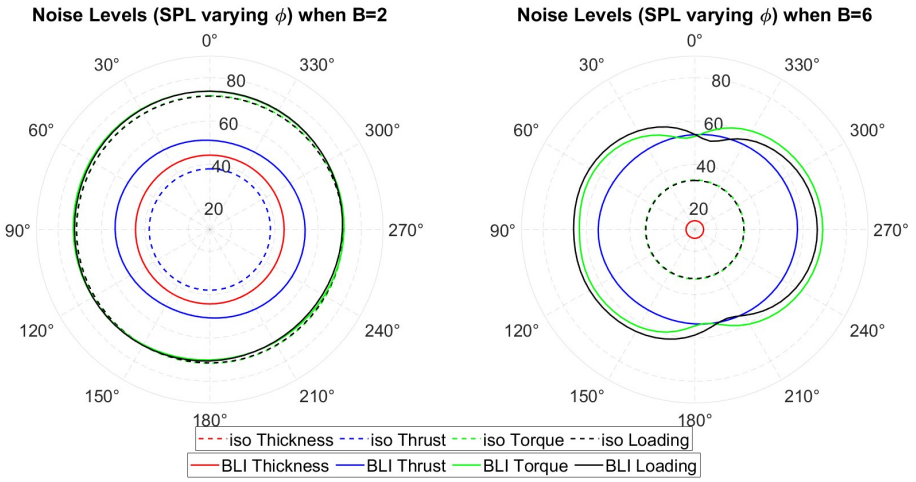


**Figure 9.25:** Directivity plots of the noise sources in the propeller rotational plane. Left: results from the 2-blade propeller ($B = 2$). Right: results from the 6-blade propeller ($B = 6$).

The variation of the propagation efficiency of the unsteady loading noise emissions can be explained by analyzing the spinning mode tip Mach number ($M_s$) and how it changes with the blade count. Figure 9.26 illustrates the trend of $M_s$ as a function of the loading harmonics $k$ for the first noise harmonic ($m = 1$) under cruise conditions with a tip Mach number of $M_t = 0.205$ for different blade counts.

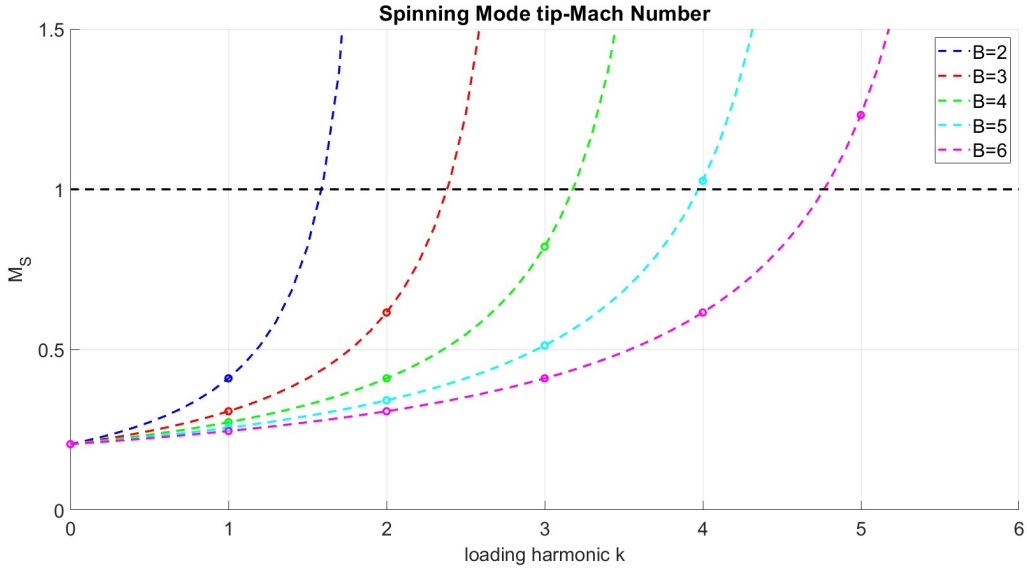


**Figure 9.26:** The spinning mode tip Mach number ($M_s$) of the first harmonic as a function of the loading harmonic $k$ for varying blade counts ($B$).

Similar to the impact of increasing the tip Mach number, reducing the blade count accelerates the growth rate of the spinning mode tip Mach number ($M_s$) as the loading harmonic $k$ increases, leading to distinct effects on noise propagation. First, at a given noise harmonic $m$, a lower blade count $B$ reduces the number of unsteady loading contributions that can effectively propagate, as contributions from loading harmonics exceeding $k = m \times B$ are cut off. Consequently, higher loading harmonic contributions are forced to propagate at higher noise harmonics, which generally exhibit lower propagation efficiency. Second, the remaining loading contributions that do propagate at a specific noise harmonic $m$ tend to have lower $M_s$ values when the blade count is reduced. For instance, when $m = 1$ and the blade count is $B = 2$, only the $k = 1$ harmonic achieves a spinning tip Mach number $M_s \approx 0.4$, which is significantly below unity. In contrast, with a blade count of $B = 6$, the $k = 4$ harmonic reaches $M_s \approx 0.6$, and the $k = 5$ harmonic attains $M_s \approx 1.2$, bringing them closer to the optimal $M_s \approx 1$, where noise propagation efficiency is maximized. Given that noise propagation efficiency peaks near $M_s \approx 1$, the unsteady loading noise contributions are less efficiently propagated when the blade count is low. Consequently, with $B = 2$, the efficiency of noise propagation for unsteady sources is lower compared to $B = 6$, where the higher blade count enhances the propagation efficiency, leading to greater noise emissions along the propeller axis. This underscores the significant influence of blade count on the balance between steady and unsteady noise sources in determining the overall noise emission characteristics.

Figure 9.27 presents the directivity plots of the total noise for propellers with varying blade counts under isolated conditions. The overall shape of these plots remains consistent across different blade counts, primarily because the torque loading noise source remains dominant in each case. As the blade count increases, the thrust steadily rises, yet the noise levels simultaneously decrease. Consequently, the Thrust Specific Sound Pressure (TSSP) progressively diminishes with the increase in blade count.

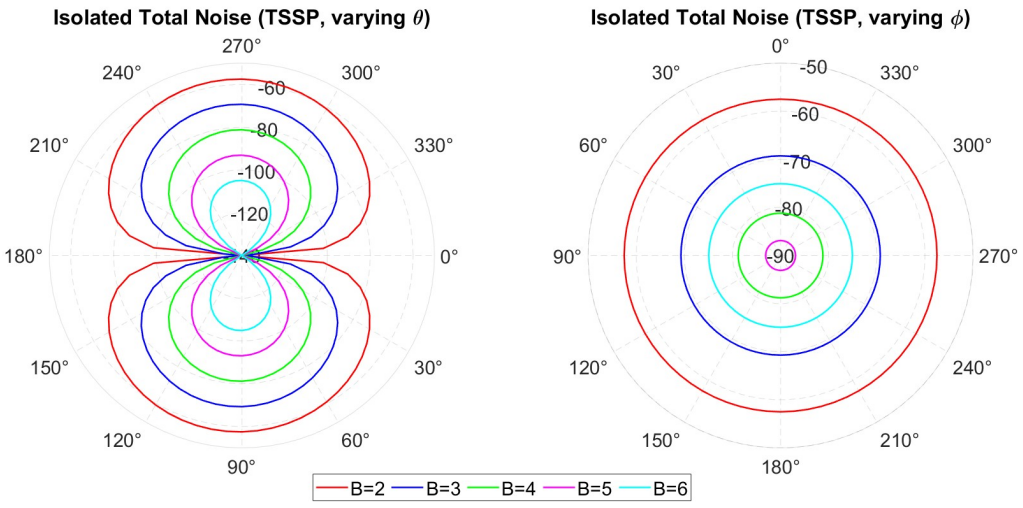


**Figure 9.27:** Directivity plots of the total noise emissions for different number of blades in the isolated case.

The directivity plots in Figure 9.24, along with the analysis of spinning tip Mach number and blade count effects, indicate that the relative significance of unsteady loading noise sources increases as the blade count rises. With a lower number of blades, the steady loading noise sources propagate more efficiently, making the torque component the dominant factor in noise emissions. However, as the blade count increases, the propagation efficiency of the steady loading noise sources diminishes, while that of the unsteady noise sources improves. This shift is evident in Figure 9.28, which illustrates that this transition in noise dominance occurs progressively. Ultimately, with a higher blade count, the thrust noise component overtakes and becomes the predominant source of noise.

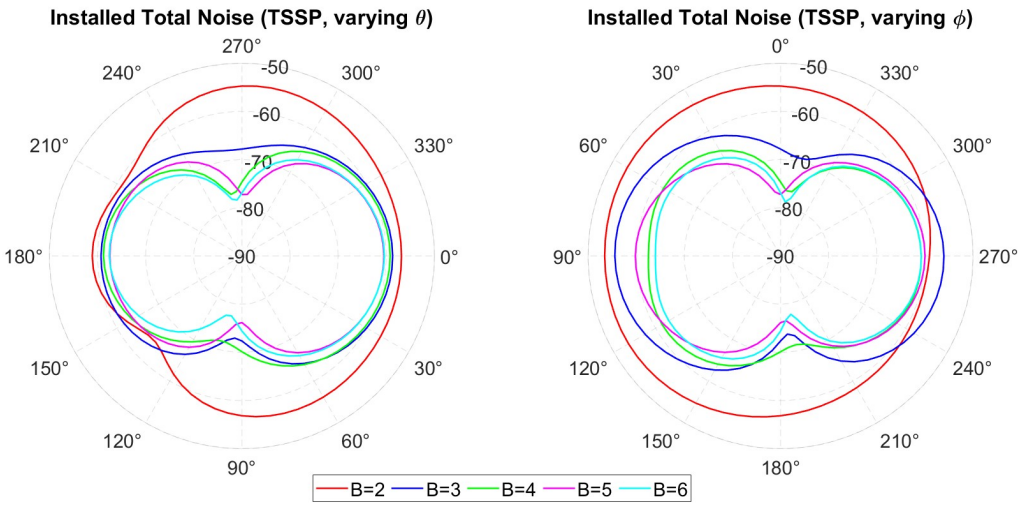


**Figure 9.28:** Directivity plots of noise emissions for different blade counts in the installed case.

Figure 9.29 provides a clear overview of how the maximum Total Sound Pressure Level (TSSP) varies with blade count. For isolated propellers, the noise levels decrease consistently and nearly linearly as the blade count increases, with TSSP values dropping from around $-54$ dB to $-104$ dB. However, the trend is different for installed propellers. When the blade count is low and the steady loading noise source—primarily the torque component—is dominant, a noticeable reduction in TSSP is observed, decreasing from approximately $-52$ dB to $-60$ dB as the blade count increases. Beyond four blades, however, the unsteady loading noise source, particularly the thrust component, becomes increasingly dominant. This dominance causes the TSSP to stabilize around $-60$ dB, indicating that the increase in thrust is insufficient to offset the corresponding rise in noise levels. Consequently, the reduction in noise that accompanies an increase in blade count for isolated propellers does not translate as effectively to installed configurations with higher blade counts.

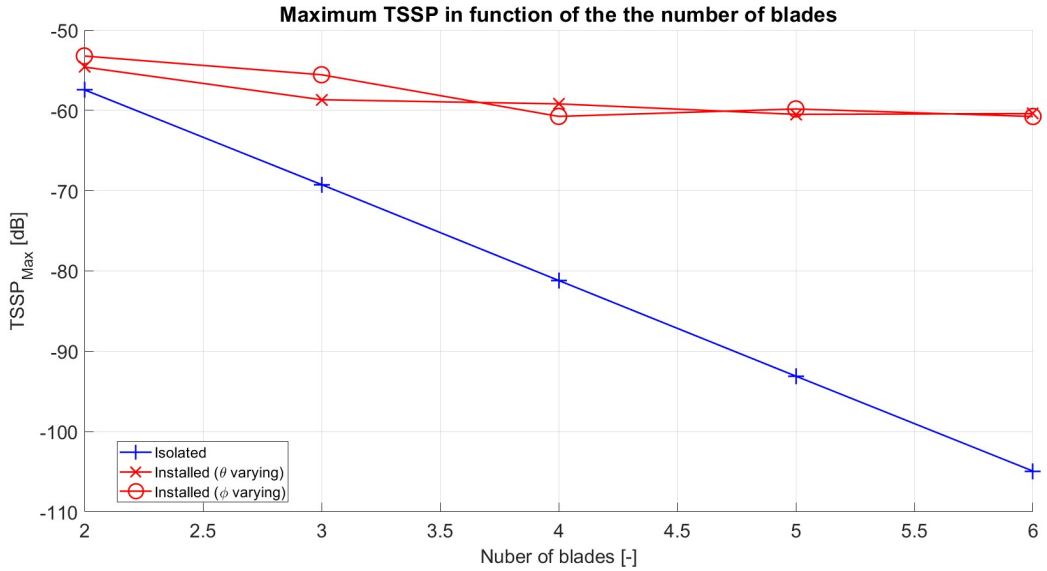


**Figure 9.29:** Variation of the maximum TSSP noise emissions in function of the number of blades at cruise conditions.

Given that the three-blade propeller in this analysis operates under the same flight velocity and advance ratio as the three-blade propeller subjected to non-zero angle of attack inflow in Chapter 7, we can make a near-direct comparison of noise emissions between the two configurations. However, it is important to note that the baseline propeller X1 used in this study features a larger hub-to-tip ratio compared to the XPROP-S propeller utilized in the angle-of-attack study. As a result, the loading distribution and thrust output of the X1 propeller are expected to exhibit slight differences from those of the XPROP-S propeller. Figure 9.30 presents the directivity plots of the three-blade propellers in both isolated and installed conditions.

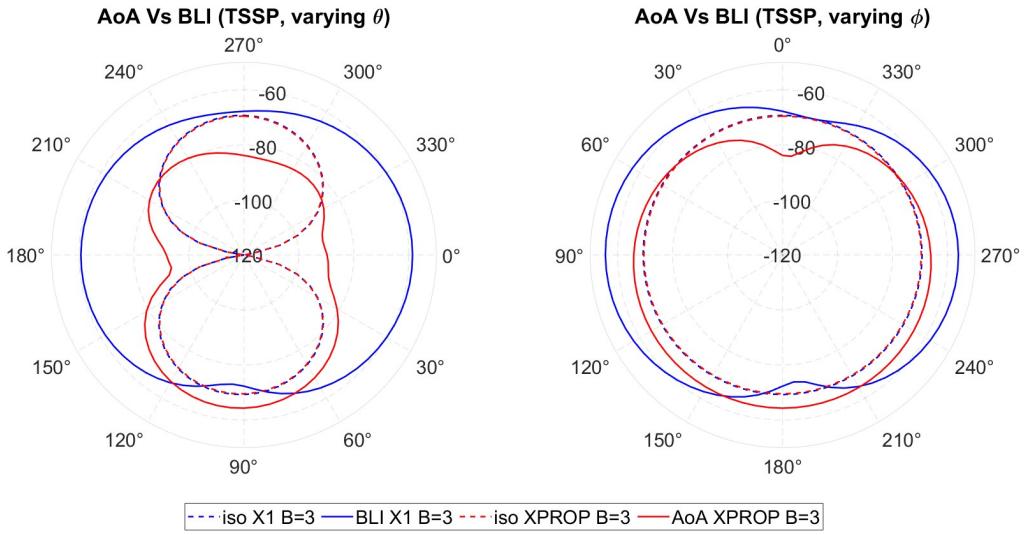


**Figure 9.30:** Directivity plots of the 3-bladed XPROP-S and X1 propellers in isolated and installed conditions.

The TSSP noise levels of the isolated three-blade versions of the XPROP and X1 propellers are nearly identical, indicating that the geometric differences between the two designs have a minimal impact once the results are normalized by thrust. However, when comparing the propeller in the Boundary Layer Ingestion (BLI) configuration to the one operating at a non-zero angle of attack, a noticeable increase in noise is observed. The maximum TSSP for the BLI configuration is approximately $-56$ dB, compared to $-64$ dB for the angle of attack case.

The directivity plots further highlight significant differences in noise patterns between the two configurations. In the angle of attack case, the noise emissions are predominantly concentrated in the propeller plane, indicating the dominance of the steady loading noise source. Conversely, in the BLI configuration, the largest noise emissions occur along the propeller axis, where the unsteady loading noise sources have the greatest impact.

Since both configurations share the same tip Mach number ($M_t$) and blade count ($B$), the differences in noise emissions can be attributed primarily to the distinct unsteady blade loading patterns associated with each inflow condition. The loading variation in the angle of attack scenario is characterized by broad, gradual oscillations, leading to a more predictable noise pattern. In contrast, the BLI configuration experiences more abrupt changes in blade loading, resulting in a noisier environment, particularly in the direction of the propeller axis.

This observation is supported by the frequency analysis shown in Figure 9.31. The angle of attack case exhibits a higher amplitude at the first loading harmonic ($k = 1$), but this amplitude diminishes sharply for higher harmonics. In the BLI configuration, however, the loading signal retains significant contributions even at higher harmonics, which are responsible for the increased noise emissions along the propeller axis. This indicates that the more complex unsteady loading, characterized by abrupt changes when the blades pass behind the vertical tail in the BLI installation, leads to greater noise levels, especially in the axial direction.

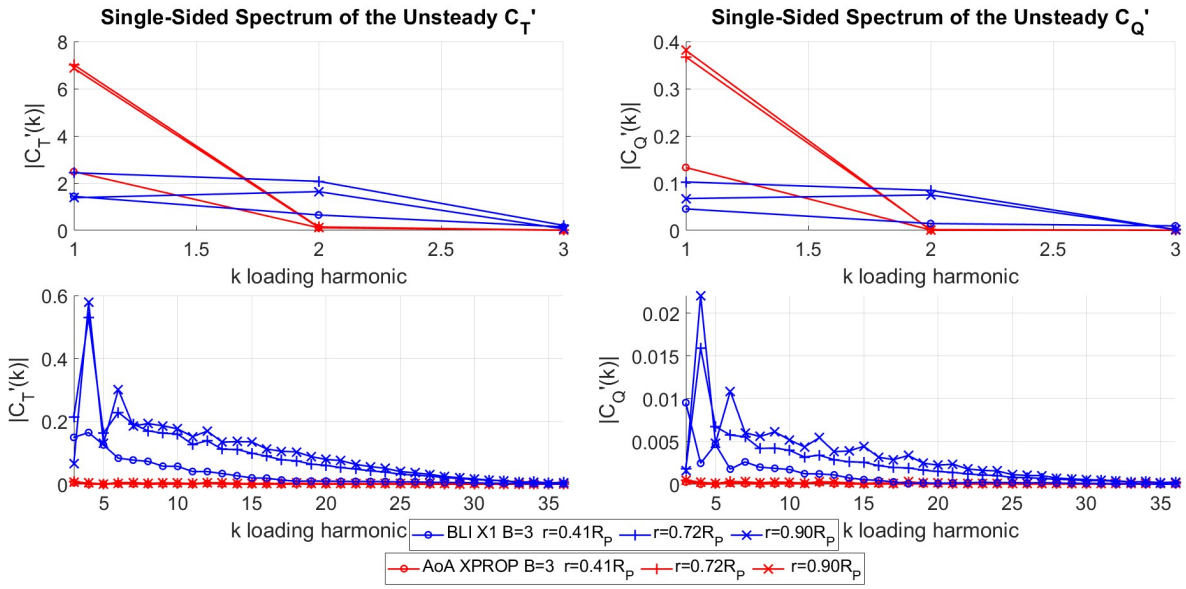


**Figure 9.31:** Single-sided Spectrum of the unsteady.

In summary, as the number of blades increases, overall disk loading rises due to the absence of a specific thrust requirement in the parametric study. This results in increased forces and power absorption by the propeller, leading to a reduction in propeller efficiency in both isolated and installed configurations. While in-plane forces generated by installed propellers scale with thrust, they remain around $1-2\%$ of the thrust for the horizontal component and about $2-3\%$ for the vertical component. These forces, while significant, are unlikely to present insurmountable challenges for control and stability but should be carefully considered during the design phase, especially for planes powered by BLI propellers with high thrust output.

The performance of installed propellers is notably influenced by blade count, with oscillations arising from inflow distortion. These oscillations are characterized by peaks at the blade passage frequency, with their amplitude decreasing as blade count increases. However, this reduction is non-linear due to complex flow distortions. Even with a high blade count ($B \geq 5$), thrust oscillation amplitudes do not fall below $2\%$ of the average thrust. Designers should anticipate vibrations from these loading changes at the blade passage frequency (BPF) and aim for a steadier performance output. To achieve reduced oscillation amplitudes, a blade count of at least $B = 5$ is recommended.

Regarding noise levels, increasing blade count generally reduces the propagation efficiency of steady noise emissions, thereby lowering noise levels. This approach is effective for isolated propellers or installations where steady noise sources are dominant. In the analysis of isolated propellers, increasing the blade count from two to six blades resulted in a noise reduction of about $39dB$, despite higher disk loading. However, in installed configurations like BLI, where unsteady loading is significant, increasing the blade count primarily reduces steady loading noise contributions while enhancing the propagation efficiency of unsteady noise components. Consequently, the unsteady loading component, particularly the thrust component, becomes dominant, altering the directivity plots. Beyond B = 2, the increase in unsteady noise sources outweighs the reduction in steady noise, causing the maximum total noise level to rise with more blades. Therefore, increasing blade count may not effectively reduce noise levels for propellers in a BLI configuration.

Two clarifications are necessary before applying these results to practical applications, such as the APPU plane. First, the propeller suction effect has not been considered, potentially leading to an overestimation of the impact of the tail's wake impingement. Second, the noise levels obtained are based on simulations with a spinning tip Mach number ($M_t = 0.206$), which is lower than what would be expected in realistic flight conditions. Higher tip Mach numbers will increase the contribution from steady noise sources, making the strategy of increasing blade count more effective at higher freestream Mach numbers.

## 9.3. Impact of the sweep distribution

The final geometric characteristic of interest in this study is the blade sweep distribution. As discussed in Chapter 3, incorporating sweep into blade geometries can effectively reduce noise levels by introducing a delay in noise emissions. This delay reduces overall noise as demonstrated in Figure 3.5. The effectiveness of sweep depends on how the geometric displacements compare to the wavelengths of the dominant noise contributions, which vary with operating conditions. Given that geometric displacement is limited, sweep has a more substantial impact on noise contributions with shorter wavelengths. This section explores the effects of varying sweep distributions on blade loading and aero-acoustic performance for both isolated and installed propellers.

In this study, the radial distribution of sweep is parameterized using the mid-chord alignment (MCA), as illustrated in Figure 4.2. The sweep is defined by two parameters: $\Lambda$ and $\lambda_2$, detailed in Chapter 8. The parameter $\Lambda$ represents the MCA at the tip, with increasing values indicating more backward sweep, as shown in Figure 8.5. The parameter $\lambda_2$ represents the forward sweep angle at the hub. When $\lambda_2 = 0°$, the blade exhibits only backward sweep; as $\lambda_2$ increases, the blade has a forward lean in the inboard section, as depicted in Figure 8.6.

### 9.3.1. Aerodynamic Performance

The initial analysis focuses on the blade loading distribution along the blade span for propellers with different sweep distributions. Four configurations are considered, including the baseline propeller with straight blades. Figure 9.32 presents the distributions of sectional angle of attack, lift coefficient, and thrust coefficient along the blade span for these configurations.

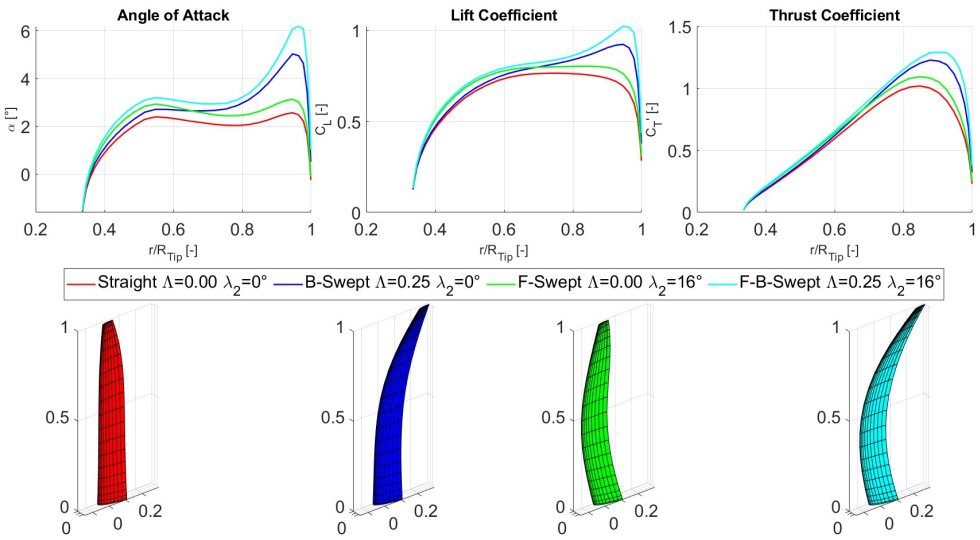


**Figure 9.32:** Comparison of sectional angle of attack, lift coefficient, and thrust coefficient distributions along the blade span for propellers with different sweep distributions in the isolated case at cruise conditions.

The results indicate that sweeping the blade generally leads to an increase in the angle of attack. Specifically, an increase in the forward sweep angle at the hub ($\lambda_2$) results in a greater increment in angle of attack in the inboard section of the blade. Conversely, an increase in the mid-chord alignment (MCA) at the tip ($\Lambda$) leads to a larger sweep angle at the tip, which in turn raises the increment in local angle of attack there. The most significant increase in the angle of attack occurs near the tip when both forward and backward sweeps are maximized ($\Lambda = 0.25$ and $\lambda_2 = 16°$), resulting in the highest sweep angle at the tip.

This increase in the local angle of attack at the tip is accompanied by a corresponding rise in the lift coefficient ($C_L$). Consequently, the increase in the lift coefficient leads to higher blade loading, as evidenced by the radial distribution of the thrust coefficient.

For all sweep configurations, the change in loading distribution is not uniform along the blade span. Instead, there is a noticeable shift in loading towards the outboard sections of the blade. This shift is more pronounced with a larger sweep angle at the tip. This phenomenon occurs because lift is the product of

the local lift coefficient and dynamic pressure. Given that the inflow velocity is greater at the blade tips due to rotation, the increase in loading is more significant at these outboard sections, resulting in a higher overall thrust distribution towards the blade tips.

The increase in blade loading observed with sweep application is also evident in the installed configuration. Figure 9.33 illustrates the differences in angle of attack, lift coefficient, and thrust coefficient distributions along the disk between the propeller with swept blades ($\Lambda = 0.25$, $\lambda_2 = 16°$) and the baseline propeller with straight blades in the BLI configuration.

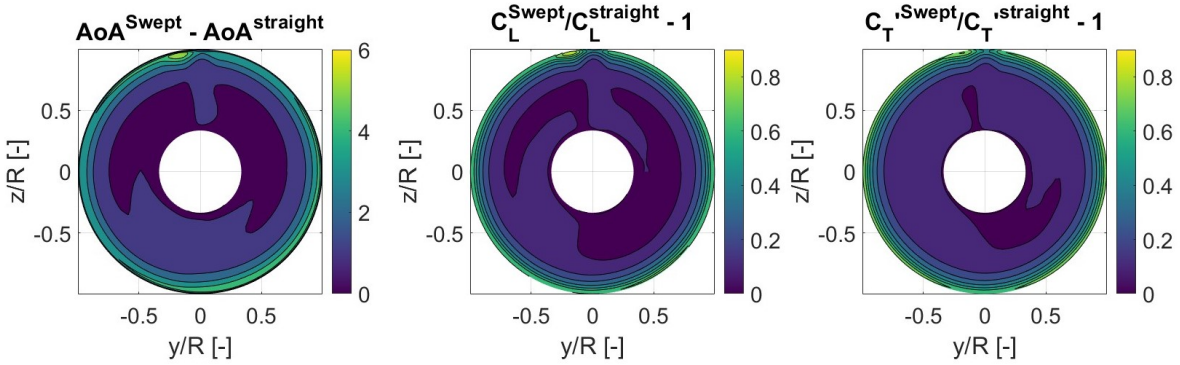


**Figure 9.33:** Comparison of sectional angle of attack and lift coefficient distributions along the blade span for propellers with swept blades ($\Lambda = 0.25$, $\lambda_2 = 16°$) and straight blades in the installed case at cruise conditions.

Figure 9.34 compares the sectional thrust coefficient across the propeller disk for installed propellers with swept blades ($\Lambda = 0.25$, $\lambda_2 = 16°$) and straight blades.

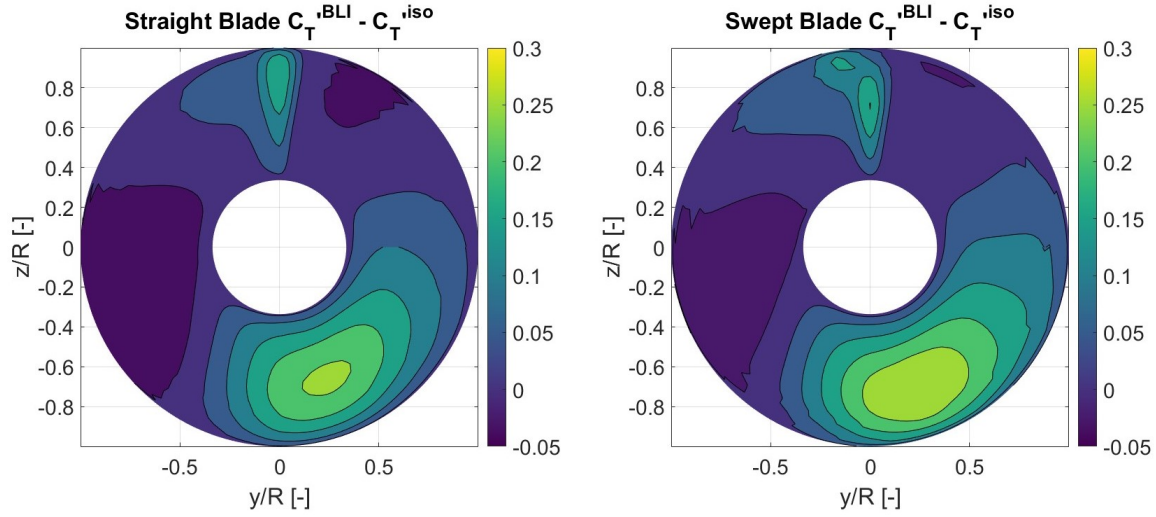


**Figure 9.34:** Comparison of sectional thrust coefficient distributions along the blade span for propellers with swept blades ($\Lambda = 0.25$, $\lambda_2 = 16°$) and straight blades in the installed case at cruise conditions.

The impact of blade sweep on thrust variations is evident in the observed differences between backward-swept and forward-swept blades. The thrust variations across the disk are similar in both cases and

are primarily governed by the inflow characteristics described earlier. However, the backward sweep introduces a noticeable delay in the interaction of the outboard blade sections with the propeller disk compared to the inboard sections. This delay results in a more gradual and spread-out variation in thrust due to wake impingement, which reduces the axial velocity in a thin vertical region of the disk.
For straight blades, all sections of the blade experience the wake impingement simultaneously, leading to a uniform response in thrust variations. In contrast, with backward-swept blades, the interaction with the tail's wake is staggered. The outer blade sections encounter the wake after the inboard sections have already moved, resulting in a delayed maximum variation at the tip and a more distributed change in the circumferential direction. This staggered interaction also leads to more progressive oscillations in loading under the fuselage, indicating that the application of sweep affects not only acoustic performance but also the phasing of unsteady loading.
Figure 9.35 illustrates these effects by showing the blade thrust coefficient as a function of azimuthal position for a reference propeller with straight blades and two propellers with different sweeps: one with forward-swept blades and one with backward-swept blades. In the case of backward sweep, the peak in loading due to wake impingement is both delayed and reduced, while forward-swept blades exhibit increased peak loading due to wake impingement compared to the straight blade of the baseline. This shift in loading characteristics underscores how sweep affects both the timing and magnitude of thrust variations, introducing a change in phase of the unsteady loading contributions from the blade sections along the blade span.

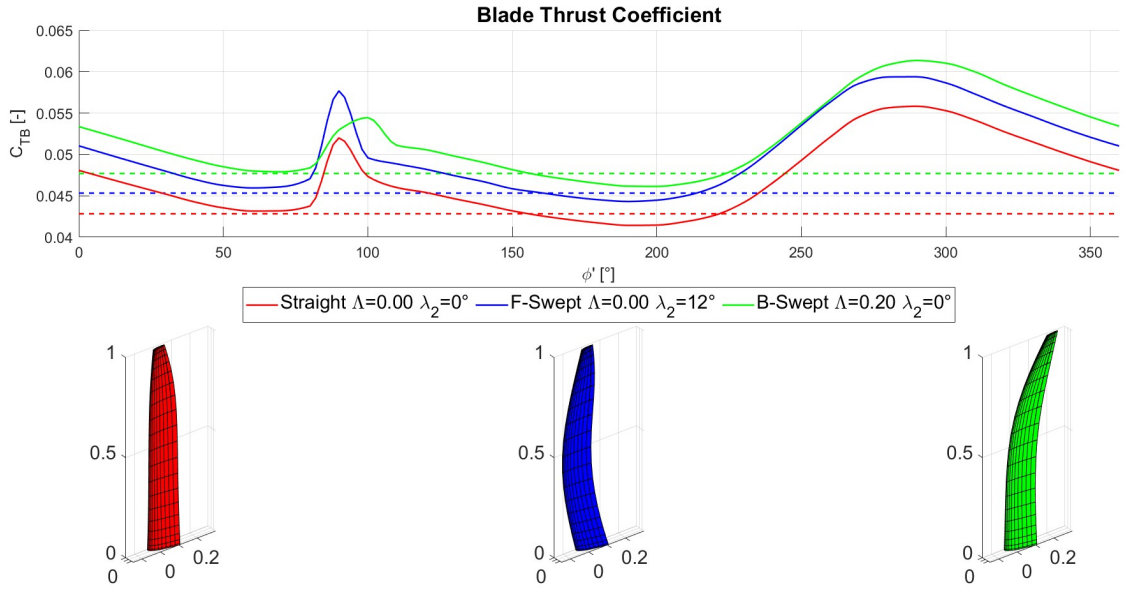


**Figure 9.35:** Comparison of blade thrust coefficient distributions along the blade azimuth coordinate for the straight blade, the backward swept blade ($\Lambda = 0.20$, $\lambda_2 = 0°$) and for the backward swept blade ($\Lambda = 0.00$, $\lambda_2 = 16°$) in the installed case at cruise conditions.

Figure 9.36 displays the Root Mean Square (RMS) values of the blade thrust coefficient changes ($C_{TB}$) for propellers in installed versus isolated conditions. This analysis reveals a clear trend: the RMS value increases with a larger forward sweep angle at the hub.
Among the different blade configurations, the forward-swept blade geometry exhibits the highest RMS value of $6.8 \times 10^{-3}$, indicating the most significant amplitude of loading oscillations. In comparison, the straight blades and backward-swept blades show lower RMS values of $6.1 \times 10^{-3}$ and $6.3 \times 10^{-3}$, respectively.
This increase in RMS for the forward-swept blades is consistent with the observed data in Figure 9.35, where the forward sweep leads to larger amplitude variations in the loading signal. The forward sweep angle accentuates the amplitude of oscillations, explaining the higher RMS value compared to the straight and backward-swept configurations.

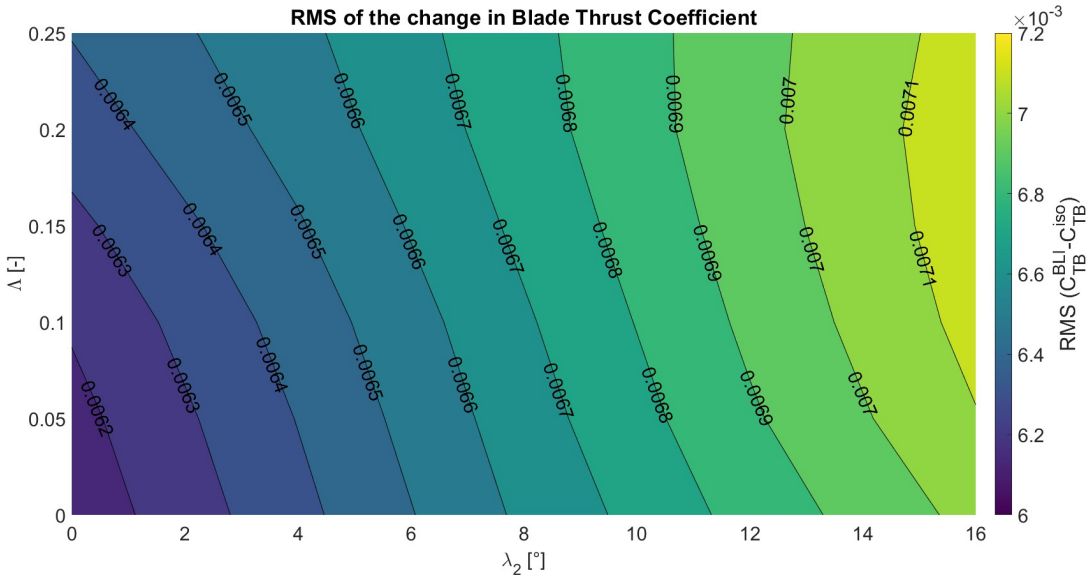


**Figure 9.36:** Root Mean Square (RMS) of the change in Blade Thrust Coefficient between isolated and installed conditions. The sweep distribution is a function of the MCA at the tip ($\Lambda$) and the forward sweep angle at the hub ($\lambda_2$).

Figure 9.37 illustrates the aerodynamic performance of isolated propellers with various sweep configurations compared to the baseline propeller with straight blades. The figure plots the thrust and power coefficients as well as the thrust-to-power ratio as functions of the sweep parameters $\Lambda$ (tip sweep) and $\lambda_2$ (hub sweep). The observed trends align with the increased loading distributions shown in Figures 9.32 and 9.34. Both thrust and power coefficients rise with increasing sweep angles. Specifically, the thrust coefficient increases by approximately $20\%$ and the power coefficient by about $18\%$ when both sweep parameters are maximized. Despite these increases, the thrust-to-power ratio shows a modest improvement of around $2\%$, as the greater thrust increment outpaces the power increment

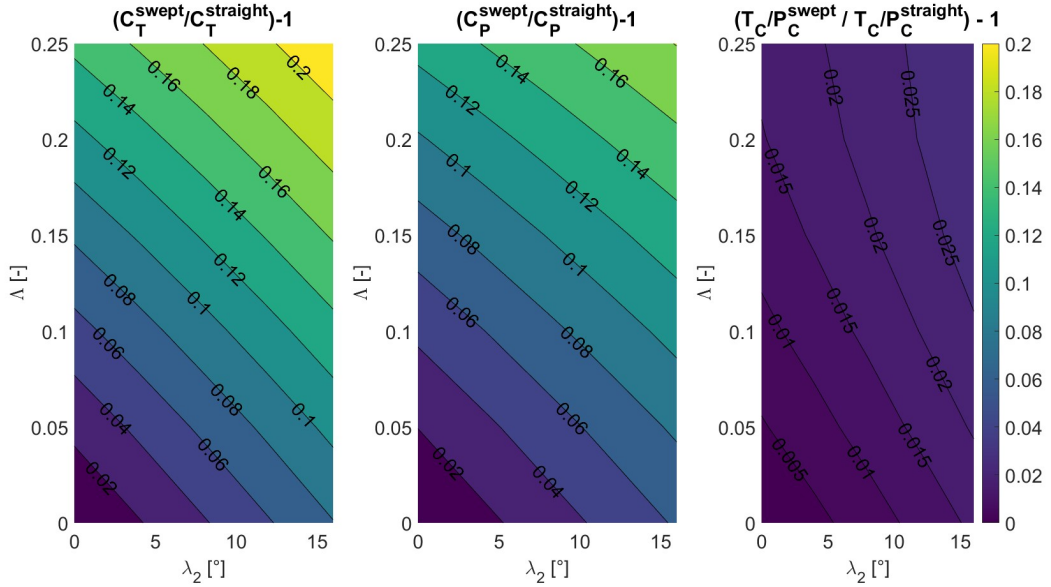


**Figure 9.37:** Difference in aerodynamic performance between the propellers with swept blades and the baseline with straight blades in isolated conditions at cruise. The sweep distribution is a function of the MCA at the tip ($\Lambda$) and the forward sweep angle at the hub ($\lambda_2$).

Table 9.4 presents the performance metrics of both the original propeller with straight blades and the propeller with the most effective swept blade configuration.

| Type of blade | $C_T$ | $C_P$ | $T_C/P_C$ |
|---|---|---|---|
| Straight blade($\Lambda = 0$,$\lambda_2 = 0°$) | 0.2569 | 0.5671 | 0.8156 |
| Swept blade ($\Lambda = 0.25$,$\lambda_2 = 16°$) | 0.3123 | 0.6695 | 0.8396 |

**Table 9.4:** Aerodynamic performance of the propeller with straight blades and the propeller with the most swept blades in isolated conditions.

The results discussed previously are based on propellers evaluated in isolated conditions. Figure 9.38 shows the aerodynamic performance metrics for propellers with swept blades in installed conditions, mirroring the pattern observed in isolated conditions. Both forward and backward sweeps contribute to performance enhancements.
Table 9.5 provides the aerodynamic performance metrics for the installed configuration, similar to those presented in Table 9.4. The comparison reveals that the performance improvements with swept blades are comparable to those observed in isolated simulations. Specifically, an efficiency improvement of around 2% is achievable in the installed configuration as well, indicating that the benefits of sweep are consistent across both isolated and installed conditions.

| Type of blade | $C_T$ | $C_P$ | $T_C/P_C$ |
|---|---|---|---|
| Straight blade($\Lambda = 0$,$\lambda_2 = 0°$) | 0.2820 | 0.5934 | 0.8554 |
| Swept blade ($\Lambda = 0.25$,$\lambda_2 = 16°$) | 0.3430 | 0.7049 | 0.8759 |

**Table 9.5:** Aerodynamic performance of the propeller with straight blades and the propeller with the most effective swept blades in installed conditions.

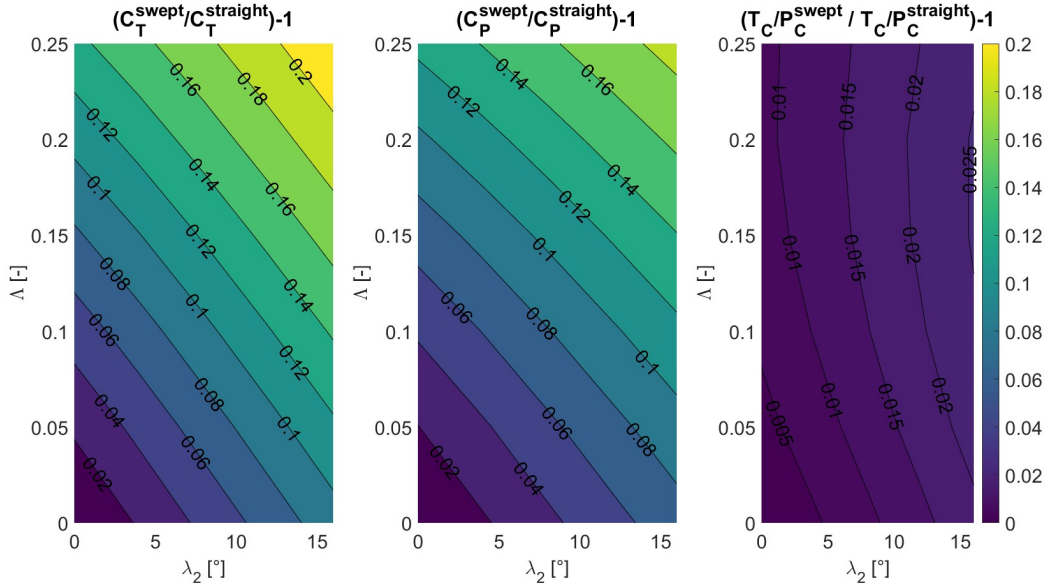


**Figure 9.38:** Difference in aerodynamic performance between the propellers with swept blades and the baseline with straight blades in installed conditions at cruise. The sweep distribution is function of the MCA at the tip ($\Lambda$) and the forward sweep angle at the hub $\lambda_2$.

### 9.3.2. Aero-Acoustic Performance

The impact of sweep distribution on noise emissions is twofold: it alters blade loading and introduces a phase delay between noise sources along the blade span. This phase delay, modeled by the phase angle $\phi_s$ in Hanson's Helicoidal Surface Theory (refer to Chapter 6), plays a crucial role in noise reduction. The effectiveness of sweep in reducing noise levels increases with the phase angle, which is larger for faster-rotating propellers due to the reduced wavelength of noise emissions at higher rotational speeds, as discussed in [2].

To assess these effects, the analysis starts with the maximum sound pressure level (SPL) for isolated propellers with different sweep distributions. Figure 9.39 illustrates the difference in maximum SPL between propellers with swept blades and the baseline with straight blades. The figure includes two graphs: the left graph reflects the combined effects of phase cancellation and changes in loading distribution, while the right graph isolates the impact of loading changes by setting the phase shift due to sweep ($\phi_s$) to zero.

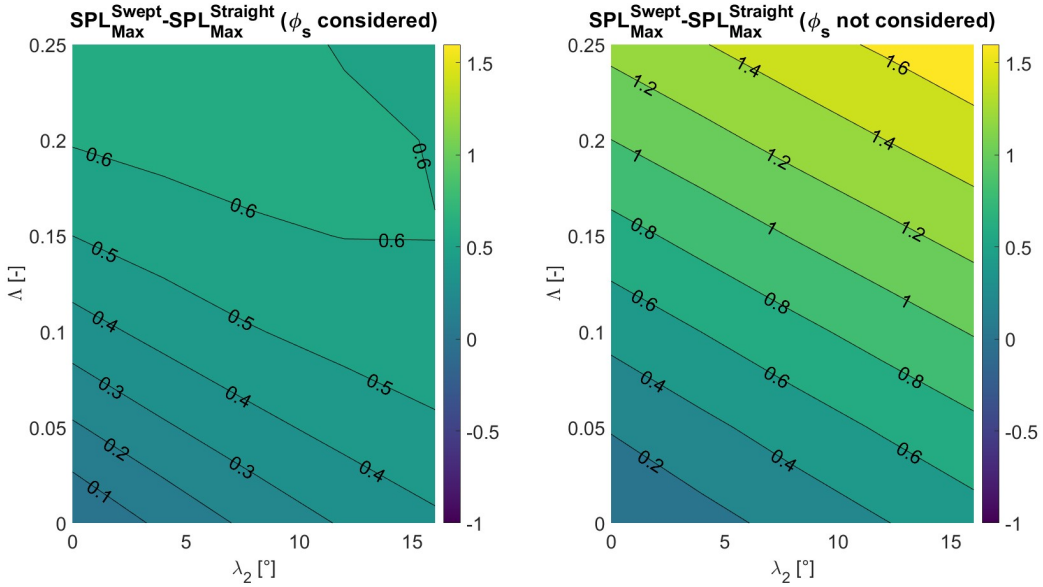


**Figure 9.39:** Difference in maximum noise emissions (SPL) between propellers adopting a sweep distribution function of the MCA at the tip ($\Lambda$) and the forward sweep angle at the hub ($\lambda_2$) in isolated conditions at cruise condition. On the left, the noise emissions with the inclusion of the phase shift due to sweep $\phi_s$. On the right, the noise emissions without the inclusion of the phase shift.

The analysis reveals that the application of sweep to propeller blades generally results in an increase in sound pressure level (SPL). As shown in the left graph of Figure 9.39, the SPL increases with sweep, with a maximum increase of $\Delta SPL_{Max} = +0.7dB$. When phase shift effects due to sweep are not considered, the noise levels rise even further, reaching up to $\Delta SPL_{Max} = +1.5dB$. This trend aligns with the observed increases in thrust and power as shown in Figure 9.37. The largest noise increment occurs with maximum forward sweep at the hub ($\lambda_2 = 16°$) and maximum backward sweep at the tip ($\Lambda = 0.25$), corresponding to the highest loading increment at the blade tip.

The detrimental impact of loading distribution changes caused by sweep outweighs the noise reduction benefits from phase shift, leading to an overall increase in noise levels. This is consistent with the findings in Chapter 3, where modern low-noise propellers aim to reduce tip loading to minimize noise. The shift in loading to the outboard due to sweep results in increased noise levels, counteracting any potential noise reduction from phase cancellation.

The effectiveness of the phase shift in reducing noise is diminished due to the low rotational speed of $M_t = 0.206$. At such low speeds, the noise wavelength is significantly larger than the geometric displacement caused by sweep, leading to a minimal phase delay between radial sections. As a result, the potential for noise reduction through phase shift is limited. At higher rotational speeds, where the spinning tip Mach number increases, the noise wavelength shortens, making phase shift more effective in reducing noise levels despite the loading distribution changes.

Figure 9.40 highlights the differences in maximum thrust specific sound pressure (TSSP) levels between swept and straight blade propellers. Normalizing the sound pressure level by the thrust shows that, when phase shift effects are not considered, the maximum TSSP remains nearly unchanged ($\Delta TSSP_{Max} < +0.1dB$) across different sweep configurations. This normalization illustrates how increased loading—and thus thrust—compensates for the increased noise emissions due to changes in blade loading.
In contrast, considering phase shift effects, the TSSP shows a reduction in noise levels. As illustrated in the right graph of Figure 9.40, applying both forward and backward sweep leads to a decrease in TSSP, with a minimum reduction of $\Delta TSSP_{Max} = -1.1dB$ occurring at $\Lambda = 0.25$ and $\lambda_2 = 16°$. This corresponds to the propeller configuration with the highest phase shift between radial sections, effectively reducing noise emissions despite the increased loading.

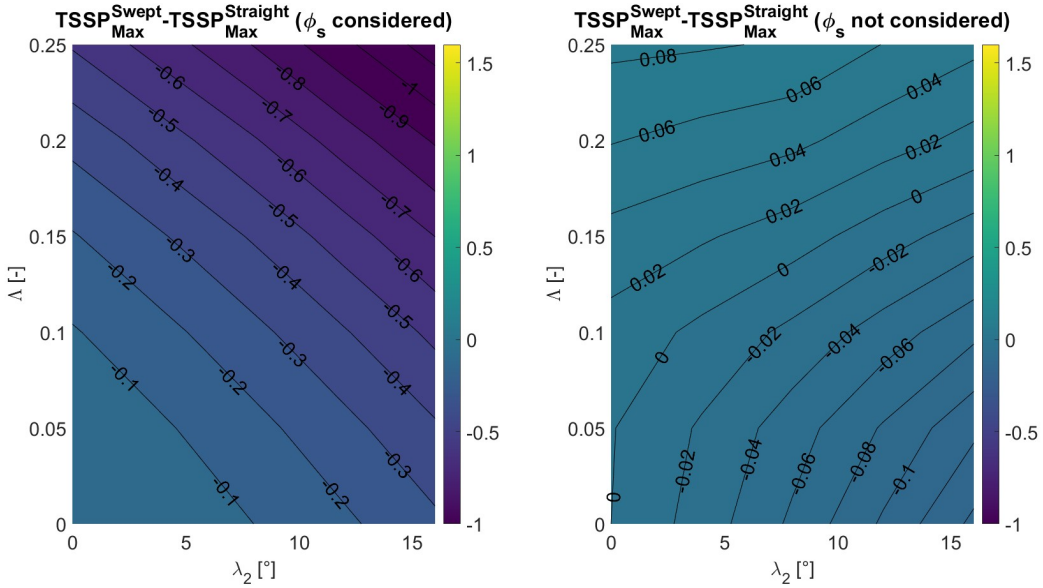


**Figure 9.40:** Difference in maximum noise emissions (TSSP) between propellers adopting a sweep distribution function of the MCA at the tip ($\Lambda$) and the forward sweep angle at the hub ($\lambda_2$) in isolated conditions at cruise condition. On the left, the noise emissions with the inclusion of the phase shift due to sweep $\phi_s$. On the right, the noise emissions without the inclusion of the phase shift.

In installed configurations, the dominance of unsteady noise sources due to varying blade loading significantly changes the impact of sweep compared to isolated propellers. As shown in Figure 9.41, the noise level variations are more pronounced in the installed case, with forward sweep increasing noise by up to $\Delta SPL_{Max} = +2.2dB$ and backward sweep reducing it by $\Delta SPL_{Max} = -4.7dB$. This contrasts with the isolated case shown in 9.39, where noise generally increased with sweep.
In the installed scenario, backward sweep can effectively reduce overall SPL, whereas forward sweep tends to raise noise levels. This difference arises from the complex interaction between blade sweep and unsteady loading noise contributions across the blade sections. Despite changes in phase shift of noise emissions due to sweep, the overall distribution of maximum noise levels remains similar, as reflected in the thrust specific sound pressure (TSSP) levels shown in Figure 9.42. This suggests that phase shift is not the primary factor in noise reduction for installed configurations.
Other key factors influencing noise levels include changes in the loading distribution along the blade span and the phasing of unsteady loading contributions. As shown in Figure 9.33, blade sweep alters the loading distribution, leading to increased noise at the tips in isolated cases. However, in installed configurations, sweep can mitigate noise by balancing the increased noise from altered loading distribution with the phase shift in unsteady loading contributions.
Figure 9.35 illustrates this effect, showing that the loading peak during tail wake impingement is higher with forward sweep and significantly lower with backward sweep. This indicates that backward sweep effectively delays the load jump encountered by various blade sections, reducing overall load jump and noise emissions. In contrast, forward sweep is counterproductive, as it aligns the contributions from

different blade sections, maximizing the loading jump and increasing noise levels.

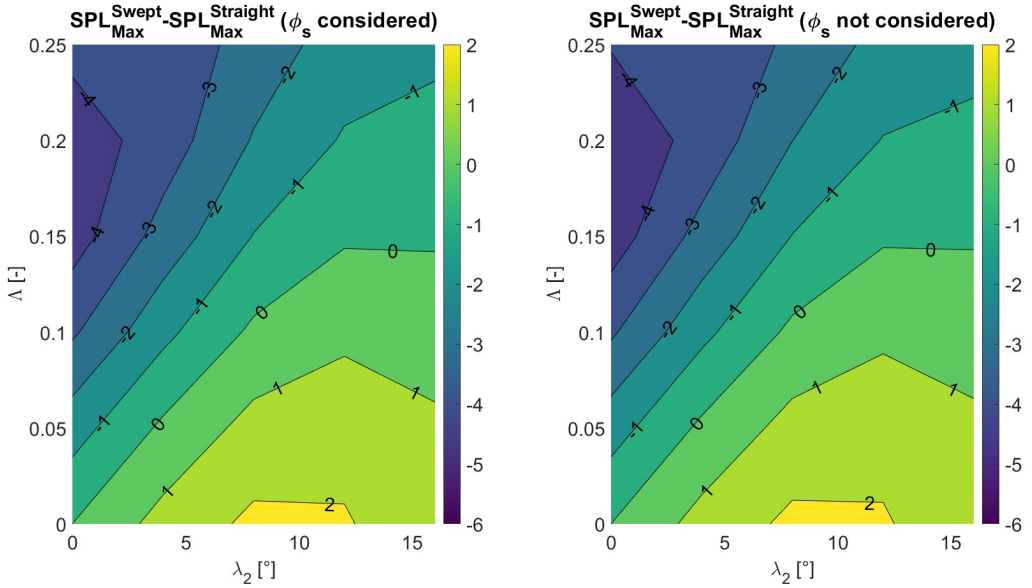


**Figure 9.41:** Difference in maximum noise emissions (SPL) between propellers adopting a sweep distribution function of the MCA at the tip ($\Lambda$) and the forward sweep angle at the hub ($\lambda_2$) in installed conditions at cruise condition. On the left, the noise emissions with the inclusion of the phase shift due to sweep $\phi_s$. On the right, the noise emissions without the inclusion of the phase shift.

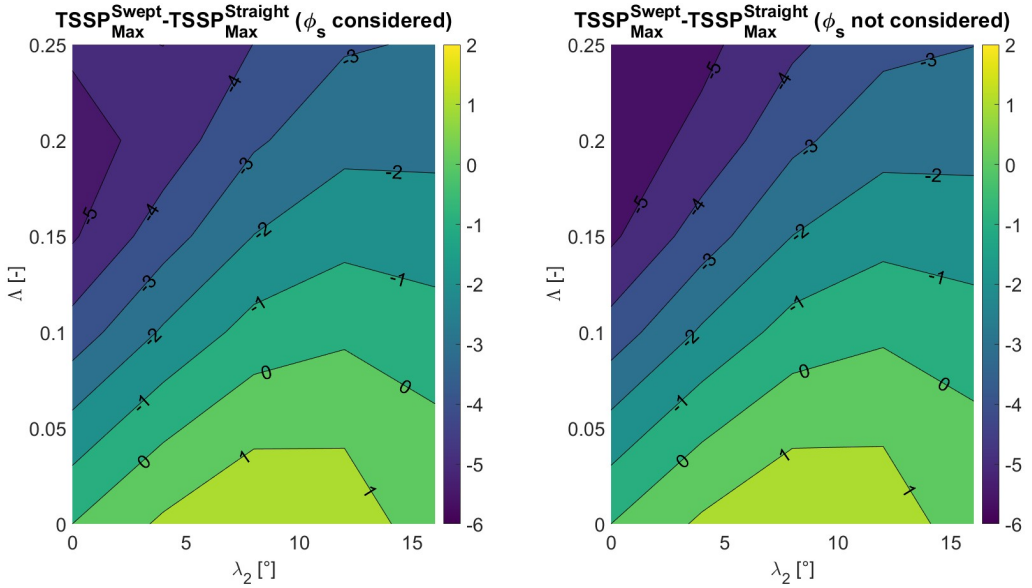


**Figure 9.42:** Difference in maximum noise emissions (TSSP) between propellers adopting a sweep distribution function of the MCA at the tip ($\Lambda$) and the forward sweep angle at the hub ($\lambda_2$) in installed conditions at cruise condition. On the left, the noise emissions with the inclusion of the phase shift due to sweep $\phi_s$. On the right, the noise emissions without the inclusion of the phase shift.

Figures 9.43 and 9.44 display the directivity plots of noise emissions for both isolated and installed propellers, comparing straight blades with various swept blade configurations.
In the isolated case, swept blades lead to a reduction in noise levels, as indicated by the TSSP. However, the overall shape of the directivity plots remains largely unchanged, suggesting that the torque noise

source continues to dominate, regardless of blade geometry.
In the installed case, the directivity plots also show a consistent shape across different sweep distributions, indicating that unsteady loading noise sources remain dominant. However, the variation in noise levels is greater and more evenly distributed across the direction of propagation, highlighting that blade sweep is more effective in altering noise from unsteady loading sources in installed configurations.

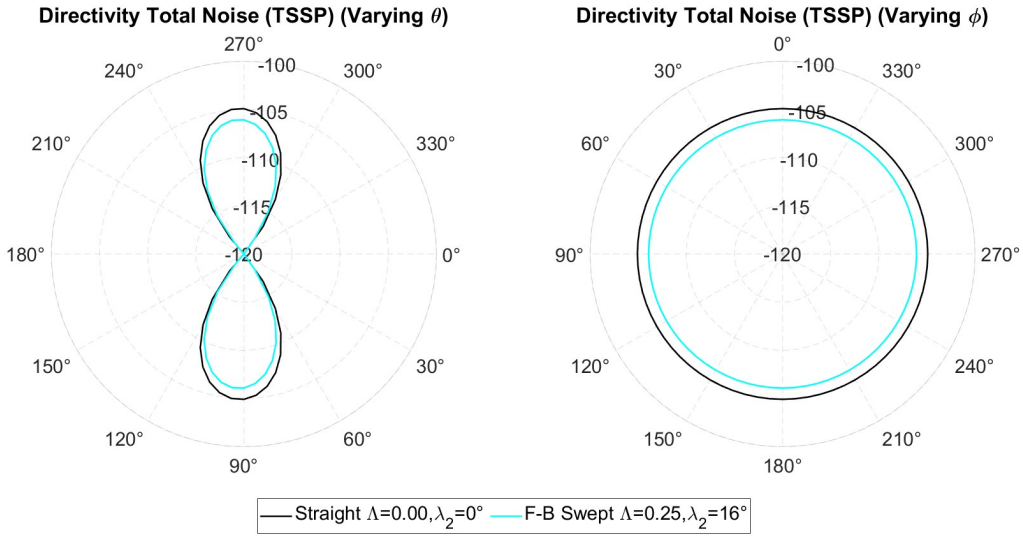


**Figure 9.43:** Directivity plots of the noise emissions in the isolated case at cruise conditions. On the left: the observers are positioned in the plane along the propeller axis. On the right: the observers are positioned in the plane of rotation.

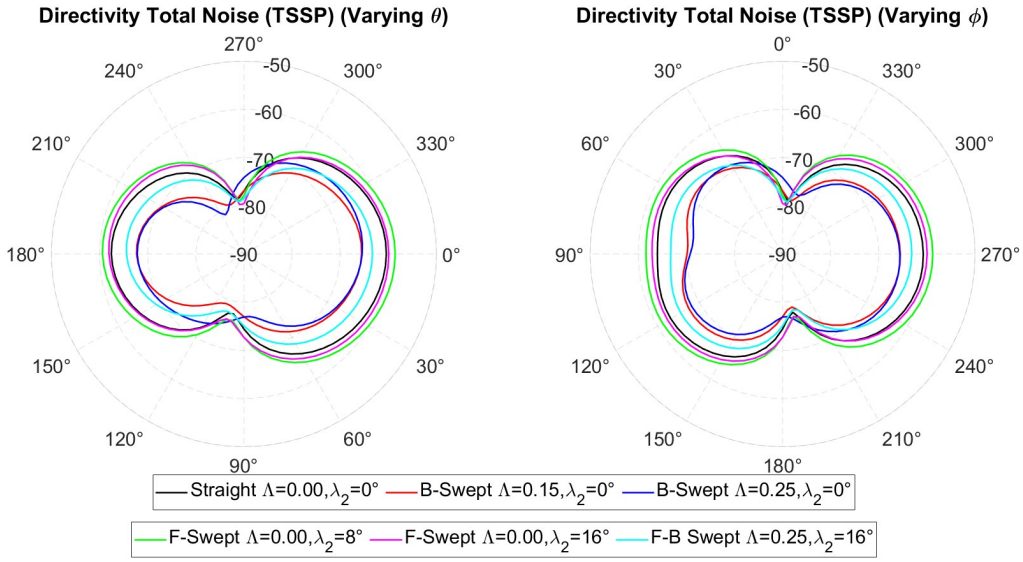


**Figure 9.44:** Directivity plots of the noise emissions in the installed case at cruise conditions. On the left: the observers are positioned in the plane along the propeller axis. On the right: the observers are positioned in the plane of rotation.

In summary, varying blade sweep has a substantial impact on propeller performance. Sweeping blades, especially with maximum tip MCA and forward sweep at the hub, increases blade loading, particularly at

the tips, leading to a $20\%$ increase in thrust and power and a $2\%$ improvement in the thrust-to-power ratio.
In installed conditions, sweep alters the timing at which different blade sections experience inflow distortions, changing the phase of unsteady loading contributions. This phase shift results in reduced amplitude of loading peaks with backward sweep and increased peaks with forward sweep.
Regarding aero-acoustics, the phase shift between noise sources along the blade introduced by sweep can reduce noise levels. However, the increased outboard loading generally leads to higher overall noise. In isolated conditions, the increase in loading typically outweighs the noise reduction from phase shift, especially at low rotational speeds ($M_t = 0.20$), resulting in higher noise levels.
In installed conditions, backward sweep significantly reduces unsteady loading noise ($\Delta SPL = -4.7dB$), while forward sweep increases it ($\Delta SPL = +2.2dB$), due to the dominance of unsteady loading noise and its sensitivity to sweep direction.
For high-speed applications like the APPU project's transport planes, higher freestream Mach numbers will enhance the effectiveness of sweep.
This analysis assumes rigid blades; however, real-world effects such as blade deformation from inertia and aerodynamic forces, as noted by J. Thielen [34], can significantly affect both thrust and noise.

# Part IV

## Conclusions and Recommendations

# 10

# Conclusions

This thesis aimed to capture the unsteady blade loading experienced by a propeller in a Boundary Layer Ingestion (BLI) installation and evaluate its impact on aerodynamic and aero-acoustic performance. Additionally, the study investigates whether altering the number of blades or the blade sweep distribution can enhance the benefits or mitigate the drawbacks of this installation.

To achieve this objective, the first step involved developing suitable numerical tools to estimate aerodynamic and aero-acoustic performance. The aerodynamic solver was based on the Unsteady Vortex Lattice Method (UVLM) due to its ability to model complex blade geometries and simulate lifting surfaces subjected to time-varying inflows. A viscous version, the Unsteady Non-Linear Vortex Lattice Method (UNVLM), was developed by coupling the UVLM with tabulated polar curves of the sections' airfoils to model features like flow separation, which could occur under installed conditions. Data obtained from this aerodynamic solver showed good agreement with data from high-fidelity model simulations and experimental campaigns. Subsequently, the acoustic solver was based on Hanson's Helicoidal Surface Theory (HST), capable of estimating the thickness and tonal loading noise sources at acceptable computational costs while modeling features like blade sweep and accounting for unsteady noise sources due to unsteady blade loading. After verifying the correct implementation of the HST model in the acoustic solver, the UNVLM and HST were coupled for use in analyzing the propeller in both isolated and installed conditions.

The first batch of analyses simulated the baseline six-bladed propeller during the climb and cruise phases in both isolated and installed conditions to assess the impact of the installation on aerodynamic and aero-acoustic performance. Then, a parametric study was conducted, progressively increasing the number of blades from two to six to estimate its impact on performance and assess how this impact changes between isolated and BLI configurations. Finally, a parametric study was conducted to evaluate the impact of the sweep distribution on aero-acoustic performance. This involved finding a suitable parameterization of the sweep radial distribution, determined by two variables: $\Lambda$ (the backward mid-chord alignment at the blade tip) and $\lambda_2$ (the forward sweep angle at the hub). The baseline six-bladed propeller was then simulated in both isolated and installed conditions with all combinations of these two sweep parameters.

## 10.1. Research Questions

The analysis described above was performed to address the research questions posed in Chapter 1, which are restated below for convenience. This section summarizes and briefly discusses the results illustrated in Chapter 9 to answer these questions.

**Research Question 1**

**What are the challenges arising from the installation of a propeller in a Boundary Layer Ingestion (BLI) position, particularly when accounting for the unsteady effects?**

The analysis in this research demonstrates that even propellers not specifically designed for Boundary Layer Ingestion (BLI) installations can benefit aerodynamically from such setups. Specifically, the time-averaged thrust-to-power ratio increased by $2\%$ to $5\%$ in the installed configuration, regardless of operating

conditions, blade count, or sweep distribution. However, when accounting for unsteady blade loading caused by circumferential distortion, new aerodynamic and aero-acoustic characteristics emerged that were not apparent in studies ignoring these flow distortions.
In a BLI installation, the inflow distortions encountered by the propeller blades are unevenly distributed across the propeller plane. For example, the flow beneath the fuselage experiences a widespread reduction in axial velocity due to the fuselage's non-axisymmetric shape. In contrast, above the fuselage, the wake from the vertical tail creates a localized region of reduced axial velocity. Consequently, blade loading increases more gradually when the blades pass beneath the fuselage and more abruptly when passing above it.
Maintaining a constant pitch setting of $\beta_{0.7R} = 45°$ while increasing spin velocity during the climb phase led to near-stall conditions on the inboard part of the blade in isolated conditions. When installed, significant reductions in axial flow due to boundary layer effects, tail wake impingement, and the non-axisymmetric fuselage further increased the angle of attack, leading to flow separation. This caused a reduction in loading in areas that experienced the highest loading increments during cruise conditions.
The unsteady blade loading results in peaky oscillations in the collective performance of the propeller rather than the smooth and steady thrust and power time-response typically expected. During cruise, these oscillations increased both thrust and power demand due to heightened loading, whereas during climb, the peaks corresponded to reductions in power demand. Despite the variability, the thrust-to-power ratio increased in both flight conditions since the rise in thrust was greater than the rise in power during cruise, and the drop in thrust was less than the drop in power during climb.
Additionally, the variable loading experienced by the blades generates in-plane forces in vertical and horizontal directions. The inflow distortion distribution in the propeller plane leads to a steady negative vertical force and an oscillating horizontal force with a wider amplitude.
Regarding noise emissions, the introduction of unsteady blade loading due to the installation leads to a significant increase in noise levels, with differences of up to 46 dB observed between the maximum noise emissions in the installed and isolated configurations. At both climb and cruise conditions, the noise emissions are dominated by unsteady loading noise sources, resulting in maximum noise emissions directed along the propeller axis. This increase in noise is evident not only in the amplitude but also in the frequency content. When unsteady loading noise sources are introduced, the emissions at higher noise harmonics ($m > 1$) are significantly elevated compared to the isolated case, where noise is primarily concentrated at the blade passage frequency (BPF), corresponding to the first noise harmonic ($m = 1$).

**Research Question 2**

**Is increasing the number of blades a valuable strategy to improve the aerodynamic performance while reducing the noise emissions of a BLI propeller?**

The parametric study where the number of blades was gradually increased was conducted without altering the operating conditions or pitch settings, as there was no specific thrust requirement imposed. This approach led to an increase in disk loading since thrust scaled with the number of blades, resulting in a reduction in propeller efficiency for both isolated and installed configurations. In-plane forces generated by the installed propellers scaled with thrust, with the horizontal component accounting for approximately $1 - 2\%$ of thrust and the vertical component about $2 - 3\%$.
The time-responses of forces and power generated by the installed propellers were notably influenced by the blade count. As the number of blades increased, the amplitude of oscillations decreased, while their frequency increased. This reduction in oscillation amplitude with a higher blade count is a well-known effect for other types of non-uniform inflows, such as a propeller operating at a non-zero angle of attack. However, in the more complex flow distortion associated with the BLI installation, the mechanism for reducing thrust variation amplitude differs slightly. The blade encountering the vertical tail's wake impingement experiences an abrupt increase in loading, which is responsible for the peaky oscillations that remain dominant even as the blade count increases. Consequently, the number of peaks in a revolution corresponds to the number of blades, leading to an increase in the frequency of these peaks with the blade passage frequency (BPF). Although the relative impact of the blade undergoing this abrupt loading change decreases with more blades, the oscillation amplitude does not reduce to zero, even with six blades. For instance, the amplitude of thrust oscillation does not fall below $4\%$ relative to the time-averaged thrust, even when the propeller has six blades. Unlike a propeller subjected to a non-zero angle of attack inflow, the reduction in amplitude

is not monotonic. For example, with four blades, the amplitude of thrust oscillation actually increases compared to a three-bladed propeller. This increase is due to the complex flow distortion associated with the BLI installation and the relative position of the blades in the propeller disk. In a four-blade configuration, the increase in blade loading experienced by the blade passing through the region affected by the tail's wake impingement is compounded by the blade simultaneously passing underneath the fuselage, where it experiences another significant increase in loading due to the fuselage's non-axisymmetric shape.
Regarding noise levels, increasing the blade count generally reduces the propagation efficiency of steady loading noise emissions, thereby lowering noise levels in isolated propellers where steady loading noise sources are dominant. However, in installed configurations like BLI, where unsteady loading is significant, increasing the blade count enhances the propagation efficiency of unsteady loading noise components while only reducing the contribution from steady loading sources. As a result, unsteady loading noise sources, particularly the thrust component, become dominant, making the reduction in overall noise levels less achievable. For example, increasing the blade count from two to six led to a reduction in noise levels of approximately $\Delta SPL_{Max} = -39$ dB in the isolated case, despite the higher disk loading. Conversely, in the BLI-installed configuration, the rise in unsteady loading noise sources outweighs the reduction in steady loading noise, causing the maximum total noise level to increase by $\Delta SPL_{Max} = +1$ dB. Therefore, increasing the blade count may not effectively reduce noise levels for propellers installed in a BLI configuration.

**Research Question 3**

**Is the adoption of swept blades an effective design choice to improve the aerodynamic performance of BLI propellers?**

The parametric study examining the impact of varying sweep distribution was conducted without imposing a specific thrust requirement, while the operating conditions were kept constant at cruise settings. Both in isolated and installed conditions, the adoption of sweep led to an increase in blade loading, particularly concentrated at the tips. This effect was most pronounced when maximum mid-chord angle (MCA) at the tip and maximum forward sweep at the hub were applied. As a result, there was an overall increase in thrust and power of up to $20\%$, and an enhancement in the thrust-to-power ratio of up to $2\%$ compared to propellers with straight blades, in both isolated and installed configurations.
When the propeller is installed, a secondary aerodynamic effect emerges: the blade sections encounter distortion at different times due to the sweep, introducing a delay and resulting in a more gradual increase in loading. This phase shift in the unsteady loading contributions reduces the amplitude of the loading peak when the blade encounters the vertical tail's wake if the blades are swept backward. Conversely, forward sweep increases this peak loading.
In terms of aero-acoustic performance, the effects of sweep are complex. One key mechanism is the phase shift ($\phi_s$) in noise emissions from the blade sections along the span. This phase shift, when integrated, generally reduces overall noise levels. However, the increased loading towards the outboard sections due to sweep can counteract this benefit, leading to higher maximum noise levels.
In isolated conditions, the noise increase due to outboard loading outweighs the noise reduction from the phase shift, resulting in a counter-intuitive increase in noise levels when blades are swept, with a maximum noise increase of $\Delta SPL_{Max} = +0.6$ dB.
When the propeller is installed and the blades are swept backward, the phase shift in unsteady loading contributions reduces the unsteady loading noise, which are the dominant noise sources in these conditions. This leads to significant noise reductions, up to $\Delta SPL_{Max} = -4.7$ dB. Conversely, forward sweep increases the unsteady loading noise, resulting in a noise penalty of up to $\Delta SPL_{Max} = +2.2$ dB.

## 10.2. Closing Remarks

The methodology adopted in this analysis successfully captured the variations in loading experienced by the blades of a Boundary Layer Ingestion (BLI) propeller. The aerodynamic solver, based on the low-fidelity Unsteady Non-Linear Vortex Lattice Method, effectively captured in-plane forces and the oscillations in thrust delivered by the entire propeller, thanks to the independent modeling of each blade. The aero-acoustic solver, utilizing Hanson's Helicoidal Surface Theory, successfully identified the primary tonal noise sources, including thickness, steady loading, and unsteady loading noise components. Both the

aerodynamic and aero-acoustic models proved to be relatively fast-computing tools, as the simulation time required to model the aero-acoustic performance of a propeller in both isolated and installed conditions remained under 15 minutes. The simplification of the wake model was crucial in achieving this efficiency, as the computational time required by the aerodynamic solver was sensitive to the resolution and dimensions of the wake.

However, the speed of computation came at the expense of accuracy in performance estimates. Specifically, the aerodynamic solver relied on the coarse Prandtl-Glauert correction model to account for compressibility effects, which limited the operational conditions of the propeller simulations. As a result, the propeller was simulated under conditions similar to those used to validate the aerodynamic solver, with the spinning tip Mach number limited to $M_t = 0.2$ during cruise and $M_t = 0.3$ during climb conditions. The study demonstrated that this parameter strongly influences the efficiency of steady loading noise propagation and the effectiveness of sweep in reducing noise emissions through phase shifts in noise sources along the blade span.

Consequently, the conclusions drawn from the parametric studies in this thesis may not be directly applicable to applications characterized by higher tip Mach numbers ($M_t$). At $M_t \approx 0.7 - 0.8$, typical of transport planes like the APPU project, the efficiency of steady loading noise propagation is significantly enhanced, leading to noise patterns at both cruise and climb that differ from those obtained using lower spinning tip Mach numbers. In this scenario, steady loading sources, particularly torque, become dominant, with the highest emissions occurring in the propeller's rotational plane. This suggests that increasing the number of blades may still be a viable strategy for reducing noise emissions, as it effectively targets steady loading noise sources. Additionally, the impact of the phase shift between noise sources along the blade span due to sweep is expected to become more pronounced at higher rotational speeds. This is because shorter noise wavelengths and the increased relative importance of the geometric displacement of blade sections—achieved through sweep distribution—amplify the effects of phase shifts.

Another limitation in accuracy arises from the manner in which the propeller was simulated in installed conditions. The velocity profile at the propeller disk, derived from CFD simulations of the fuselage, was used as the inflow for the installed propeller simulations. This approach allowed the propeller to be simulated without modeling the fuselage, using the low-fidelity approach described. However, this inherently limits the model's fidelity, as one interaction effect between the propeller and the airframe could not be modeled. Since the fuselage was simulated without the propulsor installed in the CFD simulation, the velocity distribution does not account for the suction generated by the propeller, which is expected to alter the inflow. While the overall impact of this simplification is likely minimal across the propeller disk, the suction effect is expected to reduce the velocity deficit in the region affected by the vertical tail [9]. Therefore, the variation in inflow due to the tail's wake impingement may have been overestimated in this study, leading to exaggerated loading variations when the blades pass through this region.

In summary, the methodology adopted in this research represented a good trade-off between fidelity and computational time, successfully achieving the thesis objectives for scaled propellers operating at low speeds. The inclusion of unsteady blade loading had significant effects on the aerodynamic and aero-acoustic performance of the propeller, justifying the focus on this area of research. However, the inherent limitations of this approach may restrict the applicability of the conclusions to propellers operating under conditions similar to those studied in this thesis.

# 11

# Recommendations

The research conducted in this thesis has been constrained by the use of low-fidelity methods and the limited time available, leaving ample opportunities for further investigation by other researchers interested in this topic.

**Improvement of Aerodynamic Modelling**
The low-fidelity aerodynamic model employed in this study is not suitable for accurately simulating high-speed conditions where the local Mach number exceeds $M = 0.6$. As a result, the propeller simulations were restricted to low flight speeds with corresponding low spinning tip Mach numbers $M_t < 0.3$. The study's findings highlight that noise propagation efficiency is significantly affected by the spinning tip Mach number, suggesting that the conclusions may not be directly applicable to high-speed applications, such as the APPU project.
To enhance the relevance of this research for high-speed conditions, one approach could involve using the scaled loading distributions (i.e., $C_L$ and $C_D$) obtained from the aerodynamic solver at low speeds and inputting them into the acoustic solver while applying higher freestream and spinning tip Mach numbers, as outlined in Section 9.1. Alternatively, if higher fidelity tools that accurately model transonic aerodynamics are available, repeating the analysis with these tools would ensure that the transonic effects are accurately reflected in the noise contributions.

**Consideration of Installation Effects**
The current modeling approach does not account for the propeller's suction effect, which could influence the loading and noise characteristics. Future research should explore this upstream effect and its impact on propeller loading.
Additionally, this study was conducted using a fuselage not specifically designed for propeller installation. Given that changes in inflow significantly affect loading and aero-acoustic performance, a promising area for future research could be an optimization study focused on modifying the fuselage at the propeller installation site. This study would aim to achieve a velocity distribution that maximizes the benefits of the installation while minimizing any negative impacts.

**Inclusion of Structural Dynamics**
This study did not include structural considerations, assuming that the blades were perfectly rigid. However, various studies [32], [34] suggest that this assumption may not hold, especially when blades are swept, as it could lead to a significant overestimation of loading and, consequently, noise levels. Therefore, it is recommended to couple the aerodynamic and aero-acoustic solvers with aero-elastic models to investigate the effects of blade deformations on performance and noise.

**Exploration of Additional Design Variables**
Lastly, the study was conducted using a baseline propeller that was not specifically designed for this installation, and only a few geometric parameters were varied at a time to evaluate their impact on noise levels. Future research could explore the impact of other design parameters, such as chord, twist, and camber distributions. A comprehensive optimization study where these geometric distributions are allowed to vary in conjunction with the design variables examined in this thesis would be particularly valuable.
It would be particularly interesting to assess whether the inboard shift in loading, recommended by sources

focused on designing quiet propellers [20] and BLI propellers [22], emerges as a result of the optimization, and if so, how this configuration performs.

These recommendations aim to guide future research towards achieving a more comprehensive understanding and improved design of propellers, particularly in configurations involving boundary layer ingestion and high-speed applications.

# References


[1] L.L.M. Veldhuis. *Propeller wing aerodynamic interference*. PhD Thesis. Delft, The Netherlands: Delft University of Technology, 2005.

[2] B. Magliozzi D.B. Hanson et al. “Propeller and Propfan Noise”. In: *Aeroacustics of Flight Vehicles: Theory and Practise. Volumne 1: Noise Sources 1* (1991).

[3] L. Smith Jr. “Wake Ingestion Propulsion Benefit”. In: *27th Joint Propulsion Conference, Sacramento,USA* (1991).

[4] Delft University of Technology. *Advanced Propulsion and Power Unit*. Accessed: 2024-07-02. 2024. URL: https://www.tudelft.nl/lr/appu.

[5] David S. Lee et al. “Aviation and global climate change in the 21st century”. In: *Atmospheric Environment* 43.22 (2009), pp. 3520–3537. DOI: https://doi.org/10.1016/j.atmosenv.2009.04.024. URL: https://www.sciencedirect.com/science/article/pii/S1352231009003574.

[6] Stefan Gössling et al. “The global scale, distribution and growth of aviation: Implications for climate change”. In: *Global Environmental Change* 65 (2020), pp. 102–194. DOI: https://doi.org/10.1016/j.gloenvcha.2020.102194. URL: https://www.sciencedirect.com/science/article/pii/S0959378020307779.

[7] ACARE. *Flightpath 2050 Europe’s Vision for Aviation*. Tech. rep. European Commission, 2011.

[8] Franssen EA et al. “Aircraft noise around a large international airport and its impact on general health and medication use.” In: *Occup Environ Med.* 61(5) (2004), p. 102194. DOI: https://doi.org/10.1136/oem.2002.005488.

[9] T. Sinnige et al. “APIAN-INF: an aerodynamic and aeroacoustic investigation of pylon-interaction effects for pusher propellers”. In: *CEAS Aeronautical Journal 9.2* (2018), pp. 291–306. DOI: 10.1007/s13272-017-0247-2.

[10] E.R. Booth G.L. Gentry et al. “Effect of Pylon Wake With and Without Pylon Blowing on Propeller Thrust”. In: *NASA technical memorandum 4162* (1990).

[11] Antonio Martínez Fernández et al. “Effect of a fuselage boundary layer ingesting propulsor on airframe forces and moments”. In: *Aerospace Science and Technology* 100 (2020). DOI: https://doi.org/10.1016/j.ast.2020.105808. URL: https://www.sciencedirect.com/science/article/pii/S1270963819316827.

[12] T. Sinnige. “Fundamentals of Isolated Propellers”. In: *AIAA short course, Propeller Aerodynamics* (2022).

[13] N. van Arnhem. *Unconventional Propeller−Airframe Integration for Transport Aircraft Configurations*. PhD Thesis. Delft, The Netherlands: Delft University of Technology, 2022.

[14] M. Kingan A.B. Parry et al. “Relative Importance of Open Rotor Tone and Broadband Noise Sources”. In: *17th AIAA/CEAS Aeroacustics Conference, AIAA Paper 2011-2763* (2011).

[15] D.K. Hall. “Boundary Layer Ingestion Propulsion –Benefit, Challenges, and Opportunities”. In: *5th UTIAS International Workshop on Aviation and Climate Change University of Toronto* (2016).

[16] M. Drela. “Power Balance in Aerodynamic Flows”. In: *AIAA 47* (2009).

[17] N. van Arnhem. *Design and Analysis of an Installed Pusher Propeller with Boundary Layer Inflow*. MSc Thesis. Delft, The Netherlands: Delft University of Technology, 2015.

[18] F.P. Costa et al. “Aerodynamic Analysis of Conventional and Boundary Layer Ingesting Propellers”. In: *Journal of Engineering for Gas Turbines and Power* (2023).

[19] N. van Arnhem et al. “Engineering Method to Estimate the Blade Loading of Propellers in Nonuniform Flow”. In: *AIAA Journal (2020)* (2020), pp. 1–15. DOI: 10.2514/1.J059485.

[20] C. Negulescu. “Airbus AI-PX7 CROR Design Features and Aerodynamics”. In: *SAE Int. J. Aerosp. 6(2)* (2013). DOI: 10.4271/2013-01-2245.

[21] D.B. Hanson et al. “The importance of quadrupole sources in prediction of transonic tip speed propeller noise”. In: *Journal of Sound and Vibration 62.1* (1979), pp. 19–38. DOI: 10.1016/0022-460X(79)90554-6.

[22] P. Lv et al. “Conceptual Analsis of Boundary Layer Ingestion Towards Aircraft Propulsion Integration”. In: *ISABE Conference* (2013).

[23] D.B. Hanson. “The influence of propeller design parameters on far field harmonic noise in forward flight”. In: *American Institute of Aeronautics and Astronautics (AIAA)* (1979). DOI: 10.2514/6.1979-609.

[24] Sinnige et al. “Rapid Aeroacoustic Planform Design Optimization of Installed Propellers”. In: *33rd Congress of the International Council of the Aeronautical Sciences.* (2022).

[25] C.J. Miller et al. “Noise Constraints Effecting Optimal Propeller Designs”. In: *NASA Technical Memorandum 86967* (1985).

[26] D. Ingraham. “Low-Noise Propeller Design with the Vortex Lattice Method and Gradient-Based Optimization”. In: *AIAA SciTech Forum* (2022).

[27] B. G. Marinus et al. “Aeroacoustic and aerodynamic optimization of aircraft propeller blades.” In: *16th AIAA/CEAS Aeroacoustics Conference* (2010). DOI: 10.2514/6.2010-3850.

[28] Rotterdam The Hague Innovation Airport. *Smart Rotors*. Accessed: 2024-08-24. 2023. URL: https://stichtingrhia.nl/portfolio/smart-rotors/.

[29] D.B. Hanson. “Helicoidal Surface Theory for Harmonic Noise of Propellers in the Far Field”. In: *AIAA Journal 18.10* (1980).

[30] D.B. Hanson. “Noise of Counter-rotation Propellers”. In: *AIAA/NASA 9th Aeroacoustic Conference* (1985).

[31] T. Sinnige. “Propeller modeling method”. In: *AIAA short course, Propeller Aerodynamics* (2022).

[32] O. Gur et al. “Comparison between Blade-Element models of propellers”. In: *Technion Israel Institute of Technology - 48th Israel Annual Conference on Aerospace Sciences 2008* (2008), pp. 1139–1169.

[33] O. Gur et al. “A novel approach to actuator disk modeling”. In: *32nd European Rotorcraft Forum* (2006), pp. 1–35.

[34] Jaimie Thielen. *Effects of Elasticity on Aeroacoustic Performance of Low-Noise Swept Propellers*. MSc Thesis. University of Technology of Delft, 2024.

[35] J. Katz et al. *Low Speed Aerodynamics*. 2nd ed. Cambridge University Press, 2001.

[36] Hakjin Lee et al. “Numerical investigation of the aerodynamics and wake structures of horizontal axis wind turbines by using nonlinear vortex lattice method”. In: *Renewable Energy* 132 (2019), pp. 1121–1133. DOI: 10.1016/j.renene.2018.08.087. URL: https://www.sciencedirect.com/science/article/pii/S0960148118310371.

[37] A. Gopalarathnam R. Mukherjee. “Poststall prediction of multiple-lifting surface configurations using a decambering approach”. In: *J. Aircraft* 43 (2006).

[38] H. Segawa A. Gopalarathnam. “Use of lift superposition for improved computational efficiency of wing post-stall prediction”. In: *26th AIAA Applied Aerodynamics Conference* (2008).

[39] E.A. Ebbens. *Aerodynamic modelling of open rotor-wing-flap interactions with low-fidelity methods*. MSc Thesis. University of Technology of Delft, 2022.

[40] H. Lee et al. “Review of vortex methods for rotor aerodynamics and wake dynamics”. In: *Adv. Aerodyn. 4, 20 (2022)* (2022). DOI: https://doi.org/10.1186/s42774-022-00111-3.

[41] Mark Drela. *XFOIL: An Analysis and Design System for Low Reynolds Number Airfoils*. Software. Available from: http://web.mit.edu/drela/Public/web/xfoil/. 1989.

[42] Larry Viterna et al. “Theoretical and experimental power from large horizontal-axis wind turbines”. In: *NASA Technical Memorandum* (Oct. 1982).

[43] J. E. Ffowcs Williams et al. “Sound Generation by Turbulence and Surfaces in Arbitrary Motion”. In: *Philosophical Transactions of the Royal Society of London. Series A, Mathematical and Physical Sciences* 264.1151 (1969), pp. 321–342. URL: http://www.jstor.org/stable/73790.

[44] F. Farassat et al. “Open Rotor Noise Prediction Methods at NASA Langley: A Technology Review”. In: *15th AIAA/CEAS Aeroacoustics Conference (30th AIAA Aeroacoustics Conference)* (May 2009). DOI: 10.2514/6.2009-3133.

[45] Jatinder Goyal. *Hanson’s Model in Frequency Domain - Tonal Noise of Rotors in Uniform Inflow*. 2024. DOI: 10.4121/7DA5AA45-E44B-4FA3-9407-8BF61E835D99.V1. URL: https://data.4tu.nl/datasets/7da5aa45-e44b-4fa3-9407-8bf61e835d99/1.

[46] Wouter de Gruijl. *The Impact of Installation Effects on Propeller Design Optimization for Aerodynamic and Aeroacoustic Performance*. MSc Thesis. University of Technology of Delft, 2022.

[47] Q. Li K. Öztürk T. Sinnige D. Ragni G. Eitelberg L. Veldhuis et al. “Design and Experimental Validation of Swirl-Recovery Vanes for Propeller Propulsion Systems”. In: *AIAA Journal 56.12* (2018).

[48] Nando van Arnhem et al. “Engineering Method to Estimate the Blade Loading of Propellers in Nonuniform Flow”. In: *AIAA Journal* 58 (Oct. 2020), pp. 5332–5346. DOI: 10.2514/1.J059485.

[49] Mark Kotwicz Herniczek. “Evaluation of Acoustic Frequency Methods Coupled to Blade Element Momentum Theory for the Prediction of Propeller Noise”. PhD thesis. Carleton University, 2017.

[50] Wouter de Haan. *Impact of Blade Sweep on Aerodynamic and Aeroacoustic Performance Optimization of Isolated Propellers*. MSc Thesis. University of Technology of Delft, 2021.

[51] DW Kurtz et al. “A review of aerodynamic noise from propellers, rotors, and lift fans”. In: (1970).

[52] Jatinder Goyal et al. *Aerodynamics and Far-field Noise Emissions of a Propeller in Positive and Negative Thrust Regimes at Non-zero Angles of Attack*. DOI: 10.2514/6.2023-3217.